SANDIA REPORT
SAND2006-7148
Unlimited Release
Printed October 2006

Z-Inertial Fusion Energy: Power Plant Final Report FY 2006

Jason T. Cook, Gary E. Rochau, Benjamin B. Cipiti , Charles W. Morrow, Salvador B. Rodriguez, Cathy O. Farnum, Marcos A. Modesto-Beato, Samuel Durbin, James D. Smith, Paul E. McConnell, Dannelle P. Sierra, Craig L. Olson, Wayne Meier, Ralph Moir, Per F. Peterson, Philippe M. Bardet, Chris Campen, James Franklin, Haihua Zhao, Gerald L. Kulcinski, Mark Anderson, Jason Oakley, Ed Marriott, Jesse Gudmundson, Kumar Sridharan, Riccardo Bonazza, Virginia L. Vigil, Mohamed A. Abdou, Lothar Schmitz, Alice Ying, Tomas Sketchley, Yu Tajima, Said I. Abdel-Khalik, Brian Kern, Said.M. Ghiaasiaan

Prepared by
Sandia National Laboratories
Albuquerque, New Mexico 87185 and Livermore, California 94550

Sandia is a multiprogram laboratory operated by Sandia Corporation,
a Lockheed Martin Company, for the United States Department of Energy's
National Nuclear Security Administration under Contract DE-AC04-94AL85000.

Issued by Sandia National Laboratories, operated for the United States Department of Energy by Sandia Corporation.

Available to DOE and DOE contractors from
U.S. Department of Energy
Office of Scientific and Technical Information
P.O. Box 62
Oak Ridge, TN 37831

Telephone: (865) 576-8401
Facsimile: (865) 576-5728
E-Mail: reports@adonis.osti.gov
Online ordering: http://www.osti.gov/bridge

Available to the public from
U.S. Department of Commerce
National Technical Information Service
5285 Port Royal Rd.
Springfield, VA 22161

Telephone: (800) 553-6847
Facsimile: (703) 605-6900
E-Mail: orders@ntis.fedworld.gov
Online order: http://www.ntis.gov/help/ordermethods.asp?loc=7-4-0#online

SAND2006-7148
Unlimited Release
Printed October 2006

Z-Inertial Fusion Energy: Power Plant Final Report FY06

Jason T. Cook[1], Gary E. Rochau[1], Benjamin B. Cipiti[1], Charles W. Morrow[1], Salvador B. Rodriguez[1], Cathy O. Farnum[1], Marcos A. Modesto-Beato[1], Samuel Durbin[1], James D. Smith[1], Paul E. McConnell[1], Dannelle P. Sierra[1], Craig L. Olson[1], Wayne Meier[2], Ralph Moir[2], Per F. Peterson[3], Philippe M. Bardet[3], Chris Campen[3], James Franklin[3], Haihua Zhao[3], Gerald L. Kulcinski[4], Mark Anderson[4], Jason Oakley[4], Ed Marriott[4], Jesse Gudmundson[4], Kumar Sridharan[4], Riccardo Bonazza[4], Virginia L. Vigil[4], Mohamed A. Abdou[5], Lothar Schmitz[5], Alice Ying[5], Tomas Sketchley[5], Yu Tajima[5], Said I. Abdel-Khalik[6], Brian Kern[6], .M. Ghiaasiaan[6]

[1] Sandia National Laboratories, P.O. Box 5800, Albuquerque, NM 87107, USA
[2] Lawrence Livermore National Laboratories, 7000 East Ave., Livermore, CA 94550, USA
[3] University of California, 4111 Etcheverry Hall, Berkeley, CA 94720-1730, USA
[4] University of Wisconsin, 1415 Engineering Dr., Madison, WI 53706-1691, USA
[5] University of California, 44-114 ENG IV, Los Angeles, CA 90095-1597, USA
[6] Georgia Institute of Technology, 801 Ferst Dr., Atlanta, GA 30332-0405, USA

Jason T. Cook, Editor
Sandia National Laboratories
P.O. Box 5800
Albuquerque, New Mexico 87185-MS1076

Abstract

This report summarizes the work conducted for the Z-inertial fusion energy (Z-IFE) late start Laboratory Directed Research Project. A major area of focus was on creating a roadmap to a z-pinch driven fusion power plant. The roadmap ties Z-IFE into the Global Nuclear Energy Partnership (GNEP) initiative through the use of high energy fusion neutrons to burn the actinides of spent fuel waste. Transmutation presents a near term use for Z-IFE technology and will aid in paving the path to fusion energy. The work this year continued to develop the science and engineering needed to support the Z-IFE roadmap. This included plant system and driver cost estimates, recyclable transmission line studies, flibe characterization, reaction chamber design, and shock mitigation techniques.

ACKNOWLEDGMENTS

The authors would like to acknowledge the support of the Laboratory Directed Research and Development Projects 81753 and 102362 for this research.

CONTENTS

FIGURES

TABLES

NOMENCLATURE

CEP	Chemical Engineering Plant Cost Index
CLT	Collapsed Liquid Thickness
COE	Cost of Electricity
D-T	Deuterium-Tritium
DBTT	Ductile-Brittle Transition Temperature
dpa	Displacements per Atom
DOE	Department of Energy
DWT	Demineralized Water Tank
EBW	Exploding Bridge Wire
EDX	Energy Dispersive X-Ray Spectrometer
EIA	Energy Information Administration
Flibe	$(LiF)_2$-BeF_2
FY	Fiscal Year
GEN IV	Generation IV
GNEP	Global Nuclear Energy Partnership
HE	High Explosive
IFE	Inertial Fusion Energy
ITER	International Thermonuclear Experimental Reactor
LDRD	Laboratory Directed Research and Development
LTD	Linear Transformer Driver
LTE	Local Thermodynamic Equalibrium
LWR	Light Water Reactor
MITL	Magnetically Insulated Transmission Line
MFE	Magnetic Fusion Energy
MSRE	Molten Salt Reactor Experiment
NIF	National Ignition Facility
ODS	Oxide Dispersion Strengthened
PRF	Permeation Reduction Factor
RGA	Residual Gas Analysis
RTL	Recyclable Transmission Line
SEM	Scanning Electron Microscope
STP	Standard Temperature and Pressure
TEP	Total Energy and Diagnostic Tool
TGS	Transmission Grating Spectrometer
USE	Upper Shelf Energy
UTS	Ultimate Tensile Strength
UV	Ultraviolet
VHEX	Vacuum Hydraulic Experiment
ZN	Z-Neutron

1. EXECUTIVE SUMMARY

Past z-inertial fusion energy research concentrated mainly on the full scale plant design. This year an effort was made to create a logical path to reach the ultimate goal of a fusion power plant through transmutation. To illustrate this path forward a roadmap was created outlining the current issues, needed steps, and time required to reach these goals.

The roadmap outlines the intermediate steps required to reach a full scale transmutation plant with the advent of a pure fusion energy plant being built several years later. It starts with utilizing existing facilities capable of handling various separate effects experiments. These facilities include Sandia National Laboratories' Z-beamlet and ZR where several containment and mitigation experiments can be conducted. The next step is to build a test facility (Z-Neutron or ZN) where automation, recyclable transmission line (RTL) remanufacturing, target fabrication, and driver development can take place and eventually be integrated together. With the inception of the Global Nuclear Energy Partnership (GNEP) initiative and the goal of a closed fuel cycle, an alternative use for z-pinch driven fusion arises. Work conducted through the Advanced Fusion Concepts: Neutrons for Testing and Energy Grand Challenge LDRD has shown that fusion neutrons can transmute the actinides in spent fuel [1]. The ZN facility will also be the test bed for developing z-pinch inertial fusion energy (IFE) transmutation. Once everything is integrated, ZN will become the pilot plant for the full scale transmutation plant.

Substantial progress on various power plant systems such as the RTL, flibe characterization, plant automation, power conversion systems, linear transformer drivers (LTD), and tritium permeation studies have been made. A high level systems cost analysis was also created in an attempt to optimize the number of fusion reaction chambers, target yield, and repetitive rate required to be competitive with other fusion power plant design studies.

The system cost analysis indicated that fewer chambers were more economical than the original Z-IFE power plant design of ten chambers. Three alternatives were suggested in the analysis for reducing the amount of reaction chambers needed for a 1000 MWe power plant: 1) an increase in target yield, 2) an increase in repetitive rate, or 3) both an increase in repetitive rate and target yield. In changing these parameters the number of chambers was reduced thus reducing the cost of the plant. The combination of the two options was found to be the most economical choice.

A detailed driver cost model was done in addition to the systems cost model. It includes the cost of all of the LTD components, the auxiliary equipment, and the land and facilities to support a full scale fusion power plant. The driver will be a significant percentage of the power plant cost.

Various studies of the chemical interaction between a flibe-like salt and a steel RTL post shot were conducted. This was done to gain an understanding of how the free ions of the dissociated salt and steel interact. Further experimentation on the electrical properties of a frozen flibe RTL was conducted to understand its effectiveness in transmitting the pulse to the target.

Four power conversion systems were investigated; supercritical CO_2 cycle, Rankine cycle, Brayton cycle, and a combined cycle (Brayton-Rankine). A cycle analysis of each showed how temperature and component efficiency affect the overall thermal-to-electric efficiency of the power plant. Assuming that high temperature materials would be available in the future, the cycle analysis showed that the combined cycle power conversion system was best for the Z-IFE plant.

A tritium permeation study of the piping and chamber was addressed this year. It was compared to the analysis conducted for the International Thermonuclear Experimental Reactor (ITER). Both stainless steel and reduced activation steel piping were analyzed using a DIFFUSE model. The results showed that using a permeation barrier coating on the pipes along with

optimizing partial pressure and diameter could reduce tritium leakage significantly. In fact, optimizing the piping system for Z-IFE could result in a significantly lower leakage rate compared to the results of the ITER analysis.

The shock mitigation work focused on attenuating the high energy x-rays before they reached the chamber wall. Three possible x-ray absorbing methods were investigated; thick liquid curtains, aerosols, and gas. Two possible chamber designs were proposed based on these proposed shock mitigation schemes. The first was a thick liquid blanket design and the second a first wall design.

Extensive liquid curtain research has been conducted under the Z-IFE program in previous years. Thick liquid curtains were studied because they offer both x-ray and neutron protection for the chamber wall. A new higher repetition rate was proposed for a thick liquid curtain chamber design based on the results from the systems cost analysis. This proposed chamber design required a slightly larger target yield and over fives times the repetitive rate of the original Z-IFE design. It utilized a frozen flibe RTL to lower separations and remanufacturing costs. A detailed analytical analysis of the shot timing is presented.

Due to recent research on aerosol x-ray absorption and thermal annealing, a new first wall chamber design was proposed. Modeling results of aerosols absorbing x-rays have shown promise that they may be able to mitigate fusion yields up to 3 GJ. Thermal annealing of the LWR pressure vessels around the world has shown near to complete recovery of the materials mechanical properties almost eliminating the effects of neutron embrittlement. If this is the case, the liquid curtain could be relocated to the outside of the chamber and act only as the heat transfer fluid and tritium breeder as opposed to also acting as the shock absorber in the liquid curtain design. This would greatly reduce the complexity of the internals of the reaction chamber. However, the thick liquid curtain design remains the prime candidate for shock mitigation for Z-IFE.

Previous chamber stress analyses focused on designing a chamber based on a static pressure or impulse pressure. This year a fatigue study was performed to assess the endurance limit of a chamber made from F82H steel (the baseline material for Z-IFE). A cyclic pulse to the chamber wall is inherent in a z-pinch driven inertial confinement fusion power plant. The study concluded that fatigue should be considered along with the impulse pressure when designing the chamber.

Substantial progress was made this year for the Z-IFE project. The roadmap illustrated the need to start experimentation immediately so that the base science and engineering required to build upon could be established. The initial experiments could be performed on existing facilities at Sandia National Laboratories. Significant strides were made in the areas of systems cost modeling, chamber design, and shock mitigation techniques for a Z-IFE power plant. It is time for the Z-IFE program to focus more on conducting the necessary experiments needed to prove the science and engineering required to forge ahead towards fusion energy.

2. Z-INERTIAL FUSION ENERGY ROADMAP

Inertial fusion energy (IFE) has the potential to generate safe, secure, and reliable commercial power for future generations. Lasers (National Ignition Facility-NIF), heavy ions, and more recently z-pinch technology have been used to create the necessary environment for IFE. Although the first two methods have a head start, a z-pinch driven system has been shown to be an excellent option. In addition to producing electricity, a great opportunity exists for a z-pinch driven IFE system as an alternative to fast reactors in the Global Nuclear Energy Partnership (GNEP) initiative. Research, as part of a Grand Challenge LDRD, has shown that fusion source neutrons can transmute some or all of the transuranics of spent fuel from light water reactors [1]. The reduction in heat load due to transmutation could greatly increase the storage capability of the repository and diminish some of the long lived radionuclides.

Several major issues must be addressed before this can be realized. The first issue is fusion yield. Currently, the Z-machine can not produce a sustainable fusion burn. The hope with ZR is to obtain a fusion burn with a yield on the order of 0.1 MJ. However, there is no pulsed power/fusion energy program to strive and create the higher yields that would be required for transmutation and commercial energy production. The fusion yield required is approximately 200-250 MJ for transmutation and 3-30 GJ for a power plant. A program must be created to increase the fusion yield.

The second issue is that the time between each fusion event must be reduced significantly in order to both transmute waste and produce continuous power. A fusion event must occur every 1 to 10 seconds depending on the fusion yield to generate a sufficient amount of heat for energy production and supply the necessary amount of fast neutrons needed for transmutation. This involves research on several fronts. Extensive target and mass production capabilities must be developed. A simple and light weight recyclable transmission line (RTL), which connects the target to the power source, must be designed. Placing and removing the RTL in the containment vessel will require state-of-the-art automation. Pumping the vessel and driver components down to the appropriate vacuum will also be necessary to ensure the electric pulse integrity. All these issues must be addressed in order for z-pinch driven IFE to be feasible. These issues are addressed in a roadmap developed to outline the necessary steps to achieve transmutation and fusion energy.

The Z-Inertial Fusion Energy (Z-IFE) program has developed two roadmaps. The first (original) roadmap outlines a direct path to fusion energy [2]. This roadmap describes two facilities needed to reach a full scale demo Z-pinch IFE fusion power plant. The first is a proof-of-principle (Z-PoP) facility which demonstrates repetitively rated drivers, RTL optimization, and thick liquid wall development between the years of 2007 and 2010. The next facility is a high yield engineering test facility (Phase I) which will be used to develop single shot high yield targets. Once high yield targets have been demonstrated, the engineering test facility will be modified for repetitively rated high yield shots (Phase II). The operational time required for both phase I and phase II of the engineering test facility was estimated to be 16 years from 2010 to 2026. The full scale demo power plant comes online around 2026. The original roadmap was intended to illustrate a direct and accelerated path to a Z-pinch IFE power plant.

The new roadmap creates a path for a full scale IFE transmutation plant. A key objective of this roadmap was to tie Z-IFE technology and transmutation into the GNEP initiative as part of the closed fuel cycle. The new roadmap describes the necessary science and engineering steps needed to achieve these goals by starting with small scale separate effects experiments on ZR and ending up with the full transmutation plant. The new roadmap (red) and the original roadmap (light blue) are shown in Figure 2.1.

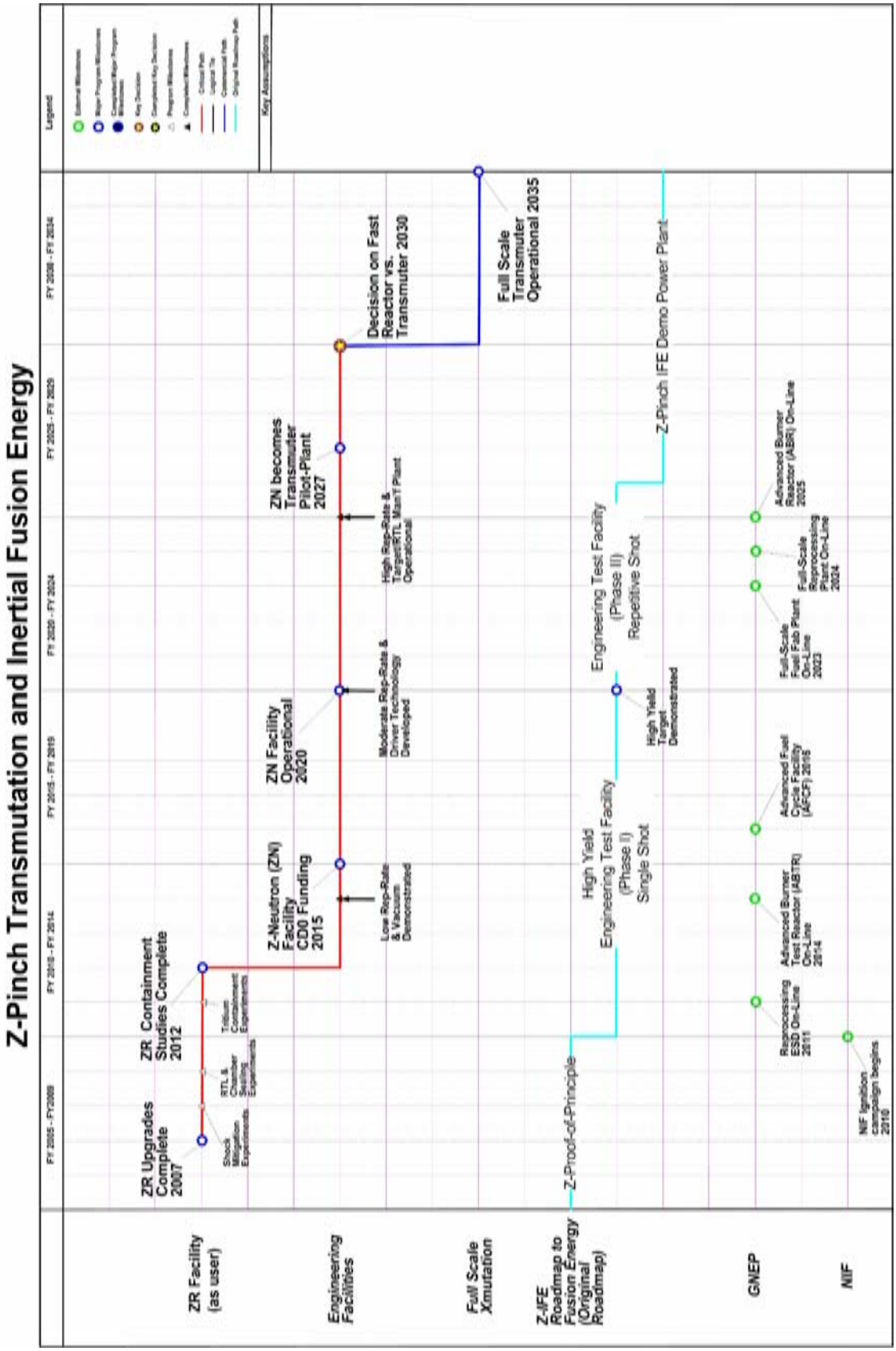

Figure 2.1: Z-IFE Roadmap for Z-pinch Driven IFE Transmutation and Commercial Power.

2.1 The Path to Transmutation and Commercial Power

The roadmap consists of a single critical path which leads to the construction and operation of a full scale transmutation plant. The required science and engineering involved in developing these facilities are nested around and feed into the critical path. The crucial facility on the critical path is the Z-Neutron (ZN) facility which evolves from a low repetitively rated testing facility to a transmuter pilot plant. The critical path, target development, RTL and target manufacturing, driver development, and repetitively rated automation are described in detail below.

2.1.1 Critical Path

The critical path starts with planned experiments utilizing the ZR machine and Z-Beamlet. Z-beamlet is a kilojoule pulsed laser that can be used to ionize gas or liquids. It will be used to demonstrate shock mitigation along with the ZR machine. Shock mitigation can be demonstrated by absorbing the x-rays produced by the fusion yield through a gas, aerosol, thick or liquid curtain medium. Several other crucial demonstrations will be performed on ZR including tritium containment post shot and the use of a conical transmission line. The expected target yield for ZR is approximately 0.01 MJ while producing 2-3 MJ of x-rays.

The Z-Neutron (ZN) Facility will be designed and built once these experiments are successful along with the demonstration of the target yield, LTD drivers, repetitive rated shots, and vacuum pumping of system components. This facility could be compared to the Advanced Burner Test Reactor, which is described in the GNEP initiative, providing a test bed for further science and engineering development. Once this facility is functional it is expected to operate at 24 fusion shots per day at 20-30 MJ, meanwhile, transmuting small quantities of transuranics. The facilities for developing the other transmutation and power plant technologies will be constructed around ZN so that they can easily be integrated together. After 8-10 years of operation ZN will become a transmutation pilot plant capable of a fusion shot every 100 seconds at a target yield of 20 MJ and will be able to transmute 12.8 kg/yr of transuranics. The goal of the pilot plant is to have several years of operational success before the ultimate decision between z-pinch driven or fast reactor transmutation is made.

If z-pinch IFE driven transmutation is chosen, possible commercial involvement may be enlisted to design and build a full scale transmutation plant capable of burning 1280 kg/yr of transuranics. This plant will also generate 1000 MWe while transmuting the waste. Eventually the demand for electricity will be so great that z-pinch driven fusion power plants will be needed. At this point 3-30 GJ of fusion yield will be required at a rate of 1 shot per 10 seconds to generate 1000 MWe of power.

2.1.2 Target Yield

Target yield development will be done in a separate facility outside of ZN. The target physicists at Sandia National Laboratories predict the maximum fusion yield on ZR will be on the order of 0.01 MJ [3]. However, it will produce 2-3 MJ of x-rays so that shock mitigation and containment experiments can be performed using this facility. A separate facility (ZX or X1) will need to be designed and built to develop and contain the larger fusion yields on the order of 3-30 MJ. The hope is a ZX facility will be built and operational by the time the work on ZN requires larger fusion yields.

2.1.3 Recyclable Transmission line and Target Manufacturing Plant

A facility for RTL and target development is necessary to achieve simple cost effective designs which can easily be manufactured and assembled together. The material for the RTL has yet to be determined, so ongoing studies and experiments on ZN will be needed. The RTL must also be easily remanufactured so that it can be used in future fusion shots. This requires significant automation to maneuver the RTL in and out of the chamber and into the manufacturing plant. A separate facility will be needed to develop the RTL and manufacturing plant. For ease of integration the manufacturing development plant will probably be located next to ZN.

Target fabrication can probably be developed in the same facility as the RTL because they are integrated together before being inserted into the fusion vessel. Ensuring a target is free of defects is crucial to creating the necessary conditions for fusion. Currently on Z they are assembled by hand which is not practical for fusion energy. This will have to become automated over time for transmutation and power production to be possible. Both the target and RTL must be manufactured at such a rate that it can support the ZN facility at the pilot plant level which requires one shot every 100 seconds. Further increase in repetitive rate will be required for the full scale transmutation and power plants.

2.1.4 Driver Development

The most capable driver for a full scale transmuter or power plant is the linear transformer driver (LTD). This driver has the potential to be repetitively rated at speeds needed for these plants. However, this driver has yet to be implemented into a system to drive a fusion reaction. Eventually, a separate facility will be needed for prototyping, assembling, and to house the massive foot print of the driver. Another crucial step in the roadmap is acquiring the necessary parts required to build the large number of LTDs. The necessity of the drivers is such that the roadmap shows research and development on LTDs starting immediately.

2.1.5 Automation and Repetitive Rate

In order for ZN to be repetitively rated at the necessary scale needed for transmutation and power, state-of-the-art automation is needed to maneuver the RTL in and out of the reaction chamber. It will also be needed in the manufacturing plant for both the RTL and target fabrication. Another crucial issue is pumping down and maintaining the necessary vacuum conditions in the RTL and chamber for each shot in a matter of seconds. Demonstrating a relatively high repetitive rate while maintaining vacuum will more than likely be necessary before ZN can be built [3].

A facility will be needed for developing the necessary automation and repetitive rate demonstration. The ZN facility will be built once a moderate rate has been demonstrated, probably on the order of one cycle per hour. Over time the repetitive rate and automation will develop so that ZN can operate at a rate of 1 shot per 100 seconds. Eventually, the rate will need to be increased to 1 shot every 10 seconds to support the full scale plants.

2.2 Z-IFE and the Global Nuclear Energy Partnership

The Global Nuclear Energy Partnership initiative strives to expand and develop safe, clean, and secure nuclear energy. The plan includes utilizing the knowledge gained by other nuclear power capable countries and advancing a closed fuel cycle. This involves reprocessing spent fuel

from LWRs and transmuting or burning some of the long-lived nuclear waste. The current plan is to use fast reactors to transmute this waste into forms that are less radioactive or have shorter half-lives. This will allow a single repository, Yucca Mountain, to store all of the remaining spent fuel waste up into the next century [4]. Z-pinch driven IFE technology offers several advantages over fast reactors for burning the actinides which is discussed in more detail in a report on z-pinch transmutation [5]. Figure 2.2 illustrates a closed fuel cycle that includes transmutation.

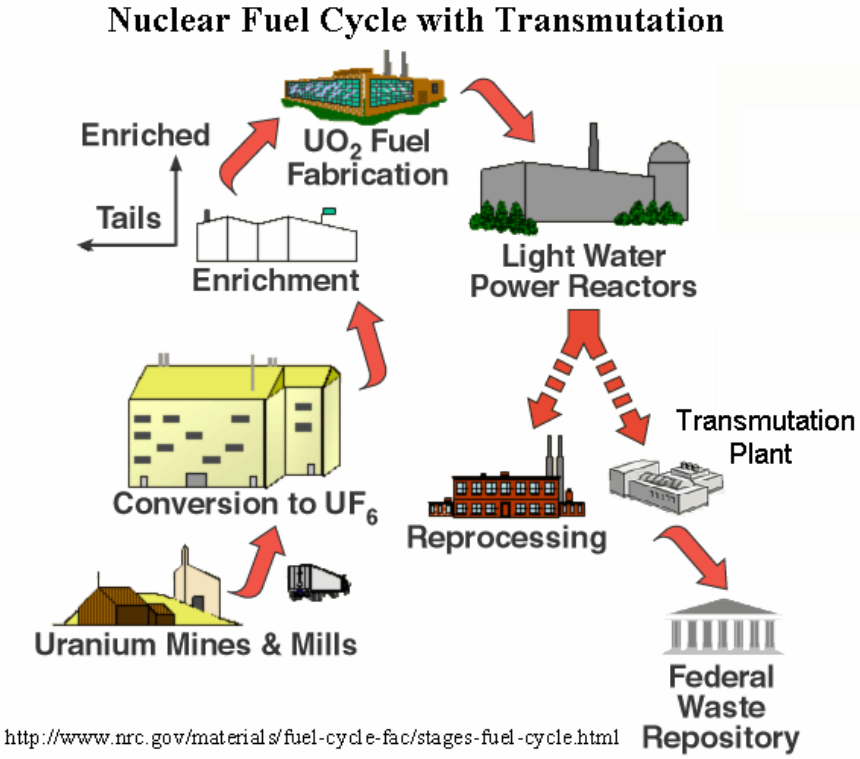

Figure 2.2: An advanced closed fuel cycle with transmutation.

As mentioned above the ultimate goal of creating this roadmap was to show how Z-IFE can be included in the GNEP initiative. Sandia National Laboratories has the state-of-the-art facilities and the full spectrum of technical capability to provide the necessary elements for a strategic initiative. The ZR-machine provides an ample facility for conducting the necessary physics and engineering experiments required for increasing fusion yield, demonstrating fusion containment, and target development. Sandia has a talented robotics group which can aid in designing the automation required for maneuvering the RTLs in and out of the containment vessel. Sandia has experts in materials science which will be valuable in several aspects of this work. Material development for the vessel, RTL, and power plant will be essential to ensure safe operating conditions. Sandia has extensive programs that support energy research and development ranging from solar and wind to nuclear power.

The green circles shown on the roadmap represent the milestones set forth by the GNEP initiative for developing a fast reactor for transmutation. However, a more realistic timeline is shown directly below the GNEP proposed timline and is what the critical path to z-pinch driven transmutation is based on. According to GNEP a full scale Advanced Burner Reactor is proposed to be on-line by the year 2025. If z-pinch driven IFE transmutation was funded as planned, then around the year 2025 ZN would be fully operational and demonstrating its capabilities.

Realistically, having a full-scale fast burner reactor on line by the year 2025 is not feasible due to all the needed research, development, and licensing before such a plant can be built. It is possible to foresee that maybe once ZN has demonstrated transmutation at a substantial scale and is ready for a full scale plant design the fast reactor will be in the same stages of development. The hope is that there will be options when a decision needs to be made to choose the technology for transmutation.

3 Z-IFE POWER PLANT SYSTEMS ANALYSIS

Rather than mount an integrated system-wide look at the Balance-of-Plant processes this year, the power plant group focused on specific problems.

The operating temperature range for the z-pinch process is narrowing to the 600 K to 900 K range. A heat source operating in this range can support commercially available Rankine cycles at the low end and the conceptual phase Brayton and combined cycles when and if they become commercially available. A simple power conversion cycle efficiency comparison was completed this year. Since any of these three generic thermodynamic cycles will work, the project will concentrate on producing a heat source compatible with one or the other of these two options, relying on such other projects as GNEP or GenIV to provide details on the options themselves.

A first order comprehensive economic model was developed by Lawrence Livermore National Laboratory (LLNL) to estimate the total capital cost of the Z-IFE power plant. This includes the driver (high level), chamber, balance-of-plant, RTL, and target factory. The capital costs are then compared with economic studies of other fusion power plant designs such as the laser driven IFE concept. It shows the economic advantage of using fewer chambers with higher repetitive rates and target yields.

Another major accomplishment this year was the production of a conceptual design for a pulsed driver scaled to support a full sized power plant, permitting an initial capital cost estimate. The driver will be expensive with a median price of $372 million per driver. The cost is dominated by the 12,600 (minimum) LTD cavities, each of which is a high technology compilation of switching and capacitance hardware. The cost analysis underlines the need for optimization aimed at cost reduction and provides insight into the best places to begin that analysis.

This year marked the beginning of modeling to predict and manage waste production. Activities concentrated on tritium production and the prediction of tritium loss to atmosphere. While this vital area needs more analysis, it would appear that the overall design of the facility allows operation within the limits of tritium release set by ITER.

The University of California at Los Angles continued experiments characterizing the debris created by a plasma discharge, and the rate and chemistry of recombination of free radicals created by the fusion reaction. These first experiments form important first steps in the many tests needed to bring Z-pinch to reality.

3.1 Cost Models for Z-IFE

Two cost models were developed this year for the Z-IFE power plant. The first was a high level comprehensive systems cost model covering the major components of the power plant. It illustrates the economic benefits of increasing the target yield and increasing the shot rate. The systems cost model for the optimized Z-IFE power plant is then compared to other IFE fusion power plant concepts based on the cost of electricity (COE). The second model was a detailed cost analysis of the linear transformer driver (LTD). This component in particular will be a significant percentage of the total cost of the power plant.

3.1.1 Systems Economic Modeling for Z-IFE [6]

An update and more comprehensive systems model for a Z-IFE electric power plant was completed this year. The code was written in Mathcad®, which makes it easy to read and easy for even novice users to exercise. All assumptions and the bases for the physics, engineering and

cost scaling relationships were documented in the code and are not reproduced in detail as part of this report. In this section, only the key assumptions and important results and findings were presented.

3.1.1.1 Target Gain and Yield

A fundamental relationship for any IFE concept is the target gain as a function of driver energy. For Z-IFE this relationship was determined based on reported results for target yield for the dynamic hohlraum [6, 8]. Figure 3.1 shows the target yield as a function of the z-pinch energy, i.e., the energy delivered to the pinch.

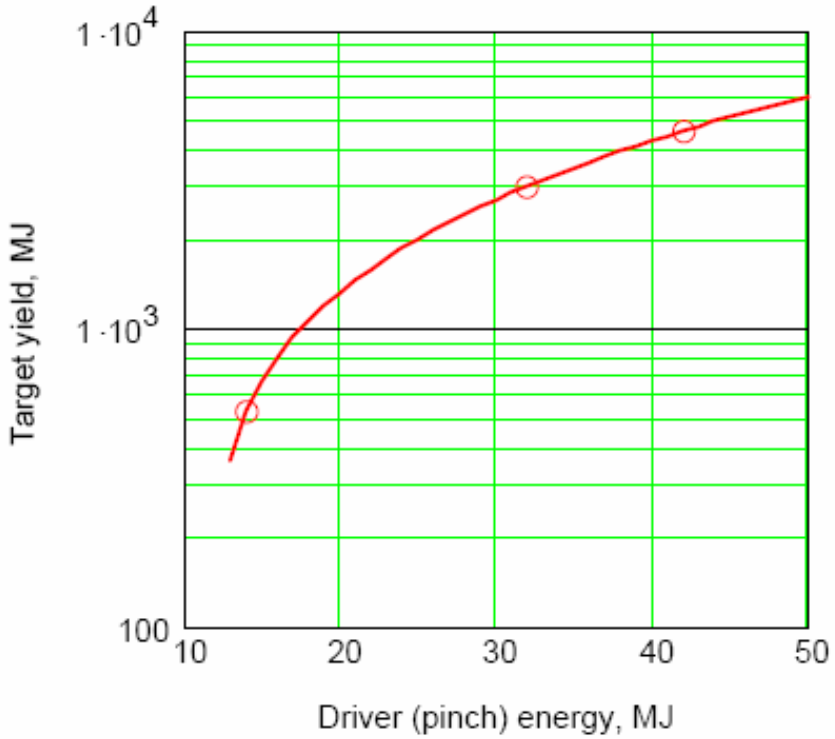

Figure 3.1: Target yield versus driver energy. Fit through three calculated cases is shown.

The fit through the three reported cases was used to determine the target gain versus driver energy as

$$G = 30.15 \cdot (E - 12.2)^{0.38} \quad for\ E > 12.2\ MJ \qquad 3.1$$

This is plotted in Figure 3.2.

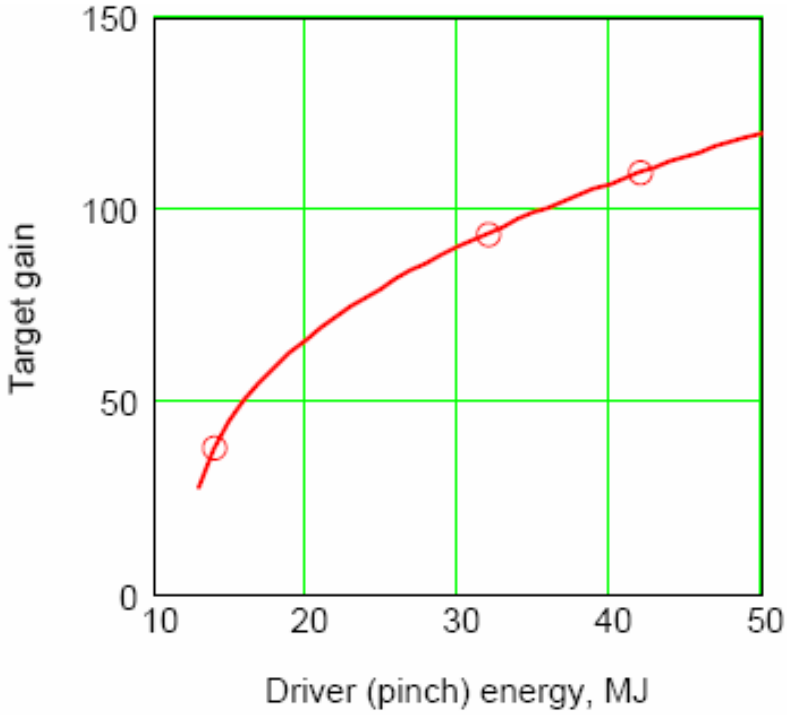

Figure 3.2: Dynamic hohlraum target gain versus driver energy.

3.1.1.2 Driver Efficiency and Cost

The Z-IFE systems code does not have a detailed model for the pulsed power driver. At this point the driver cost is simply given as the product of the energy delivered to the pinch (J) times a unit cost expressed in $/J. The driver unit cost is a variable in the cost of electricity calculation, so the user may examine the sensitivity of the results to driver cost. At the time of this report, a good unit cost estimate was not received, so the reference case value of $15/J was used to estimate the driver cost. This is based on statements by SNL researchers that current pulsed power machines cost ~$30/J and the linear transformer driver (LTD) should be a factor of two lower. The driver efficiency is assumed to be 60% based on material presented at the August 2005 Z-IFE workshop for the LTD [9]. A more detailed driver cost estimate is found in section 3.1.2.

3.1.1.3 Chamber and Power Plant

The cost scaling relationship for the chamber and power plant are based on the thick liquid wall chamber using flibe as the working fluid. The chamber cost is estimated on a $/J of structure basis. Two options are given: a chamber in the geometry of a flattened ellipsoid (original SNL design) and the more cylindrical chamber developed by LLNL and reported in FY05. The base case structure is low activation ferritic steel (F82H), but the code includes the option to use carbon-carbon composite for chamber structures, a high performance option proposed by LLNL.

The balance of plant facilities and equipment models are based on the Osiris cost scaling relationships, but escalated from 1991 dollars to 2005 dollars [10, 11]. Many of the Osiris models were based on previous design studies and for the most part were consistent with those used for HYLIFE-II [12]. The plant power conversion efficiency (total thermal to gross electric) is 42% for the steel chamber and 50% for the carbon-composite chamber.

An important design variable in the systems model is the number of chambers in the power plant. The original SNL reference design for a Z-IFE power plant consisted of ten chambers each producing ~100 MWe net power for a total plant power of ~1000 MWe, a typical standard power for this type of study. Our previous preliminary economic systems analyses indicated that a power plant with many small chambers is not competitive with a plant with fewer chambers operating at higher yield and pulse repetition rate (rep-rate). As shown in the following results, those preliminary findings are confirmed and better quantified by this year's work.

Consistent with previous SNL conceptual designs, each chamber is assumed to have an independent driver, heat transfer system and power conversion system. Only the heat rejection system (e.g., cooling towers) is shared in chamber plants.

3.1.1.4 RTL and Target Factory

The cost and power consumption of the factory needed to produce the recyclable transmission lines (RTLs) was developed and reported by SNL for two cases: steel RTLs and RTLs made of flibe [13]. The systems code includes options for both cases, but due to the significant cost and power advantages of using cast flibe RTLs, flibe is the base case in the analyses.

The cost of the fuel capsule and hohlraum connection to the RTL is also accounted for in the model. The capsule cost and cost scaling with yield and production rate are based on a detailed study completed by General Atomics for direct-drive laser IFE [14]. To account for the added cost of the dynamic hohlraum components of the target, the capsule factory cost is simply doubled. That is, the Z-IFE capsule plus hohlraum is twice the cost of the laser IFE capsule (for a given yield). The RTL and target factories were assumed to service the entire power plant, i.e., all chambers.

3.1.1.5 Total Capital Cost and Cost of Electricity

The total capital cost of the Z-IFE power plant is calculated from the sum of the direct capital costs of the driver, chamber, balance-of-plant, RTL and target factory using indirect costs equal to 93.6% of the total direct capital cost. Annual capital charges are based on a fixed charge rate of 9.66%. These capital cost factors are consistent with other fusion economic studies. Annual operation and maintenance costs are included for the power plant and target factory. The cost of electricity (COE) is then the sum of annual costs divided by the annual net energy produced. The net energy is the product of the plant net electric power multiplied by the hours of operation per year (plant capacity factor = 85%). The net electric power is equal to the gross electric power produced minus the power recirculated to 1) the driver, 2) the RTL factory, 3) the plant pumping for creating the thick liquid wall and for the heat transfer system, and 4) other auxiliary power requirements (taken as 4% of the gross electric power).

3.1.1.6 Key Results

Several key results of the systems analyses are given below. The basic plant design variables are the driver energy, chamber rep-rate, and number of chambers per plant. The net electric power of the plant can be allowed to vary with these parameters, or more instructively, fixed (e.g., at 1000 MWe) in order to compare plants that deliver the same product.

Figure 3.3 gives the driver energy required to produce a fixed net power of 1000 MWe as a function of the chamber rep-rate. Results are shown for plants consisting of 1, 3, 5 or 10 chambers (Z-IFE baseline). Note that this is the driver energy required by each chamber. At a given rep-rate, plants with fewer chambers require higher yield per pulse and thus higher driver energy. Clearly pushing the rep-rate higher than the original SNL base case of 0.1 Hz is attractive if it is technically feasible. In section 4.2.1 of this report, an estimate that a rep-rate of 0.5 Hz might be possible is described. This is higher than the 0.3 Hz quoted by SNL as a "stretch" case. At 0.5 Hz the single chamber plant requires a driver energy of ~ 42 MJ corresponding to a target yield of ~4600 MJ.

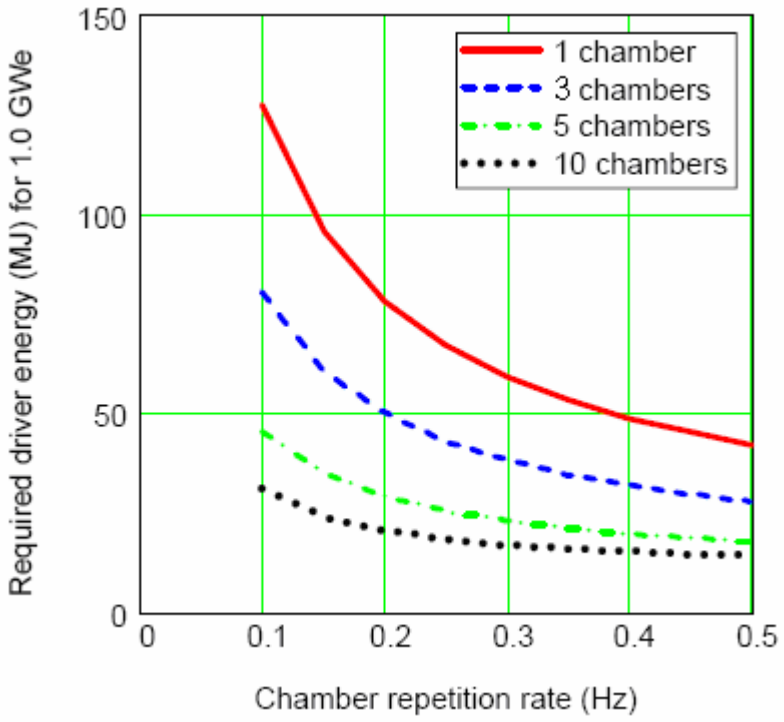

Figure 3.3: Driver energy per chamber required to achieve a net plant power of 1000 MWe versus chamber rep-rate.

The resulting COE as a function of chamber rep-rate for the 1000 MWe plant with various numbers of chambers is shown in Figure 3.4. This figure quantifies the economic advantages of configuring the Z-IFE power plant with fewer chambers and pushing the chamber pulse rate as high as possible. Only the 1 and 3-chamber plants reach a COE less than 10 ¢/kWeh. For comparison, recent MFE and IFE studies quote COEs of 7-9 ¢/kWeh. Even at that it will be hard to compete with advanced fission reactors at 4-6 ¢/kWeh (depending on the size). The single chamber Z-IFE plant operating at 0.5 Hz, has a COE of 7.0 ¢/kWeh, roughly the same as the most recent direct-driver laser IFE result of 7.2 ¢/kWeh [15]. The 10 unit, 0.1 Hz plant has a COE of ~20 ¢/kWeh, which is a factor of 2-3 higher than needed to compete with other fusion concepts.

Another way to display these results to show the range of driver energies needed is shown in Figure 3.5. Here we limit the plot range to COEs less than 10 ¢/kWeh and chamber rep-rates less than 0.5 Hz. The single chamber plant needs a driver energy > 42 MJ for a chamber rep-

rate < 0.5 Hz, and at 60 MJ, the rep-rate is down to 0.29 Hz. The 3-chamber plant has a chamber rep-rate < 0.5 Hz for driver energies > 22.5 MJ and is down to 0.3 Hz at E ~ 30 MJ. The minimum COEs occur at 20 MJ for the 1 chamber case and 16 MJ for the 3-chamber plant, but the required rep-rates of 1.8 and 1.0 Hz, respectively, are beyond the reach of the replaceable RTL concept.

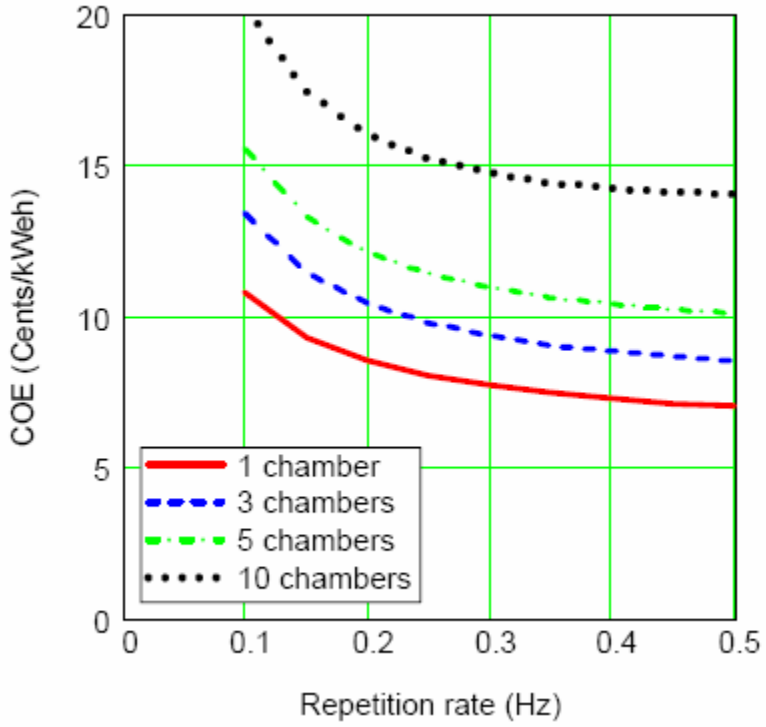

Figure 3.4: COE versus chamber rep-rate for 1000 MWe plants with 1-10 chambers per plant.

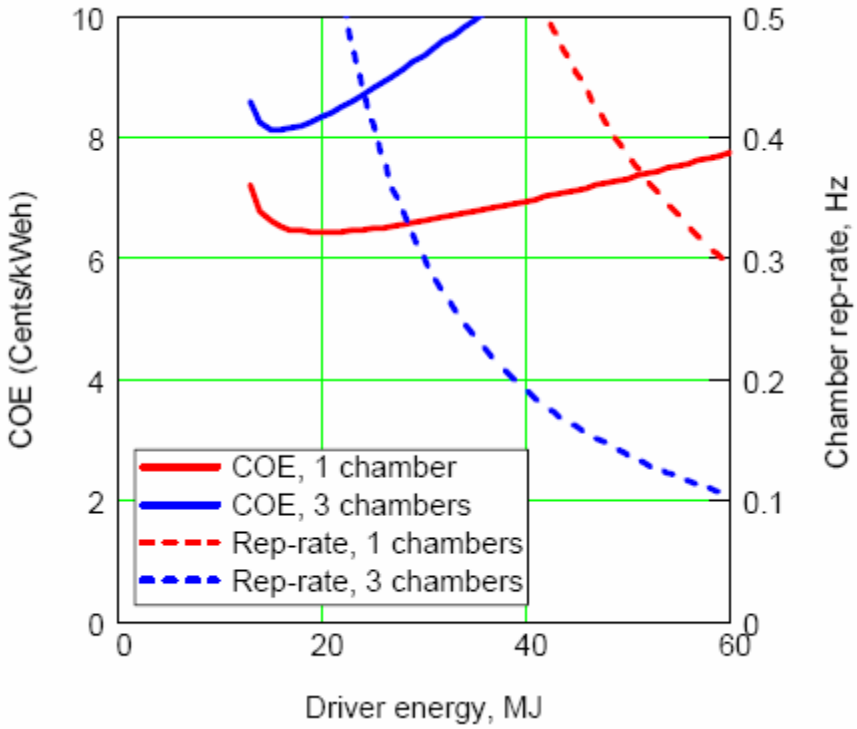

Figure 3.5: COE and chamber rep-rate versus driver energy for 1000 MWe plants with 1 or 3 chambers.

One final result highlights the dependence of the COE on the net electric power of the plant. Figure 3.6 gives the COE as a function of rep-rate for two-chamber power plants with total net powers of 500, 1000 and 2000 MWe. The 500 MWe plant has a COE > 10 ¢/kWeh over the entire range of rep-rates considered (up to 0.5 Hz). The 2000 MWe case shows the favorable economies and benefits of sharing the single RTL and target factory; the COE is down to 5.7 ¢/kWeh at 0.5 Hz. Note that the COE for the 2-chamber, 1000 MWe case is only 10% higher than for the single-chamber plant discussed previously (i.e., 7.7 ¢/kWeh instead of 7.0 ¢/kWeh at 0.5 Hz).

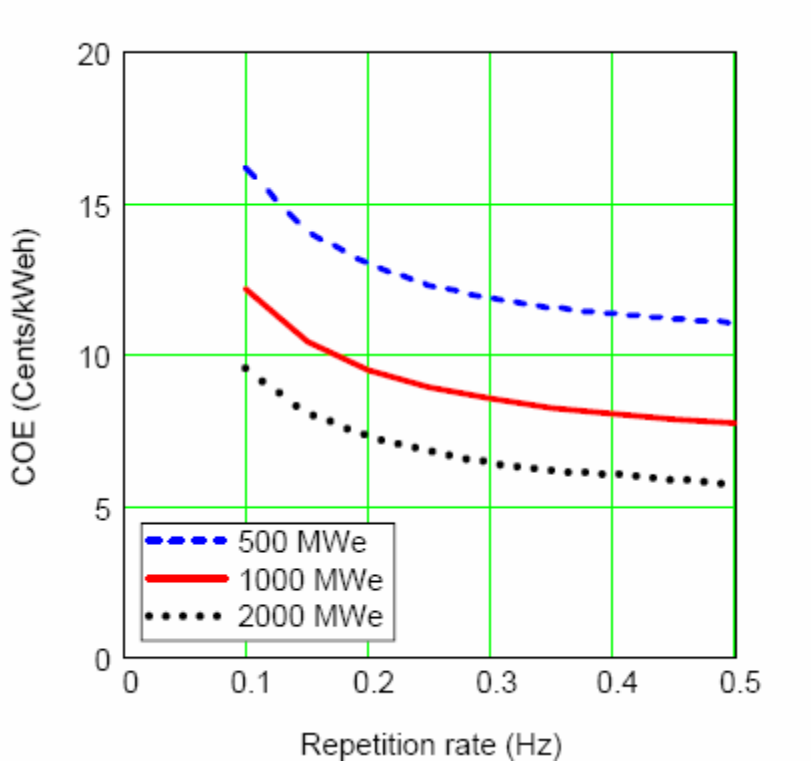

Figure 3.6: COE versus rep-rate for two-chamber plants with various net electric powers.

3.1.1.7 Conclusions and Recommendations

In summary, the results of the more detailed Z-IFE power plant systems code indicate that power plant configurations with fewer chambers (perhaps 1-3) operating at as high a pulse rate at possible (perhaps up to 0.5 Hz) have the most attractive economics in terms of COE. The COE for the single chamber plant operating at 0.5 Hz is slightly better than the most recent result for laser-driven IFE. We note that this Z-IFE systems code is a "first generation" model and as such would benefit from careful critique and further refinement. In particular, a more detailed and documented cost and performance model is needed for the driver. The code should also be updated as progress is made and new information is developed on target performance. Finally, a future version should examine the impact of fast ignition targets, which could significantly reduce the driver energy (and associated cost) needed to achieve the very high target yields that are compatible with the inherently low rep-rate and desire to minimize the number of chambers for a given net electric power.

3.1.2 Estimated Cost for a 1 PW LTD Driver

This section presents a cost estimate for an LTD based driver that delivers 1000 TW (1 PW) to the vacuum insulator stack. The estimate is a composite of parametric and stochastic estimating techniques. Figure 3.7 contains a plot of the results.

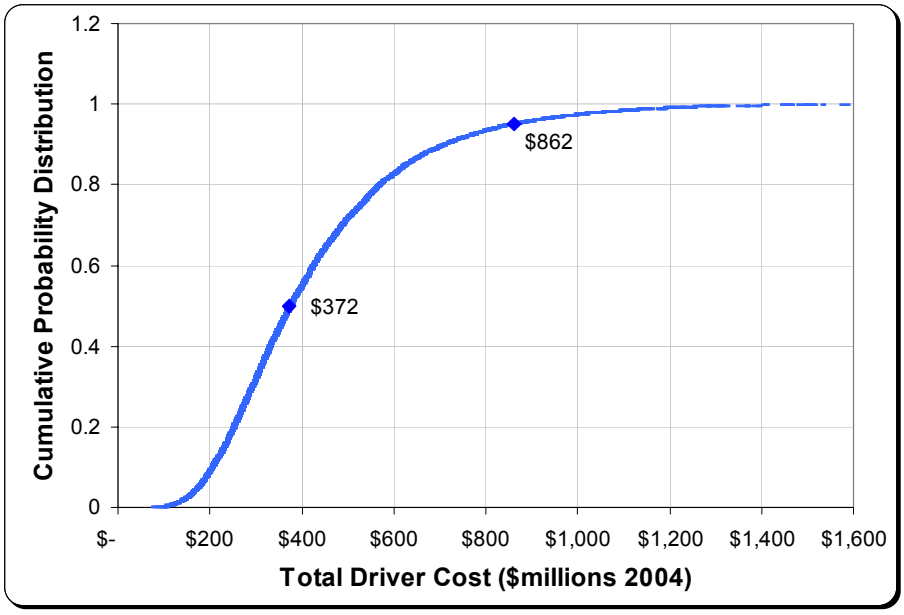

Figure 3.7: Stochastic Distribution of Capital Cost for a 1 PW Driver

The median price for a 1 PW driver would be $372 million. This cost excludes acreage and site preparation. This cost distribution is based on a Monte Carlo simulation. Using the same Monte Carlo simulation, a 1 PW driver has a 95% probability of costing less than $862 million.

The design on which the estimate is built comes from an as yet unpublished paper [16], section IV.C. Figure 3.8 contains a sketch with basic sizing information of the driver. The driver consists of a large (75 m diameter by 10 m high) water tank containing a triplate pulse transmission system connected to a vacuum stack estimated to be 20 m diameter and 10 m high. The system is driven by 210 stacks of 60 linear transformer driver (LTD) cavities for a total of 12,600 LTD cavities. The tank contains demineralized water, the initial charge of which is included in the estimate.

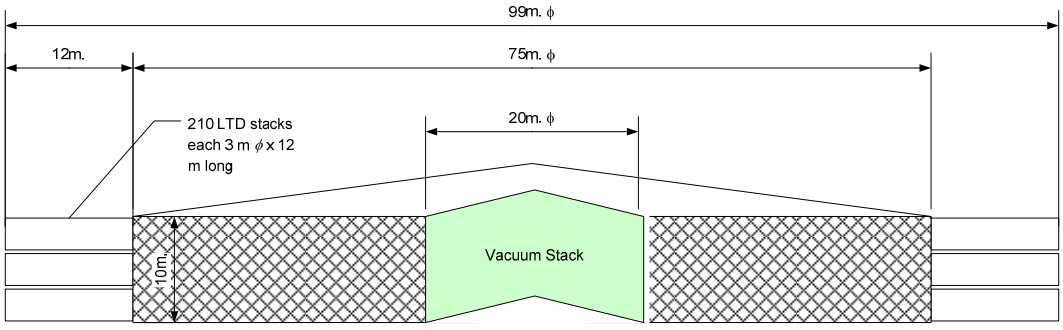

Figure 3.8: Sizing Sketch for Driver System

Table 3.1 contains for illustration the cost components extracted from the Monte Carlo analysis for the median total cost. These individual costs are only those that combined to produce the median total cost. They are not the median costs in their own individual distributions.

Table 3.1: Summary of Costs for the Case of the Median Cost

Cost Component	Cost at Median Total Cost
Demineralized Water Tank	$2,540,000
Tank Internals @10% of DWT	251,000
LTD (12,600)	358,000,000
Vacuum Stack	11,200,000
Initial Charge Demineralized Water	154,000
Total	$372,000,000

3.1.2.1 Demineralized Water Tank

The demineralized water tank was priced as a 44,200 cubic meter cone roofed stainless steel tank using data from the Ulrich and Vasudevan reference [17] which is reproduced in Figure 3.9. Tank purchase price was $674,000 using 2004 costs as the basis. These tank costs should be multiplied by a bare module factor that accounts for hookup and ancillary equipment. The bare module factor for stainless steel is 3.5 yielding a total direct cost of $2,360,000.

For variability, costs could be as much as 80% of the costs reported above. For a high estimate, assume the tank was 15 meters deep instead of 10 meters. Costs increase to $8.26 million.

3.1.2.2 Water Tank Internals

Triplate internals were assumed to cost 10% of the tank direct cost. Assume that high/low costs track at 10% of the costs reported for the tank. This is an approximation based on experience with vessel internals in general.

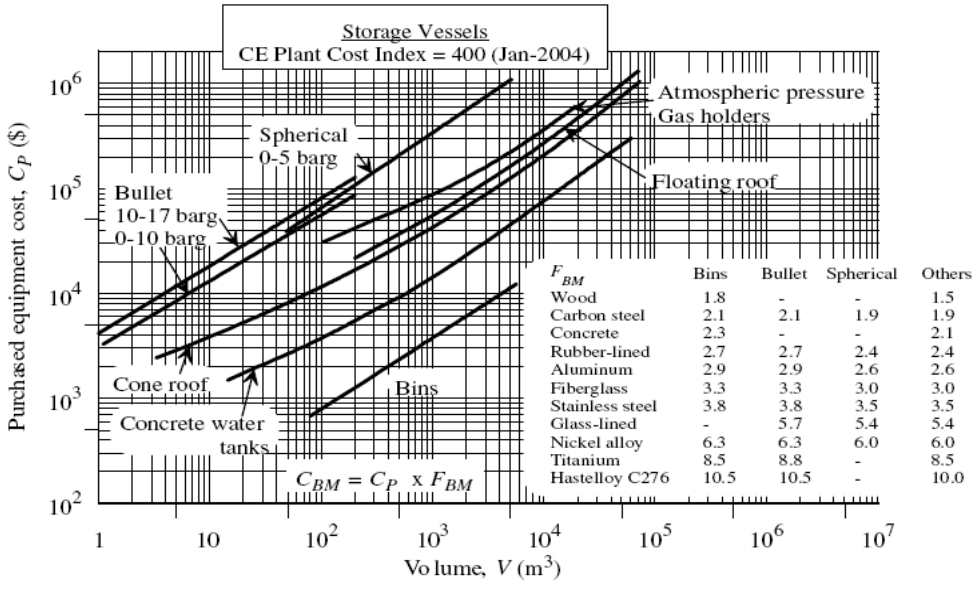

Source: Ulrich and Vasudevan [17] Figure 4.61

Figure 3.9: Purchase Price for Tanks

3.1.2.3 Linear Transmission Drivers

LTD costs amount to slightly more than 96% of the total cost. Figure 3.10 presents the results of a stochastic distribution of LTD cavity costs. The median cost for the 12,600 cavities would be $353,000,000 in 2004 dollars. There is a 95% probability that the 12,600 cavities would cost less than $844,000,000 on the same basis. The median price per unit is $28,000.

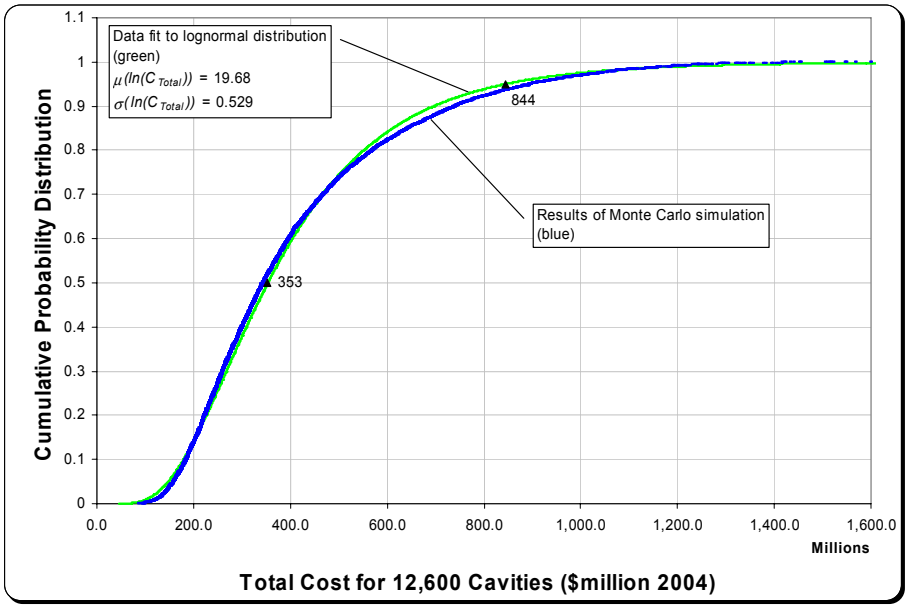

Figure 3.10: Stochastic Distribution of LTD Cavity Costs – 12600 Cavity Case

LTD cost distribution is approximated by a lognormal curve in the overall Monte Carlo simulation. This means the natural logarithms of costs are distributed normally. The mean of these natural logarithms is 19.68 and the standard deviation of these logarithms is 0.529.
Note that the median cost for 12,600 LTD cavities is $353 million while the LTD cost contribution to the median total cost shown in Table 3.1 is $358 million.

3.1.2.4 Vacuum Stack

The vacuum stack cost was estimated based on an average price per unit weight for parts manufactured from steel. This is typically taken as $20/lb. This method, as simple as it is, has proven remarkably robust. For example, a friend's new car costing approximately $60,000 weighed 1.5 tons. The vacuum stack was assumed to be a porous cylinder weighing 33.9 tons (10 m diameter and 5% porosity). This comes out to $13,600,000 direct.

These costs were in 2005 dollars, and theoretically should be deflated to a 2004 basis. However, the estimation method was so simplistic that the effort was not considered worthwhile.

For variability, assume on the low end that manufacturing cost was $15/lb. For the high end, maintain the same cost per pound and assume 10% porosity. Under these conditions, costs range from $10.2 to $27.2 million.

3.1.2.5 Initial Charge for Demineralized Water

Demineralized water was estimated at \$3.15/m^3 using the utilities estimation method proposed by Ulrich and Vasudevan [17].

$$C_{s,u} = a \cdot CEP + b \cdot C_{s,f} \qquad 3.2$$

Where

$$a = 0.007 + \frac{0.00025}{\dot{q}^{0.6}},\ b = 0.004 \qquad 3.3$$

In the above, $C_{s,u}$ represents a utility cost for demineralized water in $\$/m^3$, CEP represents the Chemical Engineering Plant Cost Index [18], $C_{s,f}$ is a fuel cost in \$/GJ and $\dot{q}$ represents demineralized water plant design capacity in m^3/s. As would be expected, demineralized water is relatively insensitive to fuel cost. Surprisingly, it is also relatively insensitive to plant size for plants bigger than 500 m^3/s. Fuel was assumed to cost \$7/GJ based on DOE EIA estimates for natural gas priced for industrial use [19]. The CEP for 2004 is 444.2.

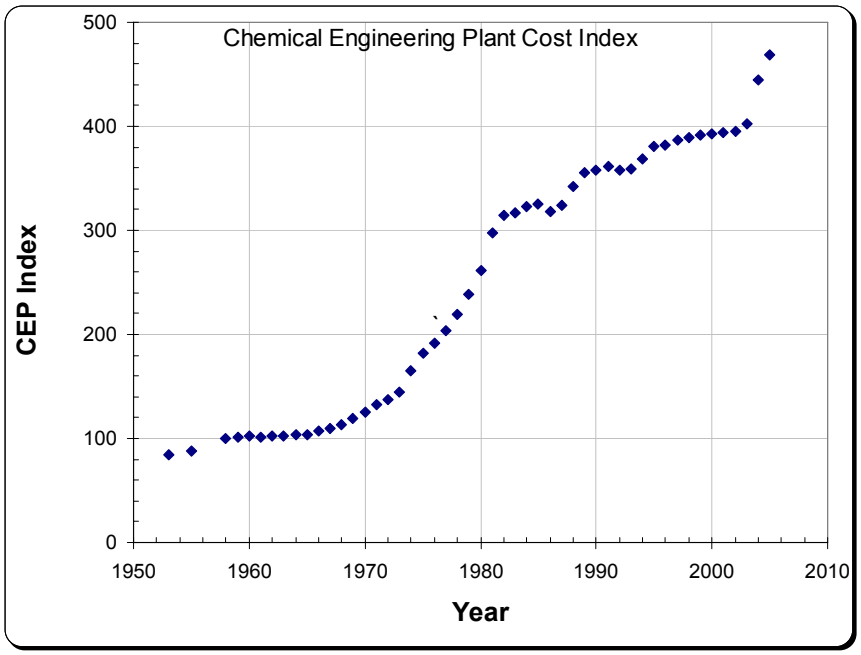

Figure 3.11: Chemical Engineering Plant Cost Index

Figure 3.11 contains CEP values for the period 1950 to 2005. As a matter of interest, note the rapid plant cost growth of the past three years. This represents worse inflation than seen during the 1980's. Assume the unit cost for demineralized water can vary between \$1.5/m^3 and \$6/m^3.

3.1.2.6 Scaling

Estimated median cost, C_{tot}, can be scaled using Equation 3.4. This is an application of equation 5.1 from the Ulrich and Vasudevan text [17]. The exponent was taken as 0.6 after inspection of Table 5-1 of the same reference.

$$C_{tot} = 372\left(\frac{TW}{1000}\right)^{0.6} \qquad 3.4$$

The relationship is scaled using power, *TW*, in terawatts delivered to the vacuum insulator stack. This cost excludes acreage and site preparation.

3.1.2.7 Cost Distribution

A Monte Carlo analysis was done using the variability numbers discussed above. Four of the five cost components are assumed to vary stochastically within triangular distributions. Their parameters are summarized in Table 3.2. Costs for the LTD were assumed to vary within a lognormal distribution as discussed above.

Table 3.2: Input to Monte Carlo Analysis

Cost Component	Low Estimate	Mode Estimate	High Estimate
Demineralized Water Tank	1,862,000	2,327,500	8,155,000
Tank Internals @10% of DWT	186,200	232,750	815,500
Vacuum Stack	10,200,000	13,600,000	27,200,000
Initial Charge Demineralized Water	66,300	139,000	265,200

The Monte Carlo model was implemented in Microsoft™ Excel. Figure 3.7 contains a plot of the results based on 10,000 iterations of model. Costs were assumed to vary independently.

3.2 Power Conversion Systems for the Power Plant

The efficiency of a power plant depends on how effectively the total thermal energy input is converted to electrical output. An effective use of the energy is often related to high operating temperature. This discussion is based on existing models developed for the supercritical Brayton cycle, Rankine cycle, helium Brayton cycle, and the combined cycle. The suitability of a specific cycle does not depend on thermal performance only, since many other constraints could impede its implementation. In some cases, economical and compatibility reasons prevent the use of some materials that show an adequate performance at high temperature. For this discussion, it is assumed that readily available materials can be used for low and high temperature applications.

3.2.1 Super Critical CO_2 Brayton Cycle

A possible power conversion system for the Z-IFE power plant or the transmutation plant could involve the use of one of the supercritical cycles, specifically the CO_2 cycle. Supercritical Brayton cycles are currently being investigated extensively at SNL and the

Massachusetts Institute of Technology (MIT) for possible use with nuclear reactors in order to reduce capital cost, shorten construction period, and increase nuclear power plant efficiency. The efficiency of the supercritical CO_2 Brayton cycle operating at moderate temperatures (~550°C) is comparable to the efficiency of the helium Brayton cycle. One drawback is the higher operating pressure (20 MPa). At this pressure, there is an abrupt property change at the CO_2 critical point. The increase in density leads to a reduction in compression work, which results in a significant efficiency improvement. X.L. Yan offered the following comparison for helium and a supercritical CO_2 turbine: 17 stages are needed for a 167 MW_e helium turbine while only 4 stages are required for a 300 MW_e supercritical CO_2 turbine. Overall, the cycle offers an attractive alternative to the steam cycle. Figure 3.12 shows the supercritical Brayton cycle components and performance comparison curves [18, 22].

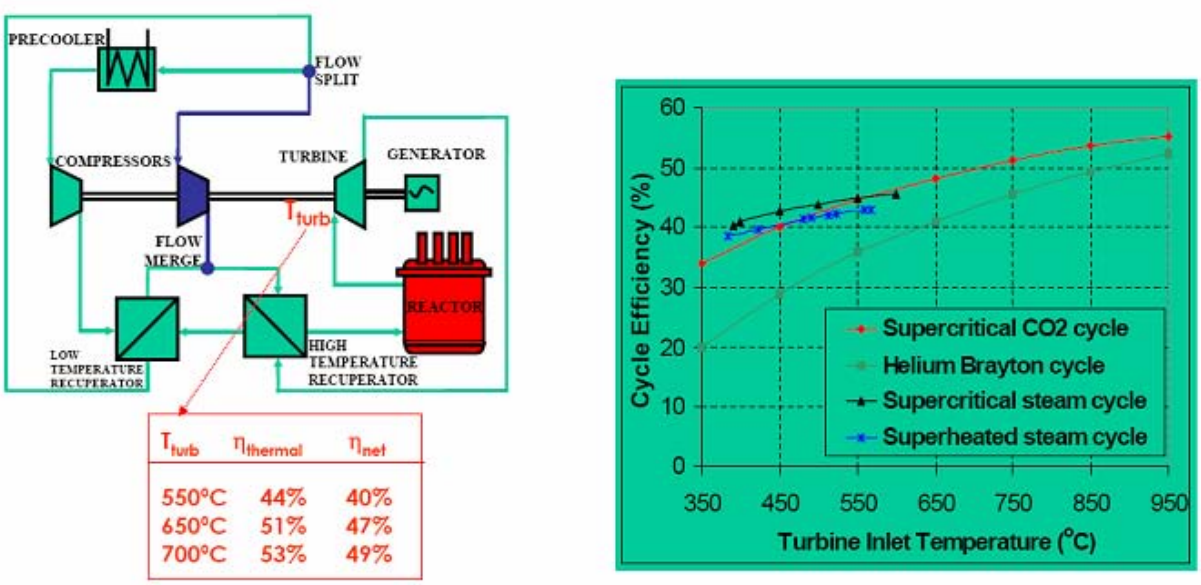

Figure 3.12: A schematic of a supercritical $C0_2$ Brayton cycle (left), and an efficiency verse turbine inlet temperature plot.

3.2.2 Rankine, Helium Brayton, and Combined Cycles

The other three power-generation alternatives presented are well-established technologies. The selection of any one of them depends mainly on its performance and suitability for a particular application. The Rankine cycle is of primary interest when the required operating temperature is relatively low (370 ºC). The helium Brayton and combined cycles are attractive when the available temperature is high (usually greater than 800 ºC). The power conversion analysis is mostly based on an energy balance. If in the near future existing materials are improved or new materials are developed for high temperature applications, the standard Rankine cycle will probably be the least attractive option. This assumes that new or improved materials are affordable and available in large quantities.

Figure 3.13 and Figure 3.14 show the Brayton and combined cycle configuration used for modeling purposes, respectively. The selected power cycles are represented by a limited number of elements. Since the principal purpose was to model a simplified cycle for evaluating the performance under different operating conditions, the number of components was kept to a minimum. Thus, only the major components are represented. In most cases, only one component represents a group of components of the same class normally present in actual cycles.

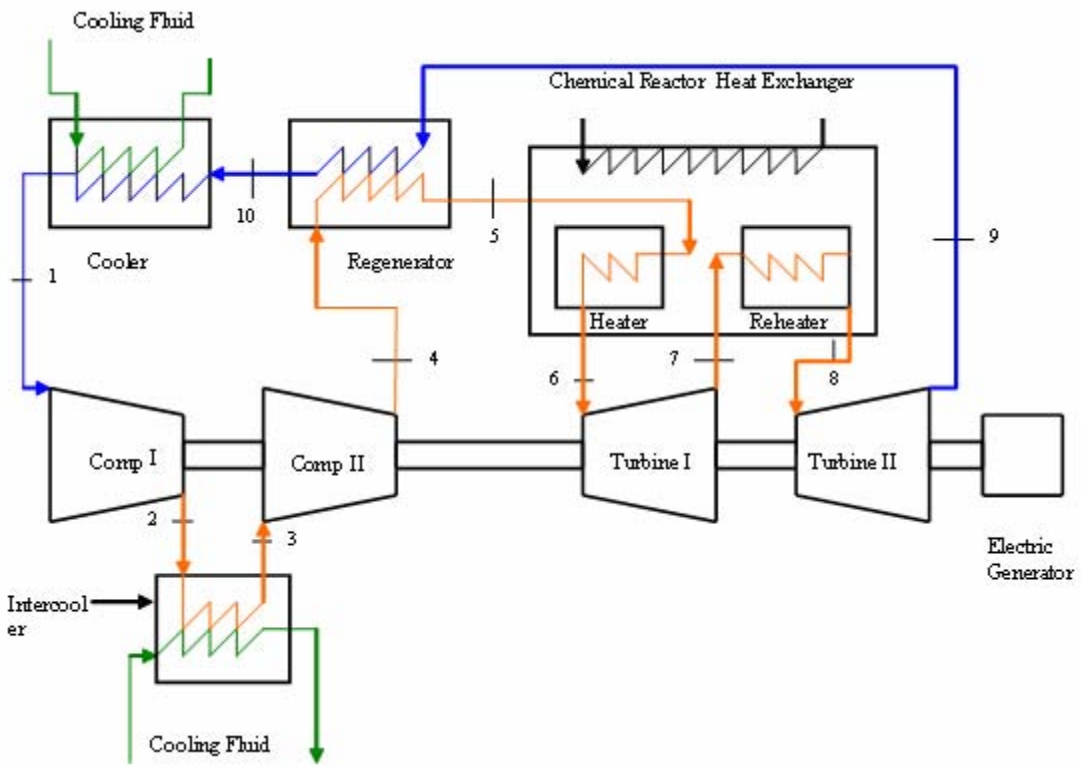

Figure 3.13: A schematic of the standard Brayton cycle.

The components for the gas cycle are the main heat exchanger (heater and reheater), high pressure turbine, low pressure turbine, high pressure compressor, low pressure compressor, regenerator, compressor intercooler, turbine exit fluid cooler, and an electric generator. Most gas power plants operate in an open cycle. If a plant operates in a closed cycle, an additional heat exchanger (the cooler) is required. In this work, helium is used as the Brayton cycle working fluid. The final selection of the Brayton cycle fluid depends on the constraints imposed by the reacting fluid. A closed cycle should be considered only when the environmental impact excludes the operation of an open cycle.

The combined cycle is a combination of a topping Brayton cycle and a bottoming Rankine cycle. The combined cycle consists of the following components: the main heat exchanger, compressor, gas turbine, steam turbine, heat recovery steam generator (economizer, evaporator, drum, and superheater), condenser, and a high pressure pump. Higher efficiency can be obtained from combined cycles since the energy contained on the gas turbine exhaust is used to generate additional power.

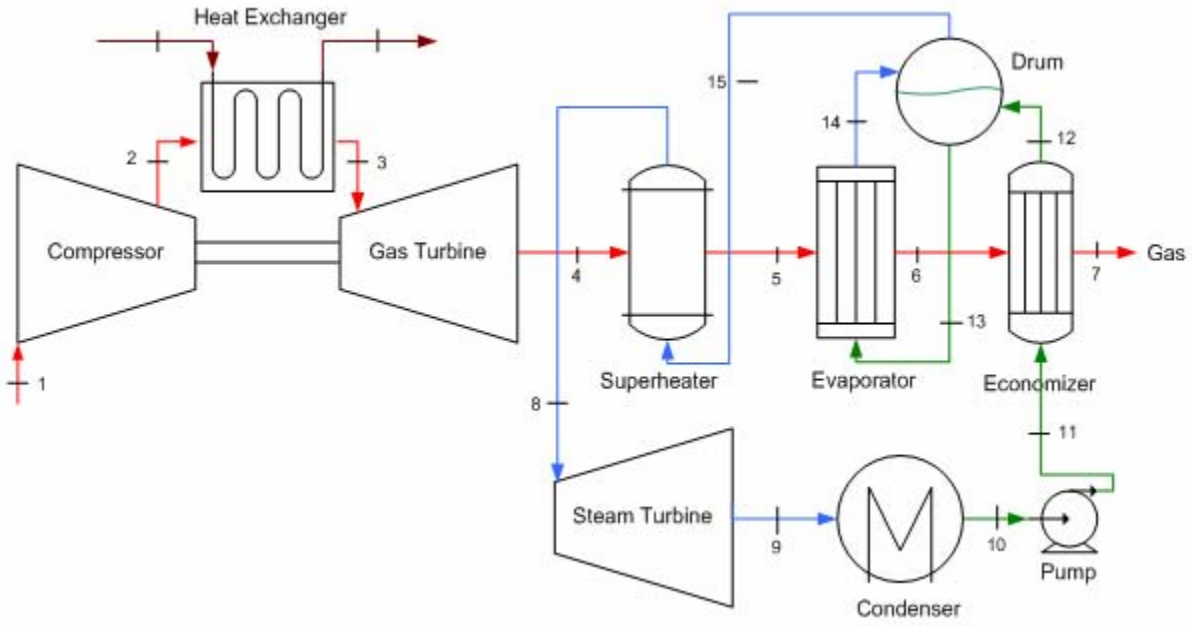

Figure 3.14: A schematic of the combined cycle.

3.2.3 An Analysis of the Rankine, Brayton, and Combined Cycles.

A parametric analysis was conducted using the Rankine, Brayton, and combined cycles. It was assumed that the thermal efficiency of the turbines, compressors and pumps were 90%, and the thermal effectiveness of the economizers, evaporators, superheaters and other types of heat exchangers were 90%. The first objective of the parametric analysis was to determine the suitability of using any of these cycles for the operating conditions set in the chemical reactor heat exchanger. If higher temperatures are allowed in the chemical reactor heat exchanger, the Brayton and combined cycles will have a great advantage.

The maximum operating temperature depends on the average flow temperature. The average flow temperature depends on the thermodynamic properties of the fluid selected and reactor type, the initial operating conditions, and the exit temperature in the chemical reactor heat exchanger. The thermal energy is transported to a power cycle through the reactor heat exchangers. The turbine inlet temperature was set to 800 K for the steam cycle and to 1000 K or more to allow operation of the gas and combined cycle. There are many losses associated with each component. The efficiency/effectiveness is used to group most of them. The impact of each component on cycle efficiency was determined by varying one parameter while keeping all others constant.

In a Rankine cycle, there is not much opportunity to increase the temperature over a wide interval due to the critical point of water. The turbine inlet temperature should not be low with respect to the saturation temperature corresponding to the operating pressure to avoid low quality vapor in the steam turbine exit. On the other hand, the temperature should not be so high that the vapor behaves as a real gas. When the steam turbine temperature increases from 675 to 800 K, the net power output increases by about 10%. The amount of energy consumed by the pump is small when compared with the energy generated by the steam turbine. Likewise, the impact of the pump performance on energy generation is not significant.

The performance of the steam turbine is of crucial importance in a vapor cycle. If the efficiency of the steam turbine is decreased from 95% to 65%, the total energy generation is reduced by about 50%. The back pressure also has a significant influence on the plant performance. The condenser usually operates under vacuum conditions which increases the vapor quality at the steam turbine exit and promotes better conversion efficiency. The energy invested to maintain the vacuum is greatly compensated. When the back pressure increases from 10 kPa to 55 kPa, the net power output is reduced by 23%.

As was mentioned previously, the helium Brayton and combined cycles probably need to wait for future material development. Nonetheless, it is important to know what the benefits and drawbacks of operating at higher temperatures are if the advances in materials allow it. By varying the turbine inlet temperature from 1000 to 1210 K, the gas cycle energy generation was raised by 23%. Both the gas turbine and compressor performance are critical to the performance of the plant. If the efficiency of either the gas turbine or the compressor is degraded from 95% to 65%, the total power output is reduced by more than a factor of 2 for the turbine and close to a factor of 2 for the compressor. The compressor inlet temperature is also of great interest. Since it has a significant impact on performance, a refrigeration system is used frequently to keep it under certain limits. When the compressor inlet temperature is raised from 270 K to 360 K, the net power output is reduced by 30%.

In a combined cycle, most of the energy is generated by the gas turbine. The efficiencies of the pump and steam turbine have a small effect on plant performance when they are compared to the impact of the compressor and gas turbine. If either the efficiency of the gas turbine or the compressor is reduced from 95% to 65%, the energy generation of the plant is reduced by about 50%. When the efficiency of the steam turbine is decreased by the same amount, the energy generation of the plant is reduced by 10%. This indicates that, if a combined cycle were used for a particular application, special attention should be placed in optimizing the whole system so that the compressor and turbine can operate at their highest possible efficiency. If the gas turbine inlet temperature is increased from 1000 K to 1300 K, the power generation of the plant is increased by 30%.

Since the objective of this analysis was to show the impact of the turbine inlet temperature on the power generation, it took into consideration the practicability of all processes involved. With a turbine inlet temperature equal to 1000 K, it is impractical to operate the bottoming cycle due to the high humidity content in the last stages of the steam turbine. In general, for specified operating conditions, the Brayton cycle consistently shows better overall performance when compared with the Rankine cycle. The better performance of the Brayton cycle can be associated with higher turbine inlet temperatures. Likewise, the combined cycle shows better performance compared to the Brayton cycle. Better performance is usually associated with even higher constraint on the minimum turbine inlet temperature. Figure 3.15 is an example of the Brayton and combined model outcomes.

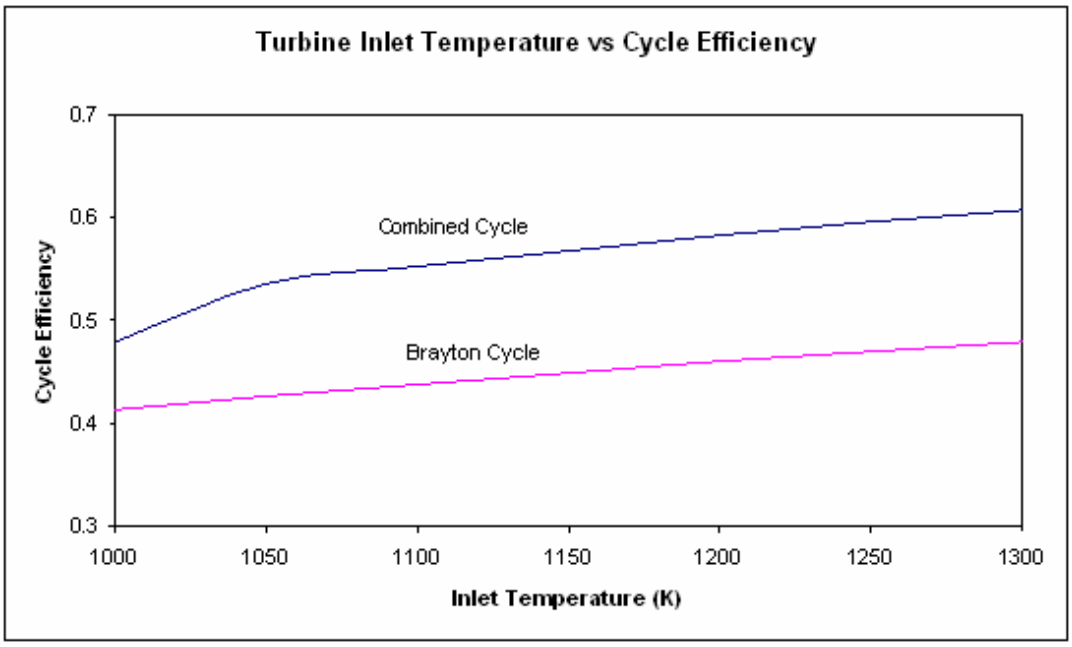

Figure 3.15: Brayton and combined cycle efficiency verse temperature.

Both the Brayton and the combined cycle become more attractive for use in the Z-IFE power plant at higher working fluid temperatures. The gas turbine dominates the generation of energy for both the Brayton and combined cycles. For similar operating conditions, the combined cycle shows better performance. Probably the major advantage of the combined cycle is the generation of additional power from the energy contained in the gas turbine exhaust.

3.3 Tritium

Tritium is essential for designing any fusion power plant. The quantity of naturally occurring tritium on earth is very small due to its short half-life (12.32 years), which makes it impossible to use in large scale operations such as fusion power plants. In order to generate a significant amount of fusion energy for power production, tritium must be created through a nuclear process. The current Z-IFE design uses flibe to breed tritium. The proposed process for extracting the tritium from flibe is explained in the Z-IFE transmutation report [5]. This section focuses on minimizing tritium permeation from the chamber and the process piping.

3.3.1 Tritium Permeation [23]

Consider the fusion plant process sketch contained in Figure 3.16. The permeation losses from the flibe circulation system are shown in the figure as heavy lines. Estimated losses are on the order of 0.0467 grams per year for the flibe system. This includes all ten fusion chambers. Such a loss rate would be slightly less than $1/20^{th}$ the total losses predicted for ITER. To ensure this level of emission, the plant is constrained to a maximum operating temperature in the flibe circulation loop of 850 K. The pipes necessary to achieve this rating were made of 304 stainless steel with a permeation barrier having a permeation reduction factor (PRF) of 100. This is a fraction of the probable permeation loss from the Z-IFE fusion plant. Additional work is needed to address other likely tritium leak sources.

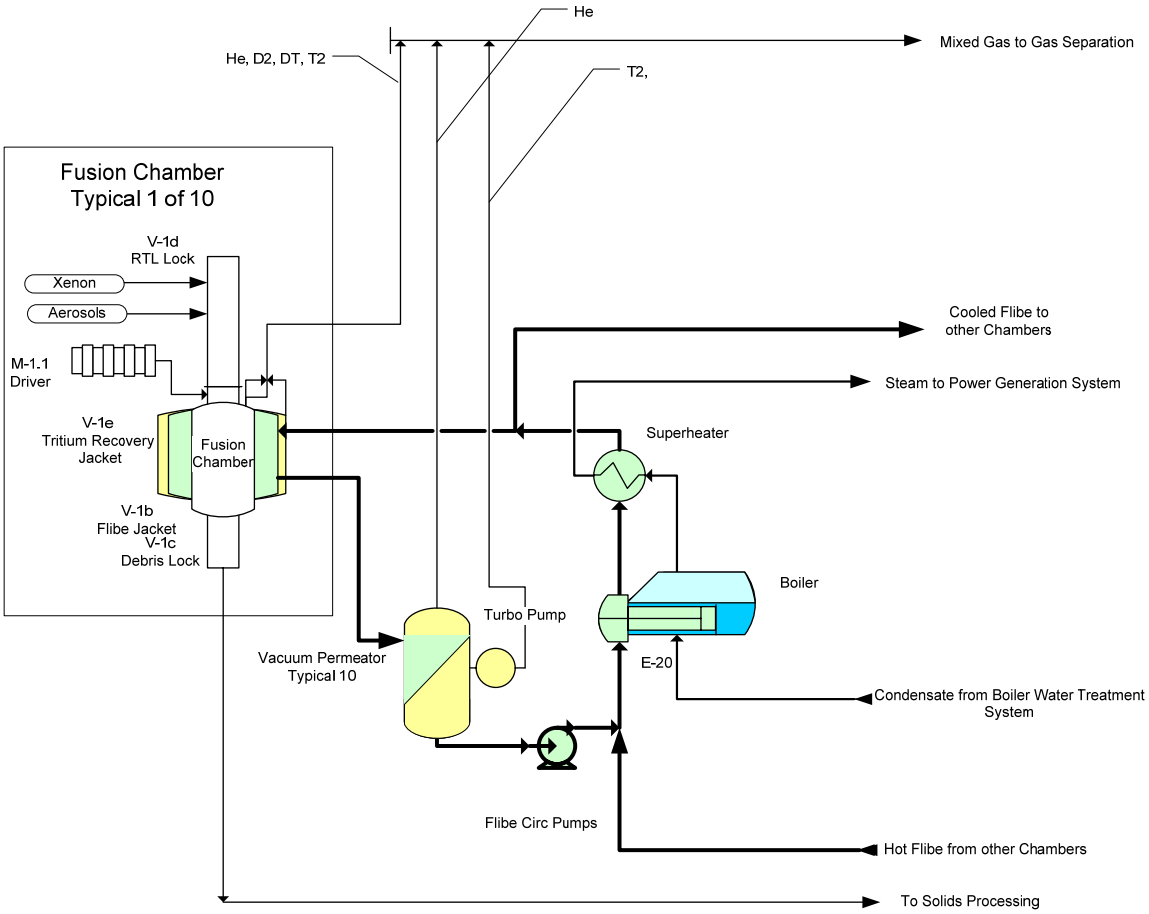

Figure 3.16: Flibe Circulation Process Sketch

The vacuum permeator shown in the process sketch (Figure 3.16) is the same device recommended for ITER. The permeate side would operate at approximately $1x10^{-5}$ Torr. This analysis makes the assumption that such a permeate pressure would result in a partial pressure on the upstream side one order of magnitude higher, or $1x10^{-4}$ Torr (1.33E-07 bar).

Figure 3.17 contains one possible plant layout for the fusion plant with the flibe piping discussed above. This is high temperature piping that is insulated with an outer metal sleeve. Neither the insulation nor the outer sleeve was assumed to provide any impediment to tritium migration.

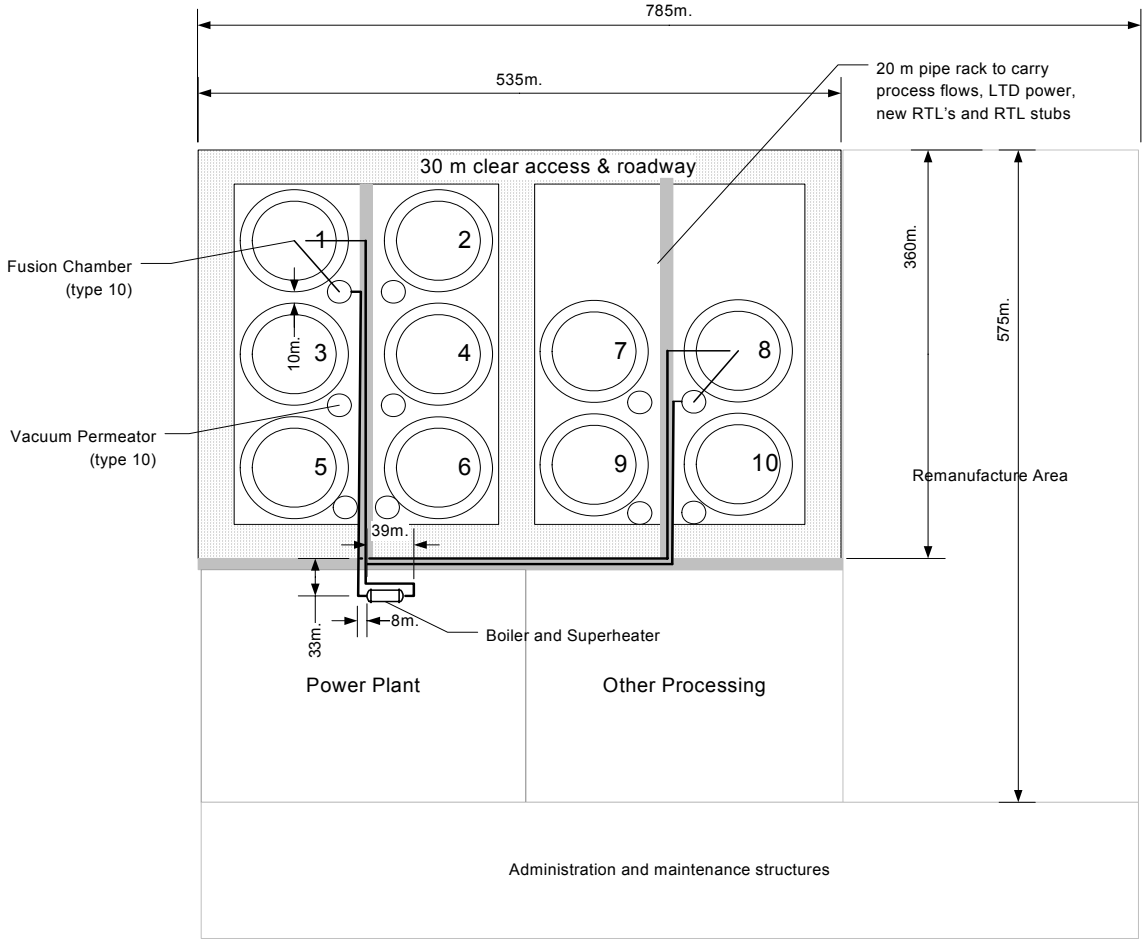

Figure 3.17: Conceptual 1 GW Fusion Power Plant Layout

The piping shown in Figure 3.17 forms a dendritic header system with two main trunks. The header telescopes to maintain a pressure drop of 0.11 bar per 100 m (0.5 psi/100 ft). That is, header diameter varies as flow varies to maintain a constant pressure drop per unit distance. The pipe inventory used in this study is shown in
Table 3.3. The total area of the piping system was increased by 25% to account for changes in elevation and other unaccounted length. While this level of allowance might be too small in tight quarters, the long lines of flat run justify it.

Piping was assumed to be 1.2 cm thick (0.5 inches). Actual pressure will be low, on the order of 1 atm gauge. Such pressure requires thin walls to contain it. Commercially in such cases, wall thickness is set by a minimum necessary to provide pipes robust enough to resist damage from handling and access during construction and operation. A typical specification for a pipe of this size (27" to 60" diameter) would be 1.2 cm (0.5 inches) thick, the wall thickness assumed herein.

Table 3.3: Flibe circulation loop pipe statistics

Piping Location	Run Count	Flow Rate (kg/s)	Run Length (m)	Pipe Diameter (m)	Surface Area (m^2)	Total Length (m)
Laterals	20	865	50	0.540	1700	1000
1 – 3, , 2 – 4, 7 – 9, 8 - 10	4	1730	100	0.700	880	400
3 to 5, 4-6	2	3460	100	0.900	565	200
5, 6 to Ht Exchanger	2	5190	100	1.10	691	200
9, 10 to Ht Exchanger	2	3460	350	0.900	1980	700
Heat exchanger external pipe	1	8650	100	1.30	408	100
				Sub-total without contingency	6220	2600
				Total with 25% contingency	7770	3250

Tritium permeation estimates were made using the DIFFUSE tritium permeation code and the piping system specification discussed above [24]. The predictions were made for two materials. Results are plotted in Figure 3.18.

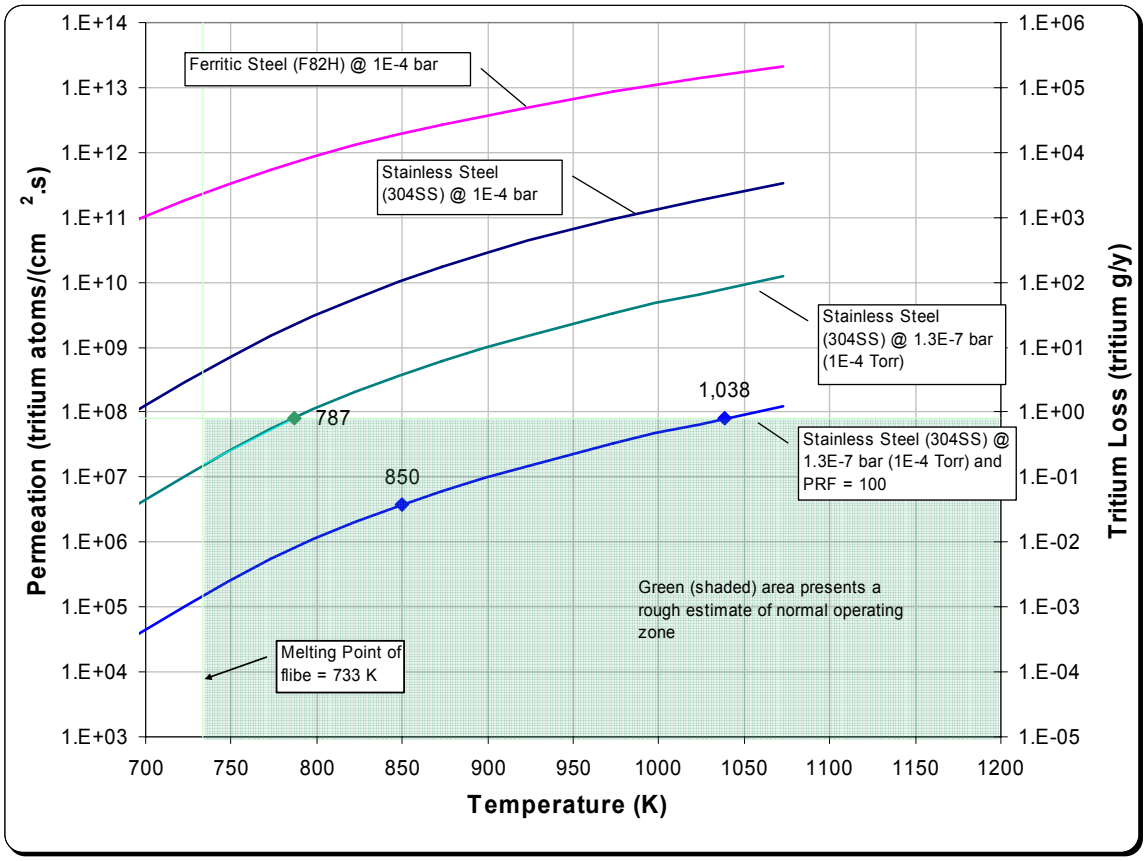

Figure 3.18: Results of DIFFUSE Code

Highest permeation rates were obtained using F82H, a type of ferritic steel designed for low activation potential [25]. F82H steel performance for $1x10^{-4}$ bar partial pressure, a concentration to be expected if tritium is allowed to accumulate without aggressive removal, is depicted in the top curve of the figure. Substituting stainless steel (Type 304) reduced permeation by up to three orders of magnitude at the same driving pressure difference, as shown by the second from the top curve in the figure [26, 27]. The next curve down shows the impact of a lower partial pressure similar to that possible on the permeate side of a vacuum permeator, $1x10^{-4}$ Torr ($1.3x10^{-7}$ bar). The last and lowest curve reflects the permeation of low partial pressure hydrogen through pipe equipped with a permeation barrier. A permeation reduction factor (PRF) of 1000 has been achieved in laboratories [28]. This lowest curve uses a PRF of 100 as a long term commercial value to be expected after significant continued development.

Imposing limiting criteria on Tritium release will be difficult in the absence of such site specifics as geography and weather and demographics. For now, the release will be compared to the ITER results. In rough numbers, ITER is currently limited to 1 gram/year of tritium release based on a 10 millirem allowable exposure at the site boundary which is about 1 km from the emission source. A limit of 1.0 g/y of tritium imposed on this piping system equals $6.2x10^{7}$ tritium atoms per centimeter per second permeation. The shaded box in the bottom of the curve reflects this limit. The box is foreshortened on the left to limit the area where flibe is liquid. The box provides an approximate map of operating space for the flibe system based on tritium release to atmosphere.

A reasonable operating temperature for a flibe system is 850 K. This allows operation approximately 100 K above freeze point, and is still low enough to avoid undue impact to piping. At this temperature, the piping system in question would allow a permeation loss of 3.8E06 tritium atoms per cm^2 per second. For this system, such a permeation rate equates to a loss to atmosphere of 0.0467 g/y, slightly less than $1/20^{th}$ of the current ITER criterion of 1 g/y. This limited release must now combine with such other sources as hydrogen piping, vessels and equipment, and periodic off-design releases.

3.3.2 Future Tritium Research

1. Consequence modeling using MACCS2 or other atmospheric transport codes that relate leakage rates to long term dose rates will be needed for future safety analyses. This will require assumptions regarding plant location.
2. Estimate tritium leakage from the gas processing system piping. This will probably add a significant mass per year to the 0.0467 g/y already accounted for.
3. Investigate a system that combines hydrogen (all forms) with carbon to form methane or larger hydrocarbons. This effectively traps the tritium, reducing permeation to the point of virtual elimination. This would allow hydrogen transport over long distances without loss. It would, however, require reforming at the downstream end.
4. Investigate tritium losses across the steam boiler and superheater into the steam system and the formation of tritiated water and possible subsequent leakage. This should be an easy investigation as similar processes occur today at commercial nuclear power plants.
5. Investigate tritium losses from such operating equipment as pumps, compressors, valves, flanges and other piping system components. These sources could be the most significant source of tritium losses.
6. Investigate the best permeation barrier to use with temperatures in the 850 K range.

3.4 Recyclable Transmission Line (RTL) and Flibe

The RTL connects the target to the driver. It has to be designed in such away that it does not add a significant amount of impedance to the path of the pulse. A significant portion of the RTL is destroyed after each fusion event. The remaining material collects in the vessel and is recycled for use in another shot. Since it is recycled after each shot the material must be such that it is easily melted and formed into the appropriate shape. Ferritic steel has been studied extensively in past Z-IFE studies as a candidate for the RTL material. Its abundance and chemical compatibility with the liquid curtain material (flibe) makes it a viable choice. A steel RTL however requires an extensive amount of energy (170 MWe of a 1000 MWe power plant) to remanufacture [31].

An alternative material to ferritic steel that has been investigated in the past was frozen or frangible flibe. Using the same material for the RTL as the liquid curtain eliminates the issue of material separations, and cuts down on manufacturing costs. Continuing optimization and characterization of frozen salt properties has been investigated further this year and is presented in section 3.4.1. Also, a proposed frozen flibe RTL design is discussed in section 4.2.1.

Flibe (LiF)2-(BeF2) and carbon steel remain the baseline materials for the Z-IFE power plant. The University of California in Los Angles conducted experiments analyzing the interaction between vapor ferritic steel and a molten flibe pool. The results are described below in section 3.4.2.

3.4.1 Characterization of Frozen Salt Properties [29]

For the design of frozen salt transmission line elements, the mechanical and dielectric properties have to be well known. In preparation for measuring the electrical properties of flibe, during 2005 an initial evaluation of the dielectric breakdown properties of ¾ x ¾" substitute frozen salt samples has been made [29]. The Na_2MgCl_4 samples produced in 2005 were cast in POCO graphite dies. The resulting surface carbon contamination provided enough electrical conductivity to prevent measuring the dielectric constant, which will be needed for electrical modeling of the RTL and to determine the appropriate driver impedance. In 2006, high purity Na_2MgCl_4 samples with a diameter of 1" and a thickness of about 1/16" were successfully produced. These samples were cast in a Hastalloy crucible. The salt was slowly heated to 480ºC under vacuum to remove water vapor. Once a homogeneous molten layer was achieved without further out gassing, the crucible was allowed to cool to room temperature slowly over a five hour time period to avoid tension and stress cracking. The chamber was then filled with dry argon gas. Thin Cu foil was attached to both sides of the sample exactly matching its diameter. The subsequent measurement of the dielectric constant was performed under Argon atmosphere to prevent conductivity changes of the sample by hydride formation. Two different devices were used: A calibrated Micona capacitance meter for DC measurements and a HP auto balance bridge for measurements at DC and frequencies up to 1 Mhz. were used. Table 3.4 summarizes the results of these measurements.

Table 3.4: Measurement of Na_2MgCl_4 dielectric constant

	ε_r (DC)	ε_r (500 kHz)	ε_r (1 MHz)
Auto balance Bridge	4.5 + - 0.2	4.65 + - 0.25	4.7 + - 0.25
Capacitance Meter	4.4 + - 0.3		

3.4.2 Interaction of Ferritic Steel Vapor and Flibe [29]

It has been expected that most of the RTL steel precipitates in the flibe coolant and can be recovered by mechanical separation. However, recent calculations show that a large fraction of the RTL (up to ½ of the total mass) will be vaporized and partially ionized by the discharge [32]. This plasma cloud composed of the constituents of ferritic steel (iron, chromium, etc) will expand and interact with the neutral gas present in the background as well as with the excited and ionized fluorine, lithium and beryllium that is generated by the absorption of the x-rays emerging from the target in the surrounding flibe liquid. The goal of the experiments described here is the characterization of the chemical composition and size distribution of the condensed vapor and precipitated steel droplets.

Figure 3.19 shows a schematic of the Z-box facility (completed in 2005) and an overview of the experimental hardware and the capacitor bank used to produce the discharge. The Z-box has excellent optical access with large UV/visible view ports for high speed cameras and optical spectroscopy. In addition, fast piezoelectric pressure sensors, Langmuir/Mach probes for flibe plasma characterization, and RGA access are provided. In-situ handling of high temperature molten salt and modifications of the experimental set-up in high purity argon are possible via gloves. For evacuation, the glove ports can be sealed. Flexible heating configurations are provided for flibe melting and casting.

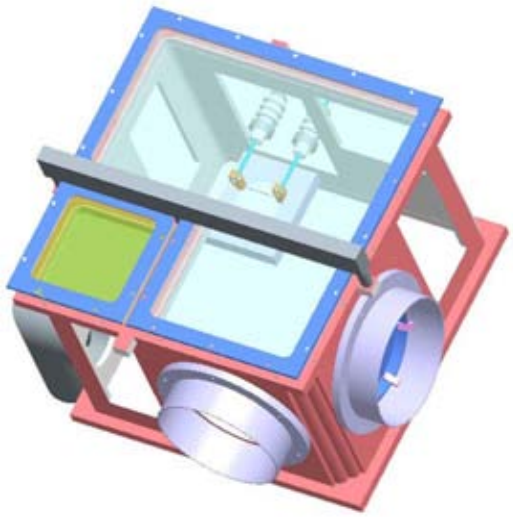

Figure 3.19: Z-Box flibe handling facility.

There are several difficulties in the laboratory handling of flibe, which greatly complicate the experiments described here. The first difficulty is the control of the impurities dissolved in the salt, which significantly modify the material properties. This limits the range of suitable containing materials, diagnostics, etc. The second problem is related to the toxicity of beryllium particulate in any of its chemical forms and composites which complicates handling and modifications of the experimental set-up. The latter is a particularly severe limitation during the initial scoping phase of this research and development project. Because of these issues the most common beryllium free mixture of salts available are used in the experiment, sodium chloride NaCl and magnesium chloride $MgCl_2$.

Each element of the salt eutectic corresponds to an element in flibe but shifted down one line in the table of elements: Li to Na, Be to Mg, F to Cl. This means that the electron valance of the atoms is the same, and the eutectic chemical bonds are similar. This is confirmed by the fact that the phase diagram of the two mixtures are actually quite similar, as shown in Figure 3.20 [33]. In addition, the thermochemical properties of the two compounds at high temperature are also very similar.

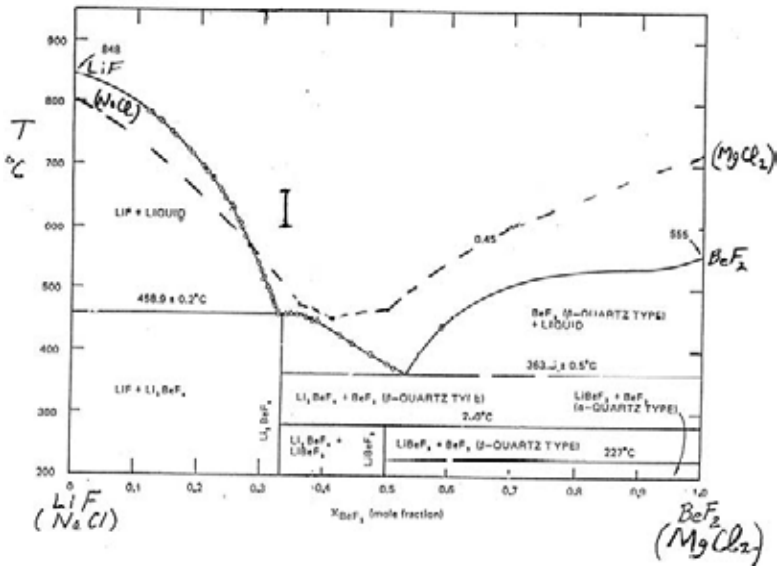

Figure 3.20: Flibe and Na_2MgCl_4 phase diagram.

Na_2MgCl_4 is produced by mixing the salts in the same eutectic composition as flibe (2/3 NaCl and 1/3 $MgCl_2$ in moles). During this preliminary phase the substitute eutectic was formed by heating the mixture inside a nickel crucible (chosen because of its inherent low reactivity with molten salts) under high vacuum to eliminate water vapor residues. The mixture was then heated to 900ºC to form the eutectic and subsequently cooled slowly. The eutectic was then re-melted in less then 1 atmosphere of argon. Once liquid, the eutectic was conditioned further under vacuum. During the experiments the salt was kept molten above the eutectic temperature of 470ºC.

The experimental investigation of the interaction of ferritic steel and molten salt vapors was started at UCLA in 2005. Capacitor discharges (1-5 kJ) were used to vaporize and ionize ferritic steel wire or mesh over a molten salt pool, using the beryllium free Na_2MgCl_4 instead of flibe. The discharge vaporized some of the molten salt surface, and the vapor interacted with the expanding metal vapors from the vaporized wire mesh (in these experiments, 300 mg of steel wool

with a wire diameter of 2 μm was used). The analysis of the process was performed by using high speed/video cameras, spectroscopic diagnostics and by surface characterization of the deposited precipitate. Figure 3.21 shows a schematic of the experimental set-up.

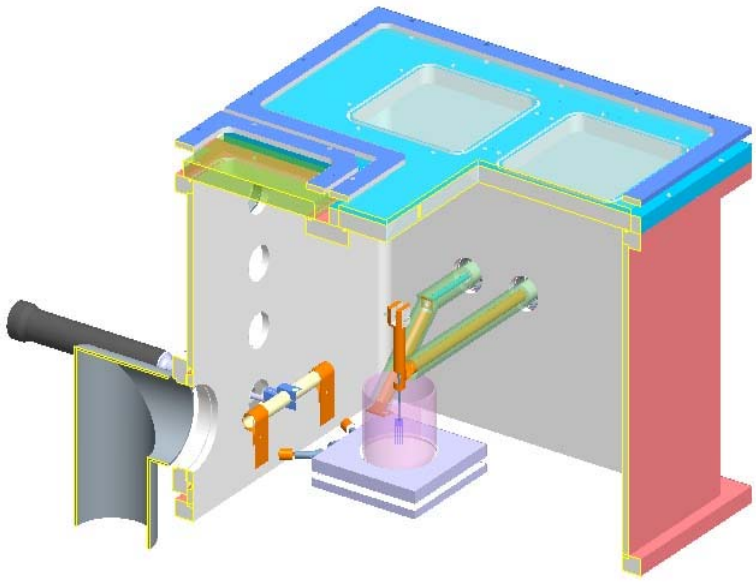

Figure 3.21: **Experimental Set-up showing 3" nickel crucible bedded in heater plate (center) with detachable heater connections (left), glass-shielded transmission line elements leading to the capacitor bank (in green), and the centrally mounted wire mesh (purple).**

Figure 3.22 shows a video frame of the discharge and the glowing salt surface recorded in the next video frame. Heating of the salt layer is mainly due to the anodic plasma heat flux which may peak at 20-50 kW/cm^2.

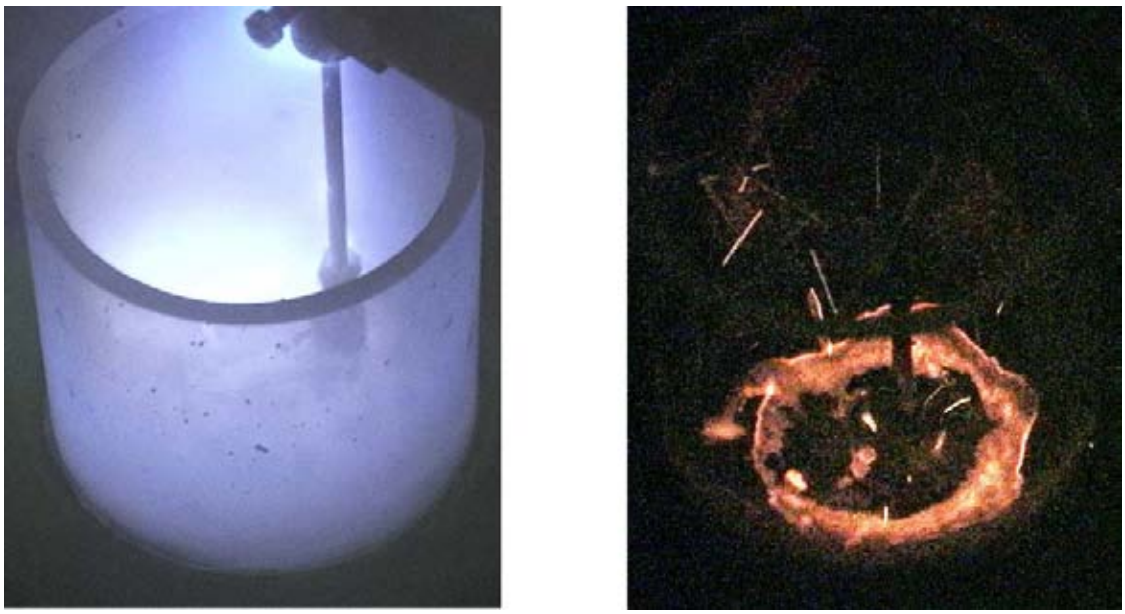

Figure 3.22: The video frame showing the plasma discharge (left) and the immediate following frame (right).

A time-integrated spectrum acquired with an Ocean Optics USB 2000 compact spectrometer shows high intensity sodium, magnesium, and chlorine lines from the molten salt pool (in addition to the Ar lines from the nearly fully ionized background gas) as well as iron lines from the exploding wire, which confirm the presence of these materials in the arc plasma. After accumulating 20 discharges (4 kJ each), the 3" diameter pyrex cylinder surrounding the discharge was removed after a clean dry argon vent of the chamber, stored in argon, and examined by SEM and EDX. A 100-200 μm thick salt layer was found on the inside wall of the pyrex tube. Figure 3.23 shows an oblique and perpendicular view of the pyrex surface. The surface morphology shows a re-deposited salt layer and abundant salt droplets (20-500 μm size, clearly visible in the oblique view). The perpendicular SEM view (Figure 3.23 (right)) shows clusters of iron droplets with a typical size distribution of 0.1-30 μm peaked around 25 μm (bright features). The purity of the salt was confirmed by the EDX spectrum taken in a region free of iron droplets (Figure 3.24). The oxygen peak was due to air (moisture) exposure in connection with the SEM work. The other impurities, Ni and Si, originate from the crucible and pyrex. The iron concentration of ~0.5 atom-percent was typical for the regions free of visible droplets and represents a lower bound of the iron content due to re-deposition and vapor condensation. The EDX spectrum originates from a surface layer 2 μm in depth. Integrating over the re-deposited part of the pyrex surface and assuming co-deposition of salt and iron, the minimum vaporized/sputtered iron quantity was calculated as 0.8 mg (or 0.04 mg per discharge shot).

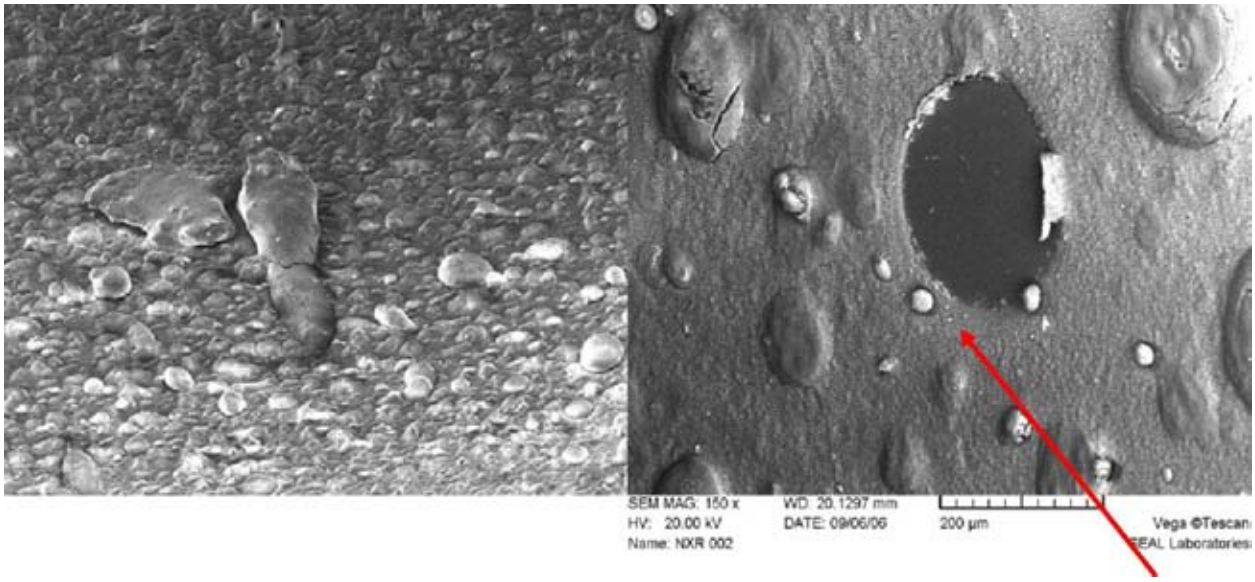

Figure 3.23: (Left) Oblique view of inner pyrex cylinder wall (the large salt droplet is 300 µm wide). (Right) A Perpendicular view showing salt and embedded steel droplets.

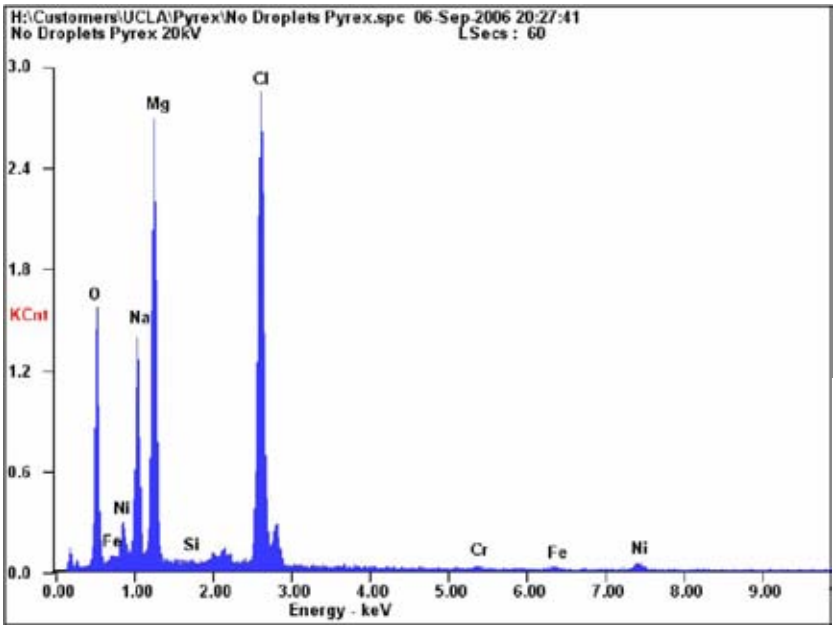

Element	Wt %	At %
NaK	14.63	17.84
MgK	44.05	50.79
SiK	00.32	00.32
ClK	36.07	28.52
CrK	01.92	01.03
FeK	03.01	01.51

Figure 3.24: EDX surface analysis: 500x500 µm refion free of iron droplets.

The EDX spectrum of a typical iron droplet (partially covered with salt) is shown in Figure 3.25. Figure 3.26 shows another region containing small steel fragments. Since the pyrex tube is an insulator, droplets smaller than 0.1 µm could not be directly observed due to space charge limitations in the SEM.

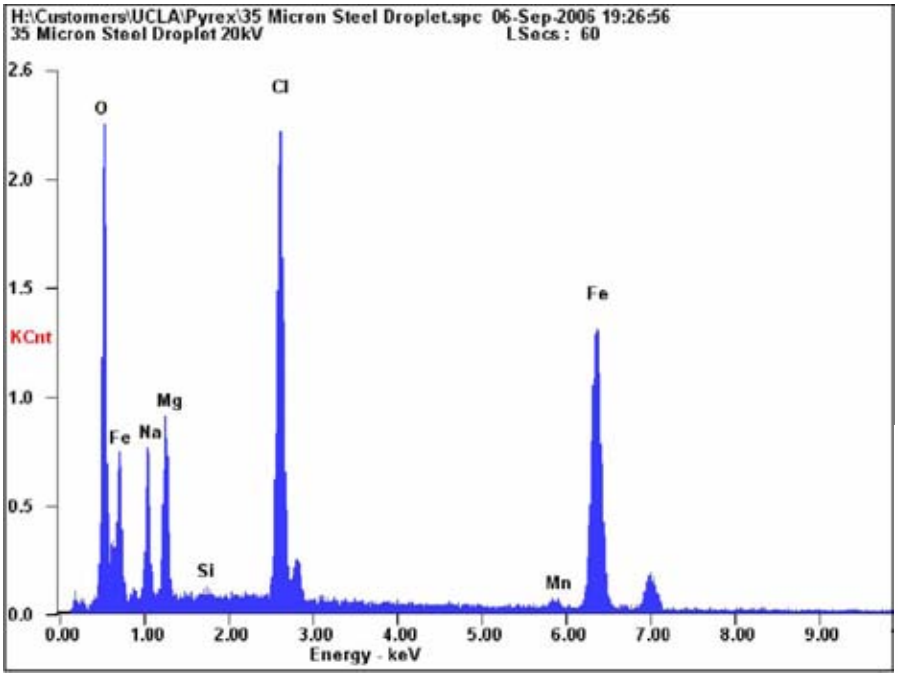

Element	Wt %	At %
NaK	13.43	21.48
MgK	14.33	21.68
SiK	00.44	00.58
ClK	23.63	24.52
MnK	01.25	00.84
FeK	46.93	30.91

Figure 3.25: EDX spectrum of 2 μm steel droplet indicated in Figure 3.23(right).

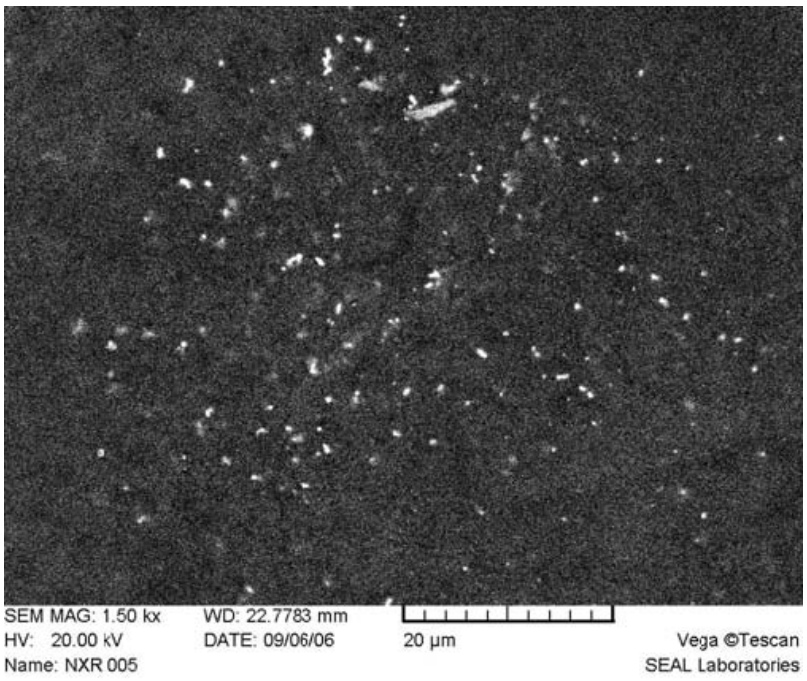

Figure 3.26: Region containing clusters of small steel droplets (0.1-1 μm typical size).

3.4.3 Chamber Dynamics [29]

3.4.3.1 Reactivity and Recycling of Transmission Line Elements

The vapor dynamics and chemical interactions of the excited/ionized vapors in the Z-IFE chamber will determine in which form the atoms recombine and ultimately precipitate in the coolant. Predicting the composition of the precipitate is crucial for evaluating which processes would be effective in the recovery of vaporized/precipitated transmission line material from the coolant loop and to design suitable means of chemical separation from the coolant.

The negative free energy of formation of lithium fluoride LiF and beryllium fluoride BeF_2 is the highest among the metal elements that would be present, at -524.2 KJ/mol and -445.4 KJ/mol respectively per fluorine atom at 1000ºC [34]. For comparison, that of iron fluoride FeF_2 is -126 KJ/mol and that of chromium fluoride CrF_2 is -157.4 KJ/mol. Thus, from equilibrium considerations, the free fluorine generated by the vaporization of flibe is expected to recombine more likely in its original chemical form. However, the recombination process is highly dynamic and the precipitate composition is expected to depend on the plasma dynamics and the density and temperature dependent recombination rates more than on equilibrium properties. Using the substitute eutectic described above in section 3.4.2, our work in 2006 is directed towards the experimental determination of the recombination rates of excited salt and ferritic steel vapors. In addition to the similarities between flibe and Na_2MgCl_4, the ratio of the free energies of formation of NaCl and $MgCl_2$ to the energy of formation of $FeCl_2$ are quite similar to the case of flibe, as outlined in Table 3.5.

Table 3.5: Free energy of formation (kJ/mol per fluorine/chlorine atom) for flibe components versus iron and chromium fluoride and for Na_2MgCl_4 salt constituents and iron.

	T = 1000 K	T = 5000 K
LiF	-401.3	-272.1
BeF_2	-445.4	-279.5
FeF_2	-212.0	-126.0
CrF_2	-157.4	-5.0

	T = 1000 K	T = 5000 K
NaCl	-238.2	-95.6
$MgCl_2$	-205.6	-46.6
$FeCl_2$	-93.5	-22.8

Regarding the separation of metal halides in the flibe coolant loop, hydro-fluorination has been investigated in the MSRE program for the removal of fluorides (by hydrogen injection) [35, 36]. This process can be used in principle to reduce halides like FeF_2, although the removal of the precipitated metal is difficult and has not been successfully demonstrated. The removal of CrF_2 is very difficult due to the low reactivity with hydrogen. Hence, future work will include measurements of the recombination rate of free fluorine and chromium in order to estimate the quantity of CrF_2 produced during the Z-IFE fusion pulses.

3.4.3.2 Recombination Rate Experiments and Calculations

Initially, the ferritic steel vapor for the recombination experiments was generated using the exploding wire technique, using the pulsed power capability of the Z-box. The main drawback of the exploding wire technique is the low pulse rate due to the vacuum vent required in between pulses for the exchange of the wire. Recently a different approach was used. A pulse hollow cathode discharge (HICAT [37], see Figure 3.27) was integrated into the Z-Box. HICAT is operated in He or Ar gas at pressures of 0.1- 6 torr and allows repetitive discharges with a typical pulse rate of 2-5 discharges per minute. For the recombination experiments, the cylindrical cathode of HICAT was lined with ferritic steel foil or a thin layer of #0000 steel wool. Fe vapor is generated primarily by ion sputtering. The concentration of Fe vapor can be controlled to some extent by the total discharge energy. Two different methods for providing free chlorine were explored. In the first approach, a heated Ni-coated crucible containing the molten salt eutectic or a wire coated with 200 mg of salt is placed near the HICAT device. In the second approach, a variable proportion of chlorine gas was mixed with the background gas to vary the free chlorine concentration independently.

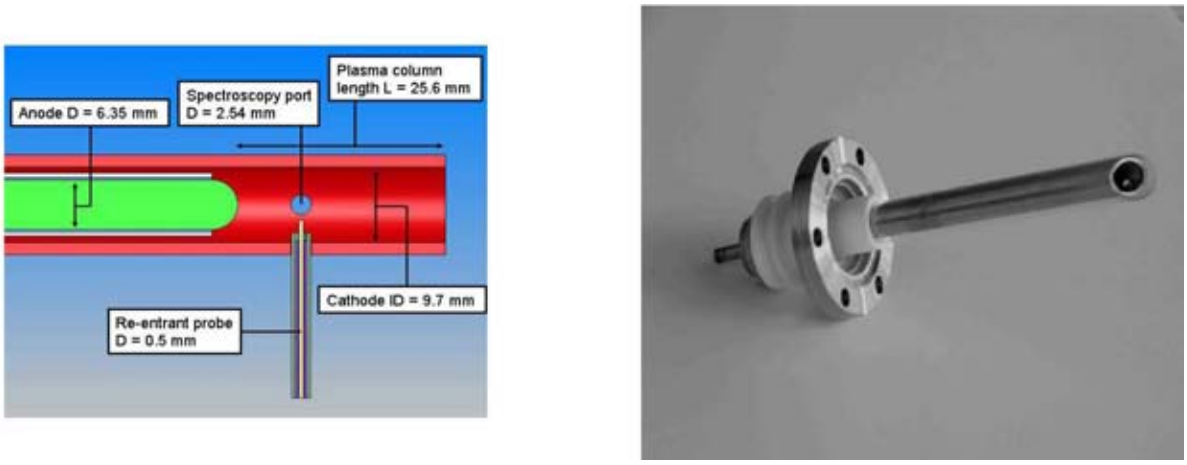

Figure 3.27: Schematic/image of HICAT device

The spectroscopic analysis is based on time-resolved line intensity measurements of the (fully dissociated) atomic species. A cross section of the arc discharge is viewed via a fiber optic coupler. Two double monochromators (2x Jarrel-Ash 0.25 m or Spex 1680) with attached photomultiplier detectors are used to measure the time resolved line intensities of spectral lines characteristic of the molten salt constituents and the vaporized metals. Atomic energy level populations depend on both the atomic number density and electron density, and on the electron

temperature. In the high density, low temperature arc plasmas are considered, the approximation of Local Thermodynamic Equilibrium (LTE) holds typically for temperatures above ~0.8 eV [38]. The temperatures of the different atomic species can then be considered equal and also equal to the electron temperature, and the population density of the atomic energy levels follows a Maxwell-Boltzmann distribution. Since the plasma temperature evolution can be determined from the line intensity ratio using a pair of lines from the same element (but different ionization stage) provided the transition probabilities, upper level energy, and statistical weights are known. The spectroscopic information can be used to extract the relative density of both the molten salt constituents and the ablating metal as a function of time by analyzing line intensity ratios (for example, $I_{Be\ I}/I_{Fe\ I}$, $I_{Li\ I}/I_{Fe\ I}$). Information about molecular recombination rates of the salt constituents in the presence of metal vapor can be deduced provided the time evolution of suitable spectral lines for all constituents is analyzed. The measurements of the substitute eutectic salt used to develop the diagnostic procedure and analysis are reported.

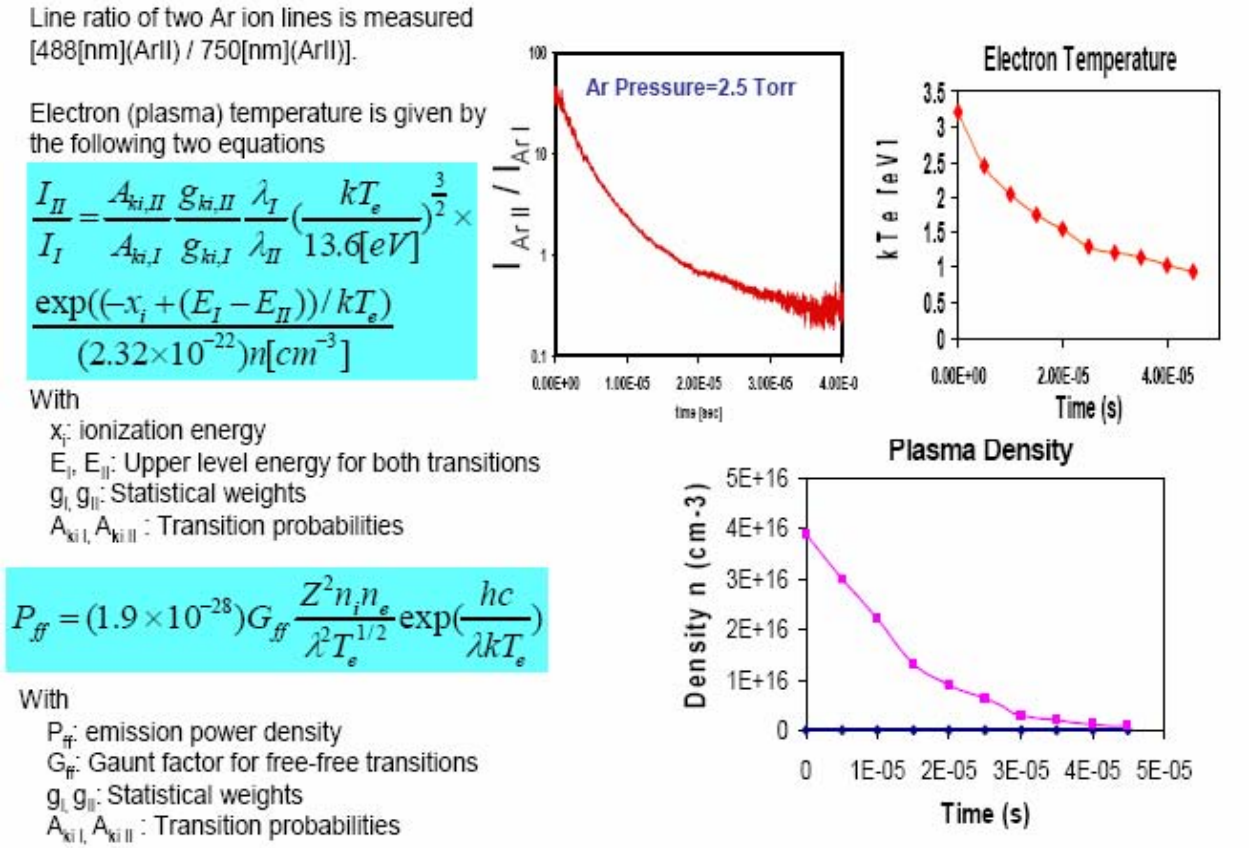

Figure 3.28: Typical argon plasma density and temperature evolution from spectroscopic line ratio measurements.

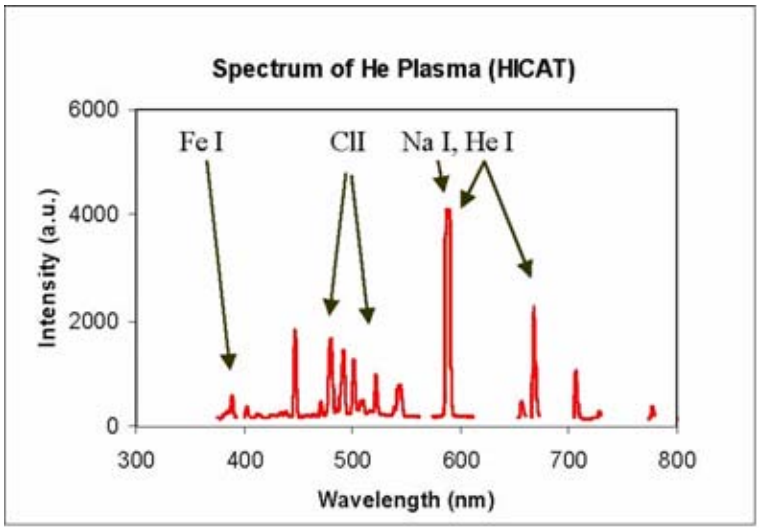

Figure 3.29: Emission spectrum with salt and ferritic steel present.

In principle, the time evolution of the Fe, Na and Cl density can be determined from the time evolution of the emission line intensities once the plasma temperature and density evolution is known. Recombination of free fluorine (or chlorine for the substitute salt) with metal (Li, Be, Fe, Cr or Na, Mg, Fe, Cr in the substitute case) is weakly temperature dependent. However, since the temperature evolution of the plasma pulse depends on the local arc plasma heat losses and cannot be independently controlled, a double pulse technique to determine the time decay of Fe, Na, and Cl densities was used (Figure 3.30). This technique allows the decoupling of the recombination dynamics from the intrinsic plasma temperature evolution. The first (high energy) pulse is used to produce and excite/ionize Fe and salt vapor. The second (low energy) pulse is applied with a time delay and is used to re-excite the amount of Fe still present at that time. The iron density ratio can be directly evaluated from the line intensity ratio of the two pulses and is a measure of the recombination rate. Helium (typically at 1.5-3 torr pressure) is used as background gas to produce the plasma. Helium has the advantage of a simpler emission spectrum with less masking of potentially interesting metal and salt emission lines.

The recombination rate for steel vapor was measured with this method. Figure 3.31 shows the time history of the discharge current and the Fe I line intensity, and Figure 3.32 demonstrates that the Fe intensity ratio (second pulse intensity divided by first pulse intensity) is inversely proportional to the chlorine concentration indicating strong reactivity. The time delay between the pulses is $\Delta\tau$ = 180 μs. The useful data range extends to a chlorine concentration of about 120 (a.u.). At higher concentration the iron density at the time of the second pulse is too low to be measured reliably. The measured recombination rate at the highest chlorine concentration (1 $x10^{-8}$ mol/cc corresponding to 150 mtorr) is ~ 10 kHz, corresponding to a rate constant $2x10^{12}$ cc/mol-s (at a helium pressure of 1.5 torr). The expected recombination rate coefficients for fluorine with Li and BeF and Fe, and for chlorine with Na, Mg, and Fe have been calculated. Reliable thermodynamic data are only available up to a temperature of 5000 K, while the plasma temperature in our experiment is 20000-25000 K (2-2.5 eV) [35].

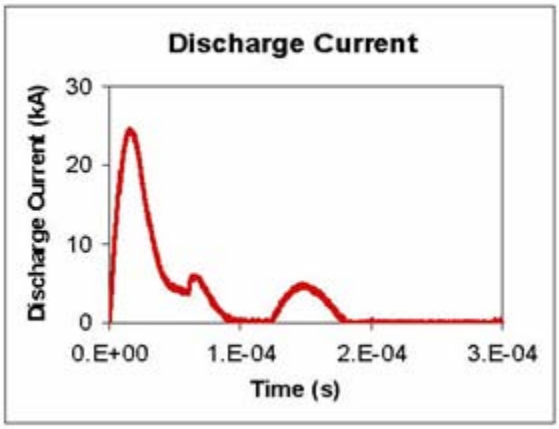

Figure 3.30: Time resolved measurement of species density.

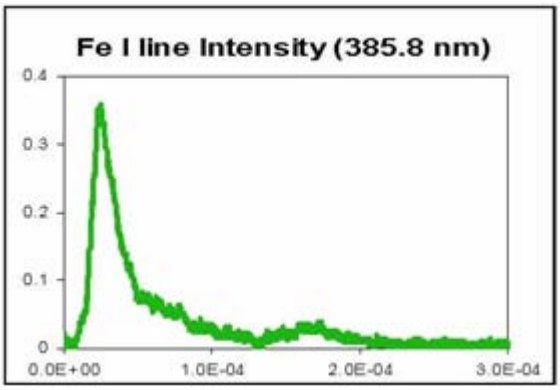

Figure 3.31: Iron I line intensity ratio (pulse 2/pulse 1) verse the relative chlorine density in the plasma, as evaluated from the 522 nm Cl II emission line.

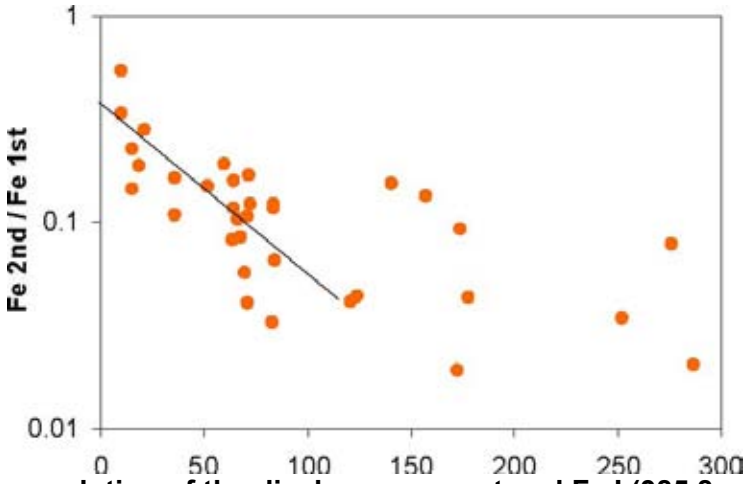

Figure 3.32: Time evolution of the discharge current and Fe I (385.8 nm) line intensity.

In the limit of low densities (which applies to the conditions expected in Z-IFE as well as to the experiments) vapor recombination rate as the result of three-body collisions and the recombination rate is proportional to the background (Helium) gas density. The recombination rates can be calculated from the dissociation rate. In the so-called strong collision regime, the dissociation rate is [39,40]

$$k_o^{diss} = [M] Z_{I,J} [\rho_{vib}(E_o) kT / Q_{vib}] e^{-\frac{E_o}{kT}} F_{anh} F_E F_{rot} F_{rot,\text{int}} \qquad 3.5$$

Here,

$$Z_{I,J} = N_A \sigma_{A-M}^2 (8\pi kT / \mu_{A-M})^{1/2} \Omega_{A-M} \qquad 3.6$$

is the gas-kinetic binary collision frequency, ρ_{vib} is the vibrational density of states, Q_{vib} is the vibrational partition function, E_o is the activation energy, and the factors F are corrections due to rotational and vibrational oscillations. The recombination rate is calculated using the equilibrium dissociation constant

$$K_c = \frac{[A][B]}{[AB]} = \frac{p}{RT} \exp(-\Delta G_o / RT) \qquad 3.7$$

Here [A], [B], and [AB] are the molar densities of the two constituent atoms and the product molecule, and $-\Delta G_0$ is the Gibbs free energy of formation. The recombination rate is then given by:

$$k_0^{rec} = k_o^{diss} / K_c \qquad 3.8$$

These rates are calculated for equilibrium conditions which may marginally hold for the expected high density in Z-IFE plasmas.

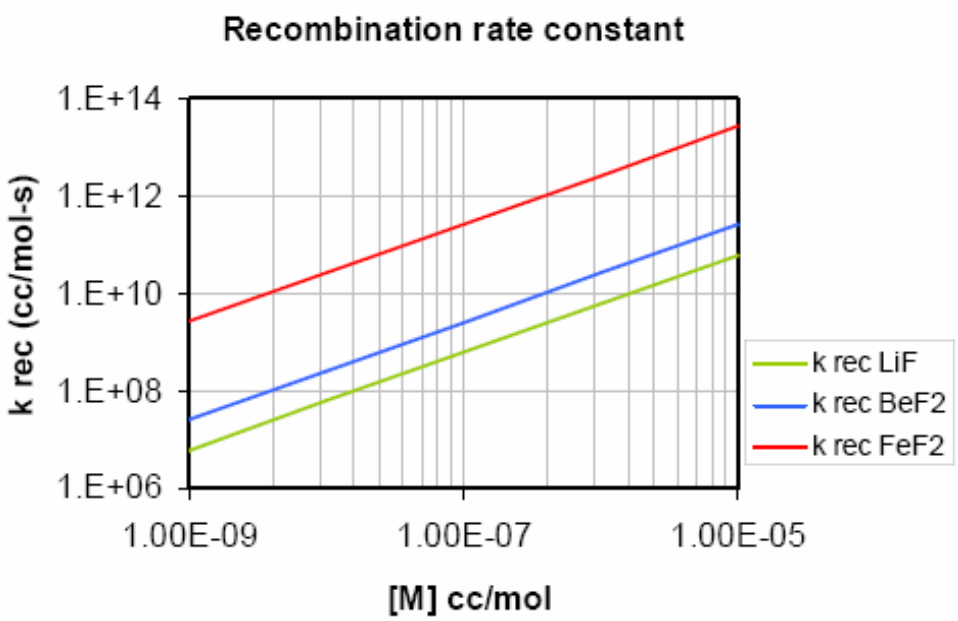

Figure 3.33: Calculated three-body recombination rate constant for flibe components and iron in Argon gas (T= 5000K).

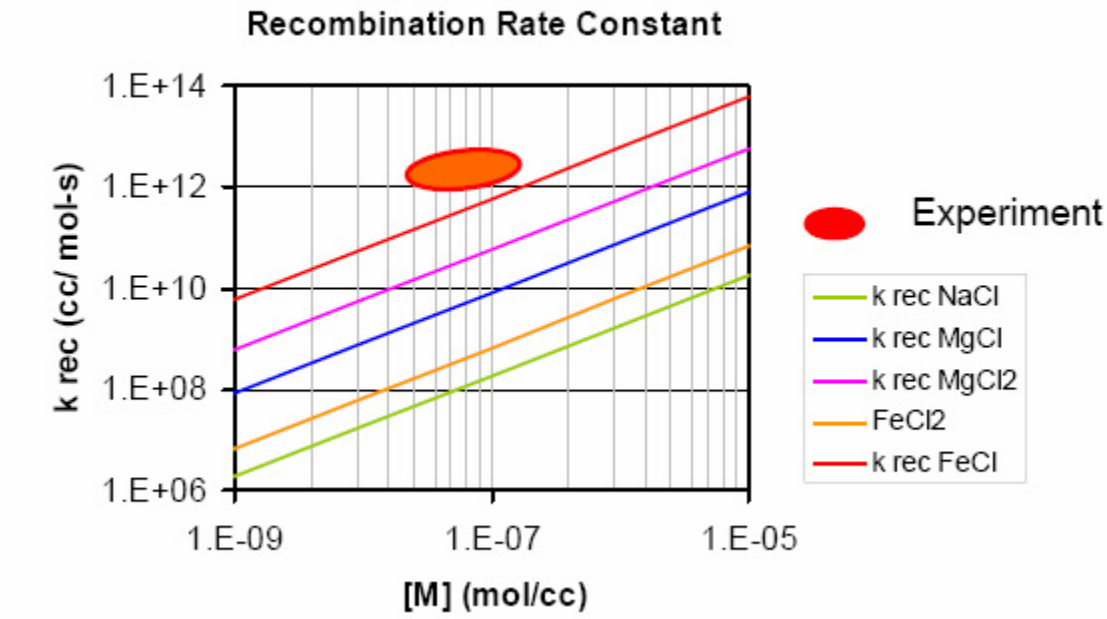

Figure 3.34: Three-body recombination rate constant for NA, Mg, and Fe with Cl in Helium gas (T=5000K).

Figure 3.33 and Figure 3.34 show a comparison of the calculated gas phase recombination rates for Li +F > LiF, BeF + F > BeF_2. and FeF + F > FeF_2 for T = 5000 K. verse the background gas concentration [M] for Argon. The latter rate is calculated to be much larger than the flibe recombination rate constants. A similar scenario is also found for the substitute salt, where the reaction Fe + Cl > FeCl is calculated to be larger than the recombination rate constants for NaCl, $MgCl_2$, and the reaction Fe + FeCl > $FeCl_2$. It should be noted that FeF and FeCl exist only at high temperature in the gas phase and are not very stable but may subsequently react with fluorine and chlorine to form stable iron halides. In summary, the preliminary experimental evidence of large recombination rates for iron-chlorine reactions is consistent with calculated results. These results indicate that reaction rates of fluorine with transmission line material may be high, and an effective scheme for reduction/removal of metal halides may be needed.

Substantial progress has been made in evaluating the condensation and recombination behavior of molten salt plasmas. The deposition of evaporated/sputtered iron from a molten salt plasma have been investigated. Preparations for tests involving a Sn wire/mesh are underway. Molten salt vacuum casting has been refined and high purity samples have been produced in preparation for electrical/mechanical testing of cast flibe. The dielectric constant of the substitute Na_2MgC_{l4} has been measured. First measurements of the iron recombination rate constant in a molten salt high density plasma have been made and suggest large reaction rates of iron with chlorine/fluorine. Based on these results, more comprehensive studies of the reaction kinetics of molten salt plasmas with iron and chromium will be needed in the future. Upgrading the spectroscopic capabilities by adding a second higher resolution (1 Angstroem) spectrometer will allow simultaneous measurement of emission lines from different elements. In addition, an effective means of separating out metal halides and precipitated metal from liquid flibe need to be investigated. The detailed spectroscopic work as well as initial separation experiments can be carried out with Na_2MgCl_4 which allows much more flexible experimentation.

3.5 Automation

The ZPoP (Proof of Principle) dynamic simulation from 2005 provides a detailed view of the automation needed for the Z-Pinch Power Plant while loading a single RTL into the chamber and removing it from the chamber. ZPoP also provides information on the automation required for an energy pulse delivered to a single chamber given through a recyclable transmission line (RTL). The baseline Z-IFE power plant operating at 0.1Hz will have ten chambers emitting high energy pulses simultaneously. This overview will discuss some of the considerations that should be accounted for in the full scale power plant operating at 0.1Hz.

3.5.1 Plant Layout

The overall layout of the Z-IFE power plant will largely determine the automation that will be required. The ZPoP simulation featured a conveyor system by WARD Systems Inc. This system contains a conveyor and battery powered Power Pallets that carry payloads along the conveyor. In the case of the ZPoP simulation, the payloads are the RTLs. A main controller is used to control the movements of the conveyors. The conveyor costs $250 per foot and each pallet is $30,000. The WARD Power Pallets will travel at speeds over 350 ft/min (roughly 3.98 mi/hr). If the WARD System is used, this speed will constrain RTL travel along the conveyor in addition to the overall layout of the conveyor system.

In order to determine the length of conveyor and the number of power pallets required, the overall design of the plant layout is needed. Some of the important features of the plant layout will include the location of the chambers and the spacing between the different conveyors. Figure 3.35 illustrates several of the major events in handling the RTLs beginning from removing the new RTLs from the storage facility (1) to the removal of used RTLs to be recycled at the manufacturing plant (7).

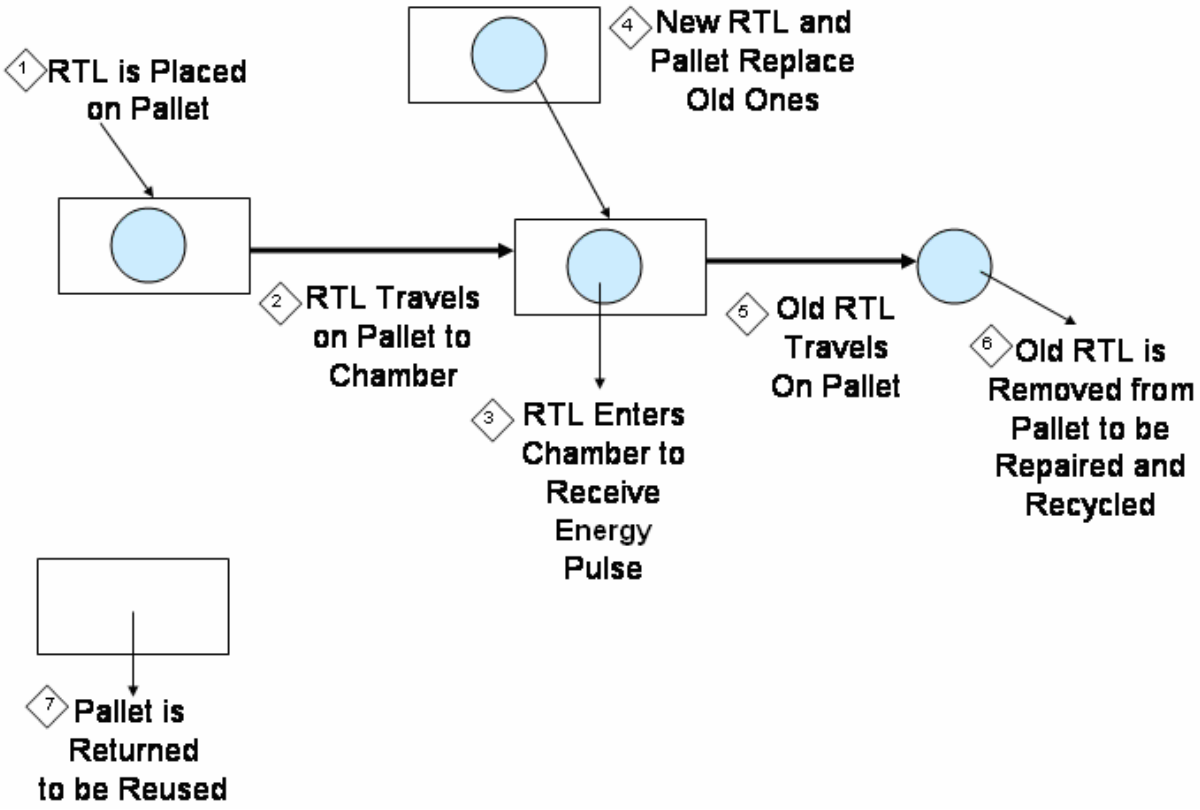

Figure 3.35: **Major Stages in transferring RTL**

As is illustrated in Figure 3.35, the RTL will be transferred to many locations within a short span of time. The ZPoP simulation demonstrates that it is dynamically feasible to insert an RTL into the chamber, remove it from the chamber and replace the used RTL with a new RTL. In the full-scale power plant ten of these cycles will be staggered at one per second so that each chamber operates at 0.1 Hz. Therefore, it is important to consider the most efficient plant layout that will allow for easy loading of the RTLs from storage, to the chambers, and then back to the manufacturing plant.

3.5.2 Loading New RTLs and Unloading used RTLs

Another key factor in the automation design is loading the new RTLs from the RTL storage and removing the used RTLs to be remanufactured. Whether or not the RTLs enter single file on one conveyor line or arrive on several conveyor lines to conserve time has yet to be determined. It is likely that the removal of the used RTLs could occur similarly to loading the new RTLs.

RTLs will be manufactured and remain in storage until they are ready for use. However, it is important to decide the number of RTLs that will be on the conveyor at any given time to determine the approximate amount of Power Pallets to purchase. In addition, the Power Pallets carrying the used RTLs will need to be cycled back to the RTL storage to transport new RTLs to the chambers.

3.5.3 Future Work

Future work regarding the automation for the Z-IFE Power Plant involves determining a plant layout that allows for efficient loading and removal of RTLs from storage and back to the manufacturing facility. The plant layout must also allow the power pallets to easily transfer the RTLs to each of the ten chambers based on the energy pulses occurring every ten seconds.

4 CHAMBER DESIGN AND SHOCK MITIGATION

A z-pinch IFE driven power plant has several advantages over laser or heavy-ion driven concepts. Laser and heavy-ions require high vacuum conditions so that the energy path to the target is unobstructed. This limits x-ray and neutron attenuation mechanisms such as gas or liquid, which can greatly reduce the impact on containment chamber wall. As a result, the laser or heavy-ion driver reactor chambers are very large to take advantage of the inverse square law that describes the attenuation of photon intensity with distance. Z-Pinch driven IFE directly links the power source to the target through a transmission line. This allows a myriad of shock mitigation schemes without having the concern of obstructing the path of lasers or heavy-ion beams. Absorbing the x-rays could greatly reduce the chamber radius needed to contain the fusion reaction.

The chamber for a z-pinch driven IFE reaction must survive under harsh conditions. It is constantly being bombarded with neutrons, RTL and target shrapnel, and x-rays. The high energy neutrons from the D-T reaction displace atoms in the crystal lattice of the chamber wall. This causes embrittlement which can greatly reduce the integrity of the wall over a long period of time. The major cause of immediate degradation in the containment vessel is x-rays depositing their energy into a small volume of chamber wall. This creates large temperature gradients in the wall, resulting in ablation that drives a shock wave through the material. This shock wave can destroy a chamber rapidly, and since IFE power plants require fusion events on the order of 0.1 to 1 Hz, it is clear that such a situation makes it impossible for a wall to last the life-time of the plant. Therefore, a shock mitigation scheme must be implemented into the chamber to absorb all or most of the x-ray energy. Several mitigation schemes are presented in this section.

Two fundamentally different chamber designs have been proposed for the Z-IFE power plant. The first was a thick liquid curtain design which mitigates the x-rays and neutrons before they interact with the chamber wall. The second design used gas or aerosols to mitigate the x-rays while allowing the neutrons to pass through the chamber wall (first wall design).

Experiments at the University of Wisconsin and University of California in Berkeley have been conducted studying the effects of shock mitigation through two-phase liquid with a small void fraction and thick liquid curtains respectively. Also, experiments characterizing two-phase turbulent jets have been conducted at The Georgia Institute of Technology. The results of the models and experiments are discussed below.

A new first wall chamber design has been proposed this year in response to some promising modeling results of aerosol mitigation. Aerosols have shown to be effective x-ray absorbers up to Z-IFE power plant target yields, which can sufficiently protect the chamber of a much smaller radius. A disadvantage of this design is that there is no protection from the high energy neutrons impacting the chamber wall. This issue may be addressed through thermal annealing. Thermal annealing has proven to effectively heal LWR pressure chamber walls and welds by allowing atoms to diffuse back into the gaps of the crystal lattice [41]. Thus, if the chamber is kept at an elevated temperature neutron embrittlement may not be an issue. RTL shrapnel may be a concern but may only have a second order effect on the vessel wall for both the thick liquid curtain and first wall chamber designs. The first wall chamber design has several advantages over the thick liquid curtain design but presents a whole new set of science and engineering issues that must be addressed in future studies.

Experiments on ZR are discussed briefly below which are outlined in more detail in the Advance Fusion Concepts Grand Challenge LDRD [1]. These will help provide crucial information on x-ray mitigation using gases, aerosols, and thick liquid curtains. They will also be necessary for demonstrating complete containment of tritium. These experiments are shown on the critical path of the roadmap and are necessary before a ZN facility can be designed and built.

Due to the cyclical nature of an IFE power plant design, fatigue will be great concern when designing the chamber. The ductility of the chamber plays a large role in determining a material's fatigue limit. The fatigue limit should be the main design parameter for the chamber instead of the maximum allowable stress based on a static pressure, which was used in previous studies. A first order fatigue analysis is described in section 4.2.5 for F82H steel in an attempt to predict that maximum design stress of the chamber.

4.1 Shock Mitigation

Shock mitigation within the reaction chamber is a crucial stepping stone on the way to developing fusion energy systems. Since a large percentage of D-T fusion reactions are in the form of x-rays, approximately 30%, most of that energy must be mitigated to dampen or eliminate a shock. The x-rays, if no mitigation medium is used, will deposit their energy into a very small volume of the chamber wall causing it to ablate, generating a catastrophic shock. An attenuating medium such as gases, aerosols, thick liquid curtains, and foams allow the x-rays to deposit their energy over a large volume thus mitigating or preventing a shock. Gas may be used for lower power fusion yields on the order of 10 MJ while aerosols, foams, and liquid curtains are needed for larger yields.

4.1.1 Shock Mitigation Roadmap

The initial set of shock mitigation experiments can be performed on Z-beamlet. Z-beamlet is a high power laser that can simulate intense photon environments as would be seen in a fusion reaction. X-rays can also be generated using this laser to further simulate a fusion event. The only limitation may be that the energy of the x-rays produced will not match that generated by a fusion reaction but still may be able to effectively demonstrate mitigation. Savings in both cost and time make experiments with Z-beamlet an attractive option as compared to ZR, so many of the initial x-ray mitigation experiments can be conducted in this facility. Once a mitigation scheme has been chosen to be the most promising, then it can be further tested on ZR.

The experiments on ZR will show that the x-rays can be mitigated sufficiently minimizing the impact to the chamber wall. The sealing of the containment chamber and transmission line post shot will also be demonstrated with these experiments. Several of the diagnostics required for these experiments will be available on ZR such as: a calorimeter to measure total radiated energy from the pinch with no time resolution, a total energy and power diagnostic (TEP) tool that measures peak pinch power levels up 350 TW, and a transmission grating spectrometer (TGS) to measure the time-resolved spectrum of the x-ray source. Thermocouples, strain gages, and gas detection equipment will also be needed but are readily available through outside vendors.

Over several years of containment studies the experiments will transition to demonstrating the containment of tritium from D-T fusion reaction. Showing that tritium can be contained safely is a crucial step for moving forward for both defense testing and power production of z-pinch technology. An illustration of the possible experimental setup on ZR is shown in Figure 4.1.

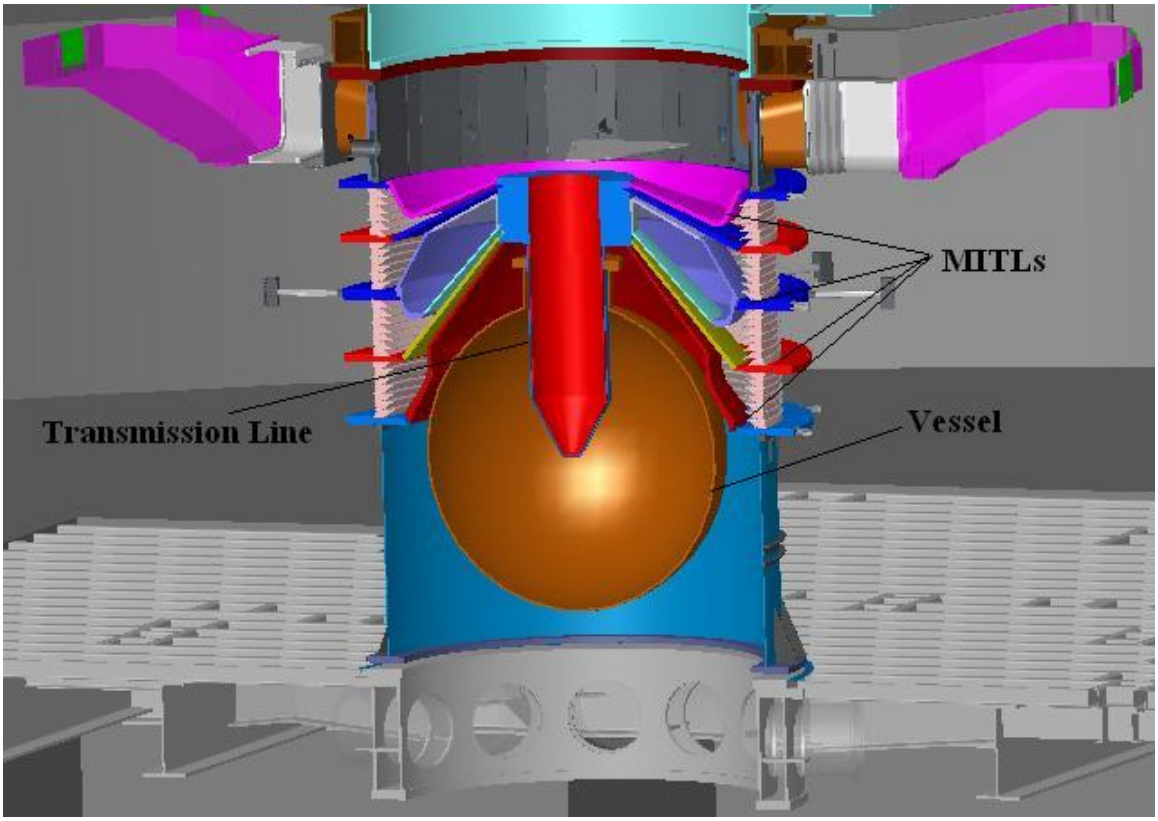

Figure 4.1: Illustration of a possible experimental setup on ZR.

A more detailed description of these experiments can be found in the Advanced Fusion Concepts: Grand Challenge LDRD [1].

4.1.2 ALEGRA Modeling of Gas Mitigation

ALEGRA, a shock physics code developed at Sandia National Laboratories, was used to estimate the amount of ionization of the gas, the temperature rise in the vessel wall, and the resulting heat load caused by a z-pinch driven IFE event. Plasma phenomena such as bremsstrahlung radiation, electron thermal conduction, material opacity, and radiation transfer were considered. ALEGRA currently does not consider plasma viscosity, a potentially-important diffusive mechanism [43, 44, 45].

Two models were created in ALEGRA. The purpose of the first model was to benchmark ALEGRA with experimental data. The second model simulates a Z-IFE like containment chamber filled with argon gas that houses a target capable of generating 10 MJ of x-rays. This would simulate more of a test type environment leading up to full scale experiments at power plant yields.

4.1.2.1 ALEGRA Simulation of Laser Ionization of Argon Gas Experiment

In order to benchmark ALEGRA for the simulation of electromagnetic radiation incident upon a gaseous environment, an experiment conducted at the University of California at San Diego was modeled [46, 47]. The laser provided 155 mJ for 8 ns at a pulse of 532 nm. The argon gas was initially at 1 atmosphere and room temperature.

Various quarter-symmetry circular 2D Cubit meshes were generated. The simulation used ALEGRA's "radiation hydrodynamics conduction" modules with an Eulerian mesh option. Whereas multiple time-step schemes are available, a constant time step of 5.0E-12 seconds was initially selected. The calculational time step and mesh size were reduced until the solution was spatially and temporally resolved.

The radiation package called the linearized diffusion model with a flux limiter based on Larsen. The boundary conditions were such that there was no displacement and no heat flux along the symmetry of the mesh. Additionally, the symmetry surfaces employed reflective boundaries. Because ALEGRA requires a curve in 2D geometry for temperature boundary sidesets, the reader will notice that a small segment of the mesh's inner radius was clipped off (see Figure 4.2). This was done to incorporate a sideset which allowed the blackbody emission of the laser photons that were emitted for 8 ns.

The argon gas was modeled using the following material models:

- ideal gas equation of state (EOS)
- Spitzer thermal conductivity
- Saha ionization
- XSN and CDF opacity models (Rosseland, absorption, and scattering)

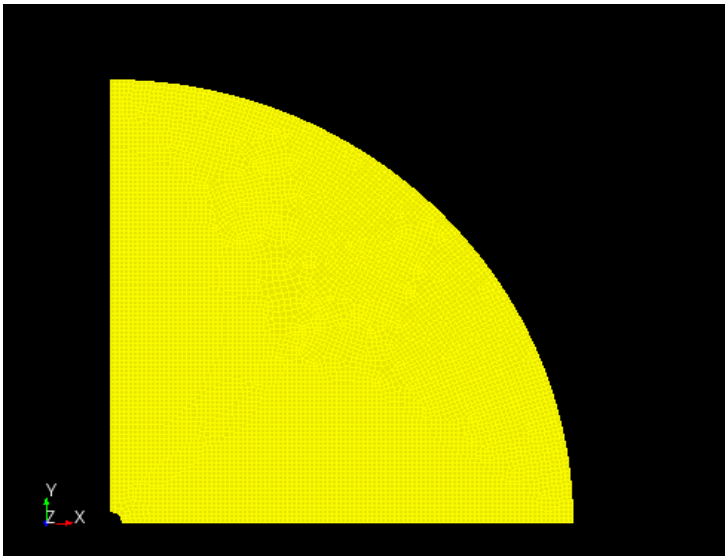

Figure 4.2: Semi-coarse laser mesh.

As shown by Table 4.1, the agreement between ALEGRA and the laser experiment was quite good. Temperatures, spark length, and degree of ionization were predicted between a few percent to up to 15% error. The ionization was measured in the experiment by using optical

emission spectroscopy. According to personal communication with Sivanandan Harilal, most of the spectral lines were due to Ar+ (singly-ionized argon), but some Ar++ (doubly-ionized argon) was also spotted [48]. ALEGRA calculated a maximum (averaged) ionization of 1.9, which compares very well with the 2 levels of ionization seen in the experiment. Figure 4.3 compares the spatial evolution of the argon spark. The ALEGRA quarter symmetry results are shown on the far left. These are to be compared directly with the quarter-symmetry data. As the figure shows, the agreement is excellent. For added convenience, the full-geometry data are shown on the far right of the figure. Notice that the data's shape tended to be spherically symmetrical for the most part. It should be pointed out that despite the reasonable agreement, better agreement is expected if ALEGRA's two-temperature models are used. Currently, due to time constraints, thermal equilibrium between the ions and electrons was assumed.

Table 4.1: Comparison of Laser Experiment Data with ALEGRA Simulation

Parameter	Data	ALEGRA
T_{max} at 22.0E-9 s (K)	35,972	33,530
T_{max} at 100.0E-9 s (K)	29,590	25,673
ΔX_{spark}(maximum transverse length) at 22.0E-9 s (mm)	4.0	4.4
ΔX_{spark}(maximum transverse length) at 100.0E-9 s (m)	5.5	5.2
α (maximum ionization during transient)	2	1.9

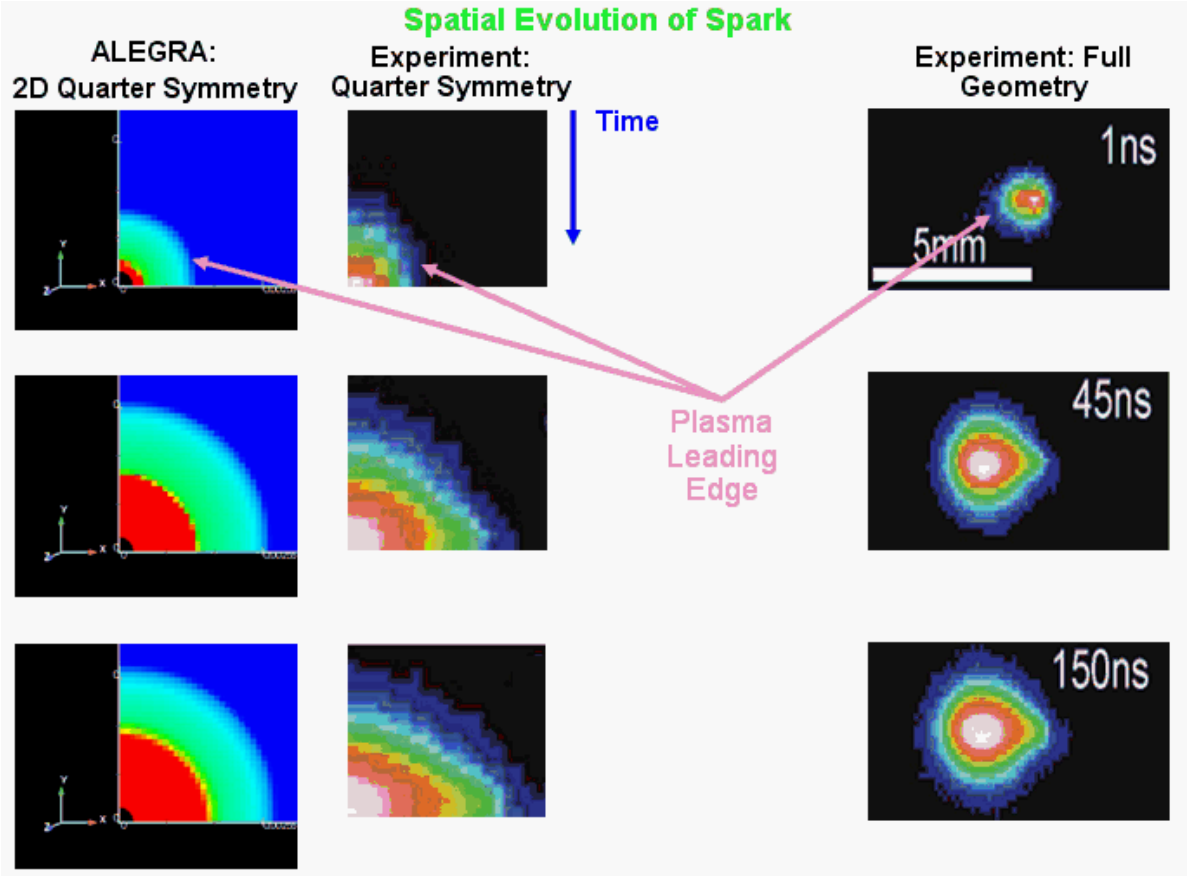

Figure 4.3: Spatial evolution of the argon spark as a function of time (UCSD laser data courtesy of Sivanandan S. Harilal).

4.1.2.2 ALEGRA Simulation of X-ray Ionization of Argon Gas within a Z-IFE Chamber

Cubit meshes were generated for 2 and 3D models representing 1/8 of a sphere. The relevant parameters were assembled into Table 2 for convenience. Like the laser simulation, the X ray simulation also employed ALEGRA's "radiation hydrodynamics conduction" Eulerian modules. In fact, many of the modules were similar, as will be shown later.

Whereas multiple time-step schemes are available, the authors chose a constant time step of 5.0E-12 s as a starting point. The calculational time step and mesh were reduced until the solution was spatially and temporally resolved. For quick turnaround testing, a 2D, extremely coarse mesh with about 2,000 elements was used. For the final calculations, about 65,000 elements were used.

The radiation package called the linearized diffusion model with a flux limiter based on Larsen. The boundary conditions were such that there was no displacement and no heat flux along the symmetry of the mesh. Additionally, the symmetry surfaces employed reflective boundaries. The outermost curve of the 2D mesh (the steel wall) was set at a constant temperature boundary condition (300 K). This temperature did not matter much, as the relatively slow transient heat conduction response of the steel meant that the outermost radial elements of the steel mesh changed very little with respect to time. Because ALEGRA requires a curve (2D) or surface (3D) for

temperature boundary sidesets, the reader will again notice that a small segment of the mesh's inner radius was clipped off; see Figure 4.4. This was done to incorporate Sideset 2, which allowed the blackbody emission of the 1.0 keV X rays that were emitted for a given time (1.0E-09 s in this case).

It should be pointed out that such numbers can be easily modified to whatever number is desired. For example, even though the black body may be at 3 keV, only 1 keV was considered.

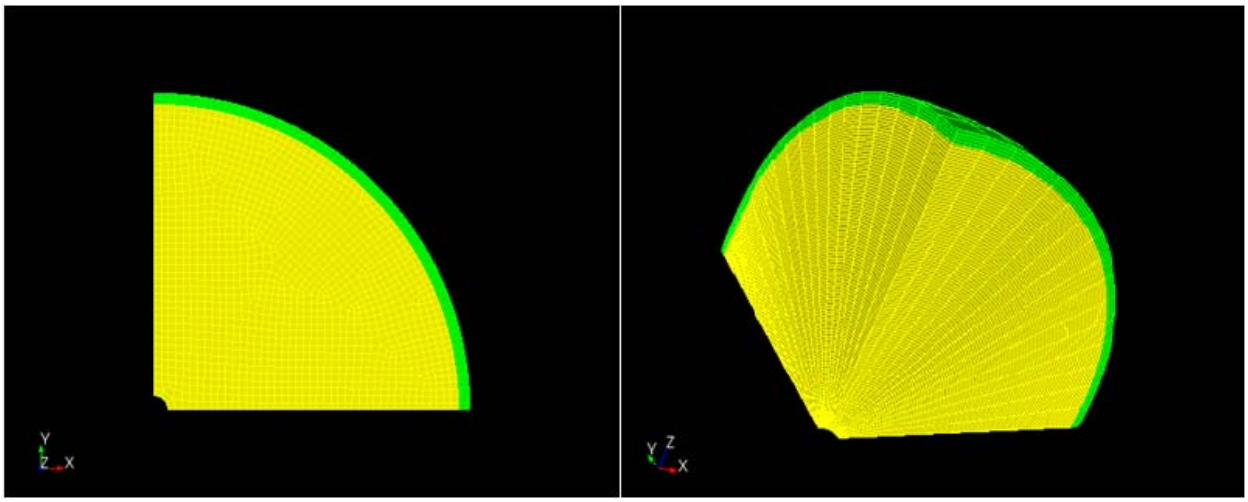

Figure 4.4: Coarse 2D (left) and 3D (right) Z-IFE chamber meshes

The argon gas was modeled using the following material models:

- ideal gas EOS
- Spitzer thermal conductivity
- Saha ionization
- XSN and CDF opacity (Rosseland, absorption, and scattering)

The steel was modeled using the following material models:

- Mie-Gruneisen EOS
- Spitzer thermal conductivity with cold material interpolation,
- Saha ionization
- XSN and CDF opacity

The Spitzer thermal conductivity was linearized from a room temperature thermal conductivity (16 W/mK).

4.1.2.3 Z-IFE Simulation Results

As the simulations began, the strong x-rays quickly ionized the first few centimeters of the argon gas, where the average ionization z was 15.6. At this point in the chamber, the plasma temperature peaked at 1.25E6 K. Because of its strong dependence on temperature, the argon opacity quickly reached very high values, causing the x-ray energy to not penetrate beyond the high temperature region. For example, at room temperature, opacity was near zero, but climbed steeply to about 1.39E5 m^2/kg. This meant that energy transfer was limited to the diffusion of heat via

electron thermal conduction. This generated a Marshak wave that initially propagated at about 100,000 m/s, but that gradually slowed down as the plasma spread outwardly and its temperature cooled. By the time the plasma hit the steel wall 1 m later, the Marshak wave was only moving at about 10,000 m/s. Furthermore, the plasma that struck the steel wall was about 25,000 K initially, with an average ionization of 1.9. Despite its high temperature, the plasma temperature adjacent to the wall quickly dropped as heat was conducted to the innermost layer of the steel wall. Nevertheless, the peak temperature at the inner surface was about 1,900 K. For comparison purposes, steel melts at about 1,700 K. It must be noted that because of the relatively-slow heat-conduction diffusion time of steel, only the first two innermost steel elements were above the melt point, and the rest remained cool. This implies that only about 0.00006 m of the steel wall melted, with the rest (0.03994 m), remained well below the melting point. Note that the excessive heat-up of the innermost part of the steel wall can be minimized relatively easily by placing a liquid wall that so it convects away the heat from the steel wall. For convenience, the key transient parameters are summarized in Table 3.

Table 4.2: Z-IFE X-ray simulation key output.

Parameter	Magnitude
Peak Argon Plasma Temperature (K)	1.25E6
Average Temperature of Argon Plasma that Reaches Steel Wall (K)	2.5E4
Peak Steel Wall Temperature (K)	1,900
Maximum Ionization of Argon Plasma	15.6
Minimum Ionization of Argon Plasma Adjacent to the Steel Wall	1.9
Peak Marshak Wave Velocity (m/s)	1.0E5
Minimum Marshak Wave Velocity (m/s)	1.0E4
Peak Absorption Opacity (m^2/kg)	1.39E5
Peak Rosseland Opacity (m^2/kg)	8.5E5
Peak Pressure (Pa)	3.7E8
Peak Electron Thermal Conductivity (W/m-K)	6.04E4

Figure 4.5 through Figure 4.10 show the transient temperature, zbar, Rosseland opacity, absorption opacity, pressure, and electron thermal conduction at 1 and 500 ns.

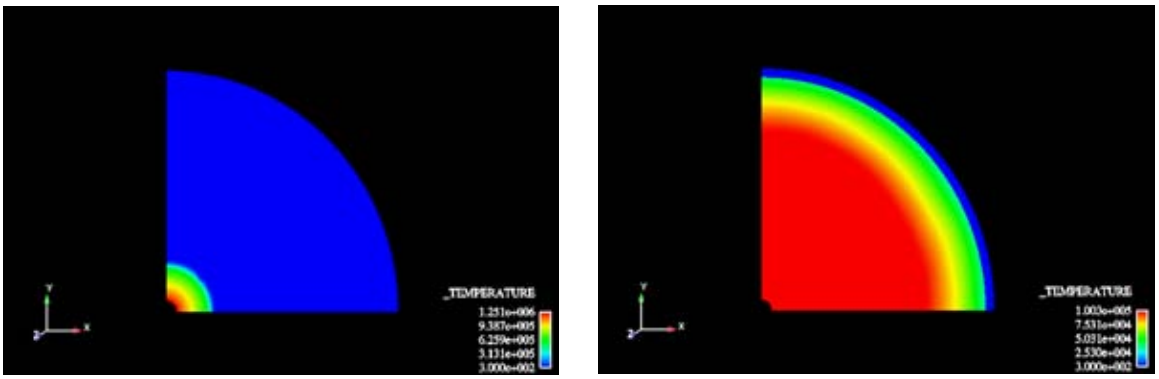

Figure 4.5: Argon temperature (K) at 1 and 500ns.

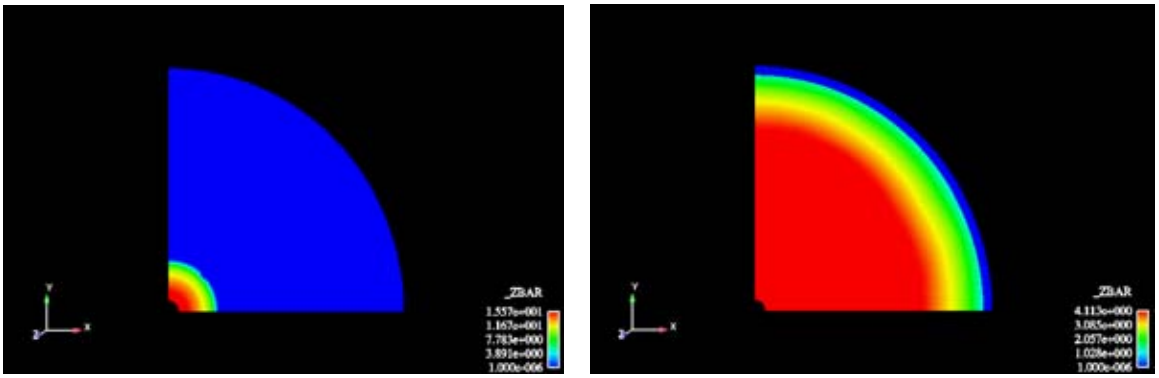

Figure 4.6: Argon zbar (-) at 1 and 500 ns.

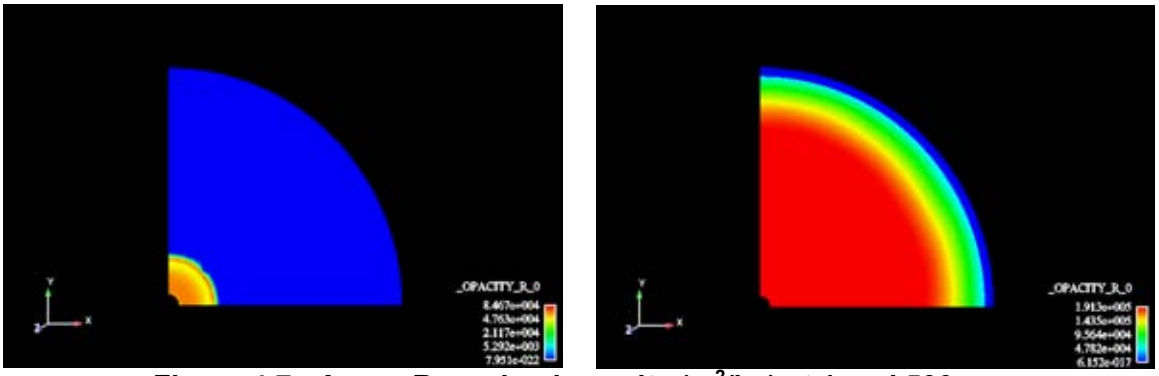

Figure 4.7: Argon Rosseland opacity (m^2/kg) at 1 and 500 ns.

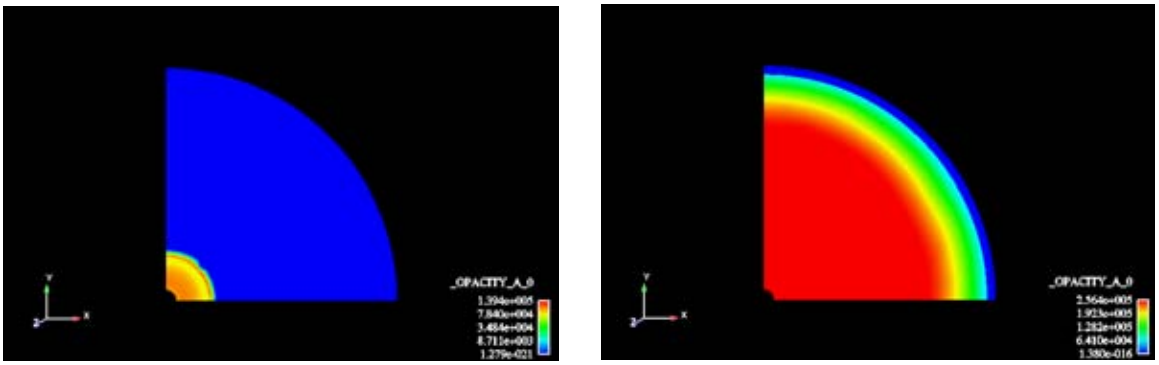

Figure 4.8: Argon absorption opacity (m^2/kg) at 1 and 500 ns.

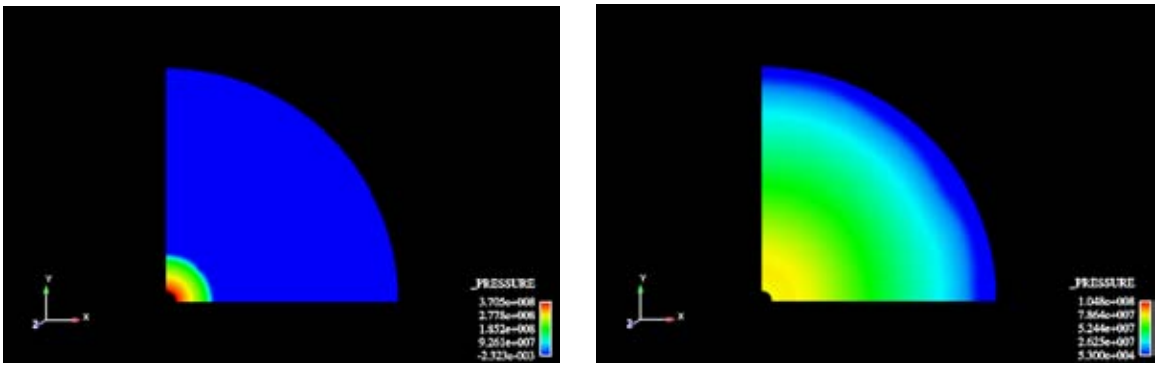

Figure 4.9: Argon pressure (Pa) at 1 and 500 ns.

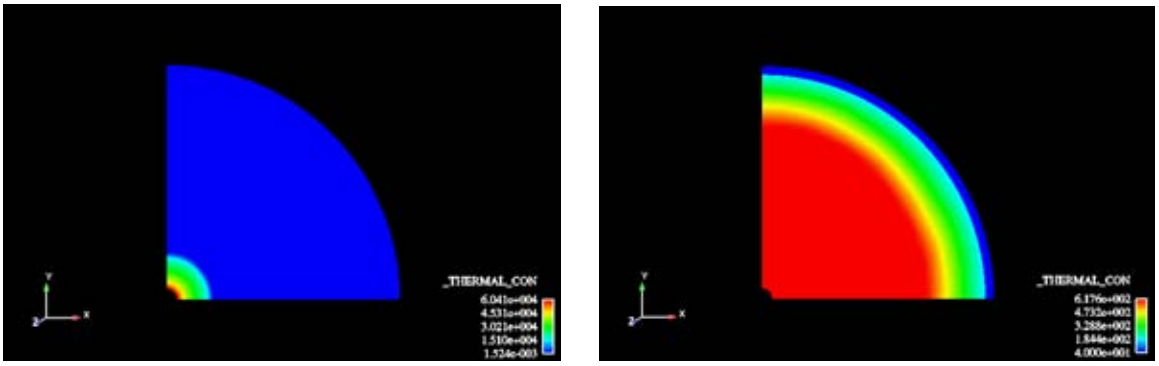

Figure 4.10: Electron thermal conductivity (W/m-K) at 1 and 500 ns.

Finally, Figure 4.11 shows EFLUX and PFLUX. EFLUX is defined as the net, time-integrated energy that has flowed across a surface (or curve in 2D). PFLUX is the total power computed at a given time step for a given surface. Therefore, PFLUX should be zero if the cumulative variable, EFLUX, is not changing. For the 10 MJ and 2D 1/4 symmetry mesh, we used ¼ the quoted energy, or 2.5E6 J (quarter domain, quarter the energy). As noted by the figure, EFLUX started at zero (and due to curve orientation has a negative value), and resulted in a deposition of 2.5E6 J, as desired. This energy was distributed during a nanosecond, so $P=E/\Delta t$ = 2.5E6/1E-9 = 2.5E15 W, which is what the PFLUX figure shows. Note that the figure shows that

the total energy insertion occurred during 1E-9 s, as expected. After that time, EFLUX stayed constant (i.e. there was no further addition of energy), and PFLUX therefore remained zero. This verified that the right amount of energy was input to the system during the right time period.

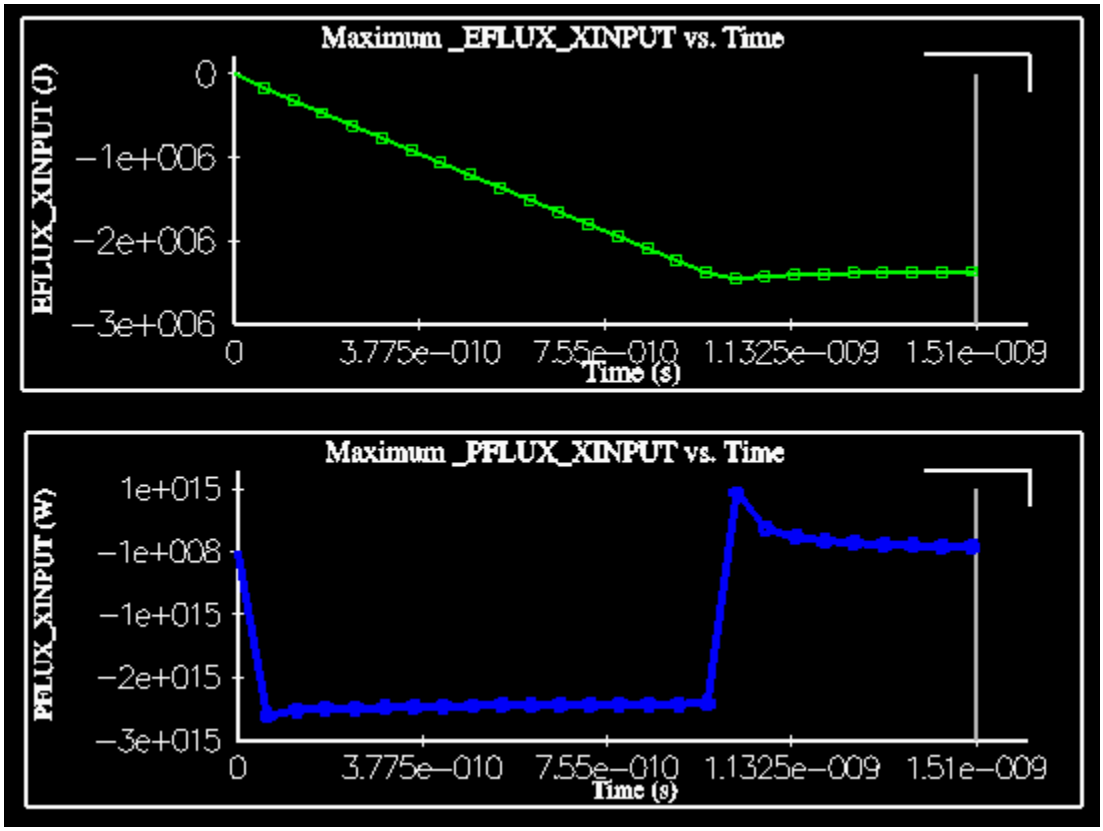

Figure 4.11: EFLUX and PFLUX as functions of time during first 15 ns of the transient.

4.1.2.4 Conclusion

The relevant models for calculation of ionized gases were discussed. The literature was consulted to determine which key parameters could determine the transient's signature. It was noted that opacity, electron thermal conduction, and degree of ionization are important, as well as several other physics. Then, ALEGRA was benchmarked against a UCSD laser experiment that ionized argon gas. The ALEGRA output for zbar, peak temperatures, and spark spatial domain agreed quite well with data.

Next, a simulation of a hypothetical Z-IFE chamber with argon gas at 53,300 Pa was conducted using ALEGRA. The calculation showed that for the first few centimeters of the 1 m chamber, the argon gas reached a peaked at 1.25E6 K, with an averaged ionization of 15.6. As the gas heated up, the absorption and Rosseland opacities increased exponentially to 1.39E5 and 8.5E4 m^2/kg, respectively. The sharp temperature increase effectively meant that the photons were not able to traverse the optically thick plasma medium. Heat was conducted away through electron thermal conduction at a large rate; the electron thermal conductivity reached a maximum of 6.04E4 W/m-K. Nevertheless, as the transient evolved, the plasma spread outwardly and began to cool down.

As a result of the heat conduction, a diffusion (Marshak) wave initially traveled at close to 100,000 m/s and proceeded to slow down as the plasma expanded and cooled. By the time the wave reached the inner steel wall, it was traveling at about 10,000 m/s, its temperature was about 2.5E4 K, and it had an average ionization of 1.9. The cool steel wall (300 K) quickly cooled the adjacent argon plasma. Nevertheless, the heat transfer caused the two innermost mesh elements of the steel wall to reach peak temperature of nearly 1,900 K. Therefore, about 0.00006 m of the steel wall melted, while the majority of the wall (0.03994 m) remained near room temperature.

Note that the excessive heat-up of the innermost part of the steel wall can be minimized relatively easily by placing a liquid wall so that it convects away the heat from the steel wall, or alternatively, the chamber diameter can be increased.

4.1.3 Single and Two- Phase Shock Mitigation (liquid Curtains)

The thick liquid blanket concept was developed to mitigate the x-rays and neutrons from the fusion reaction. Gas and aerosol mitigation only stop the x-rays while allowing the neutrons through to interact with the wall. Since thick liquid curtains have the potential to mitigate both neutrons and x-rays, they have been researched extensively in past Z-IFE work [32, 48].

Two curtain designs have been proposed. The first being separated liquid curtains that are strategically placed around the fusion source to prevent line-of-sight to the chamber wall and mitigate the shock caused by the x-rays. This curtain orientation has shown to be effective in mitigating the neutrons and x-rays very well. The only drawback is that when absorbing the x-rays an ablation shock wave is generated on the inner surface of the liquid curtains. The ablation causes the curtains to accelerate and impact the chamber wall creating a dynamic stress. Depending on the chamber radius, curtain geometry, and target yield, substantial stresses are induced in the wall due to the momentum of the liquid curtains. Figure 4.12 shows an example of a possible liquid curtain design created by LLNL [50]. The University of California at Berkeley (UCB) conducted several shock mitigation experiments involving thick liquid curtains arranged in two different geometries.

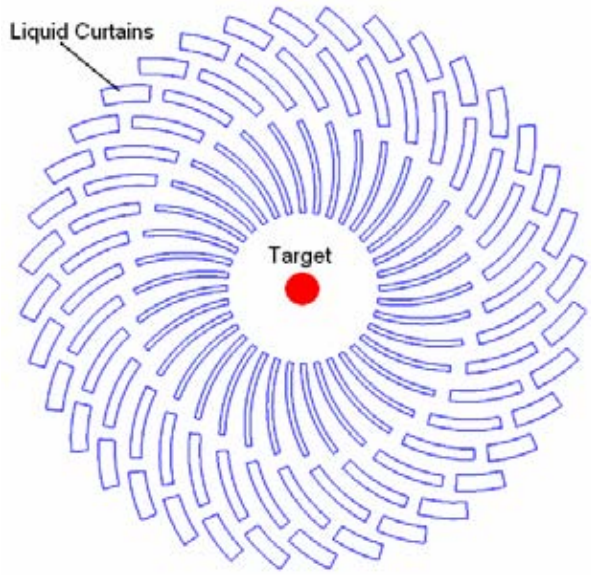

Figure 4.12: Top view of a liquid curtain design for the Z-IFE Vessel.

An alternative to this design is using a two-phase liquid curtain. The void fraction of a two-phase liquid is defined as the ratio between volume occupied by the a gas and the total volume occupied by both the liquid and gas. This can range from aerosols with a void fraction of 99% to bubbly flow with a void fraction as low as 1%. Georgia Institute of Technology (GT) and the University of Wisconsin (UW) have conducted experiments studying two-phase flow curtains. The UW experiments involved sending shock waves through oil and water with void fractions ranging from 5% to 15%. GT looked at characterizing two-phase flow jets with various void fractions and jet velocities.

4.1.4 Experimental Investigation of Chamber Liquid Structure Response [51]

The use of free jets to create a porous blanket allows for venting paths to be formed to control the transient pressure following the fusion reaction. The transient pressure contributes, along with x-rays ablations of target facing jets, to the impulse loading delivered to the liquid jets. The resulting velocity imparted to the liquid must be maintained at reasonable values to prevent erosion of solid structures resulting from impingement of high velocity sprays, jets and slugs. Porous liquid structures delay shock propagation through the liquid blanket and thus can allow for the jets to clear the chamber center before being fully accelerated outward.

Previous studies [51,53] have shown that the fluid mechanics of liquid-salt porous blanket disruptions by a fusion explosion could be reproduced with little distortion in reduced scaled facilities using room temperature water and high explosives, such as composition C4.

To study those phenomena in a Z-Pinch-chamber configuration, two annular porous liquid blankets, with different venting path and void fractions, have been tested in a sealed vacuum chamber at UCB's Vacuum Hydraulics Experiment (VHEX) under various impulse loads. A high frame rate camera and fast pressure sensors were used to record the liquid response to the impulse loading and detailed pressure history inside the pocket.

4.1.4.1 Annular Nozzles Description

In the VHEX facility, water is driven by both gravity and a vacuum induced pressure difference. The jets are created with a modular nozzle assembly. The assembly has a 30.5 cm (12") inner diameter and is 43.2cm (17") long. VHEX was fitted with an annular flow diffuser, to provide a transition between the VHEX inlet pipe and the outlet annular flows that would surround an actual recyclable transmission line in a Z-Pinch fusion power plant. The annular, modular bay used for these experiments can house a variety of nozzles (Figure 4.13).

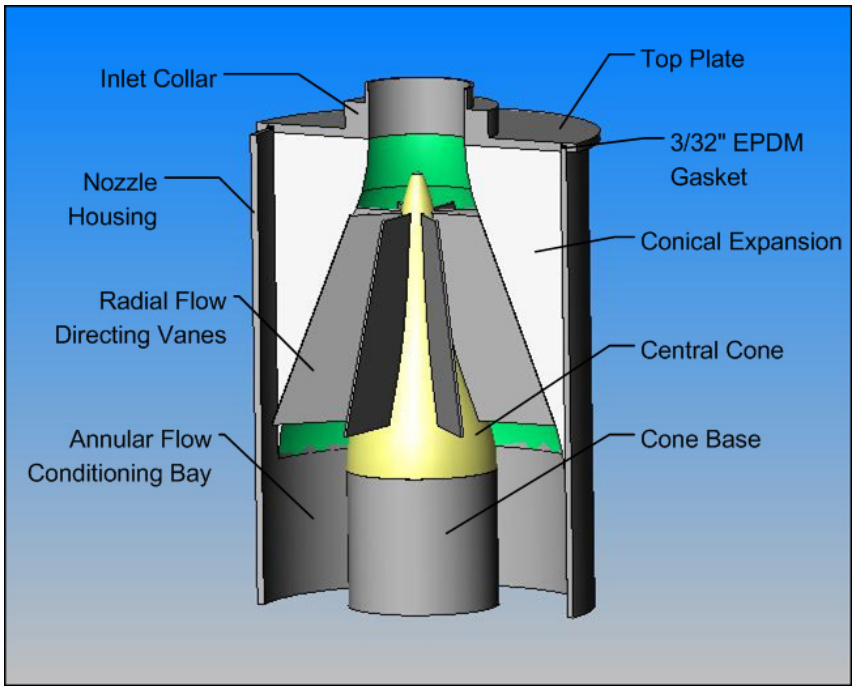

Figure 4.13: Nozzle assembly housing. Various nozzles can be inserted in the modular bay.

4.1.4.2 Diffuser Geometry

Expansion of the 10.2 cm (4 in) diameter inflow to the 30.5 cm (12 in) diameter outflow is achieved by the employment of an axisymmetric annular diffuser (Figure 4.13). The diffuser is comprised of two components, a conical expansion and a central cone with radial flow directing vanes. The conical expansion is fabricated from foam and polished fiberglass, has a length of 30.2 cm (12 in), and a total angle (2θ), wall to wall, of 44.3º. The central cone is 27.9 cm (11 in) in length with a base diameter of 14.0 cm (5.5in) and is fitted with 8, 0.16 cm (0.0625 in) thick, 25.4 cm (10 in) long, aluminum flow directing vanes, which originate 2.5 cm from the apex of the central cone [54]. The leading edge of each vane is filed to a round elliptical shape and the trailing edge sharpened off. Mounting the vanes on a slotted base and fitting 45º slices of the central cone between them ensure symmetry. The central cone with radial vanes is set upon a 14.0 cm (5.5 in) diameter, 12.7cm (5 in) tall, cylindrical base and fit into the conical expansion yielding an annular diffuser with an area ratio of 7.7.

4.1.4.3 Nozzle Geometries

Two nozzles are tested in the nozzle assembly. They are referred as phase 1 and 2 in the subsequent sections (Figure 4.14).

The phase 1 nozzle reuses a system previously developed at UCB [55]. In this configuration, the fluid is allowed to flow freely for 3.8 cm after exiting the diffuser. It then passes through a fine copper wire cloth, 15 mesh per centimeter, which is directly followed by a 10.16 centimeters (4 in) long aluminum honeycomb with hexagonal cell of size 0.318cm (1/8”). Finally, 342 cylindrical free jets are formed by passing through a 0.95 cm thick aluminum plate. The jets are arranged in 3 sets of 3 concentric rings, each consisting of 38 bores, with jets diameter increasing

radially in each set as 0.8 cm, 1.0 cm, and 1.2 cm. The total exit area of the annular curtain is 0.049 m^2. The void fraction, based on the exit jets diameters, is 49%. A picture of the complete phase 1 nozzle is depicted on Figure 4.15.a).

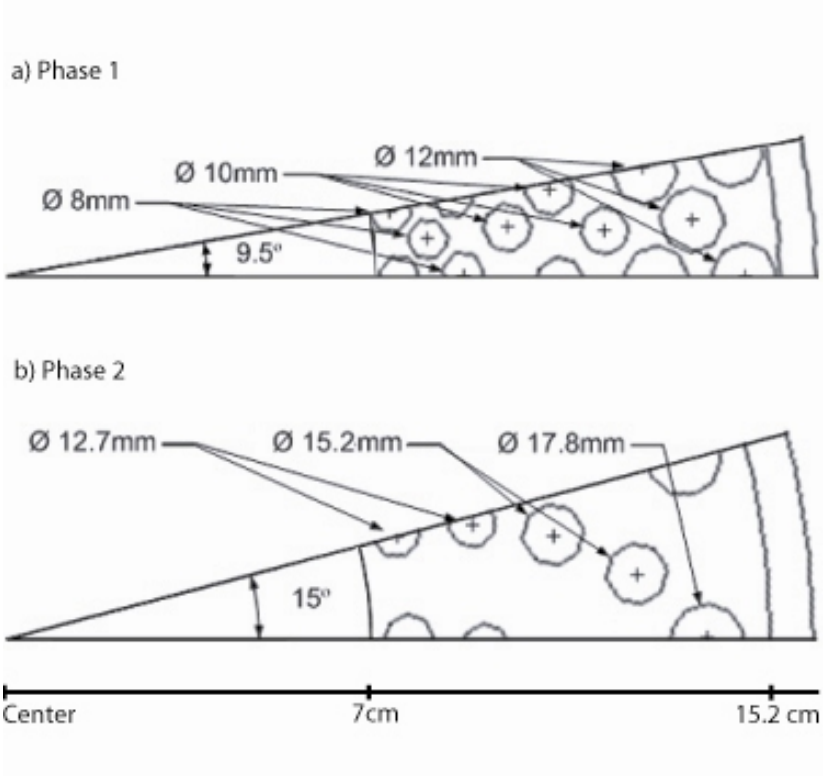

Figure 4.14: Nozzle geometries. Phase 1 nozzle is made of 38 sections similar to the section depicted here; and phase 2 is made of 24 sections. The void fraction is 49% for phase 1 and 74% for phase 2.

The phase 2 nozzle was developed and constructed for this study. In this configuration, the fluid is allowed to flow freely for 3.8 cm after exiting the diffuser. The liquid then passes through a series of three 2.2 cm thick aluminum conditioning plates and then through 5 cm long nozzle contraction plate. Each conditioning plate contains 5 concentric rings, each consisting of 24 bores, with the jet diameter increasing radially as 12.7 mm (.5 in), 15.2 mm (.6 in), and 17.8 mm (.7 in). The nozzle plate has the same geometric layout with each bore contracting inward by 0.3 cm over a distance of 3.8 cm.

The liquid conditioning sequence consists of passing the liquid through a fine stainless steel mesh, 30 mesh per inch .0065in diameter wire, and into the first plate which houses 1/16" hexagonal aluminum honeycomb, then through a larger stainless steel mesh, 18 mesh per inch 0.009in diameter wire, and into the second plate which contains only the bores. The liquid is then passed through a fine mesh again and allowed to homogenize as it passes through the third plate and into the nozzle plate. The liquid exits the nozzle plate and enters the VHEX chamber with reduced lateral turbulence. The void fraction is 74% and the exit area is 0.027m^2. Figure 4.15 b) depicts a picture of this nozzle, and Figure 4.16 shows the nozzle in operation inside the VHEX chamber.

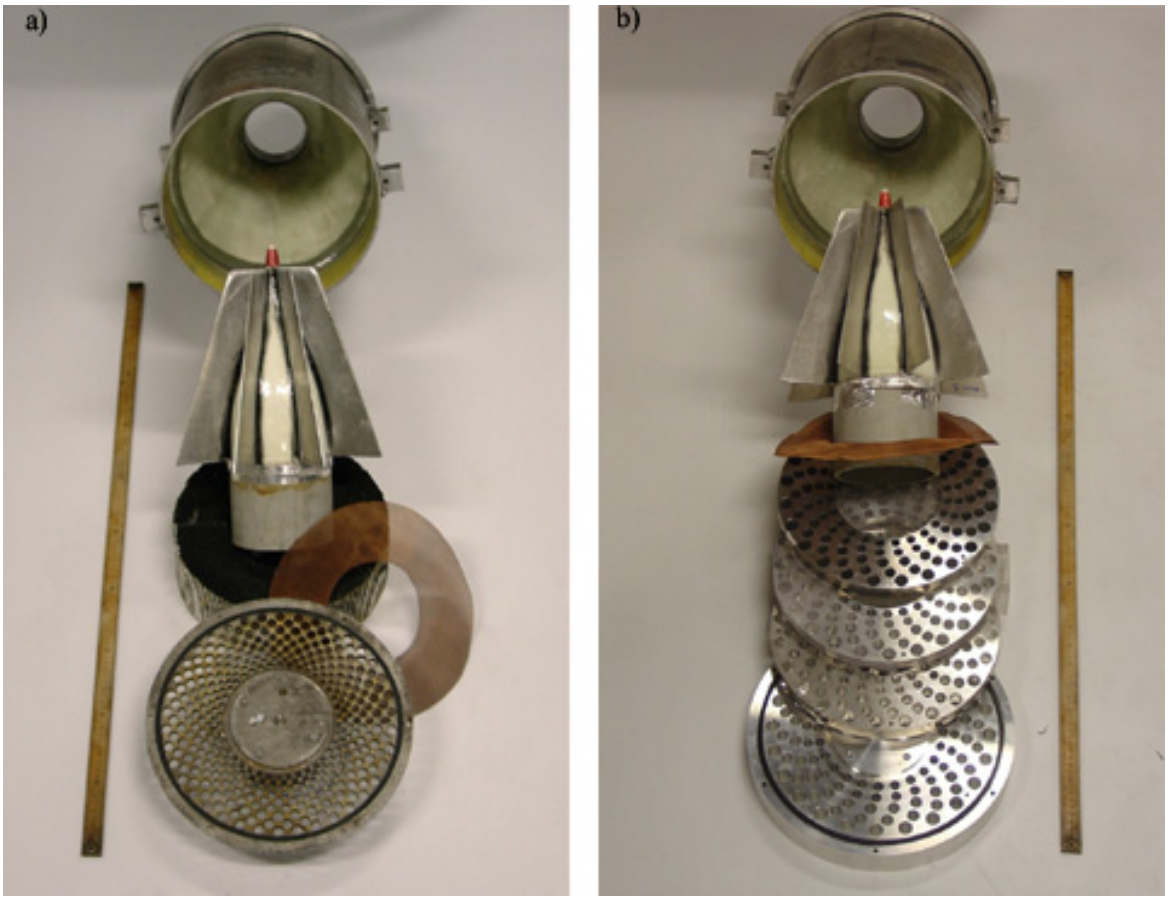

Figure 4.15: Pictures of the full nozzle assemblies, with a yard stick for reference. a) is phase 1, and b) is phase 2.

4.1.4.4 Experiment Description

In VHEX, high-explosives (composition C4) are used to simulate the scaled impulse load delivered by the fusion reaction. The C4 was detonated using exploding bridge wires (EBW) because they require a brief electrical pulse of several thousand volts and hundreds of amps to be triggered which makes them safe to work with. The quantity of high-explosives used is varied to simulate various impulse loads. An optimum impulse of 100 Pa-s is desired. The explosives are positioned at the center of the annular liquid blanket and about 12.5 cm below a mounting block that houses two pressure transducers used to record the pressure history. The mounting block is fixed under the nozzles endplate and inside the inner cavity of the jets curtain. The mounting block can be seen through the liquid curtain in Figure 4.16. Pressure measurements and videos are acquired simultaneously.

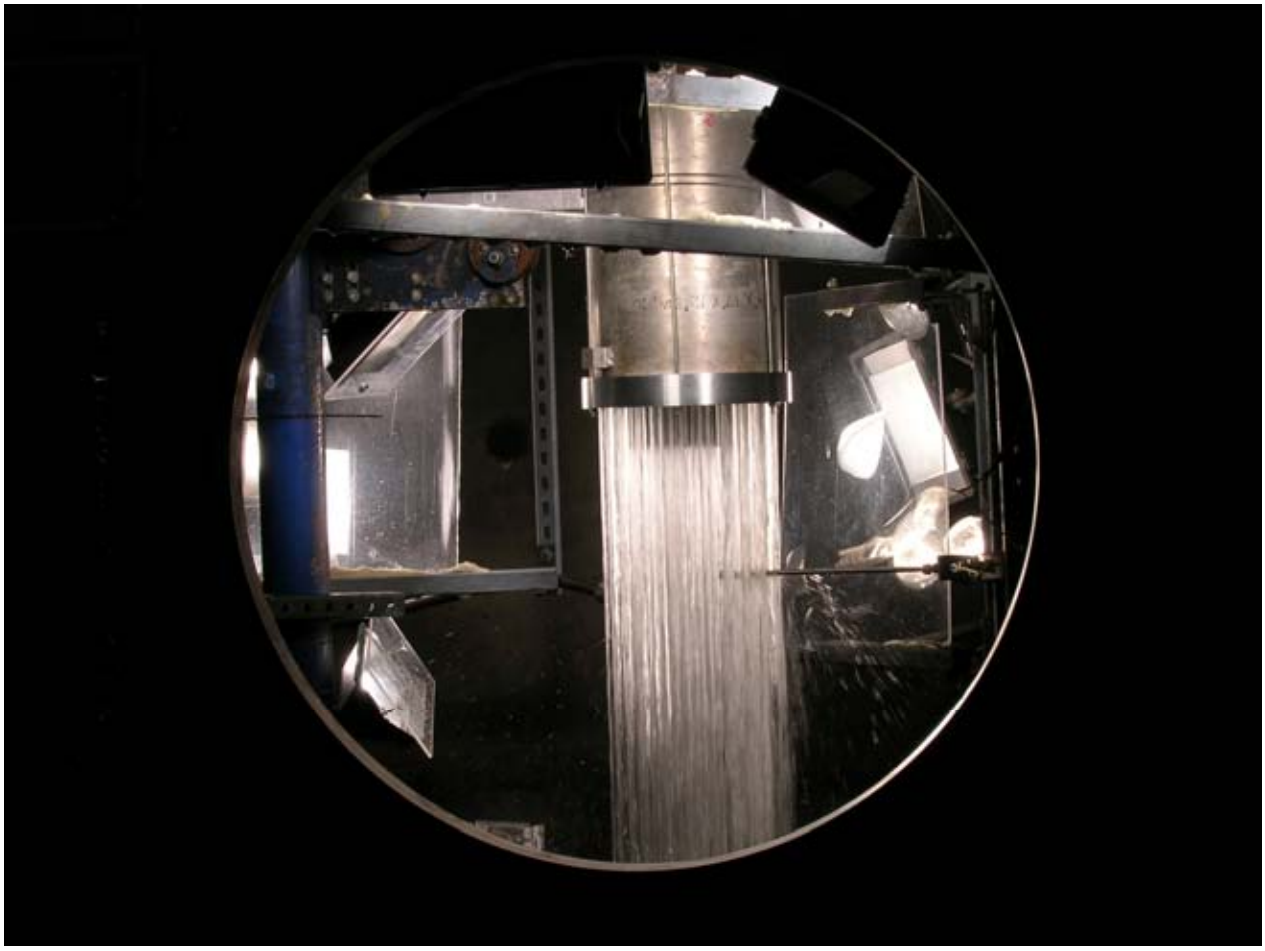

Figure 4.16: Phase 2 nozzle in operation inside the VHEX chamber. Horizontal rod entering from left supports the explosive charge located on a stalk centered in the array 10 cm above the rod.

4.1.4.5 Phase 1 Results

In phase 1, 4 sets of data were taken with respectively 0, 2.5, 5 and 23 g of high explosives. Pressure history (Figure 4.17) and high speed video (Figure 4.18) were recorded for all cases but the last where only video is available, because it was feared that the detonation might damage the pressure transducers.

Pressure History Measurements

It should be noted that at the time of completion of the report, no post processing had been performed on the pressure data yet. Hence the system vibrations have not been filtered out of the pressure data. That can result in an underestimation of the impulse, by integration of the pressure history, in the order of 50% for certain cases.

Further, due to the cylindrical geometry of the jets curtain, the shock waves are more effectively contained radially than longitudinally. The radial characteristic length is on the order of the curtain inner diameter or 16.75 cm, while the longitudinal characteristic length is about 1m. The

impulse imparted to the jets directly facing the charge is thus likely to be more important than measured. That can be confirmed from the videos by estimating the momentum of the moving jets after the explosion.

The measured raw impulses (Figure 4.17) range from 22Pa.s for a single detonator to 100Pa.s for 5g of HE; however, the actual impulses should be greater based on the above arguments. On all experiments, but with the EBW alone, the charge was held from below. This is probably the source of the dual peak observed on the pressure history of the EBW alone (Figure 4.17 a)). For that experiment, the bulky and heavy wire feedthrough of the housing was directly between the explosives and the pressure transducer. The feedthrough, which survived that particular explosion, probably created a stagnation point on the front of the shock wave. The peaks observed are then reflections of the shock wave arriving at the sensor location slightly out of phase.

Further when 5g of HE was employed, vibrations strongly affected the pressure measurements (Figure 4.17 c)). Those vibrations could be due to shrapnel hitting the pressure sensor mount. As a consequence, the impulse load is significantly misestimated.

It is very interesting to compare these impulse values, where the explosion is contained, with previous measurements in an open geometry [55]. For the latter, between 20 and 30g of HE (depending on the packing density) was required to reach an impulse of 100Pa.s, compared with a mere 5g in this study.

Visualization Results

For small impulses, the porous blanket effectively delays the liquid outwards acceleration (Figure 4.17.a) and b)) as anticipated by the snow plow model [56]. However, for larger impulses (Figure 4.17 a) and b)), the liquid is accelerated outwardly very quickly. For the case where 23g was used, it took less than 30ms for the viewing window of VHEX (a good 1.5m away from the edge of the jets) to be drenched!

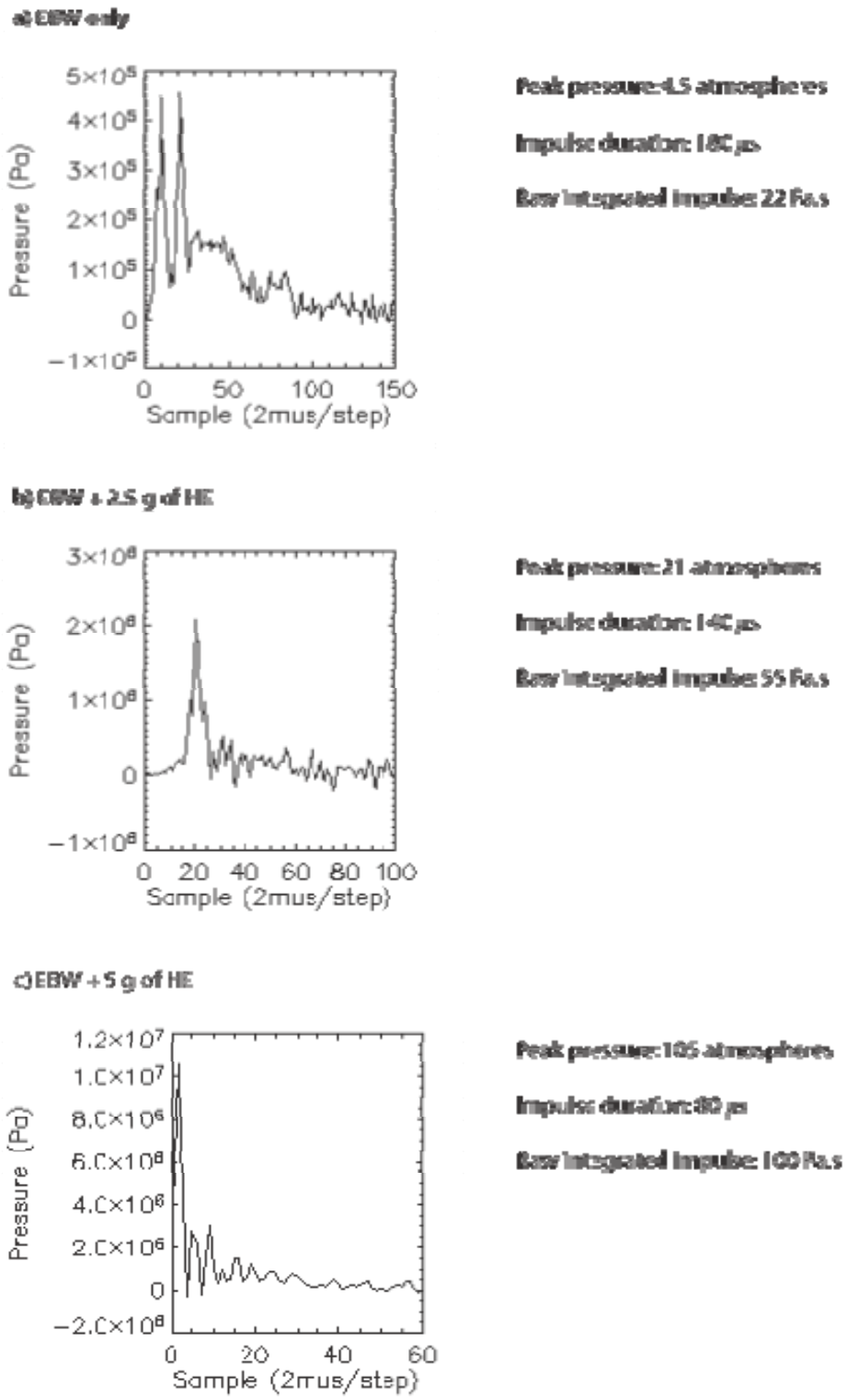

Figure 4.17: Raw pressure measurements for Phase 1 nozzle for various HE masses. Those measurements have not been corrected for vibrations which are, in certain cases, quite significant. a) corresponds to detonator alone, b) to an EBW with 2.5g of HE and c) to 5g of HE.

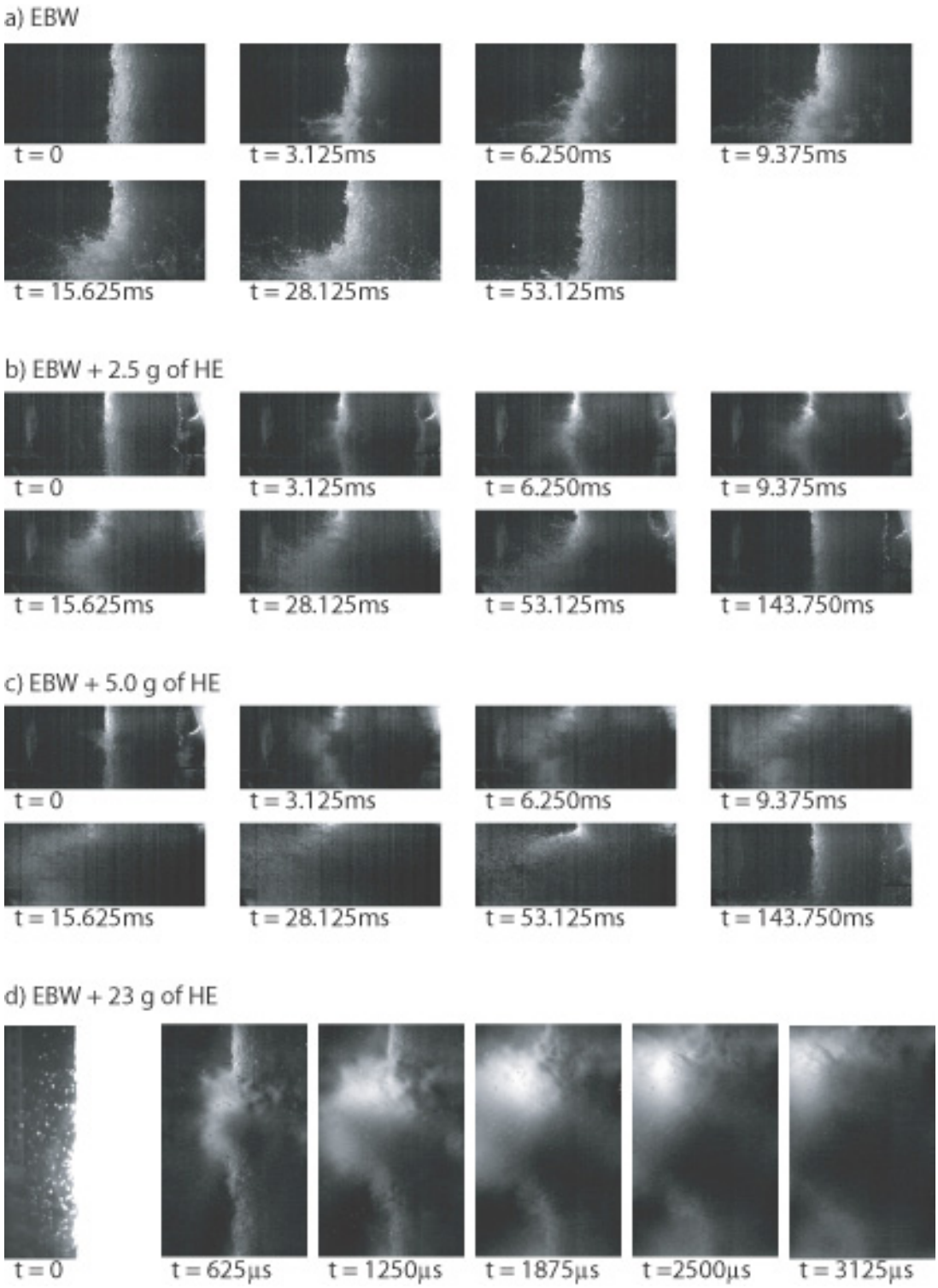

Figure 4.18: Sequences of pictures from Phase 1 jets with an increasing mass of explosives. a) is a single detonator, b) a detonator with 2.5g of HE, c) an EBW with 5g of HE and d) an EBW with 23 g of HE. At the exception of d), the sequences are started with the apparition of gas venting through the jets and ended when the chamber has been cleared. The time intervals are also identical (except for d)).

For all impulses it took nearly 144ms to clear the center of the chamber from any residual drops and sprays and have a new liquid curtain.

4.1.4.6 Phase 2 Results

In phase 2, 3 sets of data were taken with respectively 0, 2.70 and 5.25 g of high explosives. Pressure history (Figure 4.19) and high speed video (Figure 4.20) were recorded for all cases.

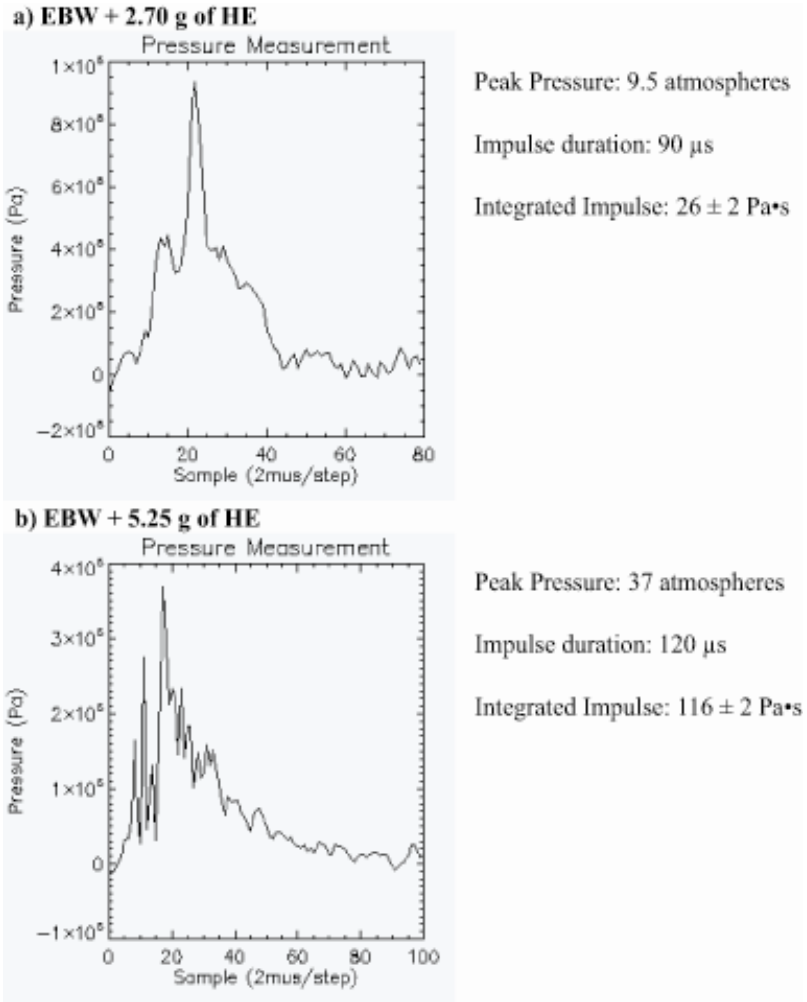

Figure 4.19: Pressure measurements for Phase 2 nozzle for various HE masses. Pressure measurement with a single EBW and no HE is not displayed because strong vibrations in the pressure sensor mount rendered data unusable.

The impulses measured with the phase 2 nozzle are smaller than in phase 1 (Figure 4.19). This demonstrates the importance of venting to reduce the impulse load delivered to the jets. It should be noted that the measurement of impulse in phase 1 for 5 g of HE (Figure 4.17 c)) are contaminated with strong vibrations, which explains why the measured impulses are similar in phase 1 and 2.

When a single EBW was used, strong vibrations were recorded by the pressure transducers. Consequently no accurate pressure history could be measured. The vibrations were probably due to shrapnel from the detonator that hit the pressure sensors mount.

In Phase 2, the camera is used at 1000 fps with a resolution of 512×768 pixels. A fast (f 1.8) 20 mm lens is used, which allows the exposure time to be reduced to 50 µs. The jet quality of the phase 2 nozzle is significantly better than in phase 1, as no drops are observed breaking off the jets.

High speed video images confirm the presence of significant venting in phase 2 experiments. For example, on the first picture of Figure 4.20 b), hot gases are present outside the jets curtain while the shadow of undisturbed jets can be discerned. The jets start moving a few milliseconds after the venting.

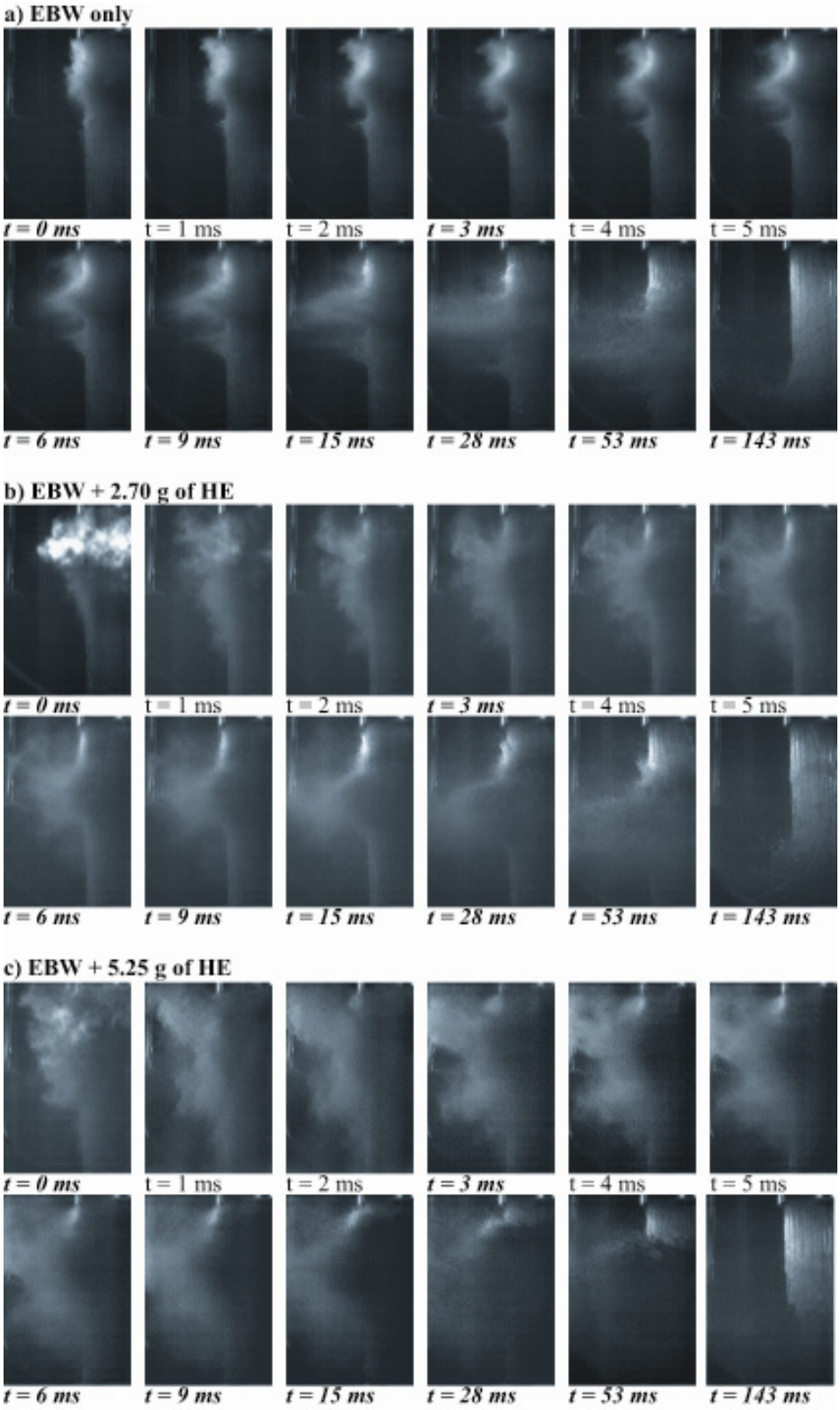

Figure 4.20: Sequence of pictures from Phase 2 with increasing amount of HE. The first frames correspond to the first picture where venting is observed, about 1 ms following the detonation. Time intervals are identical and times noted in bold italic are similar to those of Figure 4.18.

4.1.4.7 Conclusions

Two nozzles, phase 1 and phase 2, were used to study the response of porous blanket for thick liquid protection of Z-Pinch chambers. The simultaneous use of high speed camera and pressure transducers allowed the jets response to various impulse loads to be studied. In particular the importance of venting with the phase 2 nozzle to reduce the pressure build-up in the jets curtain inner cavity is illustrated. Further, for small enough impulses, the snow plow effect effectively delays the emergence of shocked liquid outside of the layer. These initial experiments provide the necessary background to develop a more effective single-phase thick liquid curtain design for Z-IFE conditions.

In the future, it could be possible to block out a small section of jets and in place insert a plate with pressure transducers mounted on it to record the impulse directly felt by the jets facing the high explosives charge.

4.1.5 Void Fraction Distribution in a Two-Phase (Gas-Liquid) Jet [57]

The hydrodynamics of falling two-phase (gas-liquid) jets were investigated. Experiments were performed using air and water. The jets were produced by injecting well mixed air-water mixtures through a 10 cm x 1 cm rectangular nozzle. The jet thickness and thickness-average void fractions were measured at nine different locations at three distances from the nozzle exit, and at three lateral locations for each specific distance from the nozzle for a total of 20 flow conditions. High speed photography and a needle tester were used for the measurements of the jet width and thickness respectively, and gamma-ray densitometry was applied for the void fraction measurement. Based on the experimental results, the two-phase jet stability was studied, and the void fractions were empirically correlated. Three different correlations were developed in order to provide flexibility with respect to their application. The correlations are of the generic form:

$$\frac{\varepsilon_g}{\varepsilon_{go}} = C_o \,\mathrm{Re}_l^a \, Fr_i^b We_l^c D^{*d} \qquad 4.1$$

where ε_g is the local void fraction, ε_{go} is the homogeneous void fraction at the nozzle exit; Re_l, We_l and Fr_l are appropriately defined Reynolds, Weber and Froude numbers, and D^* is a ratio of lengths.

4.1.5.1 Experimental Results and Discussion

Table 4.3: Experiments Conducted

Experiment	Water Flow (Q_l) in L/min and (gpm) and Inlet Liquid Velocity (U_l) in m/s	Gas Flow (Q_g) in L/min	Q_g / Q_l (%)
1	60; (15.9); 1	0	0
2	120; (31.7); 2	0	0
3	180; (47.6); 3	0	0
4	240; (63.5); 4	0	0
5	288; (76); 4.79	0	0
6	120; (31.7); 2	1.5	1.25
7	180; (47.6); 3	4.5	2.5
8	240; (63.5); 4	6	2.5
9	288; (76); 4.79	7.2	2.5
10	180; (47.6); 3	9	5
11	240; (63.5); 4	12	5
12	288; (76); 4.79	14.4	5
13	180; (47.6); 3	18	10
14	240; (63.5); 4	24	10
15	288; (76); 4.79	28.8	10
16	180; (47.6); 3	27	15
17	240; (63.5); 4	36	15
18	288; (76); 4.79	43.2	15
19	240; (63.5); 4	48	20
20	288; (76); 4.79	57.5	20

Table 4.3 is a summary of the experimental runs. Note that in each experiment the jet void fraction and thickness were measured at nine points, namely three z values (5.4 cm, 13.7 cm and 21.9 cm) from the nozzle exit, and for each z, three x locations (0 cm, -1.43 cm and 1.43 cm) from the jet centerline shown in Figure 4.21.

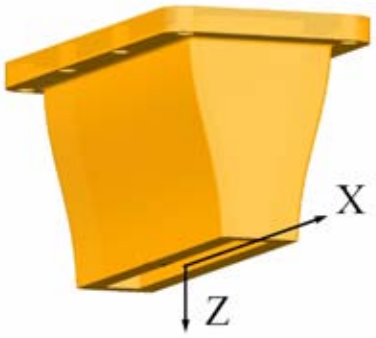

Figure 4.21: Coordinate system at nozzle exit

The gamma-ray densitometer and radiation detection station were used in order to measure the number of radiation counts for a total of 20 experiments. Five of the experiments were single phase water with initial velocities ranging from 1 m/s to the maximum value of the system of 4.79 m/s. The 15 two-phase experiments were done with initial gas fractions ranging from 1.25% to 20%. Thus, a total of 180 data points were recorded. Figure 4.22 shows the experimental setup.

Figure 4.22: Experimental setup highlighting the flow conditioner and nozzle.

4.1.5.2 Void Fraction

Using the calibration values of I_l and I_g the average void fraction across the container was calculated as

$$\overline{\varepsilon}_{g_c} = \frac{\ln\left(I_{2\phi} / I_l\right)}{\ln\left(I_g / I_l\right)}. \qquad 4.2$$

If the void fraction of the jet is assumed to be zero (in the case of single phase flow), the thickness of the jet can be determined from this technique. Moreover, regardless of the initial gas flow, the collapsed liquid thickness (denoted with subscript CLT) of the jet is determined using the following equation

$$\delta_{CLT} = L\left(1-\overline{\varepsilon}_{g_c}\right) \qquad 4.3$$

where L is the inner distance of the container (the span across which the void fraction was determined [6.35 cm]). The δ_{CLT} is plotted as a function of x position for a fixed z position for given water and air flow rates. When δ_{CLT} is plotted against x position, the plot is asymmetric about the centerline. It is proposed that the asymmetry of the δ_{CLT} is due to asymmetry within the nozzle and flow straightener as opposed to the jet hydrodynamic phenomena.

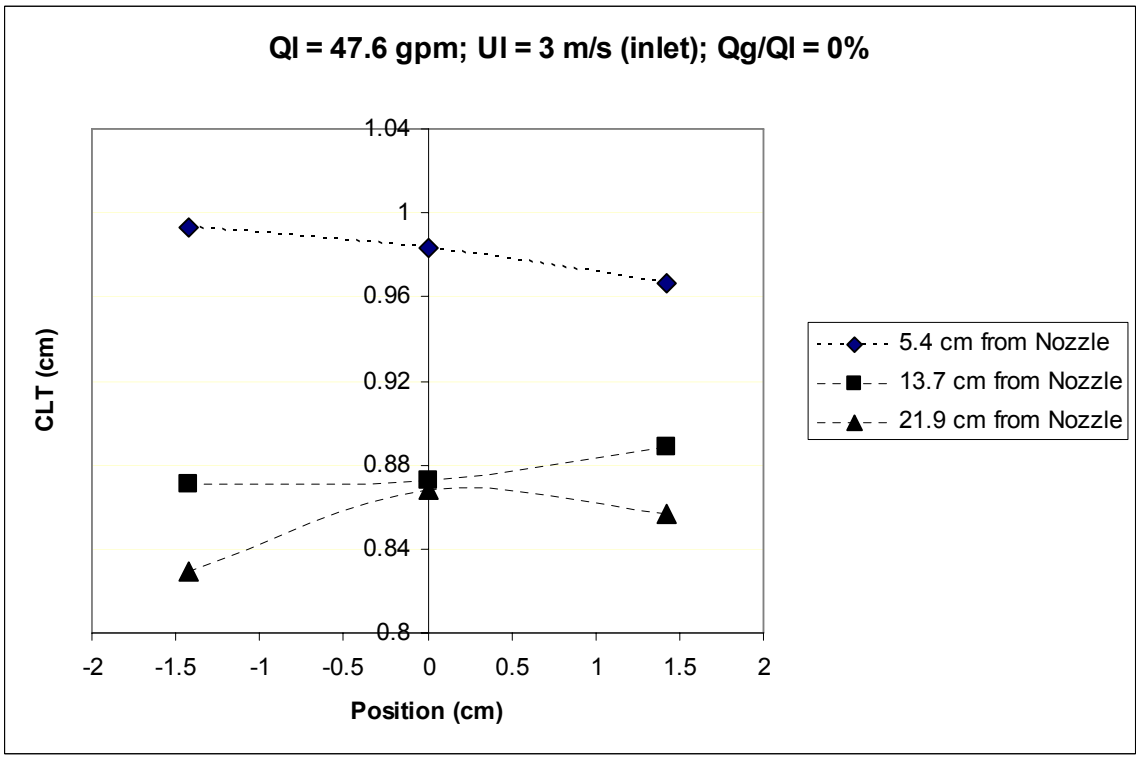

Figure 4.23: Collapsed liquid thickness versus x-position.

Figure 4.23 shows a typical asymmetric profile. Asymmetry was observed independent of gas and liquid initial flow rates. The analysis of the void fraction and other such related parameters will be one-dimensional (z-direction [distance from nozzle]) and x-averaged values will be used at each fixed z distance. Nevertheless, the occurrence of this asymmetry should be noted.

The experiments noted in Table 4.3 were repeated and the jet thickness was measured; and again the experiments were repeated and the photos needed for the jet width measurements were taken. The void fraction of the jet is then simply

$$\varepsilon_{g_j} = 1 - \left(\delta_{CLT} / \delta_{MT} \right) \qquad 4.4$$

where δ_{MT} is the measured thickness of the jet.

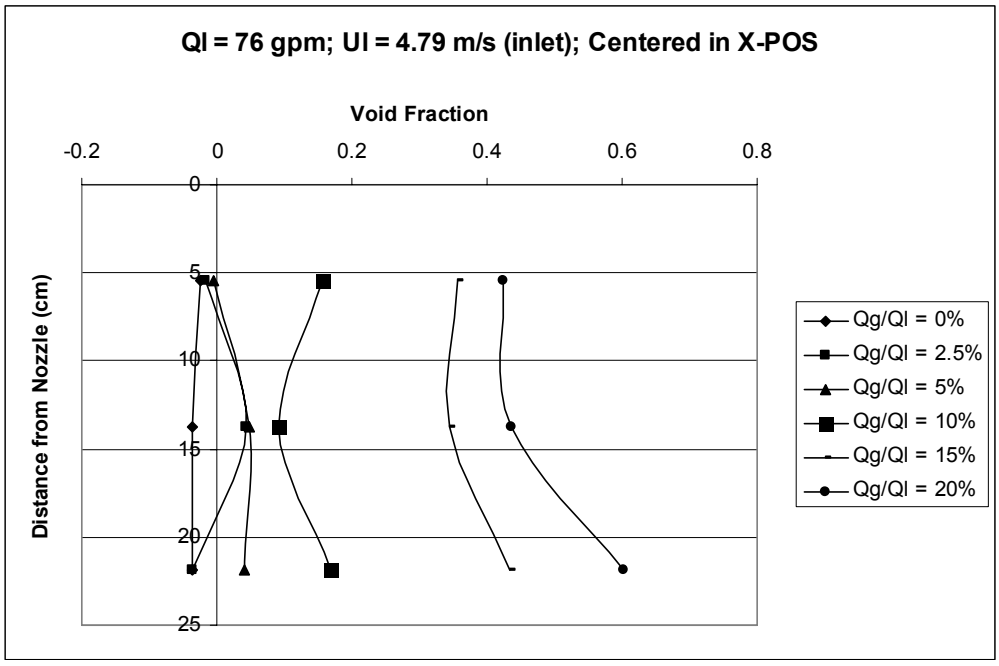

Figure 4.24: Void Fraction versus distance from nozzle.

In Figure 4.24, the void fraction of the jet is plotted against the distance from the nozzle for a fixed water flow rate. Each line corresponds to a specific gas flow rate. An atypical result of the void fraction calculations was that the void fraction was negative for low gas flow rates. The negative void fraction physically means that the collapsed liquid thickness is greater than the measured jet thickness; therefore the collapsed liquid thickness has been over predicted and or the measured thickness has been under predicted. This suggests that the error associated with one or more facets of the measurements needed in the computation of the void is on the order of the void fraction or greater. The error associated with the measurement of the thickness of the jet, while small, is likely on the order of the void fraction measurements for the range of Q_g / Q_l = 0-5%. The other potential source of error is from liquid droplet deposition onto the walls on the container while the densitometer is in use. It is difficult to predict the amount of the droplet deposition, but it would lead to a slight over prediction of the collapsed liquid thickness.

Only the high gas flow rate experiments (resulting in void fractions of 10% and greater) are shown below.

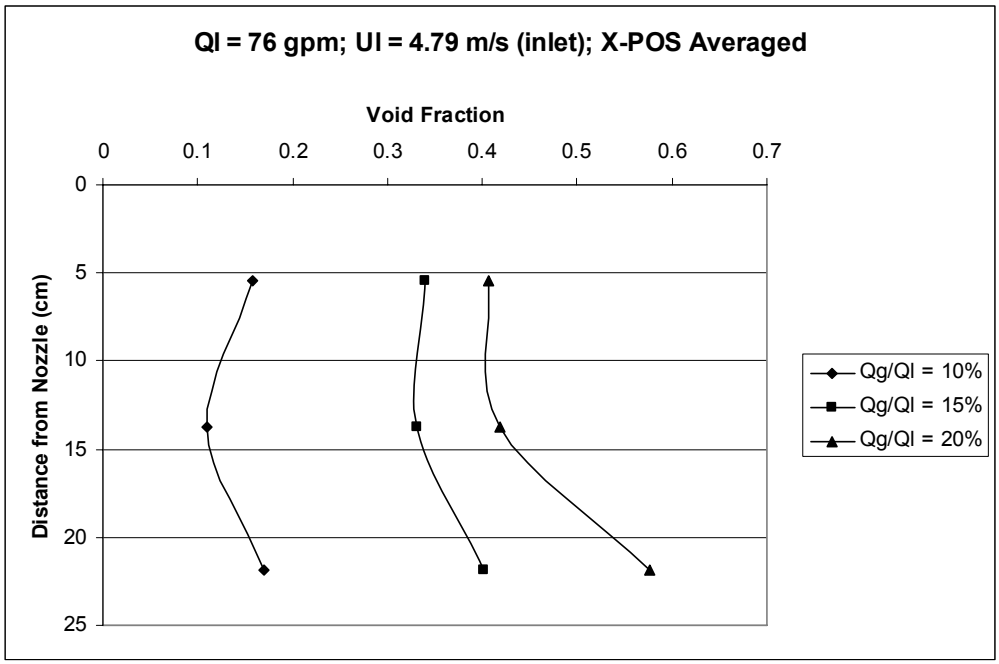

Figure 4.25: Void fraction versus distance from nozzle.

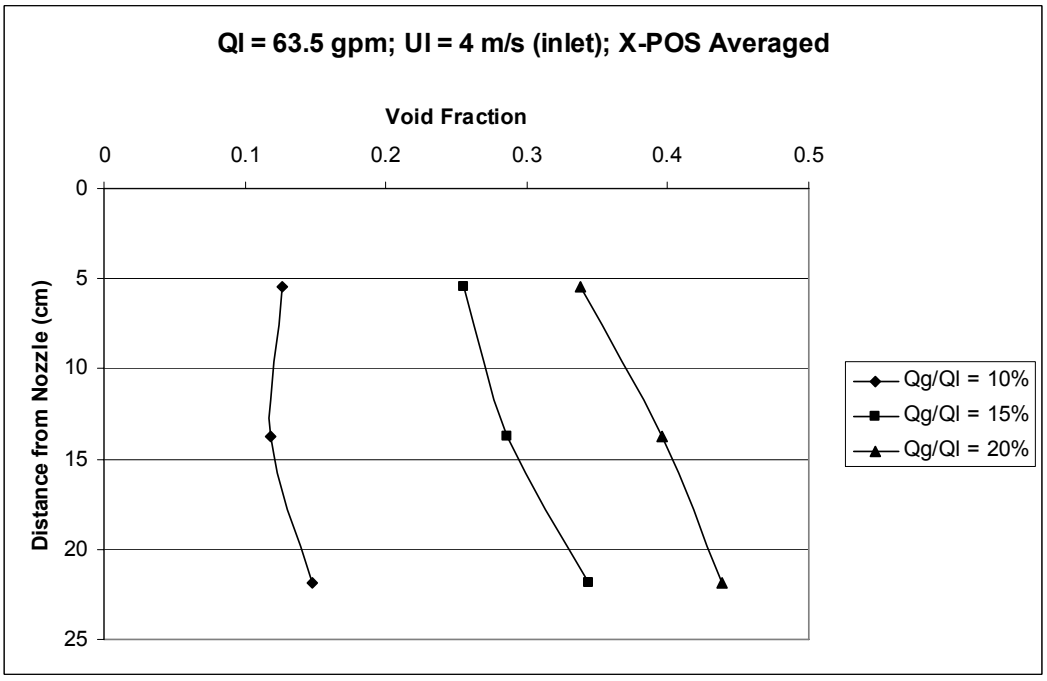

Figure 4.26: Void fraction versus distance from nozzle.

Figure 4.25 and Figure 4.26 display the six high gas flow rate experiments studied. The void fractions ranged from below 10% to almost 60%. The void fraction increases with increasing the initial gas flow rate – an expected trend. An additional trend is that the void fraction increases

with increasing distance from the nozzle. Therefore the slip ratio is decreasing since the liquid is accelerating downward, while the gas resists downward flow due to the buoyancy effect – this trend was also expected.

4.1.5.3 Velocity Slip

Once the collapsed liquid thickness, jet thickness and jet width are known, many hydrodynamic properties can be studied. The gas and liquid velocities are of interest for the slip ratio calculations, where

$$S = \frac{U_g}{U_l}, \tag{4.5}$$

$$U_g(z) = \frac{\delta_{in} w_{in} j_{g,in}}{\delta_{MT} w_{MT} \varepsilon_{g_j}}, \tag{4.6}$$

$$U_l(z) = \frac{\delta_{in} w_{in} j_{l,in}}{\delta_{MT} w_{MT} \left(1 - \varepsilon_{g_j}\right)} \tag{4.7}$$

where the "MT" subscript denotes measured values and the "in" subscript denotes nozzle dimensions. As previously discussed,

$$j_{g,in} = \frac{Q_g}{A_{in}}, \tag{4.8}$$

$$j_{l,in} = \frac{Q_l}{A_{in}} \tag{4.9}$$

where the area is simply

$$A_{in} = \delta_{in} w_{in} \tag{4.10}$$

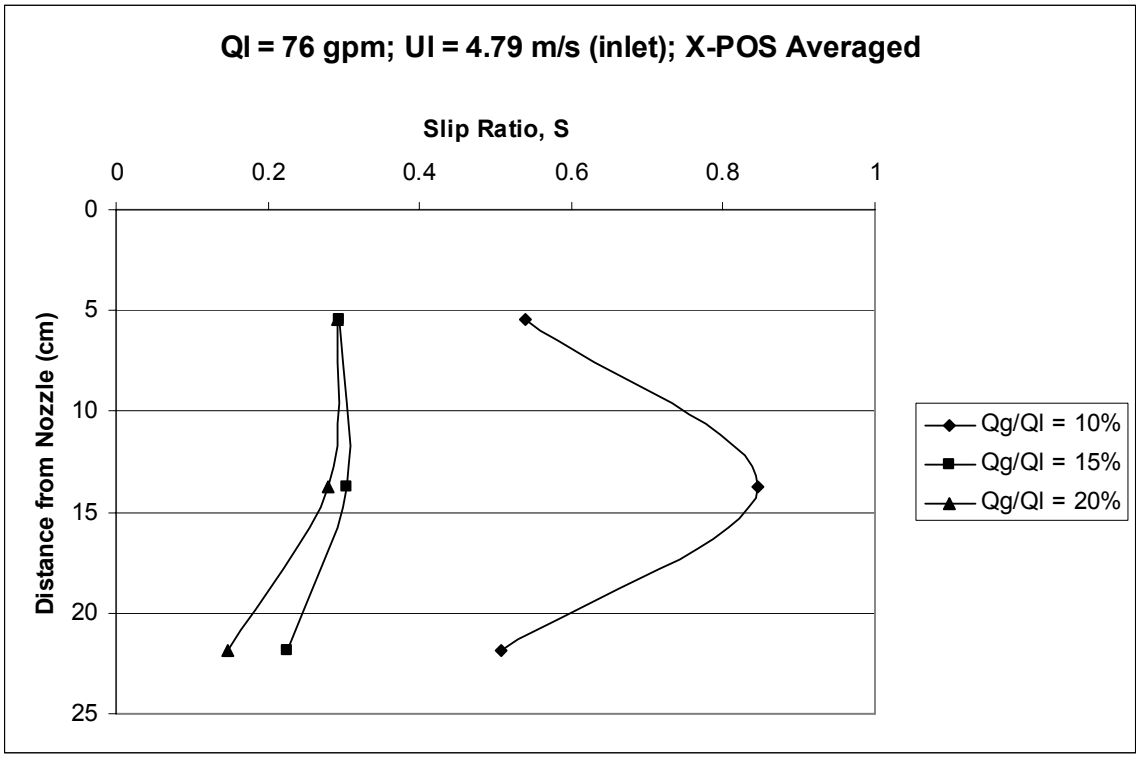

Figure 4.27: Slip ratio versus distance from nozzle.

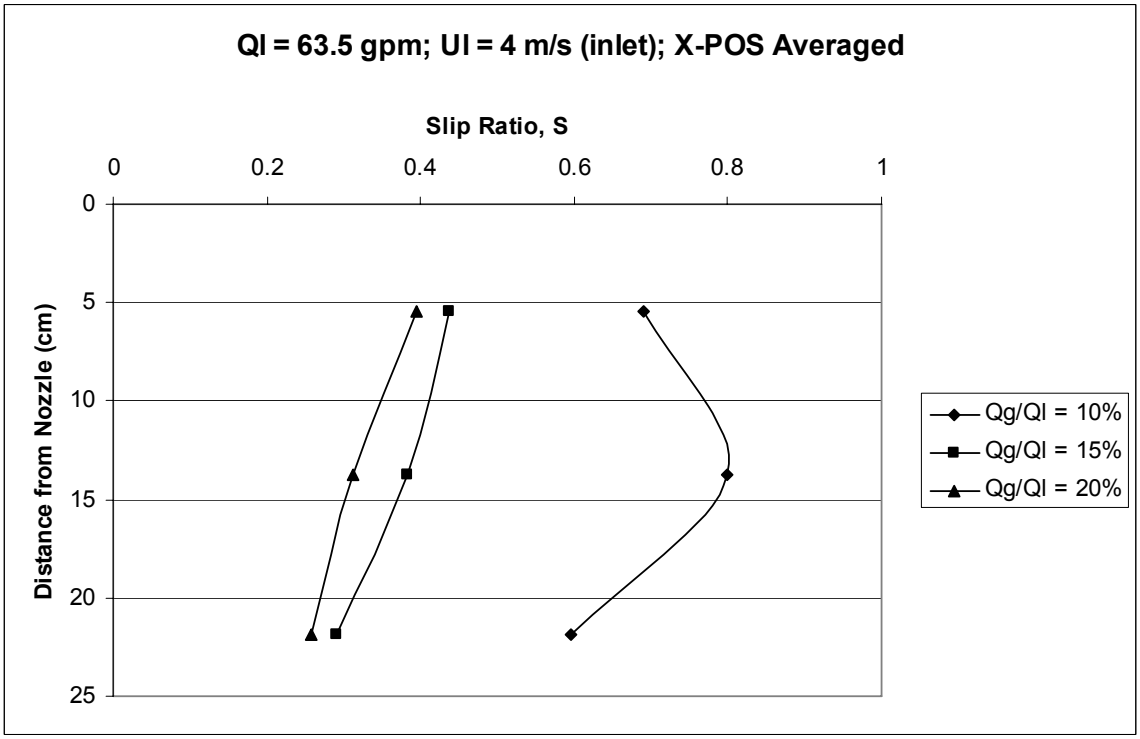

Figure 4.28: Slip ratio versus distance from nozzle

Figure 4.27 and Figure 4.28 show the relationship between the slip ratio and the distance from the nozzle. The slip ratio values ranged from less than 0.2 to greater than 0.8. Thus, at no positions studied was the gas velocity greater than the liquid velocity. Generally as the distance from the nozzle increased, the slip ratio decreased, indicting the liquid is accelerating and or the gas is decelerating.

4.1.5.4 Empirical Correlations in Plunging Jets or Nozzles

The void fraction in plunging jets or nozzles is dependent on several dimensionless parameters. These parameters are the liquid Reynolds number, the Weber number, and the Froude number, and they are defined here as:

$$Re_l(z) = \frac{U_l \delta_{MT}}{\nu_l}, \tag{4.11}$$

$$We_l(z) = \frac{U_l^{\,2} \delta_{MT} \rho_l}{g_c \sigma} \tag{4.12}$$

and

$$Fr_l(z) = \frac{U_l^{\,2}}{g \delta_{MT}}. \tag{4.13}$$

The simplest form of an empirical correlation is

$$\frac{\varepsilon_g}{\varepsilon_{go}} = C_o Re^a Fr^b We^c D^{*d} \tag{4.14}$$

where C_o, a, b, c, and d are constants. D^* is a dimensionless distance defined as

$$D^* = \left(\frac{z}{\delta_{in}} \right) \tag{4.15}$$

where z is the distance from the nozzle and δ_{in} is the nozzle thickness (1 cm). ε_{go} is the homogeneous-flow void fraction at the nozzle exit defined as:

$$\frac{Q_{g_{in}}}{Q_{l_{in}} + Q_{g_{in}}}. \tag{4.16}$$

Using the numerical software, DataFit, the constants in the above correlation were optimized, leading to the following correlation:

$$\frac{\varepsilon_g}{\varepsilon_{go}} = 2.07\times10^{-1}\left[Re_l^{-9.91\times10^{-2}} Fr_l^{-0.591} We_l^{0.772} \right]\left(\frac{z}{\delta_{in}}\right)^{0.101} . \qquad 4.17$$

The strong dependence on the Weber number is largely attributed to the two free surfaces of the jet. The above correlation is in fact a relation among ε_g, Q_l, Q_g, δ_{MT} and w_{MT}, when the nozzle geometry and fluid properties are fixed. In terms of these parameters the correlation can be recant as:

$$\frac{\varepsilon_g}{\left(\frac{Q_{g_{in}}}{Q_{l_{in}}+Q_{g_{in}}}\right)} = 2.07\times10^{-1}\left[\left(\frac{\left(\frac{\delta_{in}w_{in}\left(\frac{Q_l}{\delta_{in}w_{in}}\right)}{\delta_{MT}w_{MT}\left(1-\varepsilon_g\right)}\right)\delta_{MT}}{\nu_l}\right)^{-9.91\times10^{-2}}\left(\frac{\left(\frac{\delta_{in}w_{in}\left(\frac{Q_l}{\delta_{in}w_{in}}\right)}{\delta_{MT}w_{MT}\left(1-\varepsilon_g\right)}\right)^2}{g\delta_{MT}}\right)^{-0.591}\left(\frac{\left(\frac{\delta_{in}w_{in}\left(\frac{Q_l}{\delta_{in}w_{in}}\right)}{\delta_{MT}w_{MT}\left(1-\varepsilon_g\right)}\right)^2\delta_{MT}\rho_l}{\sigma}\right)^{0.772}\right]\left(\frac{z}{\delta_{in}}\right)^{0.101} \qquad 4.18$$

The correlation has an R^2 fit of 0.95, and the correlation values of the void fraction are compared to the measured values of the void fraction.

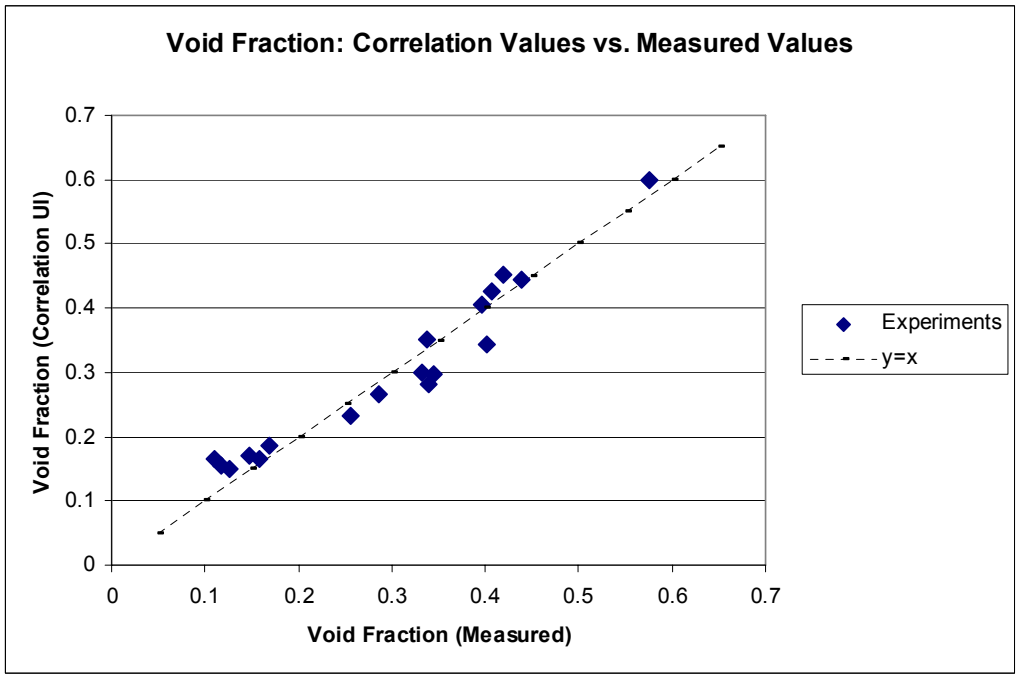

Figure 4.29: Measured void fraction versus correlation void fraction

The dashed line in Figure 4.29 represents an exact agreement between the correlation and the measured values. It is of interest to identify which experiments were outliers.

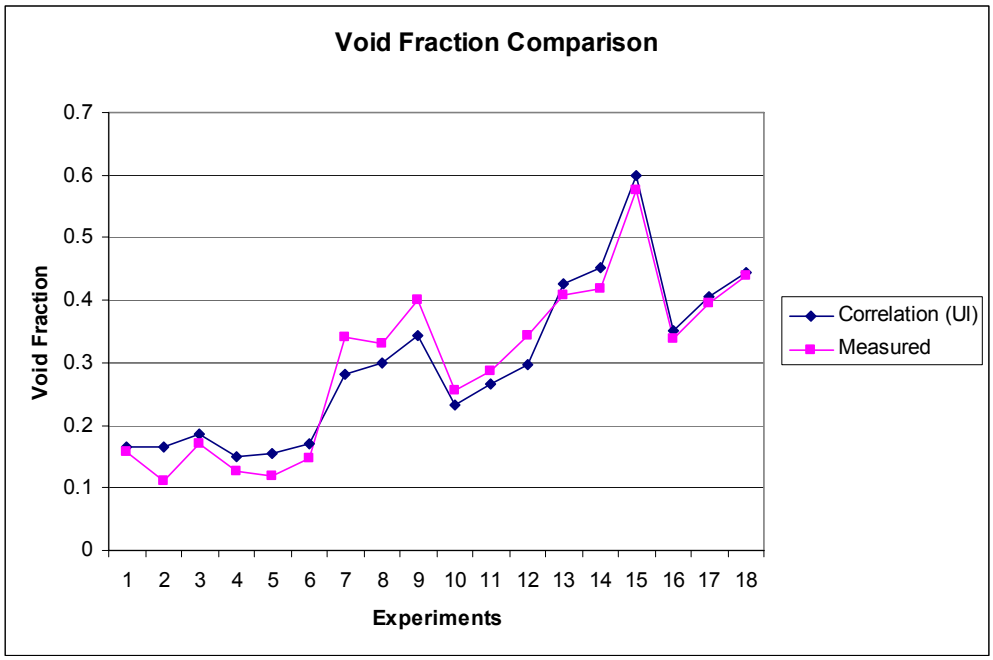

Figure 4.30: Void fraction comparison.

Figure 4.30 is shown to compare the correlation and individual measured values of the void fraction. The x-axis is setup so that the experiments (unique initial water and air flow rates) are listed in groups of three, which correspond to the three different distances from the nozzle measured (increasing distances from the nozzle). Point 2 is an outlier since measured void fraction decreased compared to point 1 as the distance from the nozzle increased.

One disadvantageous feature of the aforementioned correlation is the need for iteration in order to solve for the void fraction. This is due to the dependence of the void fraction in the liquid velocity term used in the Reynolds, Weber, and Froude numbers. Rather than using the local velocity, the superficial velocity is modified such that

$$j_l = \frac{\delta_{in} w_{in} j_{l,in}}{\delta_{MT} w_{MT}}. \qquad 4.19$$

This term is used in lieu of the U_l term in the computation of the dimensionless numbers and the correlation is still of the form

$$\frac{\varepsilon_g}{\varepsilon_{go}} = C_o Re_{lo}'^{a} Fr_{lo}'^{b} We_{lo}'^{c} D^{*d}. \qquad 4.20$$

where, now

$$Re_{lo}' = \frac{j_l \delta_{MT}}{\nu_l}, \qquad 4.21$$

$$We'_{lo} = \frac{j_l^2 \delta_{MT} \rho_l}{g_c \sigma} \tag{4.22}$$

and

$$Fr'_{lo} = \frac{j_l^2}{g \delta_{MT}} . \tag{4.23}$$

Using numerical analysis for the optimization of the constants, the correlation becomes:

$$\frac{\varepsilon_g}{\varepsilon_{go}} = 1.30 \times 10^{-5} \left[Re_l'^{1.41} Fr_l'^{-0.420} We_l'^{-0.189} \right] \left(\frac{z}{\delta_{in}} \right)^{0.118} \tag{4.24}$$

with an R^2 fit of 0.95.

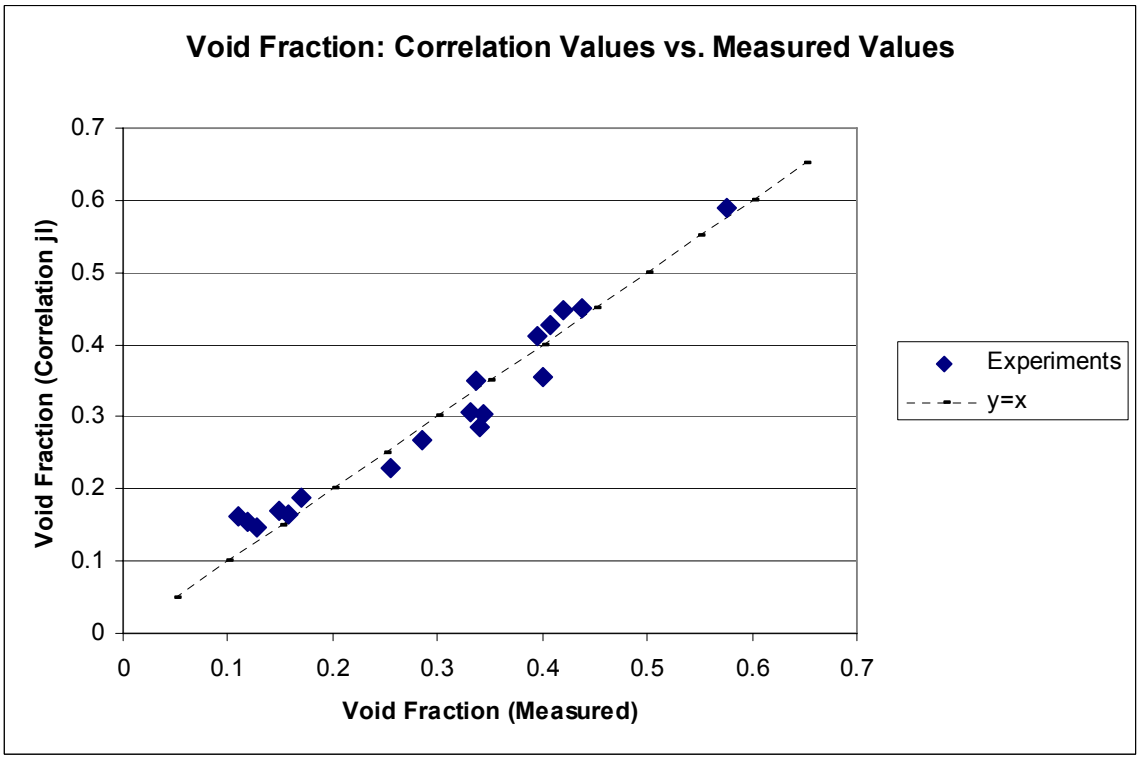

Figure 4.31: Measured void fraction versus correlation void fraction.

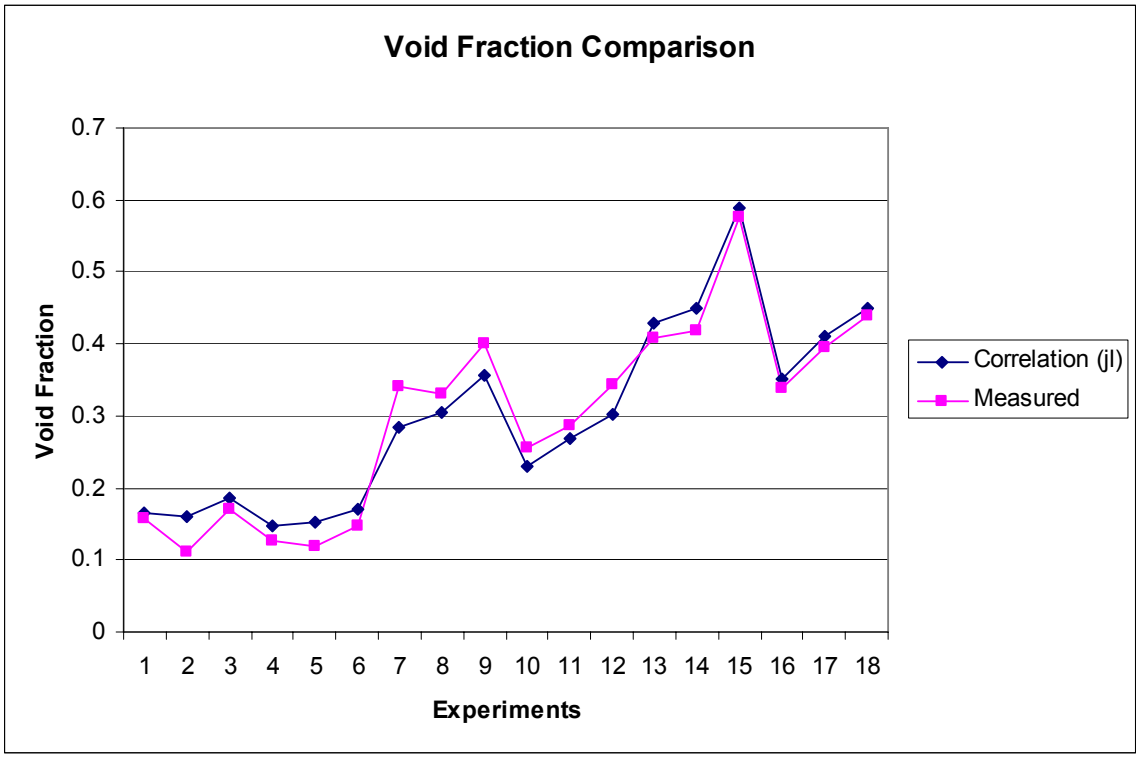

Figure 4.32: Void fraction comparison

A yet third type of correlation can be developed, and based on the generic form

$$\frac{\varepsilon_g}{\varepsilon_{go}} = C_o Re_{lo}^a Fr_{lo}^b We_{lo}^c D^{*d} \qquad 4.25$$

where

$$Re_{lo} = \frac{j_{lo}\delta_{in}}{\nu_l}, \qquad 4.26$$

$$We_{lo} = \frac{j_{lo}^2 \delta_{in} \rho_l}{g_c \sigma} \qquad 4.27$$

and

$$Fr_{lo} = \frac{j_{lo}^2}{g\delta_{in}}. \qquad 4.28$$

The advantage of this correlation is that it provides $\frac{\varepsilon_g}{\varepsilon_{go}}$ in terms of easily measurable parameters (i.e., δ_{MT} and w_{MT} are not used). The optimization of the coefficients in this correlation led to:

$$\frac{\varepsilon_g}{\varepsilon_{go}} = 1.58\times10^{-5}\left[Re_{lo}^{0.874} Fr_{lo}^{-0.252} We_{lo}^{0.306}\right]\left(\frac{z}{\delta_{in}}\right)^{0.180} \qquad 4.29$$

This correlation has an R^2 fit of 0.81, and the correlation values of the void fraction are compared to the measured values of the void fraction.

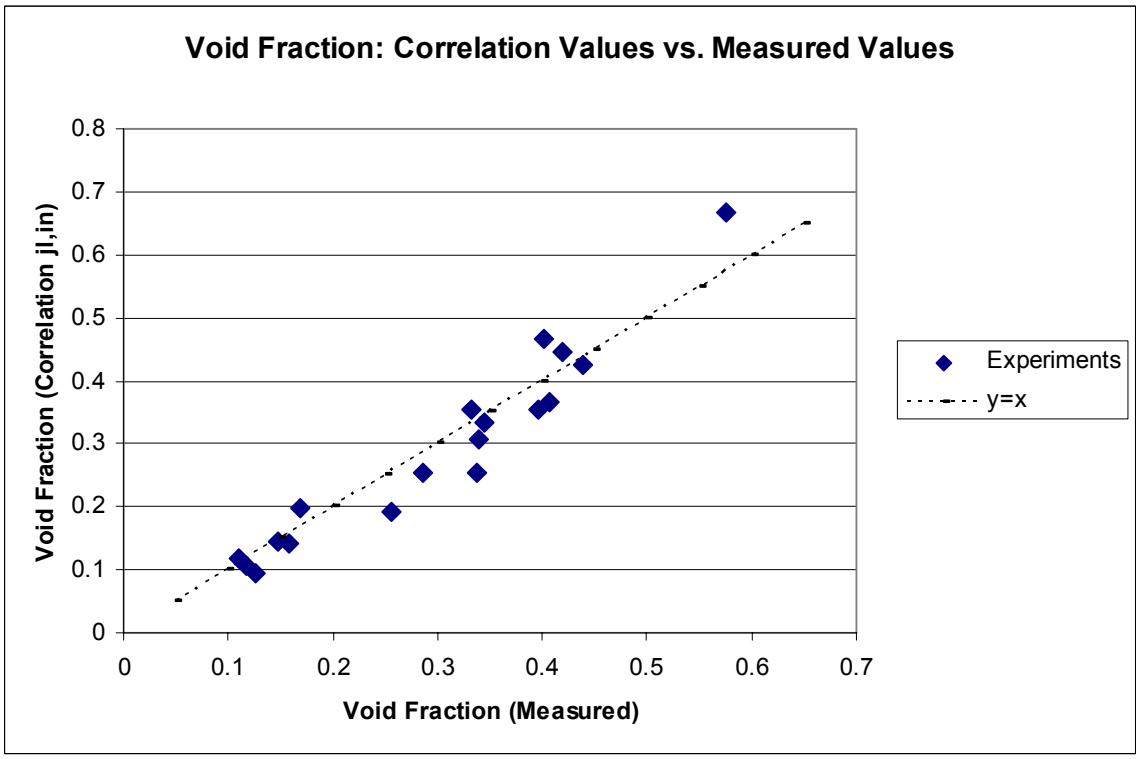

Figure 4.33: Measured void fraction versus correlation void fraction.

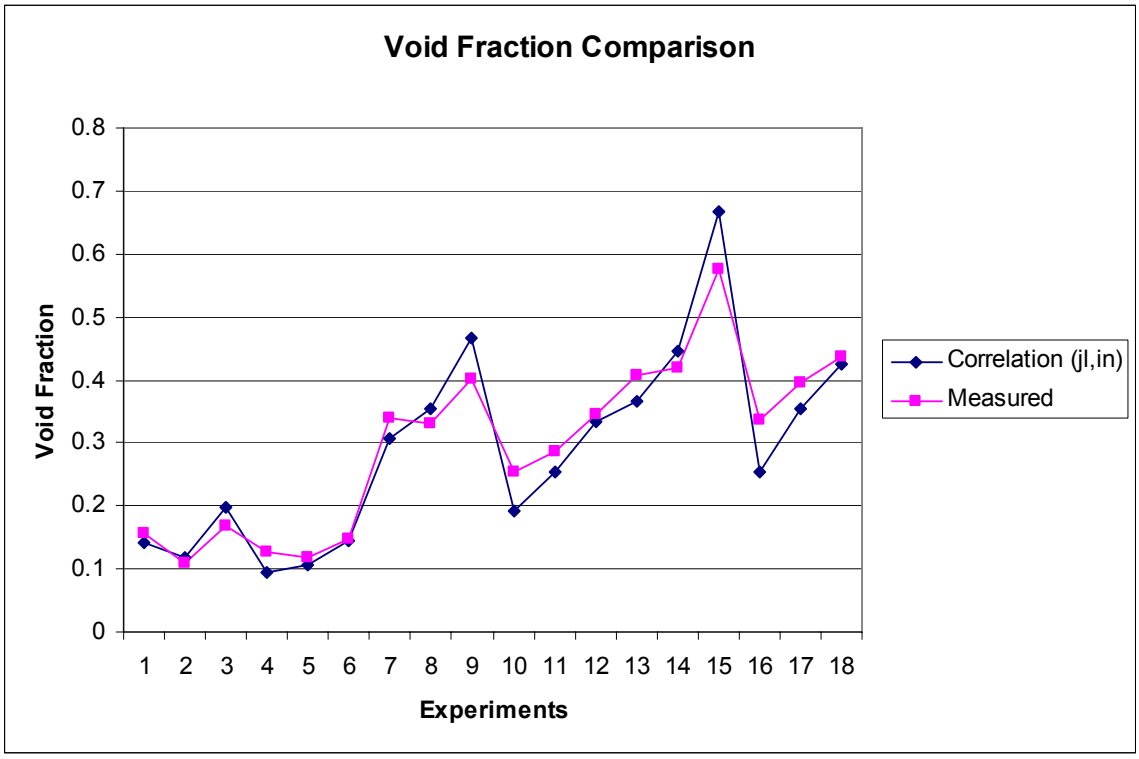

Figure 4.34: Void fraction comparison.

4.1.5.5 Gas Flow Limits

Bubbly flow is the desired flow regime for the test flow. For each flow rate of water studied, the maximum gas flow for the bubbly flow regime was visually determined. For Q_l = 60 L/min (15.9 gpm), as gas is injected into the flow, the resulting flow regime is slug flow; therefore the maximum gas flow rate (Q_g / Q_l) is equal to 0. For Q_l = 120 L/min (31.7 gpm), bubble flow regime was observed for a maximum Q_g / Q_l of 1.25% (Q_g = 1.5 L/min). If the gas flow rate is increased, the resulting flow regime is slug flow. For Q_l = 180 L/min (47.6gpm), bubble flow regime was observed for a maximum Q_g / Q_l of 15% (Q_g = 27 L/min). At this value of Q_g, spray was observed from the jet. Additional gas resulted in slug formation within the nozzle. For Q_l = 240 L/min (63.5 gpm), bubble flow regime was observed for a maximum Q_g / Q_l of 21% (Q_g = 50.5 L/min). Additional gas causes significant water spray since gas is escaping from the flow. And for Q_l = 288 L/min (76 gpm), bubble flow regime was observed for a maximum Q_g / Q_l of 21% (Q_g = 60.4 L/min). Additional gas causes significant water spray since gas is escaping from the flow.

4.1.5.6 Conclusions

In this investigation, the hydrodynamics of falling two-phase jets were investigated. The jets were produced using a vertically-oriented, 10 cm x 1 cm rectangular nozzle and using air and water as the working fluids.

A total of 20 different flow rates were studied and local void fraction measurements were performed at nine locations for each flow rate covering the z-dimension range from 5.4 cm to 21.9 cm at the nozzle exit. The collapsed liquid thickness was measured for all points using a gamma-ray densitometer, and the jet thickness was measured using a thickness tester. The void fraction was then calculated for all data points. However, due to the relatively large error associated with the jet thickness measurements as well as the potential "jet spray", the data representing low liquid flow rates were excluded, and the void fraction was empirically correlated for only the six, highest velocity tests. The local gas phase and liquid phase velocities as well as the slip ratios were also studied for the six flow rates. The limits for jet stability were qualitatively assessed.

The trends in the void fraction of the aforementioned six flow rates were studied in some detail. The void fractions ranged from below 10% to almost 60%. In all cases, however, the void fraction was greater than the volumetric flow rate ratio. Generally as the distance from the nozzle increased, the void fraction increased. Three different correlations were developed, all using inlet flow conditions and jet exit thickness, as well as two using local thickness and width measurements. The distinction between them is the definition of a velocity used in the calculation of the dimensionless numbers used in the respective correlations; the first used a localized velocity with dependence on the local void fraction and local thickness, the second used a superficial velocity and local thickness, and the third used the superficial velocity and jet thickness at nozzle exit. All three correlations fitted the data well.

The slip ratio of six different flow rates was extensively studied. The values of the slip ratio ranged from less than 0.2 to greater than 0.8. Thus, at no positions studied was the gas velocity greater than the liquid velocity. This suggests that the homogeneous equilibrium model is inappropriate (since the assumption that the slip ratio is equal to 1 is clearly invalid). Generally as the distance from the nozzle increased, the slip ratio decreased, indicting the liquid is accelerating and or the gas is decelerating. The deceleration of the gas is of course expected, due to the buoyancy effect.

The stability limits were studied for five different water flow rates. In the context of the present experiments, jet stability is primarily determined by the two-phase flow regime upstream the exit from the nozzle. The bubbly flow regime was required for the formation of a stable jet. It was observed that, when the water flow rate was small (60 L/min [15.9 gpm], 120 L/min [31.7 gpm]), the flow became slug flow almost immediately with any gas injection. For higher water flow rates (240 L/min [63.5 gpm], 288 L/min [76 gpm]), the flow became unstable only after a substantial amount of gas was added ($Q_g / Q_l > 20\%$).

4.1.5.7 Recommendations

Further study of plane two-phase falling jets with the current test facility is recommended. There are several different facets that can be elaborated. First, the number of experimental data points can be increased by studying higher water flow rates (greater than 288 L/min [76 gpm]), and by increasing the number of positions where measurements are performed for each flow rate.

As previously discussed, at low gas flow rates, the thickness measurements are slightly under-predicted and the collapsed liquid thickness values have been slightly over-predicted. It is not completely clear why this anomaly occurs, and whether the anomaly is physical or it is caused by experimental errors. If the latter possibility is to be believed, then the method used to measure the thickness of the jet is not accurate enough for measuring small void fractions (less than 10%). Further investigation of this anomaly is recommended. Another means of measurement for the jet thickness (photography, etc.) is recommended. The spray from the jet that deposits onto the container walls can possibly be estimated by normalizing the void fraction of single phase flow to 0% (if a negative value is observed due to the spray).

The measurements in this study were restricted to a minimum distance from the nozzle exit of 5.4 cm and a maximum distance from the nozzle exit of 21.9 cm. It is recommended that the facility be modified so that measurements at larger distances from the nozzle exit become feasible.

Finally, the stability of liquid jets when bubbles are generated inside the falling jet (due to flashing caused by volumetric heating for example) should be investigated in the future.

4.1.6 Shock Mitigation in Voided Liquids for Chamber Protection [58]

Inertial fusion energy (IFE) power plant designs require a shock mitigation strategy to protect the chamber from repeated thermonuclear blasts. One proposed idea for a high repetition rate (6 Hz) moderate yield (350 MJ) conceptual power plant design is to use flowing liquid flibe (F_2LiBe_4), either as sheets or jets in a staggered configuration, to protect the walls [59] and also to serve the functions of heat transfer and nuclear fuel breeding. Currently, there is an ongoing conceptual power plant design that instead utilizes high yield reactions (3 GJ) at a much lower rate (0.1 Hz), and this provides a more challenging scenario where shock mitigation becomes more important. This new design, utilizing Z-pinch technology [60], is investigating the use of foam(s) to reap the benefits that a two-phase material can provide for shock mitigation [61]. The IFE target is suspended from above in the center of the chamber filled with low pressure gas (10-20 torr), inside of a hohlraum, by a conical recyclable transmission line (RTL). The interior of the RTL will be filled with solid foam Flibe to protect the top of the chamber, while a bubbly pool protects the bottom, and foamed liquid (two-phase) jets and sheets protect the side walls.

Previous shock tube investigations for chamber protection used solid aluminum foam (as a model for flibe or PbLi foams) to study both thin foam layers, to model the vertical coolant sheets, and a thick layer, to model the RTL. A series of low Mach number experiments (M=1.34) studied the shock attenuation properties of a single 2.54 cm layer suspended in a shock tube and also the effect of two layers separated by two different spacings [62]. The pressure behind the transmitted shock was reduced by 30% (compared with the incident shock) while the wave speed was reduced by 10% for the single layer configuration in Ar initially at atmospheric pressure. The two layer configuration resulted in even greater pressure attenuation (50%) while the spacing between the layers was found to have little effect. The solid foam, to model that incorporated into the RTL, was modeled using two layers of 10.2 cm thick high-porosity aluminum foam of three different cell sizes subjected to a very strong M=6 shock wave [63]. The presence of the thick aluminum foam mitigated the shock wave; however, a very strong compression wave was transmitted through the foam. Energy absorption was found to be a function of cell size while the overall pressure load reduction was not, and larger pores were more effective at reducing the end-wall impulse.

The experiments reported here are for a new set of experiments, with varying shock strengths, M=1.4, 2.0, and 3.1, where the objectives are: 1) to study the attenuation of the shock wave as it passes through the bubble-filled, two-phase, pool, and 2) the impulse reduction observed when voids are present in the liquid. This data can then be used for initial code calculation verification and validation, before higher energy (e.g. high explosive) shock mitigation experiments are performed.

4.1.6.1 Experiment

The Wisconsin Shock Tube Laboratory [64] is utilized to conduct these shocked liquid pool studies. The 9.2 m long vertical shock tube has a large internal square cross section (25.4 cm sides), and is designed to withstand pressures of 20 MPa. Shock piezoelectric pressure transducers are mounted along a vertical wall of the shock tube to measure the transient nature of the pressure and the wave speeds. The driven section of the shock tube is filled with argon at atmospheric pressure, and nitrogen or helium is used in the driver to obtain the desired shock strength.

Figure 4.35 shows the experimental setup in the bottom of the shock tube. Gas flows through a fitting on the bottom of the shock tube into a cavity which remains slightly above atmospheric pressure. The Ar flows through a Tyvek™ layer, whose presence is necessary to prevent water from filling up the Ar cavity during experiment preparation, and then through a 2.54 cm thick aluminum foam [64, 65]. The aluminum foam is an open-celled structure, Fig. 2, with a linear pore size of 0.64 mm and 40 pores per inch (ppi), and a porosity of $\phi = 0.89$, where $\phi = 1 - \rho_c / \rho_s$, $\rho_s = 2,700$ kg/m^3 (solid Al 6061 T6 density), and the cellular density is $\rho_c = 0.11\rho_s$. The compressive yield strength for the 40 ppi foam with this porosity has a plateau of $\sigma_{yc} = 3.0$ MPa and is relatively independent of the pore size [66]. The aluminum foam creates bubbles that are small, relative to the cross section of the shock tube, and randomly distributed throughout the volume. An exhaust line is located above the pool's surface so that the pressure of the driven section of the shock tube remains at 1 atm. A solenoid-actuated valve for this line is pneumatically closed just prior to shock passage. Piezoelectric shock pressure transducers sampling at 1 MHz are located along the center of one side of the shock tube with the faces flush mounted with the shock tube wall. There are four pressure transducers located above the pool to accurately measure the speed/pressure of the initial shock wave and the transducers are vertically spaced at intervals of 2.54 cm in the pool. The appendix contains engineering drawings for the test section transducer plug, the test section, and the support structure for the aluminum foam.

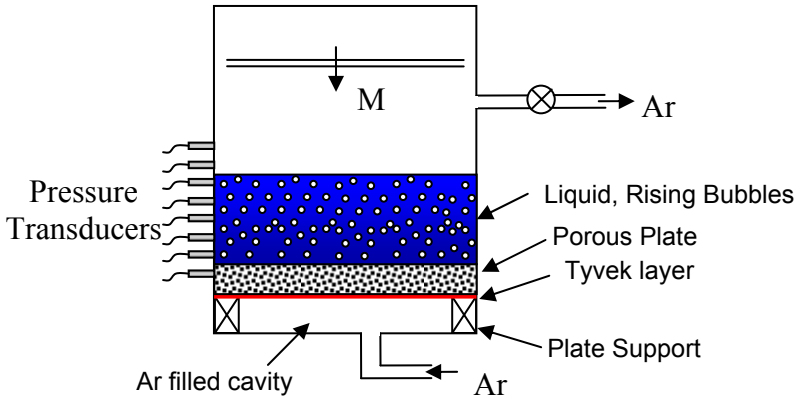

Figure 4.35: Apparatus for simulating the shock mitigation response in the lower portion of the chamber.

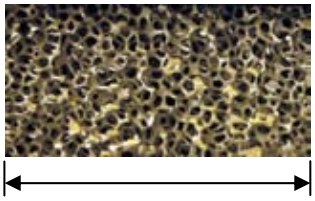

Figure 4.36: Open cell-cell morphology of the 40ppi aluminum foam used to create the bubble distribution.

Figure 4.37 and Figure 4.38 show Ar bubbling up through water and oil in a mock-up of the shock tube test section having polycarbonate walls. The bubble population in the water is uniform across the width of the pool as well as the height. The turbulent nature of the bubble-bubble interaction while rising results in non-spherical gas bubbles at any moment in time, but over time, the bubbles in water may be considered spherical with an average diameter of D=5.6 mm with a standard deviation of 2.6 mm. Void fraction of gas was controlled by measuring the volumetric flow rate, during characterization, levels up to 15% could be achieved. Numerous attempts to achieve higher void fractions were unsuccessful, including: increased flow rate (limited by the head loss of the aluminum foam); different pore size foam (no effect, most likely because porosity remained constant); and a stainless steel porous plate instead of aluminum foam (resulted in very small bubbles and very low void fraction due to high head loss). The same 15% void fraction observed in the water was also seen in the mineral oil, however, the bubbly flow was much different than the flow in water, as seen in Figure 4.37, and resulted in a bimodal bubble size distribution. The argon bubbling-up through the oil created a near-foam (in appearance) two-phase fluid, with many tiny bubbles of D<2 mm. In addition, there were a number of large-scale bubbles 15<D<30 mm that originated at the locations of small cap screws that were used to secure the porous plate to the support around the perimeter of the plate.

A final series of experiments were conducted at the high Mach number for shaving cream foam occupying the bottom 1.3 m of the shock tube. These experiments provide the contrast of a very low density, closed-cell foam, to the high-density water pool experiments.

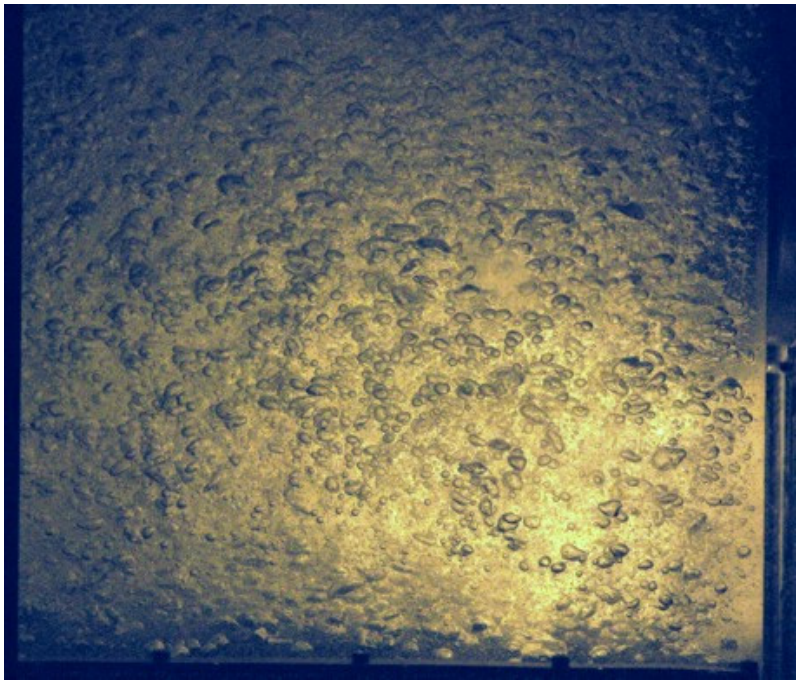

Figure 4.37: Water with 15% void fraction of Ar in a mock-up of the shock tube test section with transparent walls- the width of the test section is 25.4 cm.

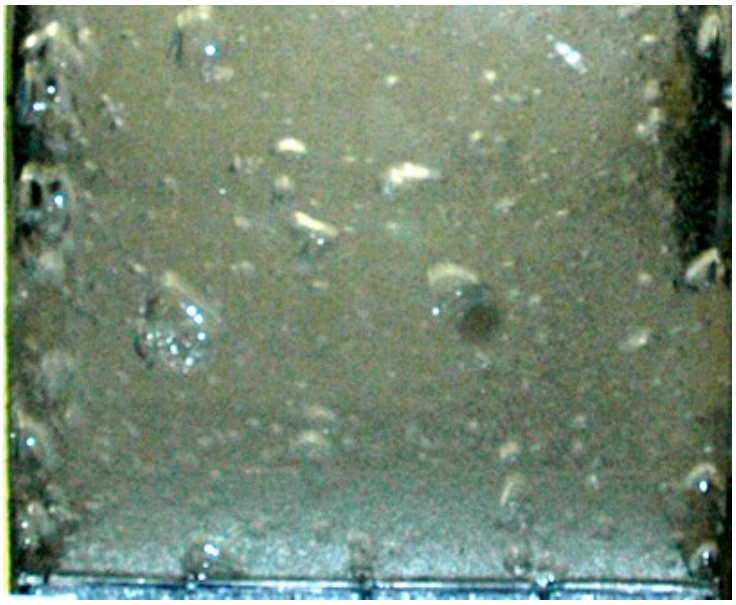

Figure 4.38: Mineral oil with 5% void fraction of Ar in a mock-up of the shock tube test section with transparent walls- the width of the test section is 25.4 cm.

4.1.6.2 Shock Strength Scaling

Calculations of the shock strength following target ignition were carried out using BUCKY [67] to determine the pressure loading on the pool in the bottom of the reactor. Pressure as a function of chamber radius is shown in Figure 4.39 for a 3.05 GJ target yield in a chamber with an initial argon gas pressure of 12 mtorr (1.6 Pa). The pressure traces for t=115 and 900 ns show the regions of the target (DT, Be, CH, Au), argon, and flibe (considered incompressible in the calculation). There is a compression wave moving radially outwards through the argon (shown at 115 ns), and when it reaches the flibe, vaporization occurs (moving back into the argon, shown at 900 ns) which raises the local pressure above that of the argon. The steepening compression wave that first reaches the flibe raises the pressure to 1 J/cm^3 ($P_{contact}$=1 MPa) and then reaches a maximum of 23 J/cm^3 (P_{max}=23 MPa). For the shock tube experiments in atmospheric pressure argon, the shock strength required for $P_{contact}$=1 MPa is M=2.85, which would then result in an ideal P_{max}=4.2 MPa for a reflected shock wave off of an incompressible boundary. To reach the maximum argon pressure calculated from BUCKY (P_{max}=23 MPa) a shock strength of M=5.8 which is above the structural design limit of the shock tube. The pressure loading of the bubbly pool in the shock tube for the considered Mach numbers is on the same order as would be expected in the Z reactor, but not as high as the maximum pressure; however, the pressure ratios, and therefore Mach numbers, would be quite different.

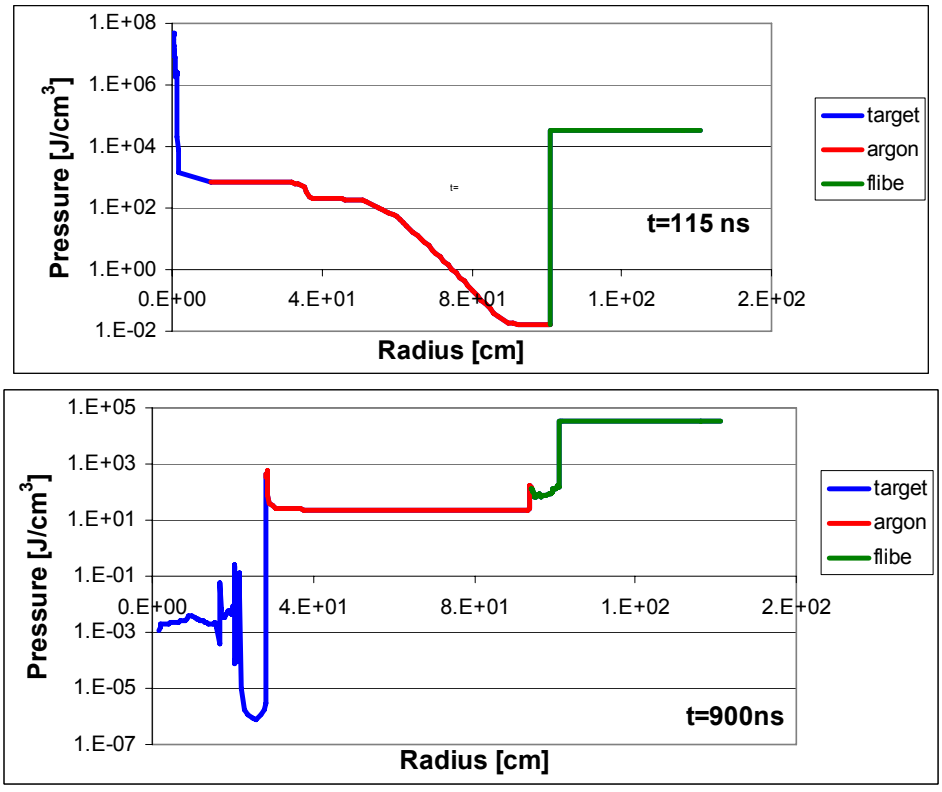

Figure 4.39: Pressure as a function of radius for the line of sight from the target to coolant pool at the bottom of the chamber calculated using BUCKY.

4.1.6.3 Results

Prior to conducting the two-phase fluid experiments, a series of calibration runs were performed to quantify the shock wave and verify the operability of the pressure transducers. The data collected from the experiments include pressure traces and material surface corrosion. This campaign consisted of a total of 52 experiments covering three Mach numbers, and the response of three different two-phase fluids of: water/argon, oil/argon, and shaving cream foam.

Pressure Trace and Impulse

Three shock strengths were chosen for these studies and the properties are listed in Table 4.4. The initial shock wave speed, W_i, is for the listed Mach number in argon at standard temperature and pressure; the reflected shock wave speed, W_r, is the calculated speed for the reflection off an incompressible surface; the gas velocity behind the incident shock is u_2; and the pressure, P, with subscripts 1, 2, and 5 are the initial pressure, the pressure behind the incident shock wave, and the pressure behind the reflected shock wave, respectively.

Table 4.4: The experiment parameters, for argon, calculated from 1-D gas dynamics.

M	W_i (m/s)	W_r (m/s)	u_2 (m/s)	P_1 (MPa)	P_2 (MPa)	P_5 (MPa)
1.4	456	343	170	0.101	0.227	0.453
2.0	646	405	363	0.101	0.482	1.52
3.1	1,001	554	672	0.101	1.19	5.26

Pressure traces from the same transducer for each of the void fraction pools are shown in Figure 4.40 for some low Mach number water pool experiments. The pressure in the pool without a void fraction resemble the P_5 plateau that would be observed for a shock wave reflected off a rigid surface, this is indicative of the relative incompressibility of the water compared with the argon. At longer times, t>1 ms, the pressure trace resembles the P_5 plateau for each of the void fractions. The early time behavior is quite variable for the different void fractions as seen in Fig. 6(b). When there is no void fraction, a near-discontinuity pressure rise is observed as would be expected for a shock wave (not traveling through the water but reflecting off the surface of the water back into the argon); however, the presence of the argon bubbles in the pool has a strong effect on the pressure traces and oscillations are observed in the traces before leveling out at later times. Each of the pressure traces for void fractions of 5, 10, and 15% argon show an initial compression that is not discontinuous, and is the response of the argon bubbles in the pool compressing. The time when the bubbles in the pool have reached maximum compression corresponds to the time of peak pressure; this is then followed by an expansion of the bubbles which reduces the pressure. Cyclic compression and expansion continues during the early times and the measured oscillations reflect this cycling, and not necessarily reverberating pressure waves in the bubbly pool. There are some higher frequency oscillatory content in the 5 and 15% argon void fraction traces which is most likely due to a proximity effect for a single bubble being closer to the transducer face (circular, 5 mm diameter) and therefore responding slightly different than the overall, average, pool response.

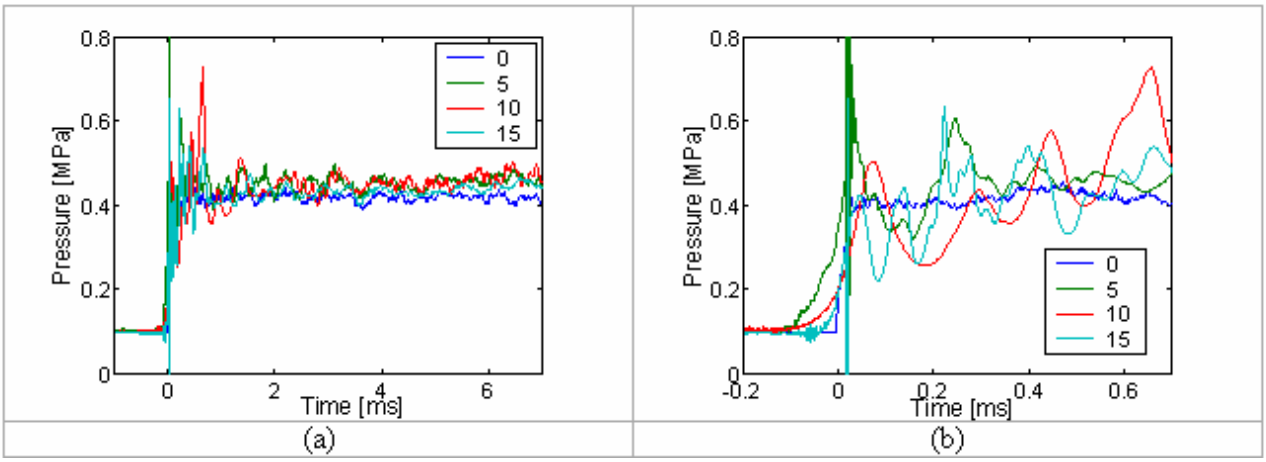

Figure 4.40: Pressure traces for M=1.4 from a transducer located 3.5 cm below the surface of the pool for 0, 5, 10, and 15 % argon void fraction.

Results for the impulse calculations are given in Table 4.5. The impulse time (t_I) is chosen as the time it takes an unattenuated shock wave to travel through the distance of the pool depth, h=0.3048 m. The impulse interval begins when a pressure is first registered by the transducer. The impulse time goes down with increasing shock strength but the impulse goes up due to the stronger effect of the higher shock strength's pressure rise. Although very different behavior is seen in individual pressure traces, the presence of argon voids in the pool has little, if no, effect on the calculated impulse at the low and medium Mach number experiments. At the low and medium Mach number experiments, the shock wave speed is well below the sound speed in water (1,500 m/s at STP) and the pool shows a primarily incompressible response to the shock loading- even though the bubbles are compressing within the pool. A pool with a much higher void fraction (e.g. foam) would be expected to show a different response, with the increased void fraction resulting in an impulse reduction. A 12% reduction was observed in the high Mach number experiments, which indicates that the compressible nature of the bubbly pool was playing a role. The wave speed of the high Mach number experiments is approaching that of the acoustical speed in pure water, thus, the response of the bubbly pool is that of a two-phase mixture and is no longer purely dominated by the incompressible nature of the water as observed in the lower shock strength experiments. Also, heating of the pool due to compression of the bubbles will lower the sound speed during the shock wave interaction.

Table 4.5: Impulse measurements for the pool with argon bubbles.

M	I_0 [Nt s]	I_5 [Nt s]	I_{10} [Nt s]	I_{15} [Nt s]	t_I [ms]
1.4	13.2	14.9	14.5	13.1	0.67
2.0	40.3	39.8	38.2	41.7	0.47
3.1	82.0	-	-	72.0	0.31

Experiments to study the response of a mineral oil pool with argon bubbles were only conducted at the higher void fraction (15%) and the high Mach number. An even greater impulse reduction was seen in this two-phase pool as the impulse dropped from 131 N-s to 86 N-s (34%). The greater reduction in impulse may be partially attributed the lower bulk modulus of oil compared to water (resulting in a lower sound speed, 1,300 m/s at STP); however, given the magnitude, it is more likely due to the very different bubble distribution of the argon in the oil, particularly the smaller bubbles that resulted in a more foamy liquid.

Using the bubbly-pool configuration, only a low gas fraction two-phase pool could be achieved. Shaving cream foam was used to contrast the behavior of a high density pool to a very low density foam which also has a closed-cell structure (density of 66 kg/m^3 and an estimated gas void fraction of 94%). The bottom 0.3 m of the shock tube was filled with the foam (shown in Figure 4.41(a) and (b) and it experienced no visible settling from the time of preparation to the time of shock arrival (typically less than 30 minutes). A pressure trace result is shown in Figure 4.42 and, for comparison, the reference is a shock wave in the gas (air). In the pure gas trace, the shock wave initially steps up the pressure to 1.2 MPa (P_2) and then at 0.8 ms the pressure is stepped up to 5.3 MPa (P_5). After 1.5 ms it is clear that the rarefaction from the shock tube driver has expanded down to the pressure transducer location which lowers the pressure in an exponentially decaying fashion. When the shaving cream foam is present, the response is much different, with the initial pressure rise showing fast compression, although not stepped as in the shock wave case, which is between the P_2 and P_5 pressures of the shock wave in the argon. At the later times, during the rarefaction phase, the exponential decay of the pressure is the same in both cases. An arbitrary time of 2 ms was chosen for comparing the impulse between the foam and no-foam cases and a reduction from 441 N-s to 344 N-s was observed, a 22% reduction. Figure 4.41(c) is a photograph, taken from higher up in the shock tube, of the top surface of the foam after an experiment. The foam expanded from the initial 0.3 m depth to 1.3 m, and by the time the high pressure had been vented and a port was opened for taking the photograph, the foam had settled to this 1.3 m depth (there are visible liquid traces on the walls that indicate that the foam had splattered during the test.) One experiment was conducted on this already expanded foam and the shock mitigation was still evident, but less effective, with an impulse of 427 N-s. Thus, it appears that the responsible mode for impulse reduction is one where the energy of the shock wave is transferred into expanding, and breaking-up, the foam. Once expanded, the foam loses most of its impulse reducing function.

Figure 4.41: Shaving cream foam photographs in shock tube, (a) side-view during fill, (b) top view pre-test, and (c) top view post test

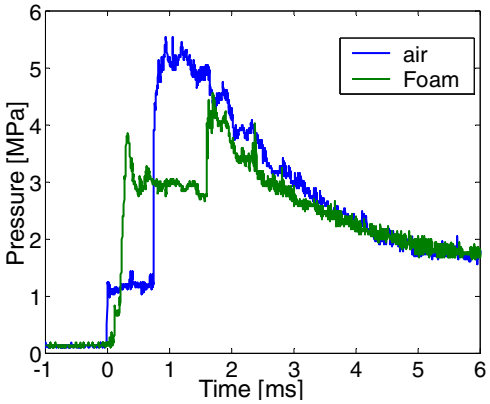

Figure 4.42: Pressure Traces from a transducer located 1 m below the surface of the shaving cream foam.

4.1.6.4 Surface Corrosion

Polished stainless steel material samples were placed in the pool for the high Mach number experiments with no void fraction and with 15% void fraction. The scanning electron microscope (SEM) images are shown in Figure 4.43 and Figure 4.44. Each sample was only exposed during one experiment. The most notable feature observed in both samples was the presence of pits following the experiment. Surface oxidation particles were concentrated in the pitted regions and were more prevalent in the experiment without argon voids. It was anticipated that more pitting would occur in the experiment with 15% argon void fraction due to the compression (and expansion, and possible jetting) of the gas bubbles near the surface of the sample; however, the amount of pitting was similar in both of the samples. The corrosion/erosion of a wetted surface, enhanced by being repeatedly exposed to shock waves, will need to be a consideration for first-wall material selection.

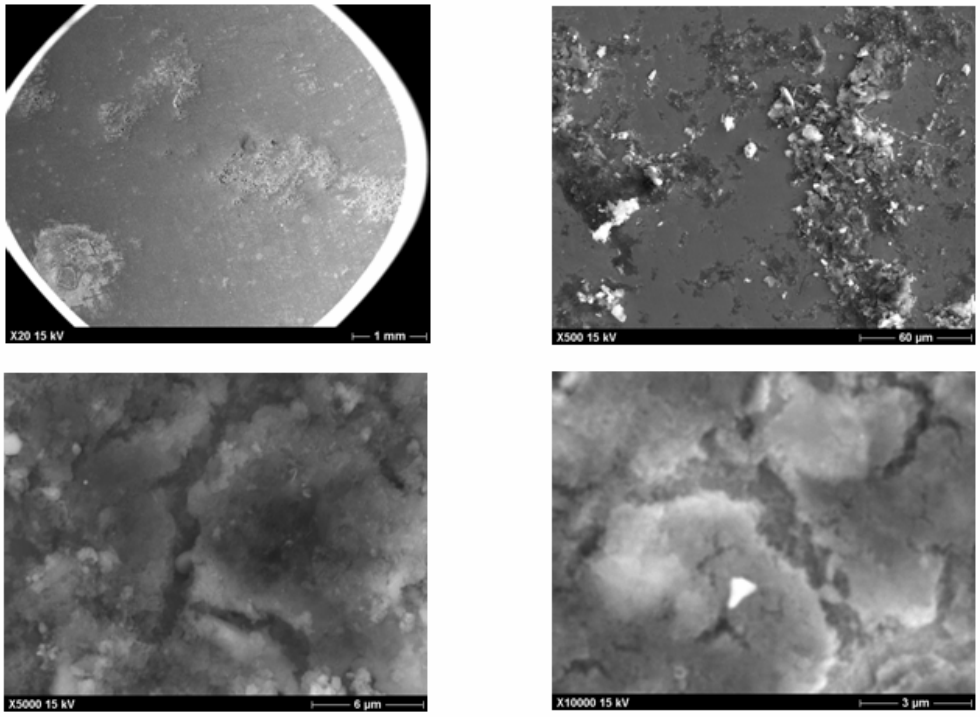

Figure 4.43: SEM images for a sample in the water pool with no void fraction shown at increasing levels of magnification.

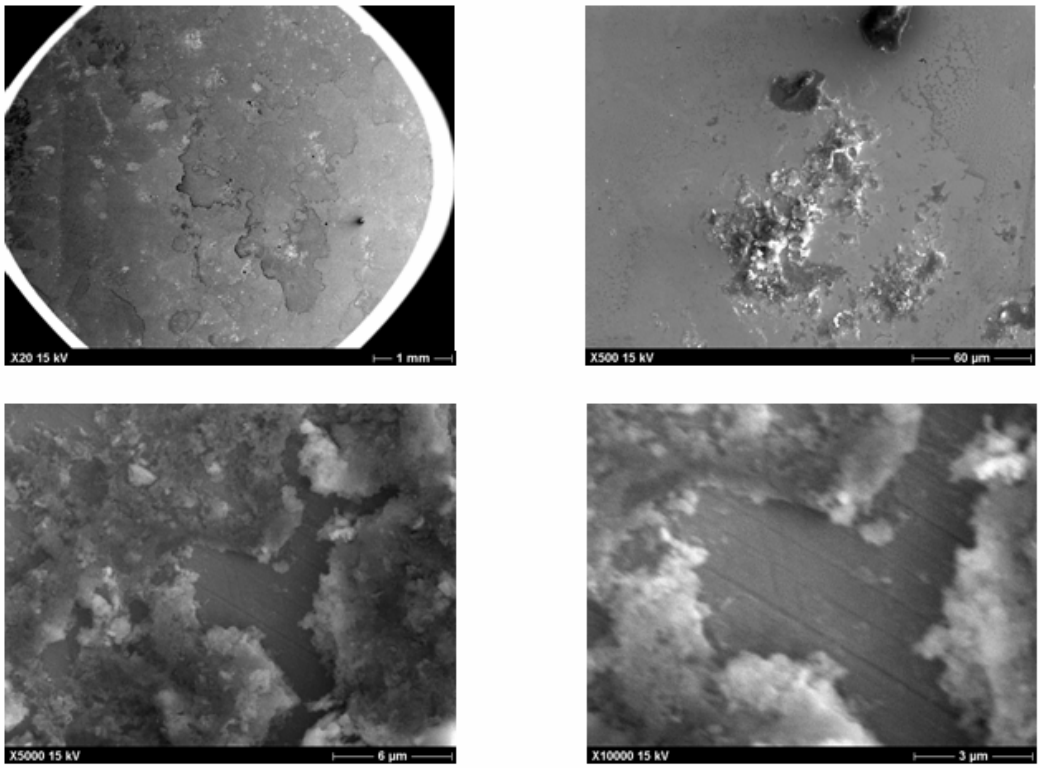

Figure 4.44: SEM images for a sample in the water pool with 15% argon void fraction shown at increasing levels of magnification.

4.1.6.5 Conclusions

A series of shock tube experiments were conducted to model the flibe pool response in the Z-chamber. Only low gas void fraction (5-15%) could be achieved by bubbling argon through an aluminum foam plate beneath a pool of liquid, either water or oil. Although the pressure traces in the pools with gas bubbles exhibited much different behavior than the measured traces for pure gas or pure liquid, the overall effect on impulse was not observed at the low and medium (M=1.4 and 2.0) experiments. The shock mitigation effect of the bubbly pool was observed in both the water and oil pools in the higher shock strength experiments (M=3.1) with the bubble distribution playing a role in the amount of observed mitigation to the impulse- smaller bubbles resulted in a foamy-like liquid resulted in greater impulse reduction. A very high gas void fraction shaving cream foam resulted in a 17% reduction in impulse for the high Mach number experiments which indicates that more experiments need to be done in the intermediate void fraction regimes to reach any conclusion about the optimum concentration of gas to liquid for shock mitigation. Polished stainless steel witness samples placed in the pools exhibited a notable amount corrosion/erosion following just a single experiment. This is a potential issue for a first wall exposed to a very high number of repeated exposures- both for the integrity of the structure and the contamination of the coolant.

4.1.7 Aerosol Shock Mitigation

Aerosol protective schemes provide a unique means by which to shield the first wall from the brunt of the x-ray energy released from the fusion burn while allowing neutrons to pass relatively unmitigated. This feature is important for designs requiring tritium breeding and/or transmutation in a blanket external to the chamber. Ultimately, the success or failure of any mitigation technique is measured by the ability to shield the first wall while inducing an acceptable stress in the containment vessel. Figure 4.45 shows a schematic of the model used in these investigations.

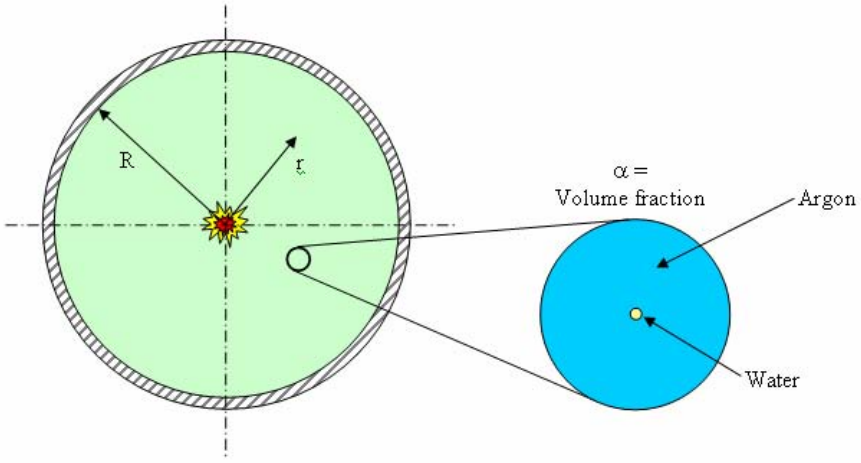

Figure 4.45: Schematic of CTH 1-D system model.

The aerosol system consisted of a water and argon matrix with a volume fraction of α = 0.3%. Water and argon were chosen because the code has well-defined equations of state for these materials. Also, these materials are likely candidates for early experiments. The water droplets each had a diameter of 30 μm and were assumed to be uniformly distributed throughout the chamber. The argon was at a pressure of 0.06 bar, roughly twice the vapor pressure of water at 300 K. Finally, the chamber was modeled as a sphere with radius R = 1 m and wall thickness of t_w = 0.04 m. The shock was generated by an x-ray source of 10 MJ depositing into the aerosol. To address the post-burn physics of a chamber filled with an aerosol, the CTH shock code was employed to model the time from immediately after detonation to the subsequent chamber dynamic response.

The CTH suite of codes was created at Sandia National Laboratories to model systems with large deformations and/or strong shocks. The code utilizes an Eulerian architecture to solve the mass, momentum, and energy equations. The x-ray energy deposition profiles were input as an initial condition of 1-D spherical gas contained by a steel vessel (Figure 4.46) [1]. These CTH runs assumed a constant x-ray source radius of 0.036 m for all cases. The code then output a time dependent response of the gas as a shock wave formed and propagated to the steel containment wall. This response does not include any high order plasma physics, *e.g.* re-radiation of the gas via Bremsstrahlung. Ultimately, the shock wave impacts the steel vessel causing a sharp rise in stress before the wave is reflected back towards the center of the chamber.

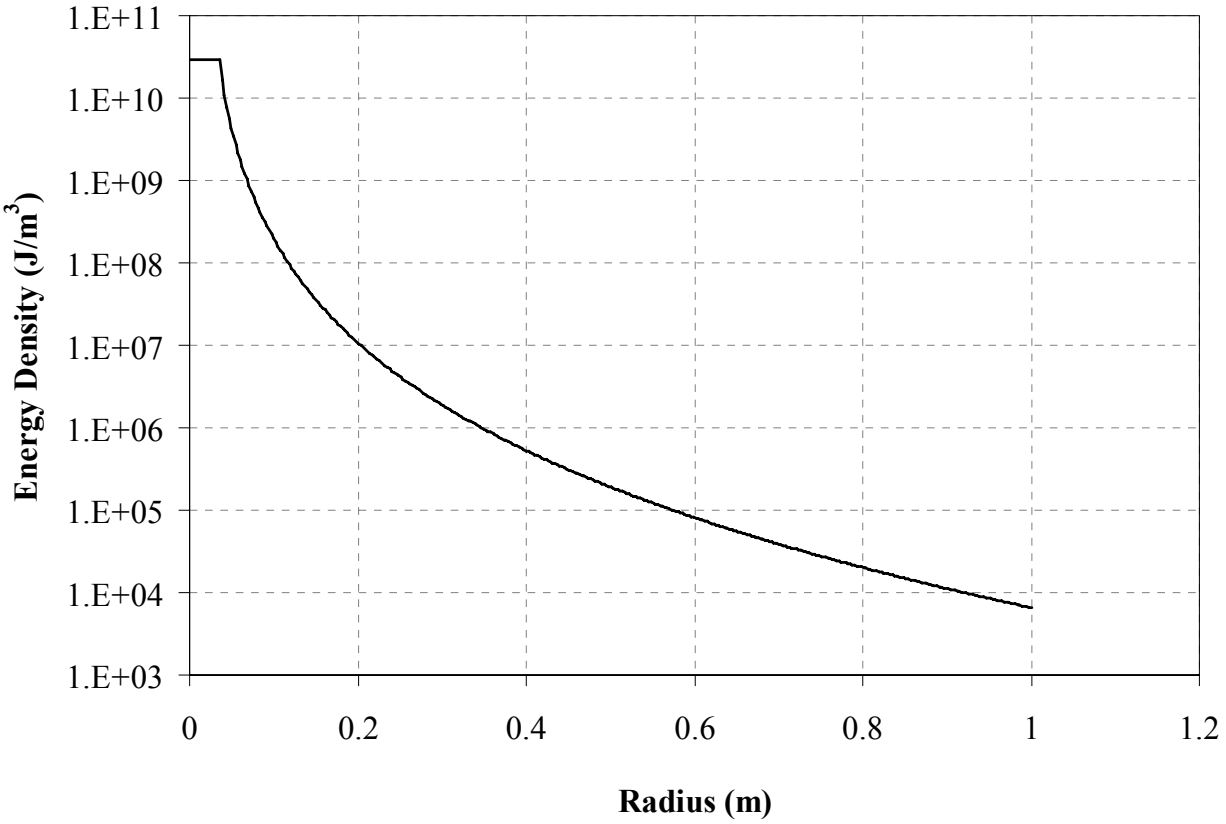

Figure 4.46: Initial energy deposition profile for the CTH simulations.

This initial modeling effort assumed all x-ray energy was deposited into the water. This assumption was made due to the water constituting 98% of the mass of the system. Figure 4.47 shows the resultant initial temperature profile of the water in the system from the deposited x-ray energy. The water near the center of the x-ray source reached temperatures exceeding 8×10^5 K. However, the water temperature drops quickly away from the center, falling below boiling at approximately r = 0.4 m.

Figure 4.48 gives the temperature profile inside the chamber at times up to 1800 μs. The model shows that the system peak temperature quickly drops, while the energy redistributes. However, this diffusion of temperature should not be confused as heat transfer. For this version of the model, the code does not treat any modes of heat transfer. Conduction was allowed in a later version of the model but did not affect the results appreciably. Rather, the change in temperature is simply due to the advection of water in the chamber.

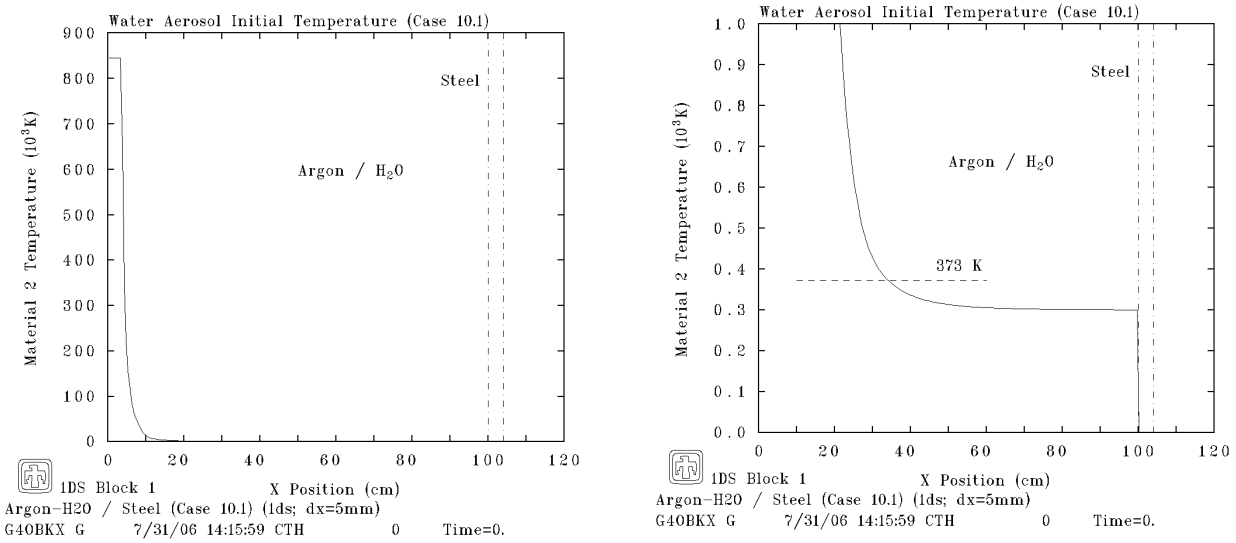

Figure 4.47: Initial temperature profile of the water in the CTH simulations.

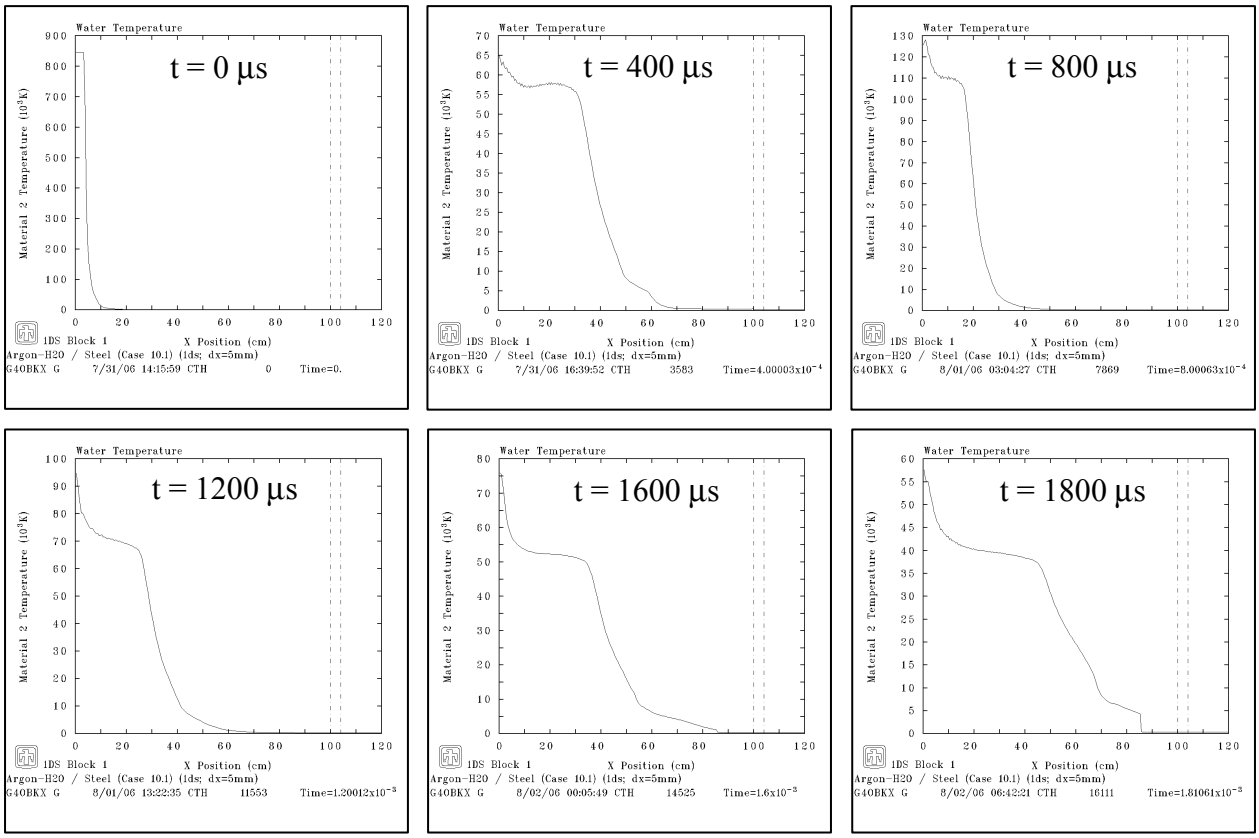

Figure 4.48: Temperature profiles in the chamber at different times for the CTH simulations.

Figure 4.49 shows the pressure histories at different locations inside the chamber. The shock wave and subsequent reflections are characterized by the sharp pressure peaks. The solid line (Case 10.1) represents the aerosol system described earlier. The dashed line (Case 9.2) denotes a system with matching dimensions but only argon gas as an x-ray mitigation shield. For protection in this system, the gas pressure must be almost nine times greater or P = 0.533 bar. The response of both systems is similar in character, but the shock wave is greater in magnitude in the aerosol protected system. This increased shock wave is perhaps due to the addition of more mass into the system, nearly 12 kg of water.

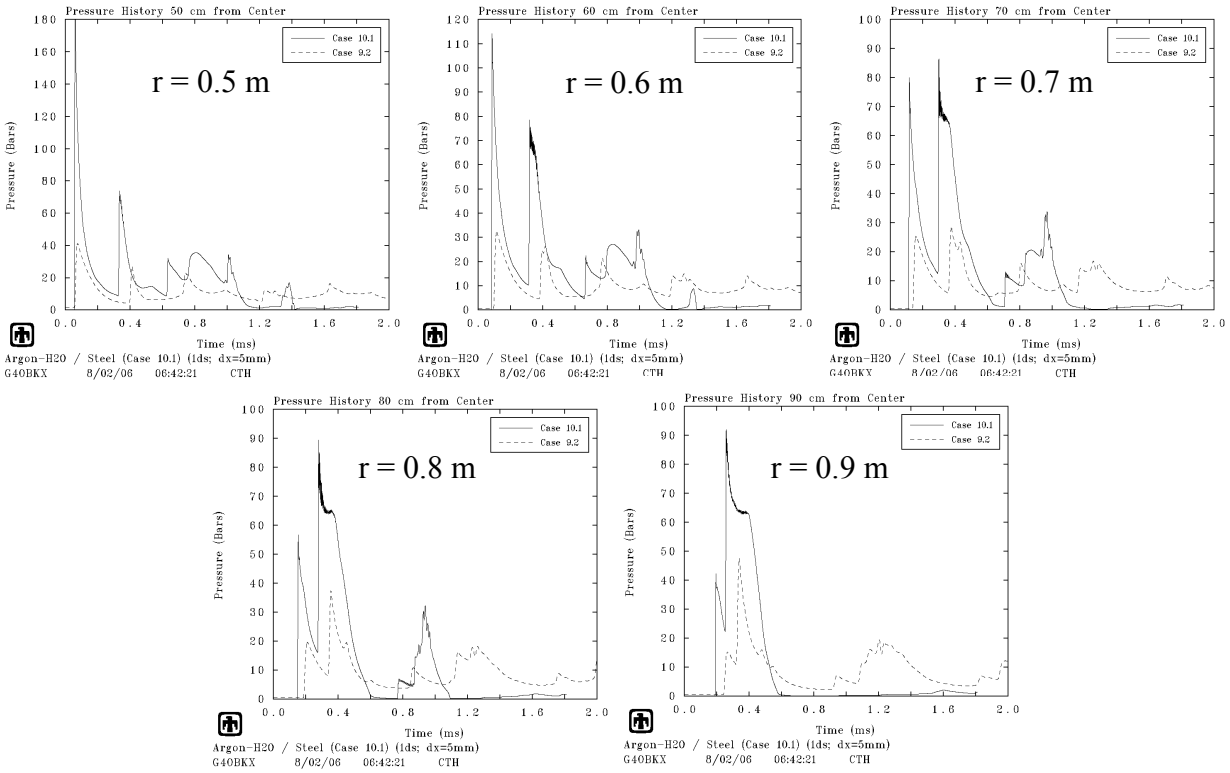

Figure 4.49: Pressure histories at different locations in the chamber for the CTH simulations.

Figure 4.50 gives the induced hoop stress in the chamber wall for the two aforementioned cases. The aerosol protected system produced a stress of nearly one and a half times that of the gas protected one. This stress is directly correlated to the strength of the shock waves interacting with the chamber walls. Still, the stress in the vessel wall did not exceed the elastic limit of common stainless steels (~ 2000 bar). Although the gas protected system does incur a lower stress, the potential shielding capacity of aerosols far exceeds that offered by gas alone. A gas system in moderately sized chambers is limited to x-ray energies of about 100 MJ and below based on the temperature rise of the gas, whereas a similar geometry with an aerosol has a limit just exceeding 1000 MJ [1].

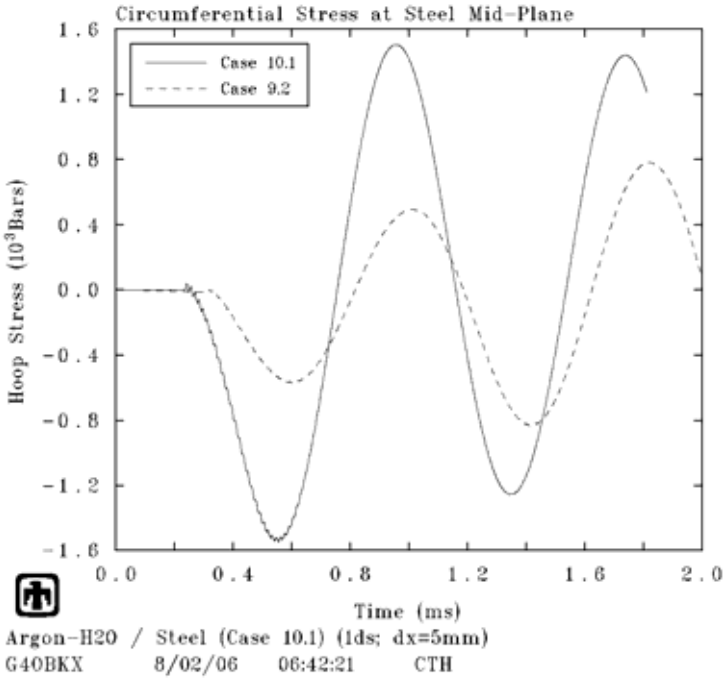

Figure 4.50: Induced hoop stress in the chamber wall as a function of time for the CTH simulations.

Water mass as a function of position in the chamber at various times is plotted in Figure 4.51. Again, the water was assumed to be distributed uniformly in each differential node at the beginning of the simulation. As time progresses, the water is preferentially pushed towards the chamber wall. The agglomeration of water is possibly an artifact of the code, which is evident at times late in the simulation. However, the first arrival of the main pressure wave that accelerates the steel shell to its motion is concluded before all the water has accumulated. Therefore, the response of the steel shell should be unaffected by this anomalous numerical result.

The response of a water-argon aerosol in a post-detonation chamber was modeled using the CTH shock code. These simulations indicated that the stress induced from the ensuing shock wave was acceptable for a chamber with the assumed geometry and construction. Further refinements of the model were attempted, including a partitioned energy deposition into the water and argon based on mass ratio (98% into the water, 2% into the argon) and a model including conductive heat transfer. Both attempts did not produce significantly different results from those already presented. The model appears to be capturing, at least to a first order approximation, the physics within and the mechanical response of the chamber to relatively short times after detonation. Future two dimensional modeling in ALEGRA, a shock physics code, will be necessary to capture the plasma physics phenomenon not available in CTH for aerosol mitigation.

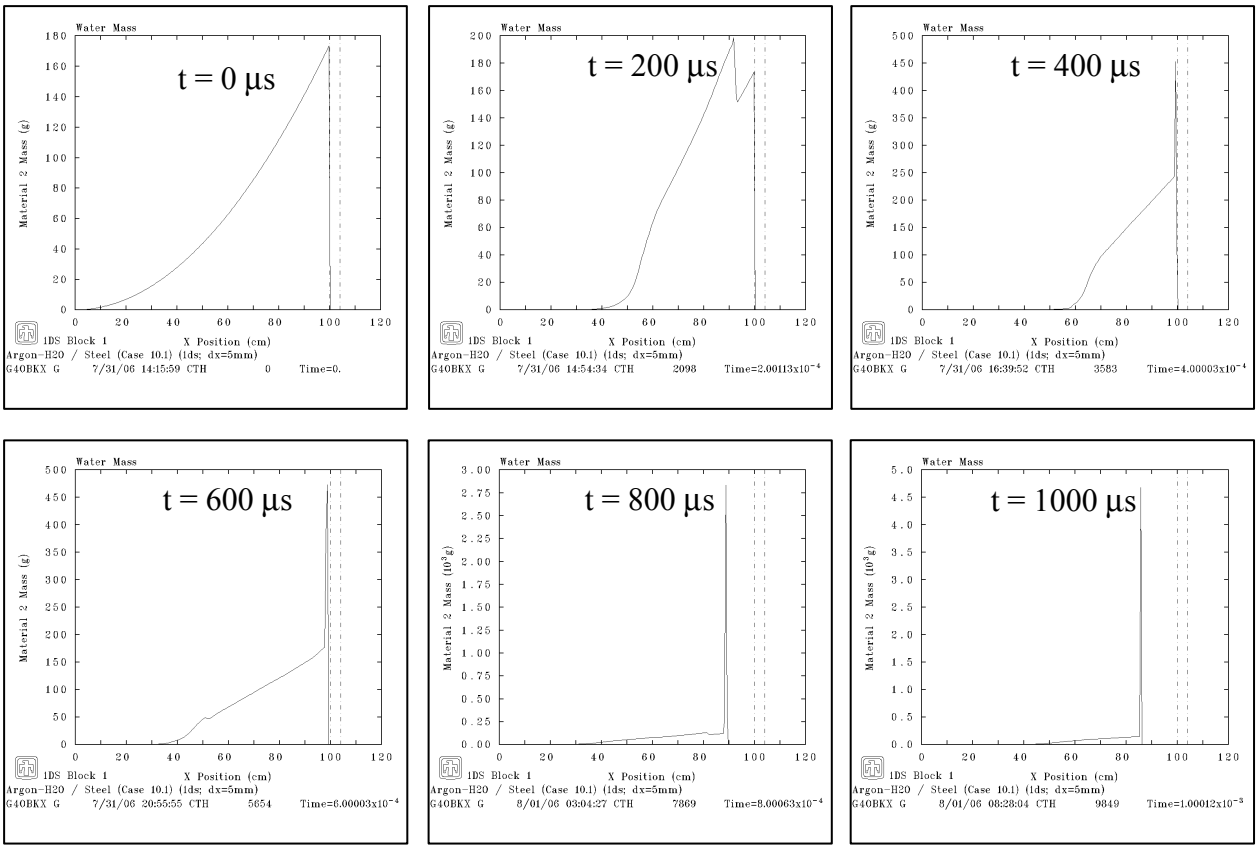

Figure 4.51: Water mass as a function of chamber position.

4.2 Chamber Design

Lawrence Livermore National Laboratories continued to optimize the thick liquid curtain chamber design this year by increasing the target yield and repetitive rate. A proposed frozen or frangible flibe RTL was used in this design to alleviate separation and remanufacturing issues immediately following the fusion event. The study focused mainly on the timing of placing and removing the RTL in and from the chamber. It is described in detail in section 4.2.1.

Due to the possibility of using aerosols to mitigate the x-rays, a first wall chamber design was proposed. This concept was first developed to be used for the transmutation plant where target yield requirements were much less compared to what was required from the power plant [5]. However, results from the computer modeling described in section 4.1.7 indicate that aerosols may be able to mitigate fusion yields upward to 3 GJ (~1000 MJ x-rays). A first wall chamber design for the Z-IFE power plant is presented in section 4.2.2.

4.2.1 Thick Liquid Curtain Chamber Design Concept and RTL Design [6]

The main features of the proposed Z-IFE chamber are shown in Figure 4.52. The 3.5-m-tall, 2.2-m-diameter (13.3 m^3) pocket protects the chamber walls by containing the x-rays and target debris generated by the fusion shot so as to delay their effect on the wall. Note that all structures are protected against neutrons, x rays, and target debris by 1 m of the molten salt flibe, which also serves as the primary coolant and tritium breeder.

The RTL is made of frozen flibe. It is shown in more detail in Figure 4.53. This RTL material is frangible meaning it shatters following a shot and quickly becomes part of the coolant. The cost advantages of the frangible flibe RTL compared to that of steel, of the rapid pulse rate of 1.9 s compared to 10 s resulting in only one chamber and power supply needed, and the liquid protection of all structures making them lifetime components should greatly enhance economics.

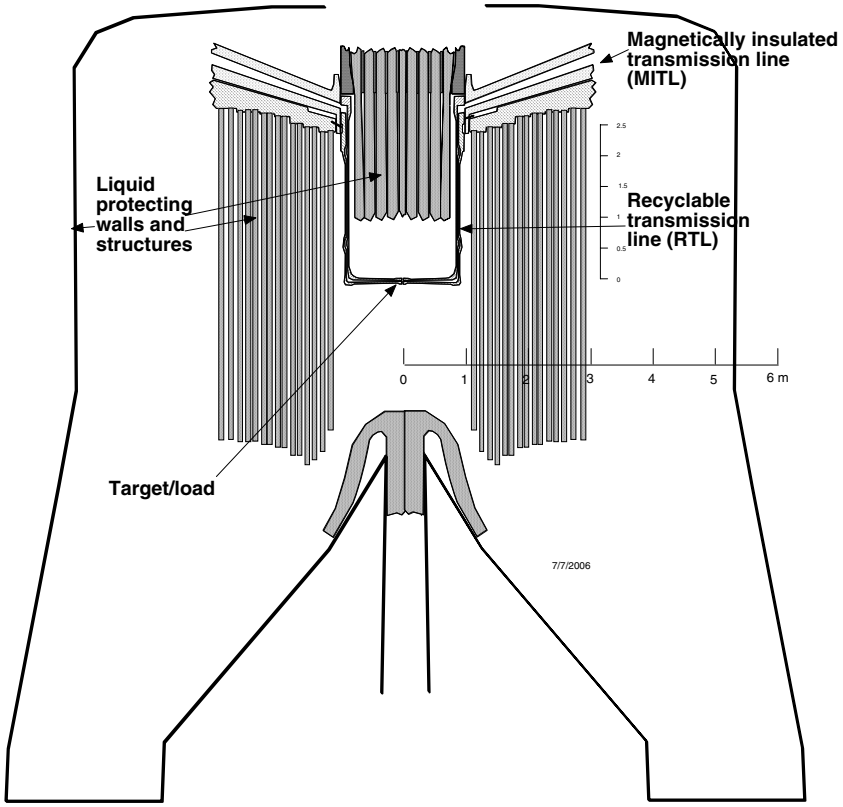

Figure 4.52: The Z-IFE chamber and 3m RTL design are shown with full neutron and blast protection of structures.

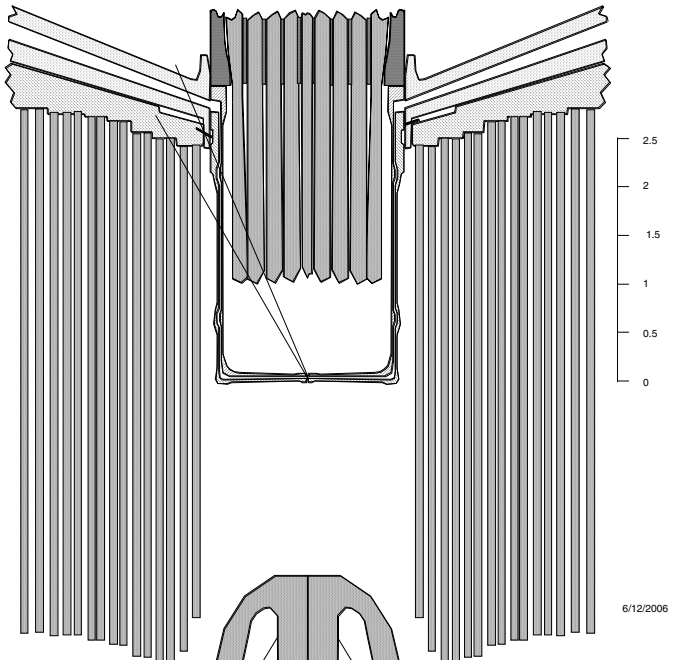

Figure 4.53: The inductance of the RTL is 15 nH out to a radius of 2 m to include some of the MITL.

4.2.1.1 Inserter Design

Figure 4.54 shows the 3-m RTL shortly before shot time with the MITL covered and the inner and outer RTL cones still separated. About 0.5 m (0.05 s) before reaching the shot position and shot time, the downward acceleration is increased from 1 g to 2 g's; which is just enough to make the inner cone close the gap to 1.5 mm at the shot position and time as shown in the next figure. The downward acceleration must be increased quickly enough so as to decisively overcome the friction that can hold the two cones together but not so rapidly as to cause the RTL to prematurely shatter. Too slow an application of force will result in jitter in the time and place of closure of the gap. The gap will be measured in realtime (possibly by radar techniques) so as to time the pulsed power system to fire when the gap is attained.

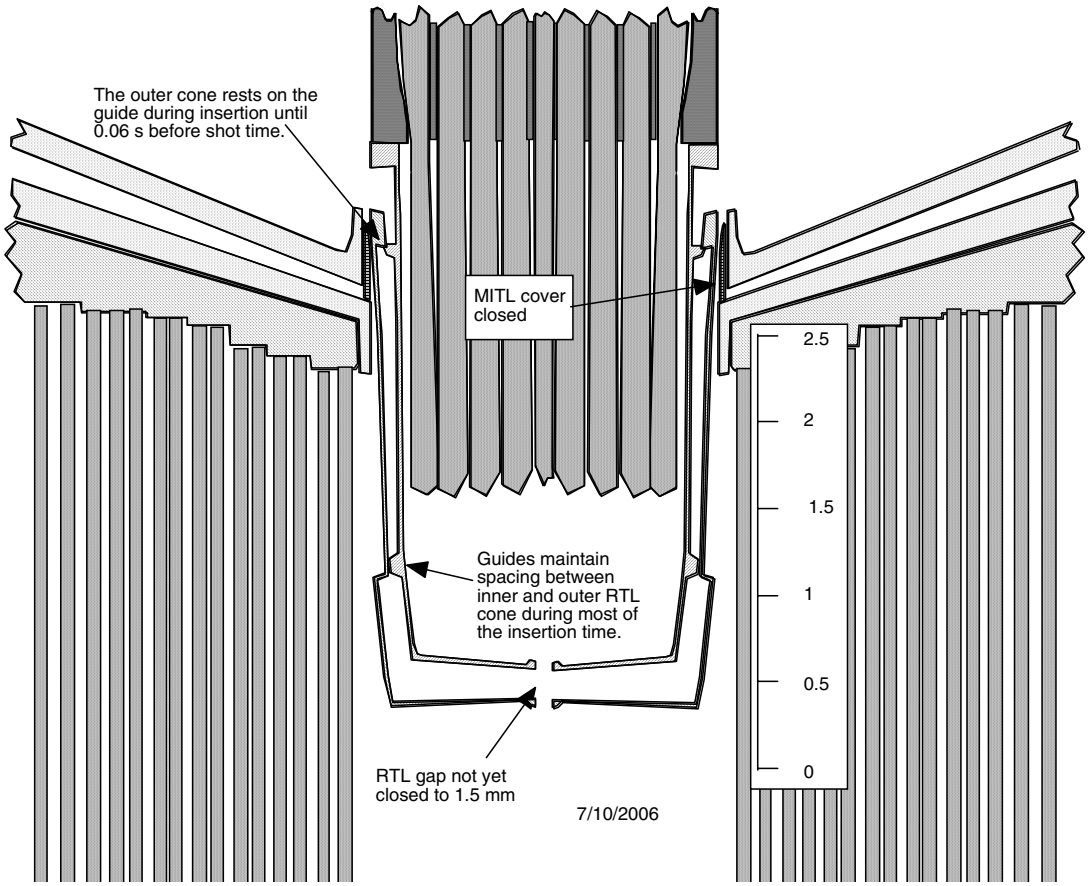

Figure 4.54: The 3m long RTL is shown shortly before shot time with its inner and outer cones still separated.

Figure 4.55 shows the RTL at shot time with the MITL uncovered. When the inner and outer RTL separation becomes 1.5 mm at the target/load, the transmission line is triggered. The RTL is traveling downward at 10 m/s and the jets at 15 m/s. The gap in the MITL and RTL varies from 15 mm at r=1 m to 1.5 mm near the target and is shown exaggerated for illustration purposes.

The pressure of the flibe vapor on the outer RTL cone would be 2 Pa at 700 °C (base case) and 5,000 Pa at 1100 °C (high efficiency design). The resulting stress in the walls of the RTL for the 1 mm thick wall case would be 6 kPa for 700 °C and 16 MPa for 1100 °C. The stress for the 700 °C case is negligible. For 1100 °C, the stress could cause failure and thicker walls would likely be needed. Thermal shock will be an important design consideration for future studies.

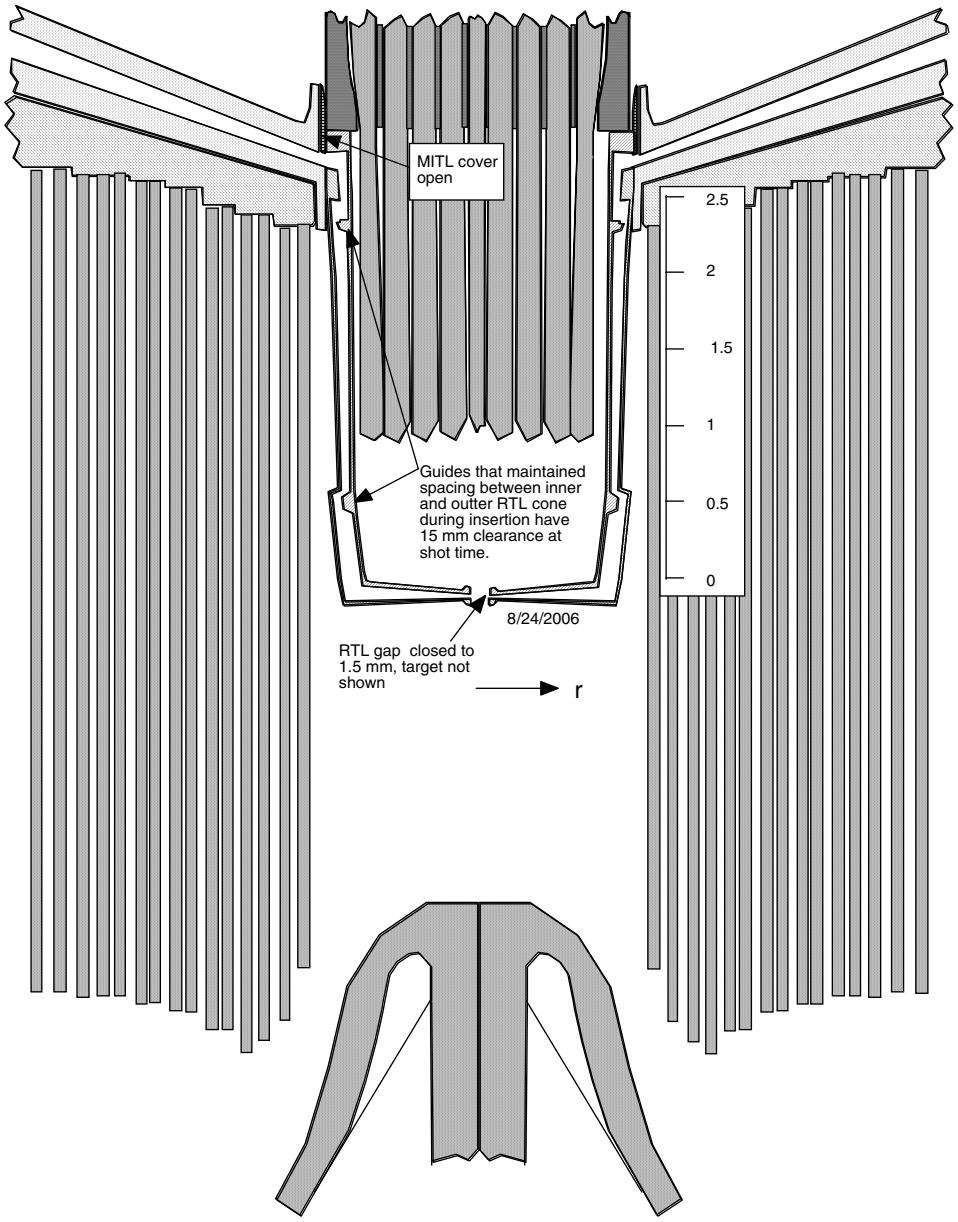

Figure 4.55: RTL at shot time with the MITL uncovered.

Figure 4.52-Figure 4.55 show a 2-m-high pulsed column of flibe above the shot. Figure 4.56 shows the design with only 1-m-high column (3 m^3) of flibe. For overcoming upward impulse due to the shot and for neutron protection, 1 m would be quite sufficient and ease injection and filling of the inserter during insertion. The fill time will be about 1 s, which gives a required fill rate of 3 m^3/s. If the flow speed in the fill pipes is kept to a reasonably low 5 m/s then the area of the fill pipes is 0.6 m^2. There would be 76 pipes of 0.1 m diameter, which would represent only a small percentage of the available area on the injection cylinder wall.

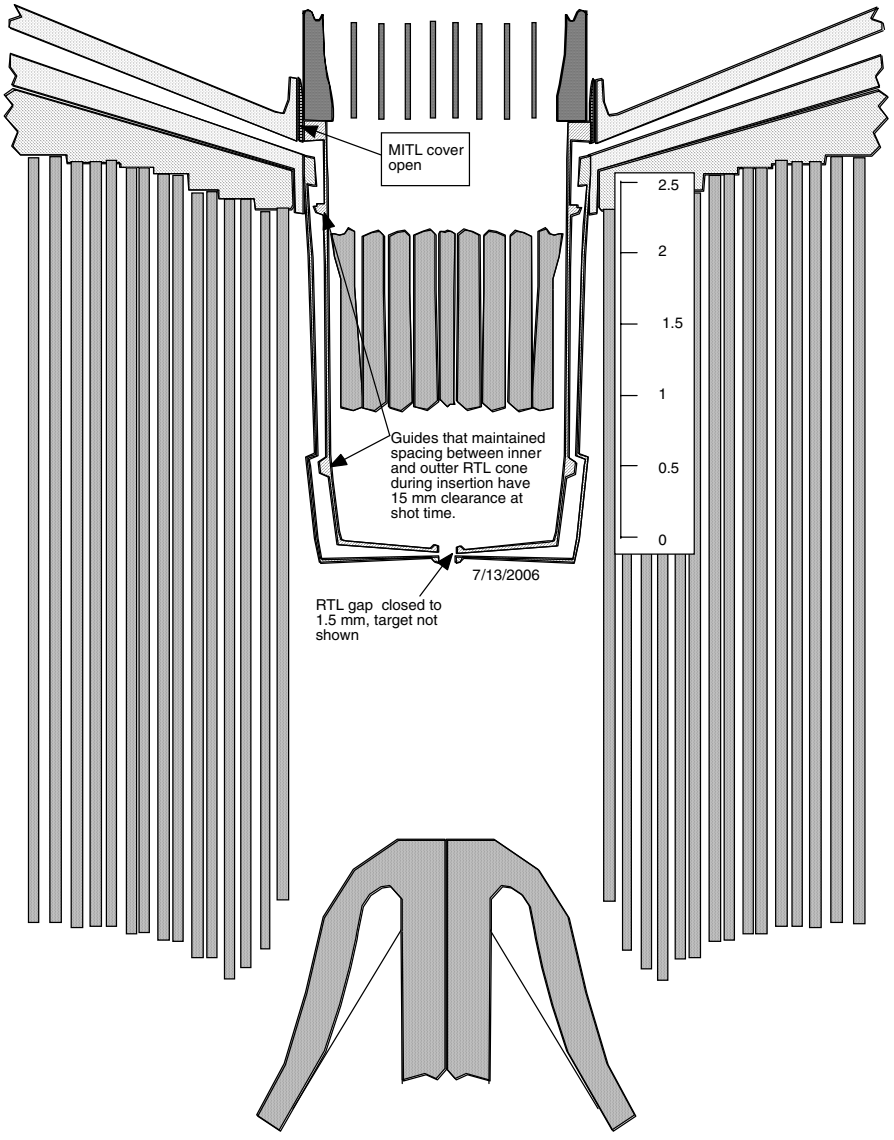

Figure 4.56: The vertical thickness of the pulsed jets above the shot point only needs to be 1m as shown here rather than the over 2m shown in prior figures.

4.2.1.2 RTL Detail

Details of the RTL are shown in Figure 4.57 and Figure 4.58. Notice the outer cone in Figure 4.57 rests on the inner cone and is centered by the inner cone. The outer cone is guided by the injection tube. The estimated mass in the two 1-mm-thick RTL cones is 90 kg plus the thicker regions of 40 kg for a total of 130 kg. A 2-mm-thick RTL set would have a mass of 220 kg.

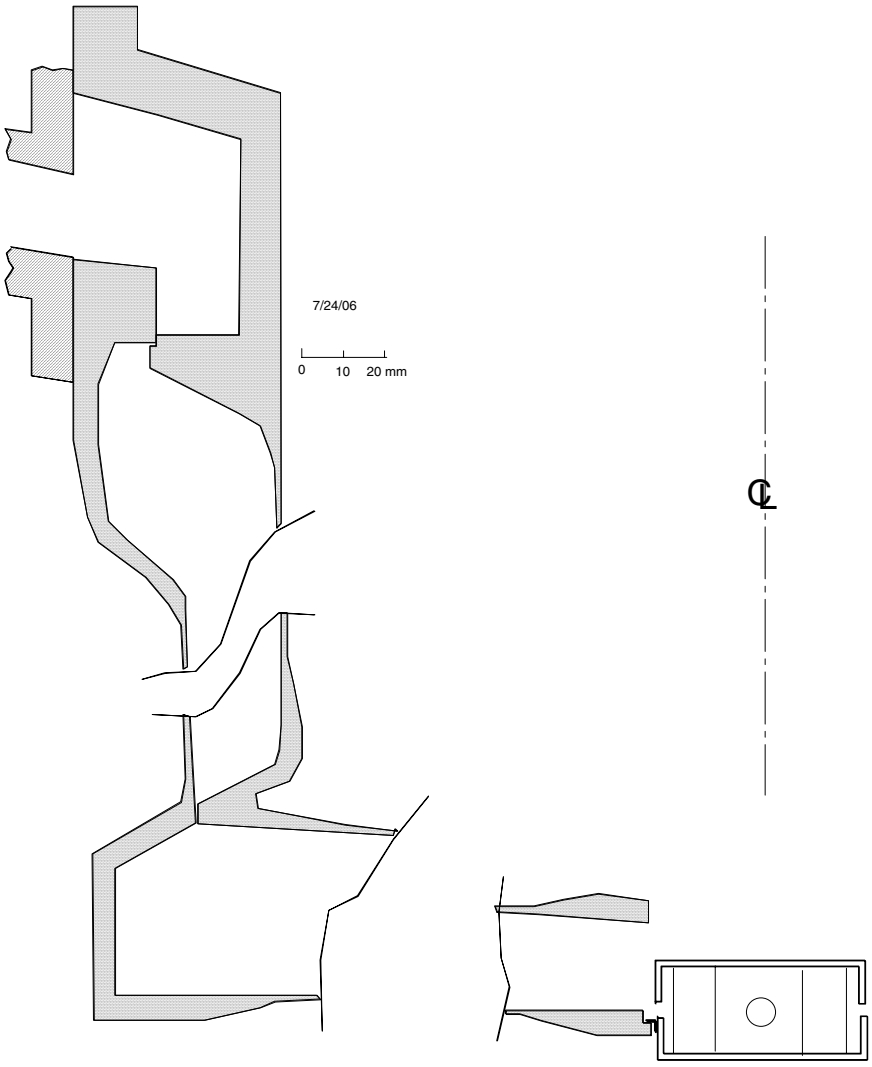

Figure 4.57: RTL before shot during insertion.

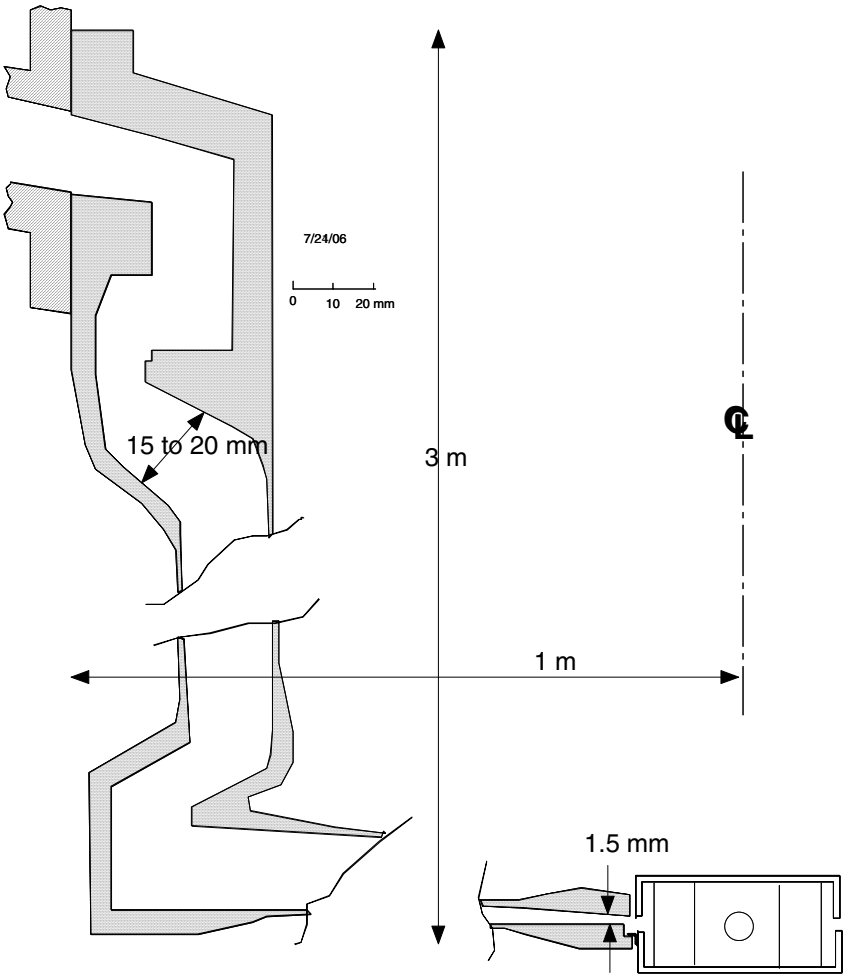

Figure 4.58: RTL at shot time.

4.2.1.3 Time-Motion Study

A time-motion analysis determines the time between shots. The following is a list of separate events that each contribute to the time elapsed between shots.

1. The RTL is translated into the breach of the injector tube and the breach cover is closed.
2. The inserter is mated to the RTL.
3. Downward motion:
   a. The inserter is accelerated downward at 1 g until a distance of about 0.53 m before the shot position.
   b. The acceleration is increased to 2 g to cause the inner RTL cone to catch up to the outer cone to within 1.5 mm at shot time.
   c. Simultaneously the cover over the MITL opening is slide upward or opened.
   d. Simultaneously the liquid is injected through a sequence of valves into the inserter cavity.
   e. Simultaneously the plunger ejects the liquid at 15 m/s (5 m/s relative to the inserter speed of ~10 m/s).
   f. The inserter is accelerated upward at 20 g but continues its downward motion until the turn around point.

4. Upward motion:
   a. The inserter is accelerated upward at 20 g to a certain point.
   b. Then the inserter is decelerated at 21 g until it comes to rest at the top.
   c. Simultaneously the breach cover is removed.
   d. Simultaneously the MITL faces are inspected by optical techniques for damage and possibly cleaned off with a broaching tool. This step might add time to the sequence.

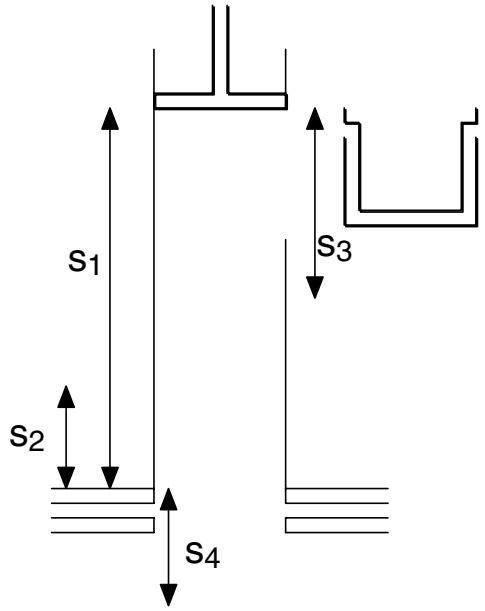

Figure 4.59: Illustration of injection sequence.

We now go into detail to estimate the time needed for each operation. Definitions are given in the Figure 4.59 above.

1. The RTL is translated into the breach of the injector tube and the breach cover is closed.

   s = distance for deceleration,
   t = time for deceleration,
   a = deceleration rate,
   v = translation speed to the breach.
   Example, s = 0.5 m, a = 1 g,

$$t = \sqrt{\frac{2s}{a}} = \sqrt{\frac{2 \times 0.5\,m}{10\,m/s^2}} = 0.32\,s \qquad 4.30$$

$$v = at = 10\,m/s^2 \times 0.32\,s = 3.2\,m/s \qquad 4.31$$

2. The inserter is mated to the RTL

Time assumed to be 0.1 s.

3. Downward motion.
   a. The inserter is accelerated downward at 1 g until a distance of about s_2= 0.6 m before the shot position. This downward motion is guided free fall. The outer cone is resting on the inner cone.

The time for the outer cone to reach the shot point is:

$$t = \sqrt{\frac{2s_1}{a}} = \sqrt{\frac{2 \times 6m}{10\,m/s^2}} = 1.1s \qquad 4.32$$

$$v = at = 10\,m/s^2 \times 1.1s = 10.1\,m/s \text{ = speed of the RTL at shot time.} \qquad 4.33$$

   b. The acceleration is increased to 2 g to cause the inner RTL cone to catch up to the outer cone to within 1.5 mm at shot time assuming a starting gap of 15 mm.

$$t = \sqrt{\frac{2s}{a}} = \sqrt{\frac{2 \times (0.015m - 0.0015m)}{2 \cdot 10m/s^2}} = 0.037s \text{ = time to close the gap.} \qquad 4.34$$

Change in speed of the inner cone relative to the outer cone.

$$\Delta v = at = 10m/s^2 \times 0.037s = 0.37m/s \qquad 4.35$$

$$s_2 \approx vt = 10.1m/s \times 0.037s = 0.37m \text{ = starting point for increased acceleration.} \qquad 4.36$$

   c. Simultaneously the cover over the MITL opening is slid upward or opened.
   d. Simultaneously the liquid is injected through a sequence of valves into the inserter cavity.
   e. Simultaneously the plunger ejects the liquid at 15 m/s (5 m/s relative to the inserter).
   f. The inserter is accelerated upward at 20 g but continues its downward motion until the turn around point.

The time to bring the inserter to 3 m from its starting position is

$$t = \frac{v + \sqrt{v^2 + 2as_2}}{a} = \frac{10.1m/s + .037m/s + \sqrt{10.62^2 + 2 \times 20 \times 10m/s^2 \times 3m}}{20 \times 10m/s^2} \qquad 4.37$$

= 0.23 s.

The time to turn-around is 0.053 s and the distance is

$$s_4 = \tfrac{1}{2} a t^2 = 0.5 \times 20 \times 10\, m/s^2 \times (0.053\, s)^2 = 0.28\, m \qquad 4.38$$

4. Upward motion.
   a. The inserter is accelerated upward at 20 g to a certain point 3 m from the starting point in 0.23 s.

The upward speed at 3 m from the starting position is

$$v = at - v_{down} = 20 \times 10\, m/s^2 \times 0.23\, s - 10.62\, m/s = 35.4\, m/s \qquad 4.39$$

   b. Then the inserter is decelerated at 21 g until it comes to rest at the top.

$$a = \frac{v^2}{2 s_3} = \frac{(35.4\, m/s)^2}{2 \times 3\, m} = 209\, m/s^2 = 21 g \qquad 4.40$$

$$t = \frac{v}{a} = \frac{35.4\, m/s}{209\, m/s^2} = 0.17 s = \text{time to bring inserter to rest.} \qquad 4.41$$

   c. Simultaneously the breach cover is removed.

   d. Simultaneously the MITL faces are inspected and possibly cleaned off.

Table 4.6: Summary of RTL cycle times.

	g force	Time, s
Load the breach	-1 sideways	0.32
Mate inserter/RTL	0	0.1
Accelerate to shot point	1 downward	1.1
Accelerate upward	20 upward	0.23
Decelerate	21 downward	0.17
Total time		1.92

The time for the various steps is tallied in Table 4.6 for a total estimated cycle time of 1.9 s. The most delicate operation occurs during loading the RTL in the breach of the inserter tube where the sideways force is 1 g. The 1 g downward motion is a force-free operation (except for the 1-2 g jerk) taking the most time. The high g force operations are without the RTL during return of the inserter to the starting point. The cycle time allows a fusion power of 3 GJ/1.9 s = 1.6 GW from one chamber.

4.2.1.4 Features of the RTL and Chamber Design

Features of the proposed RTL and chamber design are summarized here.

1. Inductance of the 3-m-long, 1-m-radius RTL transmission line is 15 nH out to 2 m radius where the gap is proportional to radius and is assumed to be 30 mm at 2 m.
2. All structures are protected by 1 m of flibe. This should result in long life structures and better economics due to reduced maintenance and downtime.
3. Guides or "bumps" in the RTL casting keep the spacing of 15 mm during insertion; gap = 0.015·r
4. The 1.5 mm gap near the target is created "on the fly" with the shot triggered when it is achieved. The inner and outer RTL cones are accelerated downward at 1 g (free fall) for 1.1 s or a distance of 5.6 m. When the RTL is 0.6 m above and 0.055 s before shot time and position the inner cone acceleration is increased to 2 g, which causes the gap to close from 15 mm to 1.5 mm at which time the transmission line is triggered.
5. The two 2-mm-thick shells making up the RTL have a mass 150 kg and assuming another 100 kg of stiffeners and electrode rings, 250 kg must be cooled from the liquid by about 400 K (heated back up by a shot) amounting to 238 MJ of lost useful yield (250 kg × 2380 J/kg·K × 400 K = 238 MJ), representing 8% yield loss. The energy conversion efficiency of the plant will be reduced by this amount. Said another way this amount of energy is not available to be converted to electricity. Clearly a lighter mass RTL cone set would be desirable. Would RTL cones of 1 mm wall thickness be practical?
6. The RTL inserter also serves as a nozzle for pulsed injection of flibe. The RTL will be moving at about 10 m/s at shot time and the liquid will be injected at about 15 m/s. The downward momentum of this liquid (60,000 Pa·s) overcomes the upward shot momentum or impulse.
7. Steady or pulsed jets protect the chamber sidewalls from neutrons and blast.
8. A mushroom jet protects the bottom of the chamber from neutrons and blast.
9. The gas in the chamber will be that of the vapor pressure of the flibe.
10. The inserter covers the 15 mm MITL opening about 1.5 ms after the shot and resurfaces or cleans the MITL electrode faces as it makes a two-way pass. The MITL cover covers the opening at all times except at shot time and a few ms afterwards. Since flibe vapor is condensable its pumping can be rapid. Very much non-condensable gas will preclude MITL operation as rapid pumping is difficult. Designs with gas fill may be unfeasible based on the inability to rapidly pump out the MITL and RTL.

The RTL shatters and is driven into downward moving liquid jets that carry them away. A worry is contamination of the interior of the MITL before closure by the inserter in 1.5 ms. Flibe vapor primarily from the transmission line current produced plasma will enter the MITL. This needs estimating.

4.2.2 First Wall Chamber Design Concept with Aerosol Mitigation

Recent x-ray mitigation models have shown the possibility of designing a chamber with a first wall. The idea of simplifying the internals of the fusion reaction chamber is beneficial. First, the flibe blanket is moved to the exterior of the reaction chamber where it is used to breed tritium and also acts as the heat transfer fluid. The reaction chamber would only contain the aerosol/gas mixture and a possible sacrificial liquid (ablation liquid) to coat the wall. Both the aerosol and ablation liquid layer could possibly be the same material as the RTL. This would simplify or

eliminate the separation issues in the internal thick liquid blanket design.. Tin and flibe have been considered as possible candidate materials for such a design. Figure 4.60 illustrates a conceptual vessel design using aerosols and a sacrificial liquid coating on the wall.

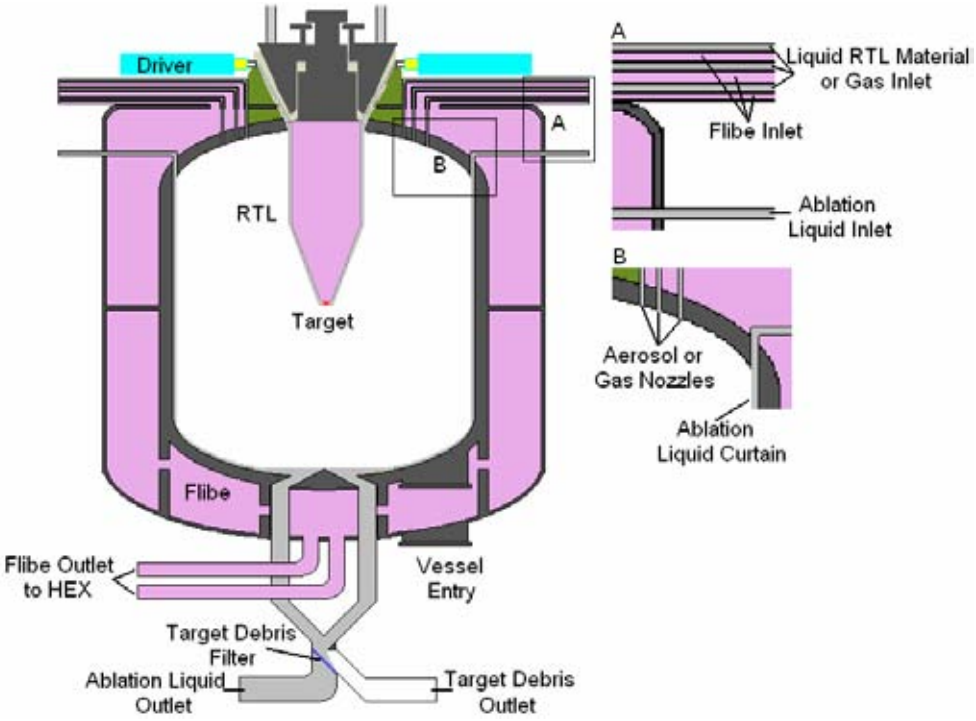

Figure 4.60: A conceptual z-pinch fusion chamber utilizing an aerosol and ablation liquid protection scheme.

The target and RTL are inserted into the middle of the chamber through a top orifice. The RTL connects to the driver and also forms a seal to contain the contents of the vessel before, during, and after the fusion reaction. If the RTL is constructed of flibe, then the inner cone is filled with flibe to protect the driver and RTL automation components from x-rays, debris, and neutrons. If the RTL is Tin, then possibly a foamed Tin can fill the inner cone of the RTL. The key idea is to keep all of the components and x-ray attenuating materials inside the chamber the same, with the exception of the target, to eliminate separation issues. A rarified gas mixed with aerosolized liquid is dispersed within the vessel through the nozzles shown in Figure 4.60 to act as the x-ray attenuating medium. A thin liquid layer (ablation liquid) coats the vessel wall and protects it from the remaining x-rays and extremely hot gas. The ablation liquid (same as RTL material) is injected into the vessel through the jets illustrated in Figure 4.60.

It may be possible to sufficiently coat the chamber walls by the aerosol jets, thus eliminating the need for additional jets for the ablation liquid. So a chamber design without the ablation jets could be conceived for the power plant. If this were the case a spherical chamber could be designed to contain the fusion reaction. Figure 4.61 illustrates a spherical chamber design concept.

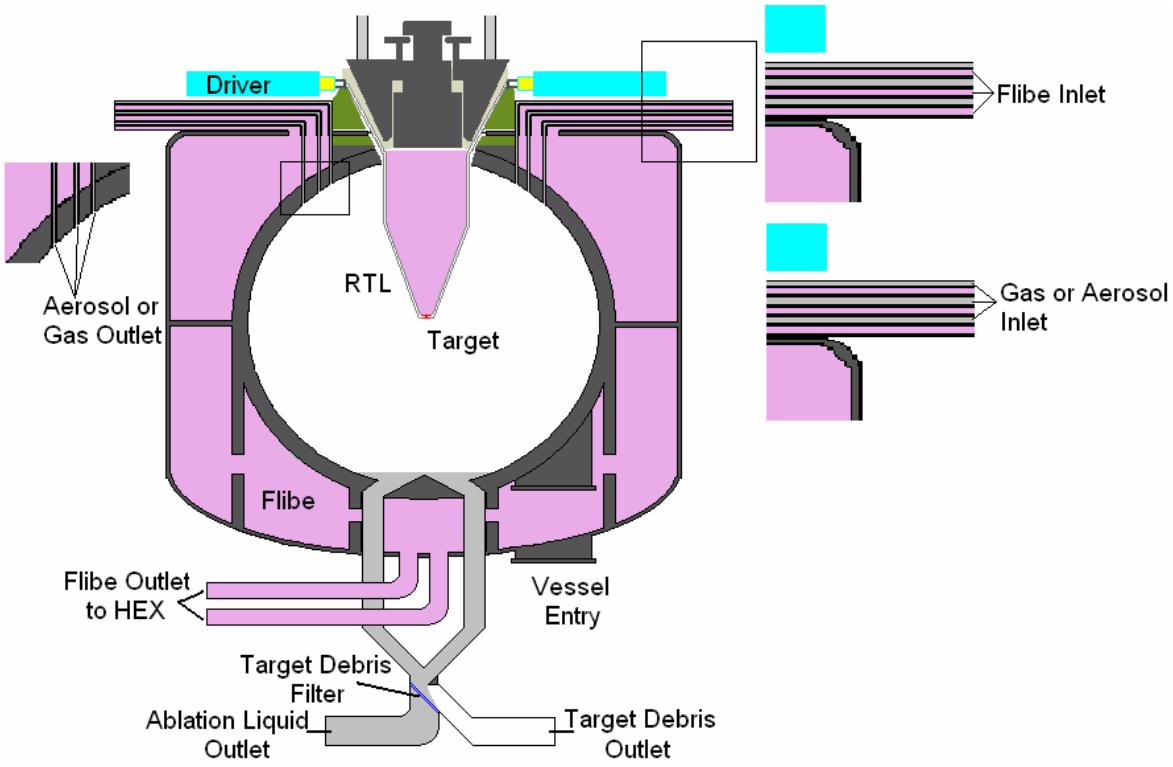

Figure 4.61: A conceptual z-pinch fusion chamber utilizing an aerosol mitigation scheme in a spherical vessel.

As shown in Figure 4.60 and Figure 4.61 the ablation liquid, aerosol, RTL, and target debris collect at the bottom of the vessel. The shrapnel from the RTL melts and mixes with the ablation liquid at which time part of it is sent to be recycled into a new RTL and the remaining material circulated back into the chamber. The target debris is filtered out from the liquid and either recycled or re-fabricated into another target. Flibe surrounds the inner chamber and acts as the tritium breeding and heat transfer working fluid. It is pumped from the top and exits through the bottom after being heated by neutron deposition.

Moving the liquid flibe to the outside of the reaction chamber may cause neutron embrittlement issues with the first wall. In addition, activation issues may also be a concern for waste disposal depending on the material chosen for the vessel. Solutions to these issues may be addressed by methods used to extend the life of LWR vessels and current fusion materials development. Neutron embrittlement may be countered by thermal annealing which is discussed briefly in section 4.2.4. Activation and waste disposal may not be as big of an issue if low activation steels are used for the chamber. The materials analyzed as possible candidates for the fusion reaction vessels for both transmutation and power plant designs are described in section 4.2.3.

4.2.3 Chamber Materials

Materials for the fusion reaction chamber were chosen on two criteria. The first was that a material maintains reasonable mechanical properties at elevated temperatures. The second was that the materials have very low elemental impurities minimizing the radioactivity of the chamber at the end-of-life of the plant. Three materials were studied based on one or both of these

criteria. The two metallic material candidates were Hastelloy and low activation F82H ferritic steel. The third material was carbon-carbon composites which was the material of choice for the thick liquid fusion chamber concept described above in section 4.2.1.

End-of-life waste analysis was performed on both Hastelloy and F82H steel chambers. ORIGEN2 was used to determine the long-lived and short-lived radionuclides that would developed over the life of the power plant in operation for 40 years. ORIGEN2 models were run under the assumption of the first wall chamber concept, meaning no neutron attenuation between the target and the chamber wall. ORIGEN2 was then used to determine the specific activity at 10000 days after the plant end-of-life or chamber discharge. The goal was to ensure that the specific activity (curies/m^3) of the chamber could be categorized as Class-C low level waste. The limits for Class C low level radioactive wastes are shown in Table 4.7 and Table 4.8 [68].

Table 4.7: Long-lived radionuclides.

Radionuclide	Concentration curies per cubic meter
C-14	8
C-14 in activated metal	80
Ni-59 in activated metal	220
Nb-94 in activated metal	0.2
Tc-99	3
I-129	0.08
Alpha emitting transuranic nuclides with half-life greater than 5 years	100 nanocuries/g
Pu-241	3,500 nanocuries/g
Cm-242	20,000 nanocuries/g

Table 4.8: Short-lived radionuclides.

Radionuclide	Concentration curies per cubic meter
Total of all nuclides with less than 5 year half-life	No limit (1)
H-3	No limit (1)
Co-60	No limit (1)
Ni-63	700
Ni-63 in activated metal	7000
Sr-90	7000
Cs-137	4600

4.2.3.1 Hastelloy

Hastelloy has good mechanical properties at elevated temperatures up to 1100 K [68]. It has a fair amount of materials characterization available in the literature because it has been considered for use in high temperature nuclear reactor designs [70]. However, it is alloyed with significant amounts of Molybdenum and Niobium which may cause a waste disposal issue at the plants end-of-life. Typical mechanical properties for Hastelloy as a function of temperature are shown below [70].

Tensile Strength (MPa) as a function of temperature (K)

$$TS = -5.0659\times10^{-6}T^3 + 9.0943\times10^{-3}T^2 - 5.2334T + 1.8537\times10^3 \qquad 4.42$$

Yield Strength (MPa) as a function of temperature (K) :

$$YS = -2.8601\times10^{-6}T^3 + 5.8034\times10^{-3}T^2 - 3.7504T + 1.2031\times10^3 \qquad 4.43$$

Elastic Modulus (GPa) as a function of temperature (K):

$$EM = 2.6541\times10^{-8}T^3 - 9.7284\times10^{-5}T^2 + 2.6188\times10^{-2}T + 2.0838\times10^2 \qquad 4.44$$

10,000 hrs Rupture Strength (MPa) as a function of temperature (K):

$$RS = 2.7870\times10^{-3}T^2 - 6.4775T + 3.7922\times10^3 \qquad 4.45$$

4.2.3.2 Hastelloy Chamber Waste and Disposal

Specific activity results from ORIGEN2 runs for a Hastelloy chamber, with an outer radius of 5.9 m and a wall thickness of 35 cm, at discharge and 10000 days later were calculated. These chamber dimensions were based on the Z-IFE baseline parameters determined in FY2005 [5]. The ORIGEN results for a Hastelloy chamber are shown in Table 4.9.

Table 4.9: The specific activity for a Hastelloy chamber at discharge and after 10000 days.

Radioactive Nuclides	Discharge	After 10000 Days	Intact Chamber (Vol.=860.3 m^3)	Compacted Chamber (Vol.=144.2 m^3)	Class C Limits
	Curies/kg	Curies/kg	Curies/m^3	Curies/m^3	Curies/m^3
H 3	4.58E-03	9.84E-04	1.43E+00	8.55E+00	no limit
C 14	4.30E-08	4.29E-08	6.24E-05	3.72E-04	8.00E+01
Co 60	1.10E+02	3.00E+00	4.37E+03	2.61E+04	no limit
Ni 59	3.22E-02	3.22E-02	4.69E+01	2.80E+02	2.20E+02
Ni 63	6.49E+00	5.28E+00	7.69E+03	4.59E+04	7.00E+03
Sr 90	4.64E-06	2.42E-06	3.52E-03	2.10E-02	7.00E+03
Nb 94	1.27E-04	1.27E-04	1.85E-01	1.10E+00	2.00E-01
Tc 99	1.60E-03	1.60E-03	2.33E+00	1.39E+01	3.00E+00

At 10,000 days (27.4 years) the intact Hastelloy chamber is below the Class C limits, except for Ni63, which it exceeds slightly. For the intact chamber to meet the limits on this nuclide, the volume would need to be about 10% larger. However, with the structural and piping supports, it is likely that the disposal volume would be 10% larger. If the chamber is dismantled and cut or disassembled into smaller sections, then it will exceed Class C limits of several isotopes.

This takes into account only the nuclides resulting from activation of the original chamber materials. Fusion, transuranic, and coolant products that contaminate the chamber walls are not taken into account and may result in the chamber being transuranic waste if it is not removed during decommissioning.

4.2.3.3 F82H Low Activation Steel

F82H (Fe-8%Cr-2%WVTa) is a low activation martensitic steel. This steel is fabricated in such away to minimize impurities that have activation issues while in operation and also for disposal. It is not produced commercially so it has not been fully thermally and mechanically characterized compared to other conventional steels, especially in the area of fatigue properties. Tavassoli et al. collected data from tests on standard specimens measuring creep and rupture strength to estimate maximum allowable stress values using internationally accepted procedures [71]. According to this study F82H steel alone maintains reasonable strength up 973K. In a study by Zinkel et al., if Y_2O_3 is added to the alloy it increases the creep rupture strength from 100 MPa to 300 MPa at a temperature of 923 K for a rupture time of 1000 hours [72]. This improvement in strength allows the material to be used for operating temperature in excess of 973 K. F82H is the leading candidate for the fusion power plant chamber because of its low-waste hazard and possibility of being used in elevated temperatures using ODS alloying. Typical mechanical properties as a function of temperature for this steel are shown below [71]. The fatigue properties are illustrated in detail in section 4.2.5.

Tensile Strength (MPa) as a function of temperature (K):

$$TS = 6.2357\times10^{-9}T^4 - 1.1166\times10^{-5}T^3 + 5.472\times10^{-3}T^2 - 1.1617T + 628.8 \quad 4.46$$

Yield Strength (MPa) as a function of temperature (K):

$$YS = -3.5596\times10^{-9}T^4 + 2.2141\times10^{-6}T^3 - 3.603\times10^{-4}T^2 - 1.8491\times10^{-1}T + 544.2 \quad 4.47$$

Elastic Modulus (GPa) as a function of temperature (K):

$$EM = 233 - 0.0558T \quad 4.48$$

4.2.3.4 F82H Steel Chamber Waste and Disposal

Specific activity results from ORIGEN2 runs for a F82H steel chamber, with an outer radius of 5.9 m and a wall thickness of 35 cm, at discharge and 10000 days later were calculated. These chamber dimensions were based on the Z-IFE baseline parameters determined in FY2005 [5]. The ORIGEN results for a F82H chamber are shown in Table 4.10.

Table 4.10: The specific activity for a F82H steel chamber at discharge and after 10000 days.

Radioactive Nuclides	Discharge	After 10000 Days	Intact Chamber (Vol.=860.3 m^3)	Compacted Chamber (Vol.=144.2 m^3)	Class C Limits
	Curies/kg	Curies/kg	Curies/m^3	Curies/m^3	Curies/m^3
H 3	5.27E-03	1.23E-03	1.62E+00	9.66E+00	no limit
C 14	5.38E-08	5.36E-08	7.05E-05	4.21E-04	8.00E+01
Co 60	1.97E-01	5.36E-03	7.06E+00	4.21E+01	no limit
Ni 59	2.26E-07	2.26E-07	2.98E-04	1.77E-03	2.20E+02
Ni 63	7.46E-05	6.07E-05	7.99E-02	4.76E-01	7.00E+03
Sr 90	3.65E-10	1.90E-10	5.50E-07	1.49E-06	7.00E+03
Nb 94	2.20E-05	2.19E-05	2.89E-02	1.72E-01	2.00E-01
Tc 99	2.05E-08	2.05E-08	2.69E-05	1.61E-04	3.00E+00

For all times evaluated from discharge after a 40 year life, to 10,000 days later, the activity of the selected nuclides are less than the limits for Class C low-level waste. This is true for both the intact chamber volume and the compact chamber volume.

4.2.3.5 Carbon-Carbon Composites

PAN (polyacrylonitrile) based fibers constitute the largest segment of the carbon fiber industry [73]. They have a high tensile strength over a large range of temperatures. Carbon fibers are joined together in various orientations in a matrix material, which is also carbon based. The carbon-based matrix does have an impact on the mechanical properties of the composite by affecting its modulus of elasticity, stress-strain behavior, bond strengths between fibers and matrix, and strength in tension [74].

The mechanical properties of carbon-carbon composites are highly dependant on the orientation of the fibers. The fibers can range from one to four dimensional geometries. The mechanical properties shown below are based on a two-dimensional arrangement of fibers. This orientation was chosen for two reasons. First, the mechanical properties for a two dimensional carbon-carbon composite were readily available. Second, internal loading applies tensional stress perpendicular to the pressure force in the chamber, which two fiber orientations should be able to address. A third fiber orientated parallel to the pressure force will probably be needed in order to handle external induced stresses in the chamber caused by the between shot vacuum condition. The external loading induced stresses are not considered for carbon-carbon composites

The major contributions to cost of carbon-carbon composites are how they are processed and cured. Depending on the application, curing temperatures can exceed 1273 K requiring use of special equipment [73]. The fatigue properties of C-C composites still need to be assessed extensively for both irradiated and normal type environments. Typical properties for PAN based C-C composites are shown below. The tensile strength increases with temperature in contrast to metal materials.

Tensile Strength (MPa) as a function of temperature (K):

$$TS = 0.0261T + 302.47 \quad (4.49)$$

Elastic Modulus (GPa) as a function of temperature (K):

$$EM = -0.0278T + 118.29 \quad (4.50)$$

4.2.4 Thermal Annealing

Thermal annealing of LWR pressure vessels to extend their operational life has been demonstrated in Europe, Russia, and the United States [41, 75, 76]. The Nuclear Regular Commission has approved an annealing process for LWR pressure vessels following the guidelines set forth by the ASME Boiler and Pressure Vessel Code [77]. The main areas of concern for LWR pressure vessels are in the weld joints in particular the beltline region. It is subject to the most intense neutron flux. The weld areas on the Z-IFE vessel will probably be the greatest concern as well.

Thermal annealing has shown to be effective in completely recovering the upper shelf energy (USE) and yield strength while partially recovering the ductile-brittle transition temperature (DBTT) of WWER-400 and WWER-1000 steels [41]. WWER-1000 and WWER-400 steels are commonly used in Russian reactor vessels. The only partial recovering of the DBTT seems to be dependant on the amount of nickel in the material [41]. Nickel, which is common alloy in weld materials, seems to both effect the extent of radiation damage and recovery of the DBTT. The time and extent of healing was greatly dependant on the annealing temperature. As the annealing temperature increased the recovery of the materials' properties increased. Annealing temperatures ranging from 420ºC to 490ºC have been investigated [41}. Thermal annealing may be useful for the Z-IFE chamber.

Candidate fusion materials have shown to be irradiation resistant at elevated temperatures. Several irradiation tests have been conducted on F82H steel and yielded similar results. Experiments showed that the yield strength of the steel under normal and irradiation conditions did not change significantly at higher temperatures. Figure 4.62 shows the yield strength of F82H steel for both normal and irradiated results as a function of temperature [72].

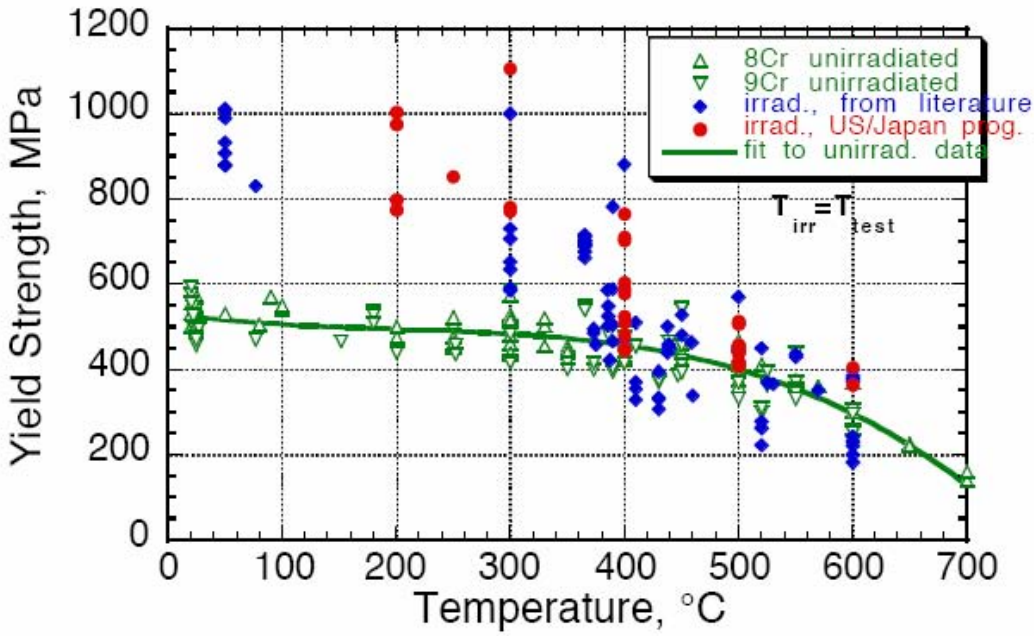

Figure 4.62: Shows a comparison between unirradiated and irradiated F82H steel versus temperature.

The green line represents the best fit curve for the unirradiated steel. At lower temperatures (0ºC- 400ºC) a significant increase in yield strength is observed for irradiated steel. As the temperature is increased above 400ºC the change in yield strength is less thus indicating thermal annealing effects.

Further studies of various fusion materials were conducted on USE and DBTT. These parameters did not show a significant change at high irradiation temperatures. If the vessel is to operate in the material's annealing range the irradiation damage effects seem to be minimal and may not pose a serious threat. Figure 4.63 shows irradiation induced shifts in the USE and DBTT versus irradiation temperature of various materials [78].

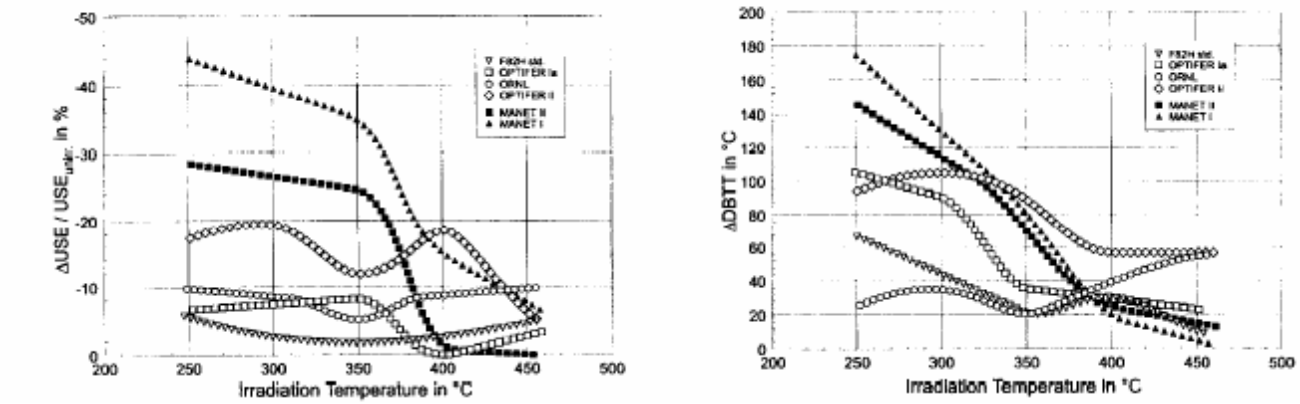

Figure 4.63: Irradiation induced shifts for upper shelf energy (left) and ductile brittle transition temperature (right) verse irradiation temperature.

Once again, as the temperature increases the difference in USE and DBTT between unirradiated and irradiated steel is insignificant. Since the Z-IFE chamber will be operating at or above the effective annealing temperature of these steels it may be possible to minimize or eliminate the effects of irradiation damage.

4.2.5 Fatigue Analysis of F82H Steel

Fatigue is a crucial design parameter for both the transmuter and power plant designs. Both vessels will be subject to cyclical loading on the order of 0.1 Hz. Effects such as irradiation damage and dynamic loading can greatly reduce the lifetime of the chamber wall. This is a first-order analysis of the expected lifetime of the inner-liner of an operating fusion reactor. The analysis uses only readily available data for F82H from the open literature. The results of the analysis are highly dependent upon the assumed sustained operating temperature of the reactor, specifically the temperature of the inner wall, and the stresses imparted to the F82H lining during operation of the reactor.

4.2.5.1 Selection of F82H Steel for the Vessel Wall

F82H is a ferritic/martensitic reduced activation steel which comprises of between 8-12wt% Cr and has been alloyed with low activation elements. Ferritic steels have also shown lower irradiation induced swelling compared to standard fission reactor stainless steel liners [79]. F82H is one of the leading candidates for fusion power systems and so a fairly large mechanical and thermal material property database exists.

The mechanical properties of F82H have shown to exhibit embrittlement in irradiation environments. However, increasing amounts of data are becoming available to account for irradiation damage. Another important area where data is becoming more readily available is in the area of welds. Irradiation damage has generally been more of a concern on the welds of fission reactor chambers, consequently, welding of the F82H steel which has not be studied in-depth must be analyzed further. Creep is another potentially harmful mechanism if the fusion system operates at temperatures above 550°C (823°K) [80]. Thus, the chamber must be designed to operate at a lower temperature where creep is not as significant.

Some of the key properties of F82H steel that are not well understood are fracture properties in radiation environments. Also, helium induced swelling of the liner material and its effects on the fracture properties. High cycle fatigue data still needs to be assessed for IFE based systems.

4.2.5.2 Vessel Dimensions and Operating Conditions

It is assumed that the reactor is a sphere with a radius of five meters. The inner lining of this sphere is composed of F82H steel. The surface area of the inner lining is 314.16 m^2 ($A = 4\pi r^2$) or 3.1416×10^6 cm^2. The lining is subjected to an irradiation pulse every ten seconds which imparts 1×10^{21} neutrons to it. So the average flux on the inner lining is:

1×10^{21} neutrons/pulse = 1×10^{21} n/10 seconds = 1×10^{20} n/s

And, the flux density is:

$(1x10^{20}n/s) / (3.1416\ cm^2) = 3.185x10^{13}$ n/s-cm2

The fluence to which the lining would be subjected is expressed in units of neutrons/cm^2. So, for example, in one hour (3600 seconds; 360 pulses) of continuous operation, the inner lining of the reactor would have a fluence of: $3.185x10^{13}$ n/s-cm^2 X $3.6x10^3$ seconds = $1.15x10^{17}$ n/cm2,

and, in one day, $2.75x10^{18}$ n/cm2,
in thirty days (one month), $8.25x10^{19}$ n/cm2,
and, in 365 days (one year), $1.00x10^{21}$ n/cm2 (= 1 dpa)

The containment vessel of a fission power reactor may experience neutron fluences on the order of 10^{19} n/cm^2 in forty years of operation. Much of the literature on the irradiated properties of F82H uses units of "dpa", displacements per atom, to quantify fluence. The conversion of fast neutrons/cm^2 to dpa is material dependent, but for F82H it is approximately10^{21} n/cm2 equals 1 dpa [80, 81, 82, 83]. The properties of the F82H steel are, of course affected by the total damage to the material (the total fluence). The time to impart a dpa of 1, 10, or 100 is 1, 10, or 100 years for the scenario analyzed.

4.2.5.3 Inner-Wall Operating Temperature

The operating temperature of the reactor, specifically the inner lining, has yet to be fixed, but may range from 600K – 900K (327ºC – 627ºC). This is an important consideration because the temperature of the F82H affects its properties and the degree to which irradiation further affects the properties. At certain elevated temperatures irradiation damage, which affects, e.g., strength and fatigue endurance, is partially or nearly completely annealed from the material. And, above a certain temperature creep affects severely affect the useful life of F82H steel.

There have been numerous studies of the creep and stress-rupture behavior of unirradiated and irradiated 8-9%Cr steels at temperatures up to 923K (650°C [0.5 T_M]) [84]. Good creep resistance exists for temperatures up to ~823K (550°C [0.45 T_M]), but poor creep resistance occurs at 873K (600°C) and above. For example, the 10,000 h creep rupture strength of F82H is 200 MPa at 823K, 120 MPa at 873K and 50 MPa at 923K. Improvements in the thermal creep resistance of reduced-activation ferritic steels can be achieved with oxide dispersion strengthened alloys.

This suggests maintaining a temperature on the inner wall of the reactor to below 823K (550ºC) to avoid the affects of creep:

Tcreep > 823K (>550ºC), Tinner-wall < 823K (<550ºC)

4.2.5.4 Irradiation Damage

At ambient temperatures irradiation damage affects the mechanical properties of F82H steel. Irradiation damage also occurs at elevated temperatures up to a certain temperature where the temperature effectively anneals out the damage (at least below some threshold of fluence or dpa). One measure of irradiation damage is an increase in yield strength of the material, or a decrease in elongation (ductility). And the temperatures at which irradiation occurs for which there is no

increase in yield strength are those for which thermal annealing mitigates the irradiation damage. Several references provide data that suggests that at irradiation temperatures of 623K – perhaps 750K (350ºC – 477ºC) the properties of the F82H are not significantly affected by the irradiation hardening at least up to ten dpa or higher [85, 86, 87, 88, 89].

Using the midrange of the temperatures for which thermal annealing seems effective, say, 673K – 723K (400ºC – 450ºC), the detrimental affects of irradiation hardening (and creep [T_{creep} > 823K (>550ºC)]) may be negligible:

Tirr. damage < 673K (<400ºC), Tinner-wall > 673K (>400ºC)

Thus, a suggested temperature range for operation of the reactor to avoid both irradiation damage effects and creep is:

823K > Tinner-wall > 673K 550ºC > Tinner-wall > 400ºC

4.2.5.5 Applied Stresses

The maximum design stress to which the inner lining may be subjected is assumed to be ¼ the ultimate tensile strength (¼UTS) of unirradiated and ambient temperature F82H. Data from typical references suggest a UTS of approximately 663.3 MPa (96.3 ksi) at approximately 293K (20C) [71, 85, 86, 87, 88, 89]. So, the maximum stress, σ_{max}, assumed for the inner wall of the lining is 663.3/4 = 165.8 MPa (24.1 ksi). (This stress shall be used for the analysis despite the fact that the UTS of F82H steel at an elevated temperature or in an irradiated condition will be less than that at ambient temperatures.) Young's modulus for F82H steel is approximately 217 GPa (31E6 psi) at a temperature of 293 K (20C) [90].

4.2.5.6 Fatigue as the Failure Mode

The assumed failure mode for the inner liner is fatigue failure. The applied stresses, ¼UTS, are below the stress required to plastically deform the material. Assuming no significant flaws in the lining, the fracture toughness should be adequate to preclude crack growth from an existing flaw. However, the lining is subjected to tensile stresses every pulse (ten seconds) and this cyclic loading of the material could induce fatigue and ultimately failure (large crack) of the liner.

Each stress impulse imparts strain to the lining. The magnitude of this strain can be used to estimate the number of cycles the lining can withstand before there may be a fatigue failure. The strain on the lining is estimated to be:

Maximum strain per irradiation pulse = ε_{max}
= maximum stress / Young's modulus = ¼UTS / Young's modulus
= 165.8 MPa / 217E3 MPa
= 0.00076 (cm/cm), or 0.076%

This strain per cycle is actually relatively low. The total strain is twice that value since the stress is reversed after the irradiation pulse. So, the total strain per cycle is:

εtotal = 0.0015 (cm/cm) = 0.15%

There is little fatigue data available for F82H steel either in the unirradiated or irradiated condition. However, total strain versus number of fatigue cycles to rupture is available in the literature. If the reactor operates in a temperature regime where thermal annealing is effective, the fatigue data for unirradiated F82H may be used. For a total strain of 0.15%, the 450ºC and 500ºC data indicate that the number of cycles to rupture may be as few as approximately 500000 cycles. Those same data indicate that to operate the reactor for five years (which translates to 15778800 irradiation pulses), the total strain should not exceed 0.05%. This would require that the maximum stress on the lining per pulse be reduced by a factor of three [71].

The Hirose et al. reference is less useful because the data are for fewer than 10000 cycles [75]. It does indicate that F82H irradiated at 363K (90ºC) can withstand fewer cycles to failure than unirradiated material when tested at 293K (20ºC). For example, at 1% total strain, F82H can with stand 4575 cycles before failure, but in the irradiated condition (0.02 dpa) only 2364 cycles. Linear extrapolation of the available Hirose data for a total strain of 0.15% suggests that the F82H lining can withstand perhaps more than 25000 cycles before failure if operating at a temperature where irradiation hardening is not a significant factor. The number of cycles may be many more than that depending on the trend of the fatigue curve at low strain / high cycle conditions [75].

The Tavassoli et al. data are plotted in Figure 4.64, below [71]. Endurance limit strain data plotted in Figure 4.64 appears to fit a log-log relationship.

$$\ln \varepsilon = \ln A + m \ln N \qquad 4.51$$

Or

$$\varepsilon = A \cdot N^m \qquad 4.52$$

A linear regression analysis of the data using Equation $\ln \varepsilon = \ln A + m \ln N$ 4.51 returns A = 5.472 and m = -0.237. The standard error of the estimate, s_{ey}, for this regression is 0.181. The dashed lines in Figure 4.64 denote bounds $3s_{ey}$ on each side of the regression. The lower bound represents a factor of safety of 1.72.

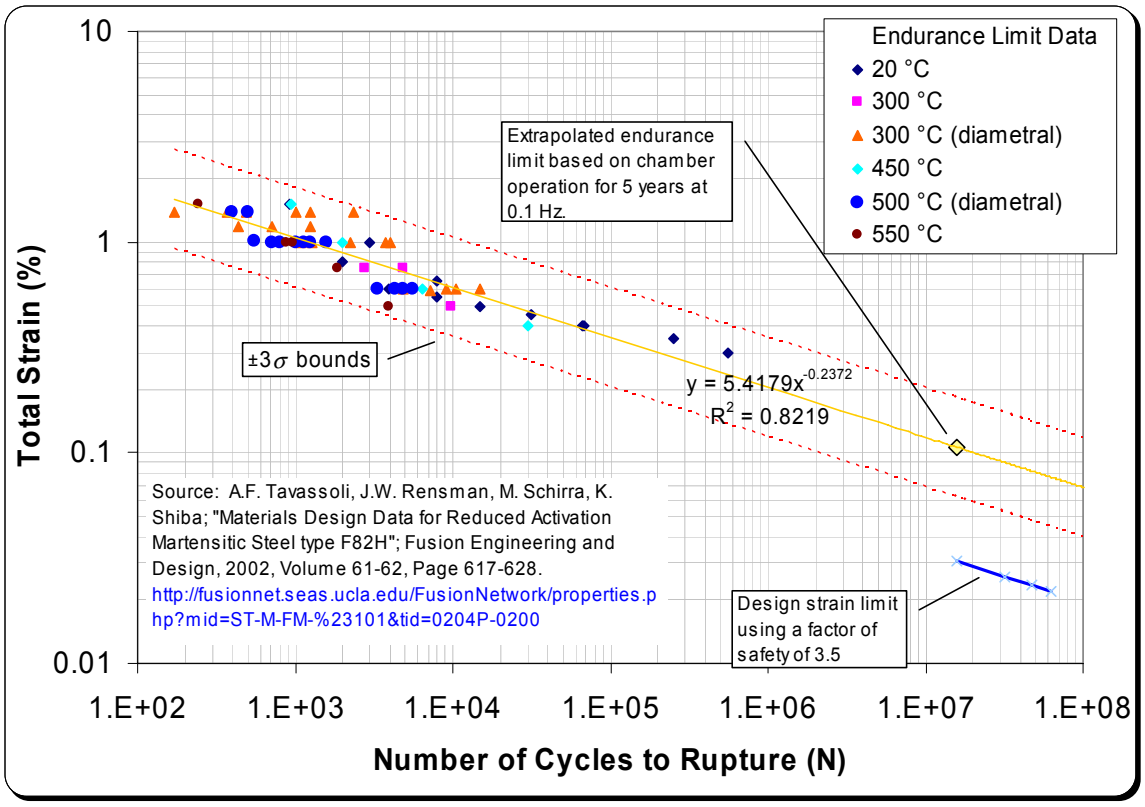

Figure 4.64: F82H endurance limit design parameters based on five year life

This factor of safety was judged inadequate based primarily on the degree of extrapolation necessary to reach the projected life for fusion equipment, in particular the chamber. A factor of safety of 3.5 is qualitatively more acceptable.

Based on this, the maximum allowable stress based on endurance limit (cycles to failure) and accounting for a safety factor on the strain (hence, stress) may be estimated for F82H from the following equation

$$s = \frac{AEN^m}{F_s}. \qquad 4.53$$

As discussed above, Young's modulus, E, for F82H is 217×10^9 Pa (217×10^4 bar). Using a factor of safety, F_s, this yields the equation

$$s = 1.18E07N^{-0.232} \text{ bar} \qquad 4.54$$

Figure 4.65 plots this equation based upon a loading frequency of 0.1 Hz.

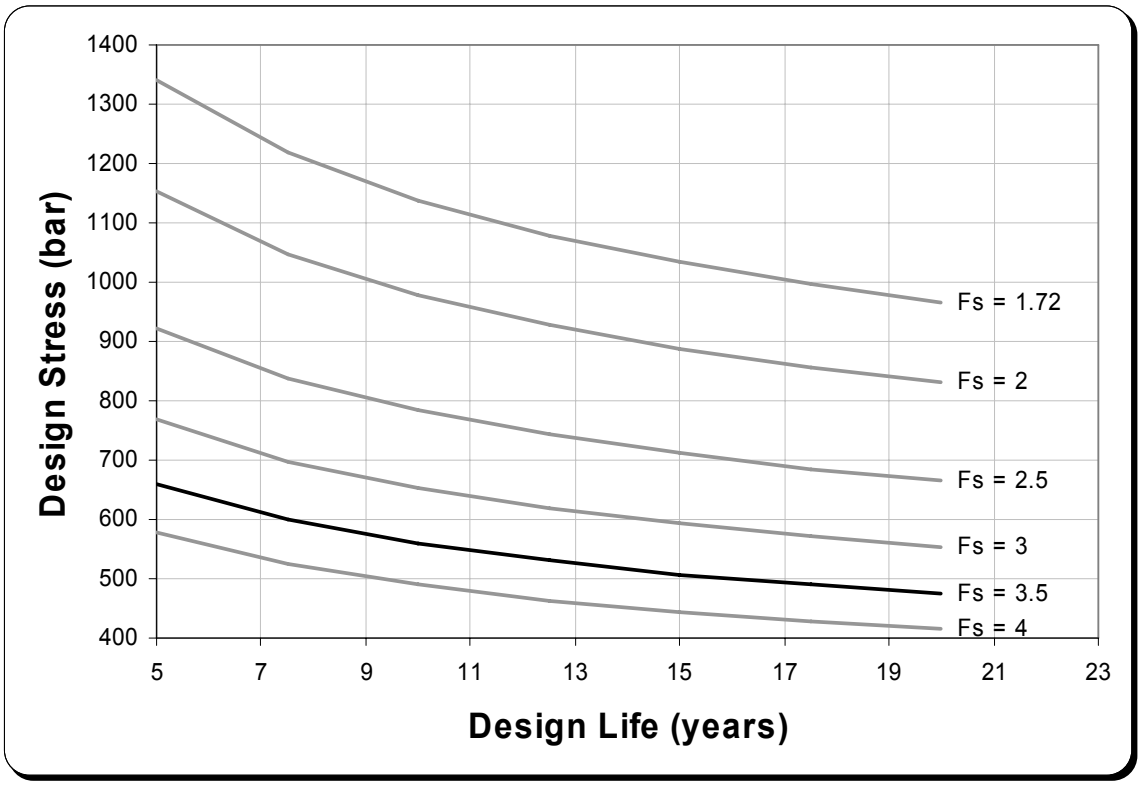

Figure 4.65: Maximum design stress versus design life based upon fatigue cycles to failure.

For a design life of, say, ten years, the F82H steel lining could tolerate a stress of approximately 560 bar (≅ 56MPa ≅ 8 ksi ≅ 0.08UTS) with a safety factor of 3.5 on the number of fatigue cycles to failure. Lesser factors of safety, or fewer years of design life, allow the applied stress to the F82H steel lining to be increased.

5. CONCLUSION

In the six months given to work on the Z-Inertial Fusion Energy (Z-IFE) late start LDRD, an effort was made to create a logical path to reach the ultimate goal of a fusion power plant. To illustrate this path forward a roadmap was created outlining the current issues, needed steps, and time required to reach these goals.

The purpose of the roadmap is an attempt to gain an understanding on what it would take to develop Z-IFE fusion energy. It begins with utilizing existing facilities capable of handling various separate effects experiments. These facilities include Sandia National Laboratories' Z-beamlet and ZR where several containment and mitigation experiments can be conducted. The next step is to build an engineering test facility (ZN) where automation, RTL, target fabrication, and driver development can take place and eventually be integrated together. With the inception of the Global Nuclear Energy Partnership (GNEP) initiative and the goal of a closed fuel cycle, an alternative use for z-pinch driven fusion arises. Work conducted through the Advanced Fusion Concepts: Neutrons for Testing and Energy Grand Challenge LDRD has shown that fusion neutrons can transmute the actinides in spent fuel. The ZN facility will also be the test bed for developing Z-IFE fusion transmutation. Once these concepts are integrated, ZN becomes a pilot plant which will be the final stage before the full scale transmutation and power plants are built.

Z-IFE progress this year is an extension of the work competed for the Advanced Fusion Concepts Grand Challenge LDRD, with a focus on the full scale transmutation and power plants [1]. The grand challenge LDRD concentrated on developing the early steps in the roadmap involving containment experiments on ZR.

Substantial progress was made in the areas of shock mitigation, chamber design, RTL development, Flibe chemistry, and systems cost models for both the transmutation and power plants.

- The transmutation work focused on designing a chamber capable of utilizing the high energy neutrons from a z-pinch reaction to burn actinides. The key advantages to transmuting actinides with this design are: a safer design compared to faster reactors, no additional actinides are created since no fertile material such as uranium is required, and provides valuable operating experience that will be needed for the full scale power plant. A separate report, "Fusion Transmutation of Waste: Design and Analysis of the In-Zinerator Concept," describes this work in more detail[5]
- A systems cost model was created to optimize the number of chambers, the target yield, and shot rate needed for a fusion power plant. The results indicated that less chambers at a higher repetitive rate and yield are more economical than the original Z-IFE power plant design of ten chambers.
- A detailed cost analysis of the linear transformer driver (LTD), the device that supplies the power to the fusion target, was conducted for the power plant facility. The results indicated that it will be a significant percentage of the total cost of the plant.
- Various studies between the chemical interaction between a flibe like salt and a steel RTL post shot were conducted. This was to gain an understanding of how the free ions of the dissociated salt and steel interact. Further experimentation on the electrical properties of a frozen flibe RTL was conducted to understand its effectiveness of transmitting the pulse to the target.
- An analysis on four power conversion systems was conducted; supercritical CO_2 cycle, Rankine cycle, Brayton cycle, and a combined cycle. Assuming that high temperature materials are available in the future, the analysis shows that the combined cycle is best for both transmutation and power plants.

- A tritium permeation study of the piping and chamber was addressed this year. It was compared to the analysis conducted for the International Thermonuclear Experimental Reactor (ITER). The results showed that using a permeation barrier coating on the pipes along with optimizing partial pressure and diameter could reduce tritium leakage significantly.
- A new higher repetitively rated thick liquid curtain chamber design was proposed based on the results from the systems cost analysis. This proposed chamber design requires a slightly larger target yield and over fives times the repetitive rate of the original Z-IFE design.
- Modeling results of aerosols absorbing x-rays show promise that they may be able to mitigate fusion yields up to 3 GJ. Based on these results a new first wall chamber design was conceived that may significantly reduce the complications associated with the thick liquid curtain designs.

The research this year is leading towards an experimental program to address issues such as x-ray mitigation and containment, rapid vacuum development, driver testing, RTL optimization, target development, and automation. Sandia has the state-of-the-art facilities and the full spectrum of technical capability to provide the necessary elements for a strategic initiative. The ZR-machine provides an ample facility for conducting the necessary physics and engineering experiments required for increasing fusion yield, demonstrating fusion containment, and target development. Sandia has a talented robotics group which can aid in designing the automation required for maneuvering the RTLs in and out of the containment chamber. Sandia has experts in materials which will be valuable in several aspects of this work. Material development for the vessel, RTL, and power plant will be essential to ensure safe operating conditions. Sandia has extensive programs that support energy research and development ranging from solar and wind to nuclear power. There are also several years of research completed through the Z-IFE program on using z-pinch IFE to create commercial power. Recently the focus of Z-IFE has shifted to include using z-pinch fusion for transmutation, tying Z-IFE directly into the GNEP initiative and its focus on a closed nuclear fuel cycle. Sandia National Laboratories leads the way in developing z-pinch driven IFE energy for both power production and transmutation.

6. REFERENCES

1 Executive Summary

2 Z-Inertial Fusion Energy Roadmap

1. Morrow, C. et al., "Roadmaps and Containment Concepts for Early Z-Pinch Fusion Applications," Sandia National Laboratories, To be published SAND report, SAND#### (2006).
2. Olson, C., Personal Conversation, (October 2006).
3. Vesey, R., Slutz, S., & Mattsson, T., Personal Conversation, (June 2006).
4. "The Global Nuclear Energy Partnership: Greater Energy Security in a Safer, Cleaner World," Power Point Presentation: Department of Energy, USA, February 2006.
5. Cipiti, B. et al., "Fusion Transmutation of Waste: Design and Analysis of the In-Zinerator Concept," Sandia National Laboratories, To be published SAND report, SAND#### (2006).

3 Z-IFE Power Plant Systems Analysis

6. Meier, W.R., & Moir, R.W., "Analysis in Support of Z-Pinch IFE and Actinide Transmutation- LLNL Progress Report for FY-06," Lawrence Livermore National Laboratories, UCRL-TR-224558, (2006).
7. Olson, C., "Target Physics Scaling for Z-Pinch Inertial Fusion Energy, "Fusion Science and Technology, 47 1147-1151 (2005).
8. Vessy, R., "Multi-GJ Indriect-Drive Targets for Z-IFE Using the Double Ended Hohlraum, "Z-IFE Workshop, SNL (Aug. 2005).
9. Melhourn, T., "Overview of Targets for IFE," Z-IFE Workshop, SNL (Aug. 2005).
10. Meier, W.R. et al., "OSIRIS and SOMBRERO Inertial Fusion Power Plant Designs, "WJSA report WJSA-92-01, DOE/ER/541000-1 (March 1992).
11. Meier, W.R., Bieri, R.L., "Economic Modeling and Parametric Studies for Osiris- AN HIF-Driven IFE Power Plant," Fusion Technology, 121, 1547 (1992).
12. Moir, R.W. et al., "HYLIFE-II progress report" LLNL Report UCID-211816 (1991).
13. Rochau, G., "Power Plant Utilizing Z-Pinch Fusion Technology," Z-IFE Workshop, SNL (Aug. 2005).
14. Rickman, W., & Goodin, D., "Cost Modeling for Fabrication of Direct Drive Inertial Fusion Energy Targets," Fusion Science and Technolgy, 43, 353 (2003).
15. Meier, W.R., "Systems Modeling and Analyses – Progress Update and Recent Results," HAPL Project Meeting (ORNL, MARch 21-22, 2006), LLNL document UCRL-PRES-219894.
16. Stygar, W.A., Cuneo, M.E., Headley, D.I, Ives, H.C., Leeper, R.J., Mazarakis, M.G., Olson, C.L., Porter, J.L., Wagoner, T.C; Architecture of PetaWatt-class Z-Pinch Accelerators; Unpublished draft; 2006.
17. Ulrich, G.D., Vasudevan, P.T.; Chemcial Engineering Process Design Process Design and Economics a Practical Guide; 2nd edition; Process Publishing; 2004; ISBN 0-9708768-2-3.
18. Chemical Engineering Magazine ongoing feature.
19. http://www.eia.doe.gov/; U.S. Department of Energy, Energy Information Administration.
20. http://www1.jsc.nasa.gov/bu2/learn.html NASA; Cost Estimating Web Site; Learning Curve Calculator

21. Dostal, V., Driscoll, M.J., Hejzlar, P., Wang, Y., "Supercritical CO2 cycle for Fast Gas-Cooled Reactors," Proceedings of ASME Turbo Expo 2004, Power for Land, Sea, and Air, June 14-17, Vienna, Austria, 2004.
22. Pikard, P., Energy Conversion, Workshop for Universities, Githersburg, MD, 2004.
23. Williams, S. & Causey R., Personal communication on Tritium recovery and processing. DIFFUSE models, Sandia National Laboratory, Livermore, July 2006.
24. Baskes, M.I.; DIFFUSE-83; SAND83-8231; 1983.
25. Serra, E., Benamati, G., Ogorodnikova, O.V., Hydrogen isotopes transport parameters in fusion reactor materials; J. Nucl. Mater.; 255 (1998) 105.
26. Sugisaki, M., Furuya, H., Ueki, H., Ejima, S.; Surface Reaction and Bulk Diffusion of Tritium in SUS-316 Stainless Steel; J. Nucl. Mater.; 133&134 (1985) 280
27. Sugisaki, M., Furuya, H., Ono, K, Idemitsu, K., Tritium Solubility in SUS-316 Stainless Steel; J. Nucl. Mater.; 120 (1984) 36.
28. Hollenberg, G.W., Simonen, E.P., Kalinin, G., Terlain, Tritium/hydrogen barrier development; Fusion Eng. & Design 28 (1995) 190.
29. Abdou, M., Schmitz, L., Ying, A., Sketchley, T., & Tajima, Y., "UCLA Research Activities in Support of the Z-Pinch IFE Program – Final Report for FY06," University of California at Los Angles (2006).
30. Calderoni, P., Schmitz, L., & Ying, A., Progress Report to Sandia National Laboratories (1995).
31. Cipiti, B., "RTL Manufacturing Plant Options: Z-Pinch IFE Final Report," Sandia National Laboratories (2005).
32. Morrow, C. et al., "ZIFE Project Process Flow Sheet Preparation for Z-Pinch Driven Fusion Power Plant," Sandia National Laboratories (2005).
33. Moir, R., Personal Correspondence, Lawrence Livermore National Laboratories (2006).
34. Chase, W.M., "JANAF Thermochemical Tables," Journal of Physics and Chemistry Ref. Data, 14, Suppl. 1 (1985).
35. Baes, C.F., "The Chemistry and Thermodynamics of Molten Salt Reactor Fuels," Journal of Nuclear Mateials, 51, (1974) 149.
36. Nishimura, H. et al., "Chemical Behaviour of Li2BeF4 Molten Salt as a Liquid Tritium Breeder" Fusion Engineering and Design, 58-59 (2001) 667.
37. Schmitz, L., Calderoni, P., Ying, A., & Abdou, M., JNM 337-339 (2005) 1096.
38. Griem, H., "Plasma Spectroscopy" McGraw Hill, New York (1984), pp. 267.
39. Gardiner, W.C., "Combustion Chemistry, Springer, New York (1984), pp. 177.
40. Chan, X.M., Schrock, V.E., & Peterson, P.F., Fusion Technology 21 (1992) 1536.

4 Chamber Design and Shock Mitigation

41. Kryukov, A.M., Nikolaev, Yu.A, & Nikolaeva, A.V., "Behavior of Mechanical Properties of Nickel-Alloyed Reactor Pressure Vessel Steel Under Neutron Irradiation and Post-Irradiation Annealing," Nuclear Engineering and Design, 186, p. 535-359, (1998).
42. Romero, D.H., Personal interview July 2006, Sandia National Laboratories
43. Brunner, T.A. et al., "A User's Guide to Radiation Transport in ALEGRA-HEDP, Version 4.7-beta," Sandia National Laboratories, SAND200x.
44. Brunner, T.A. et al., "ALEGRA-HEDP: Version 4.6 (revised)," Sandia National Laboratories, SAND2005-draft, February 2005.

45. Haill, T.A. et al., "ALEGRA-MHD: Version 4.6," Sandia National Laboratories, SAND2004-5997, January 2005.
46. Bindhu, C.V. et al., "Laser Propagation and Energy Absorption by an Argon Spark," *Journal of Applied Physics,* 94, 12, p. 7402-7407 (2003).
47. Harilal, S.S., "Spatial and Temporal Evolution of Argon Sparks," Applied Optics, 43, 19, July 2004.
48. Harilal, S.S., Personal communication, University of California at San Barbra, September 2006.
49. Olson, C. et al., "Z-Pince IFE Program: Final Report for FY04," Sandia National Laboratories, SAND-2005-2742P (2005).
50. Abbot, R.P., "Z-IFE Chamber Design and Modeling," Lawrence Livermore National Laboratory, Z-IFE Program Workshop August 2, 2005
51. Bardet, P.M., Abbott, R.P., Campen, C., Franklin, J., Zhao, H., & Peterson, P.F., "Experiment Investigation of Z-Pinch IFE Chamber Liquid Structure Response," University of California at Berkeley (2006).
52. Peterson, P.F., "Design Methods for Thick-Liquid Protection of Inertial Fusion Chambers," Fusion Technology, 39 (2) (2001) 702-710.
53. Pemberton, S., Jantzen, C., Kuhn, J., & Peterson, P.F., "Partial-Pocket Experiments for IFE Thick-Liquid Pocket Disruption and Clearing," Fusion Technology, 39 (2001) 726-731.
54. Rao, D.M., "Method of Flow Stabilixation with High Pressure Recovery in Short, Conical Diffusers," Aeronautical Journal, 75(725) (1971) 336.
55. Bardet, P.M., Debonnel, C.S., Freeman, J., Fukuda, G., Supiot, B., & Peterson, P.F., "Dynamics of Liquid-Protected Fusion Chambers," Fusion Science and Technology, 47(2005) 626-636.
56. Cooper, P.W., *Explosives Engineering,* Wiley-Verlach, New York, NY, 1996.
57. Kern, B., Abdel-Khalik, S.I., & Ghiaasiaan, S.M., "Void Fraction Distribution in Two-Phase (Gas-Liquid) Jets for Z-Pinch IFE Reactor Applications," Georgia Institute of Technology, Z-IFE (2006).
58. Anderson, M., Oakley, J., Marriott, E., Gudmundson, J., Sridharan, K., Vigil, V., Rochau, G., & Bonazza, R., "Shock Mitigation Studies in Voided Liquids for Fusion Chamber Protection," University of Wisconsin- Z-IFE FY06 Final Report, Madison, WI, 2006.
59. Moir, R., "HYLIFE-II: A Molten-Salt Inertial Fusion Energy Power Plant Design-Final Report," Fusion Technology, 25, 5-25 (1994).
60. Olson, C. et al., "Development Path for Z-Pinch IFE," Fusion Science and Technology, 47, 633-640 (2005).
61. Kitagawa, K., Yokoyama, M., & Yasuhara, M., "Attenuation of Shock Waves by Porous Materials," 24th International Symposium on Shock Waves Proceedings, Beijing, China, Paper 2692 (2004).
62. Anderson, M.H., Oakley, J.G., Vigil, V., Rodriquez, S., & Bonazza, R., "The Dynamics of a Shock Wave and Aluminum Foam Layer Interaction," 25th International Symposium on Shock Waves Proceedings, Bangalore, India, Paper 1197 (2005).
63. Anderson, M.H., Puranik, B.P., Oakley, J.G., Brooks, P.W., & Bonazza, R., "Shock Mitigation Studies of Solid Foams for Z-Pinch Chamber Protection," report following the Z-Pinch IFE Workshop, Sandia National Laboratories, Albuquerque, NM, Aug 1-2, 2005.
64. Anderson, M.H., Puranik, B.P., Oakley, J.G., Brooks, P.W., & Bonazza, R., "Shock Tube Investigation of Hydrodynamic Issues Related to Inertial Confinement Fusion," Shock Waves, 10, 5, 377-387 (2000).

65. Gibson, L.J., & Ashby, M.F., "Cellular Solids, Structure & Properties," Pergamon Press, Oxford, 1988.
66. Energy Research and Generation, Inc. "Duocell Aluminum Foam Brochure," 900 Stanford Ave., Oakland, CA, (510) 658-9758.
67. Heltemes, T.A., Marriott, E.P., Moses, G.A., Peterson, R.R., "Z-Pinch (LiF)2-BeF2 (flibe) Preliminary Vaporization Estimation Using the BUCKY 1-D Radiations Hydrodynamic Code," 21st IEEE/NPSS Symposium on Fusion Energy (SOFE), 26-29 Sept. 2005, Knoxville, TN.
68. 10 CFR 61.55, Technical Requirements for Land Disposal Facilities, Waste Classification.
69. American Society of Mechanical Engineers, "ASME Boiler and Pressure Vessel Code," New York, NY: ASME (2004).
70. Special Metals Corporation, Downloaded from the World Wide Web July3, 2005, www.specialmetals.com.
71. A.F. Tavassoli, J.-W. Rensman, M. Schirra, K. Shiba, "Materials Design Data for Reduced Activation Martensitic Steel type F82H", Fusion Engineering and Design, 2002, Volume 61-62, pp 617-628.
72. Zinkle, S.J., Robertson, J.P, and Klueh, R.L., "Thermophysical and Mechanical Properties of Fe-(8-9)%Cr reduced activation steels," Fusion Materials 24: Semiannual Progress Report (1998), 135-43.
73. Pierson, H.O., "Handbook of Carbon, Graphite, Diamond and Fullerenes – Properties, Processing and Applications," William Andrew Publishing/Noyes (1993).
74. Papakonstantinou, C.G., Balaguru, P., and R.E. Lyon, "Comparative study of high temperature composites," Composites: Part B 32 (2000), 637-49.
75. Mager, T.R., "Thermal Annealing of an Embrittled Reactor Vessel: Feasibility and Methodology," Nuclear Engineering and Design, 124, p.43-51 (1990).
76. Reijo, P., & Torronen, K., "On Thermal Annealing of Irradiated PWR Pressure Vessels," International Journal of Pressure Vessels and Piping, 75, p. 1075-1095 (1998).
77. Vassilaros, M.G., Mayfield, M.E., & Wichman, K.R., "Annealing of Nuclear Reactor Pressure Vessels," Nuclear Engineering and Design, 181, p.61-69 (1998).
78. Reith, M., Dafferner, B., Rohrig, H.D., "Charpy Impact Properties of Low Activation Alloys for Fusion Applications after neutron Irradiation," Journal of Nuclear Material, 233-237 (1996) p. 351-355.
79. "Introduction to Fusion Power Plant Materials," Downloaded from the World Wide Web: http://www.msm.cam.ac.uk/phase-trans/2006/Irradiated_Steel/Irradiated_Steel.html#SECTION00232000000000000000
80. "Materials for the Plasma-Facing Components of Steady State Stellarators" Down loaded from the World Wide Web: <http://www-fusion.ciemat.es/SW2005/talks/BoltH_Talk.pdf>
81. Irradiation Behavior of Three Candidate Structural Materials for ADS Systems: EM10, T91, and HT9 (F/M Steels)," Downloaded from the World Wide Web. <http://www.extremat.org/media/static/Paper%201116%20-%20Lucon1.pdf>
82. Shiba, et al., "Tensile results of low-activation martensitic steel irradiated in HFIR RB-11J and RB-12J spectrally tailored capsules", Fusion Materials Semiannual Progress Report (DOE/ER-0313/28) pp.131-135, June 2000.
83. Depreist, Kendall Russell, Org. 01384, *communication*, July 2006.
84. Zinkle, S.J., Robertson, J.P., Klueh, R.L., "Thermophysical and Mechanical Properties for Fe-(8-9)%Cr reduced activation steels" Oak Ridge National Laboratory <http://www-ferp.ucsd.edu/LIB/PROPS/FS/FS.html#8>.

85. Hishinuma, A. Kohyama, R.L. Klueh, D.S. Gelles, W. Dietz, K. Ehrlich, “Current status and future R&D for reduced-activation ferritic/martensitic steels” Journal of Nuclear Materials, 1998, Volume 258-263, pp. 193-204.
86. Kohno, Y., Gelles, O.S., Kohyama, A., Tamura, M., Hamilton, M.L., “Irradiation Response of F82H, a Reduced Activation Fe-8Cr-2W Martensitic Steel” Fusion Materials Semi-Annual Progress Reports, 1991, Volume 10, pp. 78-85.
87. Miwa, Y., Jitsukawa, S., Yonekawa, M., “Fatigue properties of F82H irradiated at 523K to 3.8 dpa”, Journal of Nuclear Materials, 2004, Volume 329-333, pp. 1098-1102.
88. Shiba, K., Enoeda, M., Jitsukawa, J., “Reduced Activation Martensitic Steels as a Structural Material for ITER Test Blanket” Journal of Nuclear Materials, 2004, Volume 329-333, pp. 243-247.
89. Shiba, K., Klueh, R.L., Miwa, Y., Robertson, J.P, Hishinuma, A., “Tensile Behavior of F82H with and without Spectral Tailoring”, Journal of Nuclear Materials, 2000, Volume 283-287, pp. 358-361.
90. Shiba, K., Yamanouchi, N., Tohyama, A., “Preliminary Results of the Round-Robin Testing of F82H”, Fusion Materials Semi-Annual Progress Reports, 1996, Volume 20, pp 190-194.
91. Hirose, T., Tanigawa, H., Ando, M., Kohyama, A., Katoh, Y., Narui, M., “Radiation Effects on Low Cycle Fatigue Properties of Reduced Activation Ferritic/Martensitic Steels”, Journal of Nuclear Materials, 2002, Volume 307-311, pp. 304-307.

DISTRIBUTION

Wayne Meier (Lawrence Livermore National Laboratory)
Ralph Moir (Lawrence Livermore National Laboratory)
Per F. Peterson (University of California at Berkeley)
Philippe M. Bardet (University of California at Berkeley)
Chris Campen (University of California at Berkeley)
James Franklin (University of California at Berkeley)
Haihua Zhao (University of California at Berkeley)
Gerald Kulcinski (University of Wisconsin)
Mark Anderson (University of Wisconsin)
Jason Oakley (University of Wisconsin)
Ed Marriott (University of Wisconsin)
Jesse Gudmundson (University of Wisconsin)
Kumar Sridharan (University of Wisconsin)
Riccardo Bonazza (University of Wisconsin)
Virginia Vigil (University of Wisconsin)
Mohamed Abdou (University of California at Los Angles)
Lothar Schmitz (University of California at Los Angles)
Alice Ying (University of California at Los Angles)
Tomas Sketchley (University of California at Los Angles)
Yu Tajima (University of California at Los Angles)
Said Abdel-Khalik (Georgia Institute of Technology)
Brain Kern (Georgia Institute of Technology)
M. Ghiaasiaan (Georgia Institute of Technology)

1	MS0123	D. Chavez, LDRD Office	01011
1	MS0513	Rick Stulen	01000
1	MS0701	Peter Davies	06700
1	MS0719	Paul McConnell	06793
1	MS0724	Les Shephard	06000
1	MS0736	Ron Lipinski	06771
1	MS0736	JD Smith	06772
1	MS0748	Ben Cipiti	06763
1	MS0748	Virginia Cleary	06761
1	MS0748	Jason Cook	06763
1	MS0748	Sam Durbin	06763
1	MS0748	Cathy Farnum	06763
1	MS0748	Rodney Keith	06763
1	MS0748	Charlie Morrow	06763
1	MS0748	Gary Rochau	06763
1	MS0748	Sal Rodriguez	06763
1	MS0748	Matt Turgeon	06764
1	MS0748	Mike Young	06763
1	MS0771	Dennis Berry	06800
2	MS0899	Technical Library	04536
1	MS1190	Keith Matzen	01600
1	MS1190	Craig Olson	01600
2	MS9018	Central Technical Files	08944